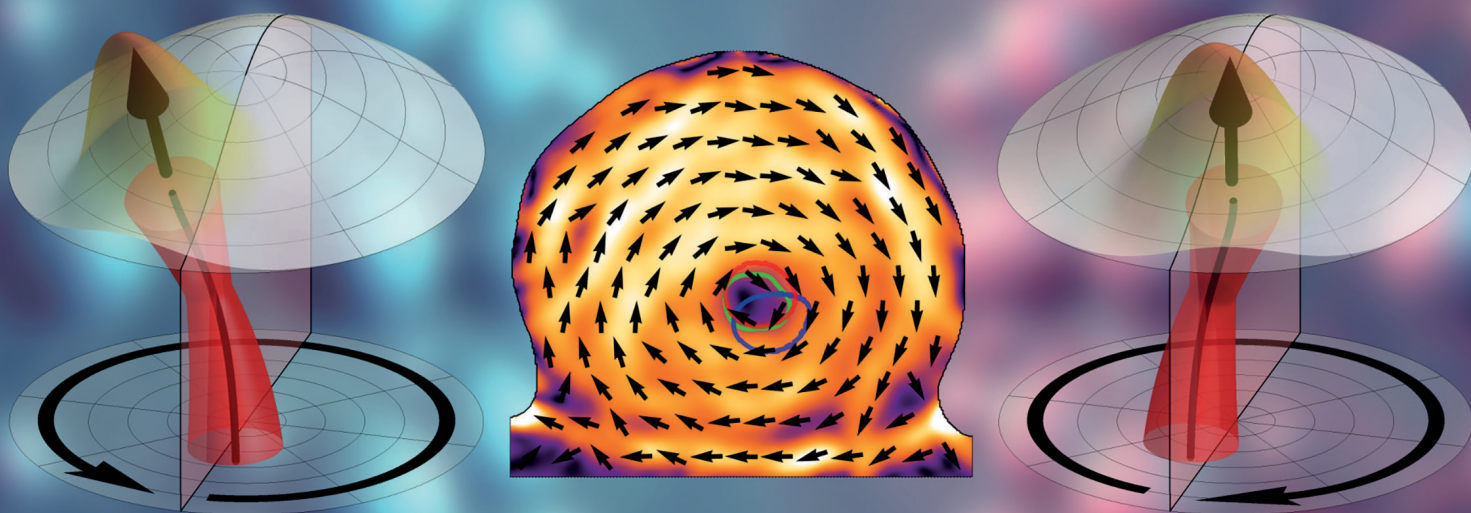


ANNUAL REPORT 2023

Institute of Ion Beam Physics
and Materials Research



Wissenschaftlich-Technische Berichte
HZDR-129

Annual Report 2023

**Institute of Ion Beam Physics
and Materials Research**

Editors

J. Fassbender, M. Helm,
M. Zahn, P. Zahn

Cover Picture - New dimension of chirality coupling in topological magnetic textures

Symmetry effects are fundamental in condensed matter physics as they define not only interactions but also the resulting responses of the intrinsic order parameter, depending on its transformation properties with respect to the operations of space inversion and time reversal. In magnetism, chiral effects can be obtained through the inversion symmetry breaking within the lattice unit cell or the sample's shape. Here, we demonstrate experimentally and theoretically the existence of a static homochiral 3D texture characterized by two magnetochiral parameters being magnetic helicity of the vortex and geometrical chirality of the core string itself in a cap-like asymmetric permalloy ($\text{Ni}_{81}\text{Fe}_{19}$) structure.

The figure shows two possible homochiral deformations of the vortex string depending on the sign of the vortex helicity: for positive helicity, the vortex core has a right-handed rotation (left panel), while for negative helicity, the vortex core is left-handed (right panel). The central panel shows the experimentally observed vortex core in an asymmetric cap structure, with green, red, and blue lines depicting the detected core position and the calculated ones for positive and negative vortex helicities, respectively.

Image: © HZDR / Oleksii Volkov

For further information see:

Volkov, O.; Wolf, D.; Pylypovskyi, O.; Kakay, A.; Sheka, D.D.; Büchner, B.; Faßbender, J.; Lubk, A.; Makarov, D.

Chirality coupling in topological magnetic textures with multiple magnetochiral parameters
Nature Communications **14**, 1491 (2023), DOI: [10.1038/s41467-023-37081-z](https://doi.org/10.1038/s41467-023-37081-z)

Many thanks for providing material and for technical assistance to: S. Gebel, S. Kirch, T. Grüning, M. Hiller, A. Wagner, O. Volkov, E. Dimakis, V. Iurchuk.

Print edition: ISSN 2191-8708

Electronic edition: ISSN 2191-8716

The electronic edition is published under Creative Commons License (CC BY-NC-ND 4.0):

URN: [urn:nbn:de:bsz:d120-qucosa2-910724](https://nbn-resolving.org/urn:nbn:de:bsz:d120-qucosa2-910724)

URL: www.hzdr.de/publications/Publ-39003

Published by Helmholtz-Zentrum Dresden - Rossendorf e.V.

This report is also available at <https://www.hzdr.de/FWI>.

Helmholtz-Zentrum Dresden - Rossendorf e.V.

Institute of Ion Beam Physics and Materials Research (IIM)

Bautzner Landstraße 400

01328 Dresden

Germany

Directors

Prof. Dr. M. Helm

Prof. Dr. J. Fassbender

Phone

+49 351 260 2260

+49 351 260 3096

Fax

+49 351 260 3285

+49 351 260 3285

Email

m.helm@hzdr.de

j.fassbender@hzdr.de

www.hzdr.de/FWI

Preface by the directors

The year 2023 was highly successful, marked by significant high-level publications and the acquisition of new projects. The latter is increasingly crucial given the tight budget in 2023, which is expected to become even tighter in 2024 due to rising costs and well-deserved salary increases for our employees. As a result, we must reduce the number of our non-permanent scientific staff, which will impact future productivity.

Despite these challenges, our performance in 2023 remained outstanding with a total of 178 refereed publications and an average impact factor of 8.1. Notable publications include 8 from the Nature Publishing Group, 7 from Advanced (Functional) Materials, 4 from ACS Nano, and 2 from Angewandte Chemie. Our excellence was further recognized by the HZDR Research Award, which again went to our Institute, this time awarded to Dr. Oleksii Volkov and Dr. Oleksandr Pylypovskyi from the Department of Intelligent Materials and Devices for their theoretical and experimental investigations into chiral symmetry breaking in magnetic 3D textures. Furthermore, Dr. Lukas Körber, who completed his PhD in 2023 with summa cum laude, was the recipient of both the Helmholtz Doctoral Award in the research field of Matter and the HZDR Doctoral Award. Prof. Manfred Helm was honored as an APS Fellow.

In 2023, the majority of newly approved projects are financed by the Saxonian Ministry of Science, Culture and Tourism and the Helmholtz Initiative and Networking Fund which is a confirmation of the application relevance of our research.

Our infrastructure upgrades are progressing as planned. The new AMS (Accelerator Mass Spectrometry) building was handed over to us in fall 2023. This year, we anticipate the arrival of our new 1 MV accelerator, which will be a dedicated AMS system. We aim to achieve full user operation by 2025.

Finally, we extend our heartfelt thanks to all partners, friends, and organizations who supported our progress in 2023. We are particularly grateful to the Executive Board of the Helmholtz-Zentrum Dresden-Rossendorf, the Ministry of Science, Culture and Tourism of the Free State of Saxony, and the Federal Ministries of Education and Research, and of Economic Affairs and Climate Action. Many partners from universities, industry, and research institutes worldwide have been essential to our development. Lastly, the directors wish to thank all members of our institute for their exceptional efforts and contributions in these extraordinary times.



Prof. Manfred Helm



Prof. Jürgen Fassbender

Contents

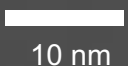
Selected Publications

Copyright remarks	9
Coupling of terahertz light with nanometre wavelength magnon modes via spin-orbit torque	11
Salikhov, R.; Ilyakov, I.; Körber, L.; Kákay, A.; Gallardo, R.A.; Ponomaryov, A.; Deinert, J.-C.; de Oliveira, T.V.A.G.; Lenz, K.; Fassbender, J.; Bonetti, S.; Hellwig, O.; Lindner, J.; Kovalev, S.	
Integration of Multifunctional Epitaxial (Magnetic) Shape Memory Films in Silicon Microtechnology	20
Fink, L.; Kar, S.; Lünser, K.; Nielsch, K.; Reith, H.; Fähler, S.	
Pattern recognition in reciprocal space with a magnon-scattering reservoir	27
Körber, L.; Heins, C.; Hula, T.; Kim, J.-V.; Thlang, S.; Schultheiss, H.; Fassbender, J.; Schultheiss, K.	
Ferromagnetic Interlayer Coupling in CrSBr Crystals Irradiated by Ions	34
Long, F.; Ghorbani-Asl, M.; Mosina, K.; Li, Y.; Lin, K.; Ganss, F.; Hübner, R.; Sofer, Z.; Dirnberger, F.; Kamra, A.; Krasheninnikov, A.V.; Prucnal, S.; Helm, M.; Zhou, S.	
Novel Mixed-Dimensional hBN-Passivated Silicon Nanowire Reconfigurable Field Effect Transistors: Fabrication and Characterization	40
Ghosh, S.; Khan, M.B.; Chava, P.; Watanabe, K.; Taniguchi, T.; Prucnal, S.; Hübner, R.; Mikolajick, T.; Erbe, A.; Georgiev, Y.M.	
Giant THz Nonlinearity in Topological and Trivial HgTe-Based Heterostructures	50
Uaman Svetikova, T.A.; de Oliveira, T.V.A.G.; Pashkin, A.; Ponomaryov, A.; Berger, C.; Fürst, L.; Bayer, F.B.; Novik, E.G.; Buhmann, H.; Molenkamp, L.W.; Helm, M.; Kiessling, T.; Winnerl, S.; Kovalev, S.; Astakhov, G.V.	
Atom counting with accelerator mass spectrometry (Abstract)	57
Kutschera, W.; Jull, A.J.T.; Paul, M.; Wallner, A.	
Roadmap for focused ion beam technologies (Abstract)	58
Höflich, K.; Hobler, G.; Allen, F.I.; Wirtz, T.; Rius, G.; McElwee-White, L.; Krasheninnikov, A.V.; Schmidt, M.; Utke, I.; Klingner, N.; Osenberg, M.; Córdoba, R.; Djurabekova, F.; Manke, I.; Moll, P.; Manoccio, M.; De Teresa, J.M.; Bischoff, L.; Michler, J.; De Castro, O.; Delobbe, A.; Dunne, P.; Dobrovolskiy, O.V.; Frese, N.; Götzhäuser, A.; Mazarov, P.; Koelle, D.; Möller, W.; Pérez-Murano, F.; Philipp, P.; Vollnhals, F.; Hlawacek, G.	
Band-to-band tunneling switches based on two-dimensional van der Waals heterojunctions (Abstract)	60
Chava, P.; Fekri, Z.; Vekariya, Y.; Mikolajick, T.; Erbe, A.	
Statistics	
User facilities and services	63
Ion Beam Center (IBC)	63
Free Electron Laser (FELBE)	65
Experimental equipment	66
Doctoral training programme	72
Publications	73
Patents	90
Concluded scientific degrees	93
Awards and honors	94

Invited conference contributions	96
Conferences, workshops, colloquia and seminars	101
Exchange of Researchers	105
Projects	106
Organization chart	111
List of personnel	112

Selected Publications

Image: HZDR / E. Dimakis, R. Hübner



10 nm

Copyright remarks

The following journal articles are reprinted with kind permission from:

Coupling of terahertz light with nanometre wavelength magnon modes via spin-orbit torque

Salikhov, R.; Ilyakov, I.; Körber, L.; Kákay, A.; Gallardo, R.A.; Ponomaryov, A.; Deinert, J.-C.; de Oliveira, T.V.A.G.; Lenz, K.; Fassbender, J.; Bonetti, S.; Hellwig, O.; Lindner, J.; Kovalev, S. *Nature Physics* **13**, 529-535 (2023)

© 2023 The Authors.



Creative Commons BY-4.0 License

DOI: 10.1038/s41567-022-01908-1

Integration of Multifunctional Epitaxial (Magnetic) Shape Memory Films in Silicon Microtechnology

Fink, L.; Kar, S.; Lünser, K.; Nielsch, K.; Reith, H.; Fähler, S.

Advanced Functional Materials **33**, 2305273 (2023)

© 2023 The Authors. Published by Wiley-VCD GmbH, Weinheim



Creative Commons BY-4.0 License

DOI: 10.1002/adfm.202305273

Pattern recognition in reciprocal space with a magnon-scattering reservoir

Körber, L.; Heins, C.; Hula, T.; Kim, J.-V.; Thlang, S.; Schultheiss, H.; Fassbender, J.; Schultheiss, K. *Nature Communications* **14**, 3954 (2023)

© 2023 The Authors



Creative Commons BY-4.0 License

DOI: 10.1038/s41467-023-39452-y

Ferromagnetic Interlayer Coupling in CrSBr Crystals Irradiated by Ions

Long, F.; Ghorbani-Asl, M.; Mosina, K.; Li, Y.; Lin, K.; Ganss, F.; Hübner, R.; Sofer, Z.; Dirnberger, F.; Kamra, A.; Krasheninnikov, A.V.; Prucnal, S.; Helm, M.; Zhou, S.

Nano Letters **23**, 8468-8473 (2023)

© 2023 The Authors. Published by American Chemical Society



Creative Commons BY-4.0 License

DOI: 10.1021/acs.nanolett.3c01920

Novel Mixed-Dimensional hBN-Passivated Silicon Nanowire Reconfigurable Field Effect Transistors: Fabrication and Characterization

Ghosh, S.; Khan, M.B.; Chava, P.; Watanabe, K.; Taniguchi, T.; Prucnal, S.; Hübner, R.; Mikolajick, T.; Erbe, A.; Georgiev, Y.M.

ACS Applied Materials and Interfaces **15**, 40709-40718 (2023)

© 2023 The Authors. Published by American Chemical Society



Creative Commons BY-4.0 License

DOI: 10.1021/acsami.3c04808

Giant THz Nonlinearity in Topological and Trivial HgTe-Based Heterostructures

Uaman Svetikova, T.A.; de Oliveira, T.V.A.G.; Pashkin, A.; Ponomaryov, A.; Berger, C.; Fürst, L.; Bayer, F.B.; Novik, E.G.; Buhmann, H.; Molenkamp, L.W.; Helm, M.; Kiessling, T.; Winnerl, S.; Kovalev, S.; Astakhov, G.V.

ACS Photonics **10**, 3708-3714 (2023)

© 2023 The Authors. Published by American Chemical Society



Creative Commons BY-4.0 License

DOI: 10.1021/acsphotonics.3c00867

Atom counting with accelerator mass spectrometry

Kutschera, W.; Jull, A.J.T.; Paul, M.; Wallner, A.

Review of Modern Physics **95**, 035006 (2023)

© 2023 American Physical Society

DOI: 10.1103/RevModPhys.95.035006

Roadmap for focused ion beam technologies

Höflich, K.; Hobler, G.; Allen, F.I.; Wirtz, T.; Rius, G.; McElwee-White, L.; Krasheninnikov, A.V.; Schmidt, M.; Utke, I.; Klingner, N.; Osenberg, M.; Córdoba, R.; Djurabekova, F.; Manke, I.; Moll, P.; Manocchio, M.; De Teresa, J.M.; Bischoff, L.; Michler, J.; De Castro, O.; Delobbe, A.; Dunne, P.; Dobrovolskiy, O.V.; Frese, N.; Götzhäuser, A.; Mazarov, P.; Koelle, D.; Möller, W.; Pérez-Murano, F.; Philipp, P.; Vollnhals, F.; Hlawacek, G.

Applied Physics Reviews **10**, 041311 (2023)

© 2023 The Authors. Published by AIP Publishing



Creative Commons BY-4.0 License

DOI: 10.1063/5.0162597

Band-to-band tunneling switches based on two-dimensional van der Waals heterojunctions

Chava, P.; Fekri, Z.; Vekariya, Y.; Mikolajick, T.; Erbe, A.

Applied Physics Reviews **10**, 011318 (2023)

© 2023 Author(s). Published under an exclusive license by AIP Publishing

DOI: 10.1063/5.0130930



Coupling of terahertz light with nanometre-wavelength magnon modes via spin-orbit torque

Received: 18 May 2022

Accepted: 2 December 2022

Published online: 30 January 2023

Ruslan Salikhov¹✉, Igor Ilyakov², Lukas Körber^{1,3}, Attila Kákay¹, Rodolfo A. Gallardo⁴, Alexey Ponomaryov², Jan-Christoph Deinert^{1,2}, Thales V. A. G. de Oliveira^{1,2}, Kilian Lenz¹, Jürgen Fassbender^{1,3}, Stefano Bonetti^{5,6}, Olav Hellwig^{1,7}, Jürgen Lindner¹ & Sergey Kovalev²✉

Spin-based technologies can operate at terahertz frequencies but require manipulation techniques that work at ultrafast timescales to become practical. For instance, devices based on spin waves, also known as magnons, require efficient generation of high-energy exchange spin waves at nanometre wavelengths. To achieve this, a substantial coupling is needed between the magnon modes and an electro-magnetic stimulus such as a coherent terahertz field pulse. However, it has been difficult to excite non-uniform spin waves efficiently using terahertz light because of the large momentum mismatch between the submillimetre-wave radiation and the nanometre-sized spin waves. Here we improve the light-matter interaction by engineering thin films to exploit relativistic spin-orbit torques that are confined to the interfaces of heavy metal/ferromagnet heterostructures. We are able to excite spin-wave modes with frequencies of up to 0.6 THz and wavelengths as short as 6 nm using broadband terahertz radiation. Numerical simulations demonstrate that the coupling of terahertz light to exchange-dominated magnons originates solely from interfacial spin-orbit torques. Our results are of general applicability to other magnetic multilayered structures, and offer the prospect of nanoscale control of high-frequency signals.

The increasing demand for fast and energy-efficient communication and data processing stimulates new concepts for terahertz spintronics and magnonics. These concepts require ultrafast (that is, at timescales of picoseconds and below) manipulation of the magnetic spin degree of freedom for the generation of spin currents and short-wavelength magnons at terahertz frequencies^{1–3}. Owing to their terahertz spin dynamics, antiferromagnetic materials have been the particular focus of

research within the past decade^{4–6}. Terahertz spin pumping via antiferromagnetic magnon excitations can also be realized, as demonstrated recently^{7,8}. To generate resonant excitations at terahertz frequencies in technologically relevant metallic ferromagnets, high-energy spin waves have been proposed^{9–14}. In these studies, nanoscale-wavelength spin waves are launched by making use of laser-pulse-driven spin currents—that is, optically induced spin-polarized electrons that move

¹Institute of Ion Beam Physics and Materials Research, Helmholtz-Zentrum Dresden-Rossendorf, Dresden, Germany. ²Institute of Radiation Physics, Helmholtz-Zentrum Dresden-Rossendorf, Dresden, Germany. ³Fakultät Physik, Technische Universität Dresden, Dresden, Germany. ⁴Departamento de Física, Universidad Técnica Federico Santa María, Valparaíso, Chile. ⁵Department of Physics, Stockholm University, Stockholm, Sweden. ⁶Department of Molecular Sciences and Nanosystems, Ca' Foscari University of Venice, Venice, Italy. ⁷Institute of Physics, Chemnitz University of Technology, Chemnitz, Germany. ✉e-mail: r.salikhov@hzdr.de; s.kovalev@hzdr.de

Article

into the interface region of an adjacent ferromagnetic layer. There, the net angular momentum flow creates a spin-transfer torque that acts on the magnetization, consequently exciting high-frequency spin dynamics. As a result, an interface-localized broadband wave packet of nanometre-wavelength magnons launches from the top surface into the depth of the ferromagnetic layer¹¹, followed by its reflection at the layer's bottom surface. This finally results in perpendicular standing spin waves (PSSW), which are detected by using magneto-optical techniques^{9–14}.

Besides optical light, broadband terahertz radiation has been suggested as a means to access ultrafast magnetization dynamics^{15–25}. In this case, the magnetic field component of the terahertz pulse is coherently coupled to the spin system via the Zeeman interaction, and accordingly results in a torque that drives magnetization dynamics at picosecond timescales^{15–24}. However, the excitation of non-uniform and short-wavelength coherent spin waves using a terahertz light source has not been reported yet. This is due to the very inefficient coupling involved, as the momentum of the terahertz light and that of short-wavelength magnons are different by orders of magnitude. Here we overcome this obstacle and demonstrate an efficient and coherent excitation of nanometre-wavelength spin-wave modes in Ta/Py/Pt (where Py is Ni₈₁Fe₁₉) trilayers using a broadband terahertz pulse with about 1 ps duration. Unlike the above-mentioned excitation schemes, the coupling of the terahertz radiation to the spin waves is realized via the spin-orbit torque (SOT)²⁶, which has been predicted to be efficient even at terahertz frequencies^{27,28}. We used a single-cycle terahertz pulse to induce a current in the Ta and Pt metallic layers. This electrical current was then converted into a spin current via the spin Hall effect, which in turn generated a torque acting on the magnetization of the Py layer. Owing to the strong localization of the spin polarization, short-wavelength coherent magnons were excited at the two Py interfaces, and propagated towards each other, resulting in PSSW modes. We demonstrate that the terahertz SOT induces PSSW modes in Py films of 6–12 nm thickness with mode dispersion in agreement with the exchange-dominated analytical relation of the spin-wave-resonance (SWR) frequency $f_{\text{SWR}}(k)$ (Kittel formula) given by:

$$2\pi f_{\text{SWR}} = 2\pi f_0 + (D_{\text{ex}}/\hbar)k^2. \quad (1)$$

In equation (1) f_0 is the uniform mode frequency of the ferromagnetic layer, D_{ex} is the exchange stiffness parameter, \hbar is the reduced Planck constant and $k = \pi n/d_{\text{py}}$ is the wavenumber, which is indexed by the number of nodes, n , in the Py layer of thickness d_{py} . As we show below, no PSSW modes were detected in Ta/Py/Ta and Pt/Py/Pt trilayers with symmetric interfaces, confirming that the direct coupling of the magnetic field of the terahertz radiation to the Py layer cannot be the source of the detected spin waves.

Experiment

To study spin dynamics, we employed time-resolved magneto-optics in a Faraday configuration, as schematically shown in Fig. 1a. An intense single-cycle terahertz pulse is focused onto a trilayer sample and the sample's magnetization state is then probed by polarization rotation of a delayed 100 fs probe pulse with a central wavelength of 800 nm. The terahertz and probe pulses are collinear and have normal incidence with respect to the sample surface. In this configuration, the polarization of the probe pulse is sensitive to the out-of-plane (z axis) magnetization component, which is driven by the terahertz radiation. A more detailed description of the pump-probe experiment is provided in the Methods.

We studied Ta(3 nm)/Py(9 nm)/Pt(2 nm) samples, as shown in Fig. 1a (the thickness of each individual layer is given in parentheses). As reference samples, we also used Ta(3 nm)/Py(9 nm)/Ta(3 nm) and Pt(2 nm)/Py(9 nm)/Pt(2 nm) samples with symmetric interfaces. All samples were deposited on transparent double-sided polished quartz glass, as well as on Al₂O₃ substrates with a substrate thickness of 3 mm.

Different substrates are used to account for the back-reflected terahertz signal in transmission geometry. We employed a 50 mT external magnetic field (\mathbf{H}_{Ext}) to keep the samples magnetically saturated with the magnetization (\mathbf{M}) in the film plane, with the option to make it parallel or orthogonal to the magnetic field component of the incident terahertz pulse (\mathbf{H}_{THz}).

Figure 1b presents a comparison of the time-resolved magnetization dynamics in asymmetric Ta/Py/Pt versus symmetric Ta/Py/Ta samples (the symmetric Pt/Py/Pt sample shows an identical response to the Ta/Py/Ta; see Supplementary Note 1 and Supplementary Fig. 1). A typical coherent response driven by the Zeeman interaction between the Py magnetization and \mathbf{H}_{THz} (seen as a single-cycle transient of about 1 ps duration) is evident for all samples^{17,20–23}. The Zeeman torque-driven magnetization dynamics in the asymmetric and symmetric samples result in a similar signal, which we will refer to as the Zeeman torque signal (ZTS). In contrast to the samples with symmetric interfaces, once the terahertz pulse has passed through the sample, the signal of the Ta/Py/Pt sample clearly exhibits additional features in the form of oscillations at longer delay times (see the black curve in Fig. 1b). The amplitude of the magnetization's precessional signal, A_{SWR} , is about 7.5% of the ZTS amplitude A_{ZTS} for this particular sample, as indicated by the dashed lines in Fig. 1b. The frequency of the oscillations is calculated to be at 0.29 ± 0.01 THz, which we attribute to the SWR mode with $n = 2$ in equation (1). Both the ZTS and SWR show a linear response with respect to the amplitude of the terahertz field (Supplementary Note 2 and Supplementary Fig. 2), indicating that they are not due to the heat deposited by the radiation. Furthermore, the absence of the SWR in the Ta/Py/Ta (and Pt/Py/Pt) sample suggests that \mathbf{H}_{THz} alone cannot be the driving force for the detected spin-wave excitations. In the following, we show instead that the SOT is the mechanism responsible for the observed magnon modes, employing the characteristic symmetry of SOTs induced by the terahertz field.

To confirm that both ZTS and SWR signals from the Ta/Py/Pt sample are magnetic in origin, we present in Fig. 1c the response of the Ta(3 nm)/Py(8.6 nm)/Pt(2 nm) sample with the magnetization aligned perpendicular (black curve) or parallel (red curve) to \mathbf{H}_{THz} . The vanishing ZTS in the parallel configuration indicates its magnetic origin, since the Zeeman torque is zero for a magnetization oriented parallel to \mathbf{H}_{THz} (ref. 23). Similarly, the SOT is inefficient for electrical fields orthogonal to the in-plane magnetization^{26–30}, hence the SWR signal was not detected. We attribute the small ZTS visible in Fig. 1 to a slight misalignment, possibly also due to a non-ideal polarization of the terahertz field. We also checked the effect of reversing the external magnetic field \mathbf{H}_{Ext} on the Faraday signal (Fig. 1d). Both the coherent and the oscillatory responses reversed their sign on reversal of the sign of \mathbf{H}_{Ext} . The sign inversion of the ZTS was expected, as the Zeeman torque is asymmetric under magnetization reversal²³. The asymmetric behaviour of the SWR signal is a further indication that the SOT is the driving mechanism, as we reason below.

To explain the asymmetric behaviour of the SWR signal in Fig. 1d, we start with the Landau–Lifshitz–Gilbert equation:

$$\partial_t \mathbf{m} = -\gamma(\mathbf{m} \times \mathbf{H}_{\text{eff}}) + \alpha \mathbf{m} \times \partial_t \mathbf{m}. \quad (2)$$

In equation (2) $\mathbf{m} = \mathbf{M}/M_s$ is the magnetization unit vector normalized to the magnetization at saturation M_s , γ is the gyromagnetic ratio, t is time and α is the Gilbert damping parameter. The effective field \mathbf{H}_{eff} is given by:

$$\mathbf{H}_{\text{eff}} = \mathbf{H}_{\text{Ext}} + \mathbf{H}_{\text{THz}} + \mathbf{H}_{\text{FL}} + \mathbf{H}_{\text{DL}}, \quad (3)$$

where we consider the SOT-induced field-like \mathbf{H}_{FL} and damping-like \mathbf{H}_{DL} equivalent fields with $\mathbf{H}_{\text{FL}} \propto (\mathbf{z} \times \mathbf{j})$ and $\mathbf{H}_{\text{DL}} \propto (\mathbf{j} \times \mathbf{z}) \times \mathbf{m}$ (refs. 26,29,30). Here \mathbf{j} is the electrical current density induced by the terahertz field

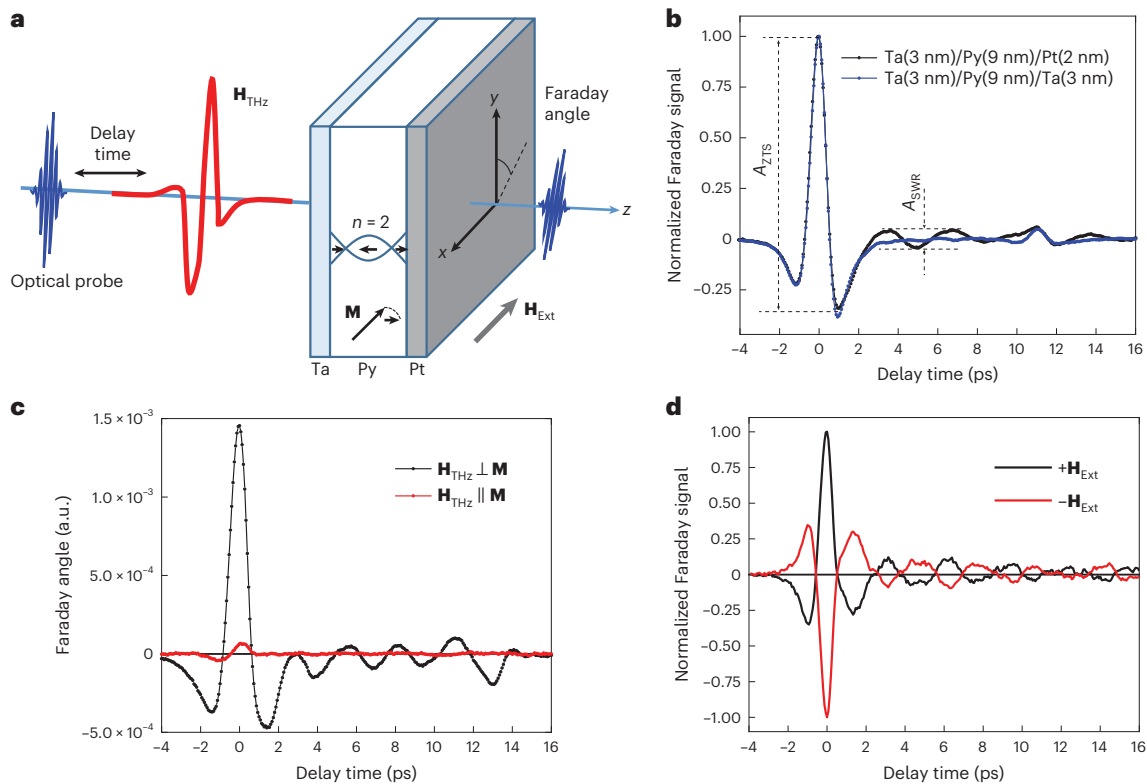


Fig. 1 | Terahertz SWR excitation in a Py layer. **a**, Schematic of the experiment. The single-cycle terahertz pulse is incident on the Ta/Py/Pt sample, which excites standing SWR modes in the Py layer. The z-axis dynamic component of the Py magnetization is detected using a 100 fs laser-probe pulse via the Faraday rotation effect. **b**, Comparison of the magnetization dynamics in two different samples with symmetric (Ta/Py/Ta) and asymmetric (Ta/Py/Pt) interfaces. The spin-wave excitation, which follows the ZTS, is evident (much more pronounced) for the asymmetric sample. **c,d**, Comparison of the magnetization dynamics

in the Ta/Py/Pt sample for Py magnetization aligned perpendicular (black) and parallel (red) with respect to \mathbf{H}_{THz} (**c**) and for different polarities of the external magnetic field (**d**), which is perpendicular to the terahertz magnetic field. The deviations in the precessional oscillation seen at a delay time beyond 11 ps in (**b**) and (**c**) result from back-reflected terahertz radiation of the SiO_2 substrate, which vanishes when we use an Al_2O_3 substrate with larger refractive index in **d**. a.u., arbitrary units.

and \mathbf{z} is the unit vector normal to the sample plane. According to equations (2) and (3), the field-like torque is antisymmetric on inversion of the magnetization, whereas the damping-like torque is symmetric. This points to the fact that the field-like torque is responsible for the terahertz-generated SWR signals, explaining the 180° phase shift in Fig. 1d. The reason for the field-like torque prevailing over the damping-like one in our experiment requires further study. We note, however, that when the magnetization lies in the film plane, \mathbf{H}_{FL} could be much larger than \mathbf{H}_{DL} , in contrast to a canted magnetization state³¹. Finally, we exploited the asymmetry of the field-like torque when the sample was flipped with respect to the incident beam direction. This is shown schematically in Fig. 2a.

According to equations (2) and (3), inverting the order of the Ta/Py/Pt layers with respect to the beam direction should not change the sign of the signals induced by \mathbf{H}_{THz} , whereas \mathbf{H}_{FL} is expected to reverse its direction due to the opposite sign of the spin Hall angle in Ta and Pt, as illustrated in Fig. 2a. Accordingly, opposite directions of the torque would lead to a 180° phase shift in the dynamical components of the magnetization. This scenario is revealed in our experiment in Fig. 2b: when the sample is mounted with the Ta layer side towards the incoming beam, the ZTS induced by \mathbf{H}_{THz} is identical to that observed with the flipped sample (that is, with the Pt layer towards the incoming beam). The SWR signal, however, displays a 180° phase shift, confirming the SOT scenario illustrated in Fig. 2a. Exploiting the opposite symmetry of the two main effects, we could isolate the dynamics of the SOT-induced effect by determining the difference of the signals recorded with the sample mounted in opposite configurations. The difference signal,

shown in the inset of Fig. 2b, reveals clear damped oscillations at a frequency of 0.29 ± 0.01 THz.

The time delay scans of the difference signal for different Py thicknesses are presented in Fig. 3a. All samples displayed damped oscillations, and we fitted our data using a decaying cosine function. The thickest 12 nm Py sample exhibited a more complex dynamical behaviour, therefore the best fit to the curve was achieved using a superposition of three damped cosine functions³²:

$$\psi(t) = \sum_{i=1}^3 a_i e^{t/\tau_i} \cos(2\pi f_i t + \varphi_i) \quad (4)$$

where $\psi(t)$ is the time-dependent difference signal, a_i and φ_i are the initial amplitudes and phases of the i th mode and f_i and τ_i are the frequency modes and characteristic damping times. The inset in Fig. 3b shows the mode frequencies as a function of k^2 for the 12 nm Py sample. The dependence on the wavenumber squared is evident, which we fitted using equation (1). The SWR frequency as a function of Py layer thickness for all Ta/Py (d_{Py})/Pt samples is plotted in Fig. 3b. As expected, the frequency increased with decreasing Py thickness and reached 0.6 ± 0.01 THz for $d_{\text{Py}} = 6$ nm. The fit using equation (1) revealed that the SWR mode in all samples corresponded to the $n = 2$ mode, and the extracted exchange stiffness was $D_{\text{ex}} = 240 \pm 20$ meV \AA^2 ($A_{\text{ex}} = 8 \pm 0.8$ pJ m^{-1} , where A_{ex} is the exchange constant). This value is similar to that reported previously for thin Py films^{33,34}; furthermore, the fit to the multiple modes of the 12 nm Py sample (inset in Fig. 3b) revealed identical D_{ex} , indicating that the exchange stiffness did not

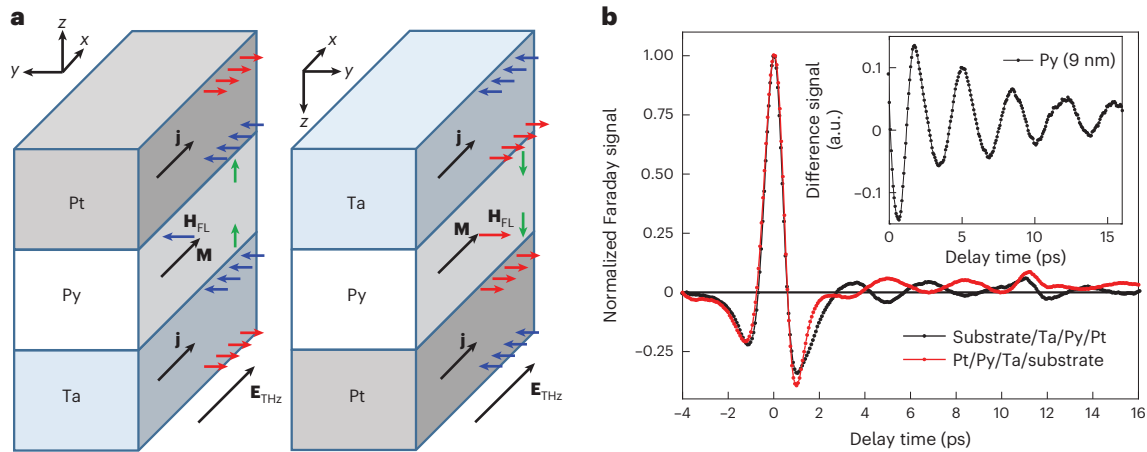


Fig. 2 | Geometry-dependent SOT-driven magnetization dynamics. **a**, The half-period terahertz field E_{THz} generates electrical currents j in the Pt and Ta layers. The spin Hall effect converts the charge currents into respective spin currents, leading to a spin accumulation at the Py interfaces. As Ta and Pt have spin Hall angles of opposite signs, the polarization of the accumulated spins is identical at both interfaces (blue arrows). When the sample is flipped around the x axis (keeping the direction of M constant) the spin accumulation changes sign (red arrows). This results in an opposite direction of the field-like SOT

effective field H_{FL} in these two geometries and, accordingly, opposite torques on M . The z -axis-projected dynamic magnetization components have antiphase time evolution at the interfaces (due to their opposite torques, marked by green arrows), which can be detected by comparing the SWR signals for the two configurations. **b**, Experimental comparison of the magnetization dynamics in the Ta/Py/Pt sample for the aforementioned configurations. The antiphase behaviour of the SWR signals is evident. The inset shows the difference signal of the black and red curves.

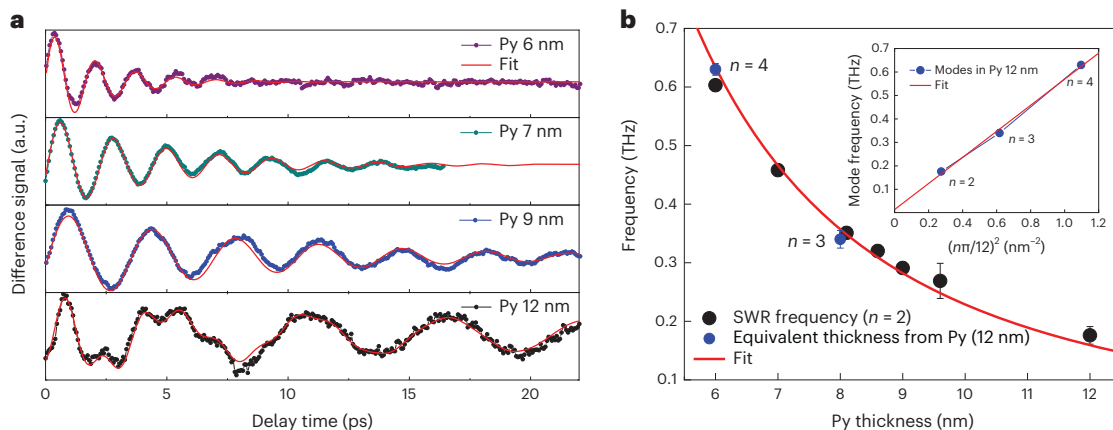


Fig. 3 | Terahertz SWR modes in Py samples with different thicknesses. **a**, Difference time delay scans in Ta/Py/Pt samples with Py thicknesses of between 6 nm and 12 nm. The presented signals are the result of the difference between two Faraday signals, as previously shown in Fig. 2b. The red lines are the fit to the data points using a decaying cosine function. The 12-nm-thick Py sample exhibits three modes $n = 2, 3, 4$. **b**, Resonance frequency of the $n = 2$ mode as a function of Py thickness (black circles). The blue circles represent the frequency for the equivalent thickness of $n = 3$ and $n = 4$ modes detected in the 12-nm-thick Py

(inset). The equivalent thickness is calculated as a corresponding thickness of $n = 3$ and $n = 4$ modes recalculated to the $n = 2$ mode. The red line is a fit to all data points, representing the universal $1/d_{\text{py}}^2$ behaviour for $n = 2$ modes in Py films with different thickness, and for different modes in the 12-nm-thick Py. Vertical error bars are extracted from the fitting errors in the analysis of the difference time delay scans using the decaying cosine function. If not otherwise shown, the error bar is smaller than the symbol size.

change much when the Py thickness was decreased down to 6 nm. Modes larger than $n = 2$ became visible in 12 nm Py as the thickness of the metallic sample was comparable to the probe light penetration depth, which was typically 10–15 nm (refs. 35–37). The details of the mode-selective detection in our experiment are discussed below. The relaxation time of the SWR increased with Py thickness. The effective damping parameter of the $n = 2$ mode in the 9 nm Py sample was calculated to be $\alpha_{\text{eff}} = 0.062 \pm 0.002$, which is comparable to the values reported for the PSSW modes at 0.3 THz (refs. 12,13). This value, however, is larger than $\alpha_{\text{eff}} = 0.014$ of the $n = 2$ mode in 50-nm-thick Py³², suggesting a substantial wave number-dependent damping contribution at terahertz frequencies^{12,38,39}.

Micromagnetic modelling

To gain further insight into the origin of the SWR signal in the Ta/Py/Pt asymmetric system, we modelled the magnetization dynamics microscopically using the MuMax3 code⁴⁰ (see the Methods for details). The magnetic properties of the samples, as well as the asymmetric pinning due to different surface anisotropies at Ta/Py and Py/Pt interfaces, were extracted from the ferromagnetic resonance characterization discussed in the Supplementary Note 3 and Supplementary Fig. 3. We note that no SWR was obtained in the simulations when a homogeneous or linearly decaying profile of H_{THz} (ref. 22) was assumed within the Py thickness. This also confirmed that the direct action of H_{THz} on the magnetization (Zeeman torque itself) cannot be the origin of the SWR signal.

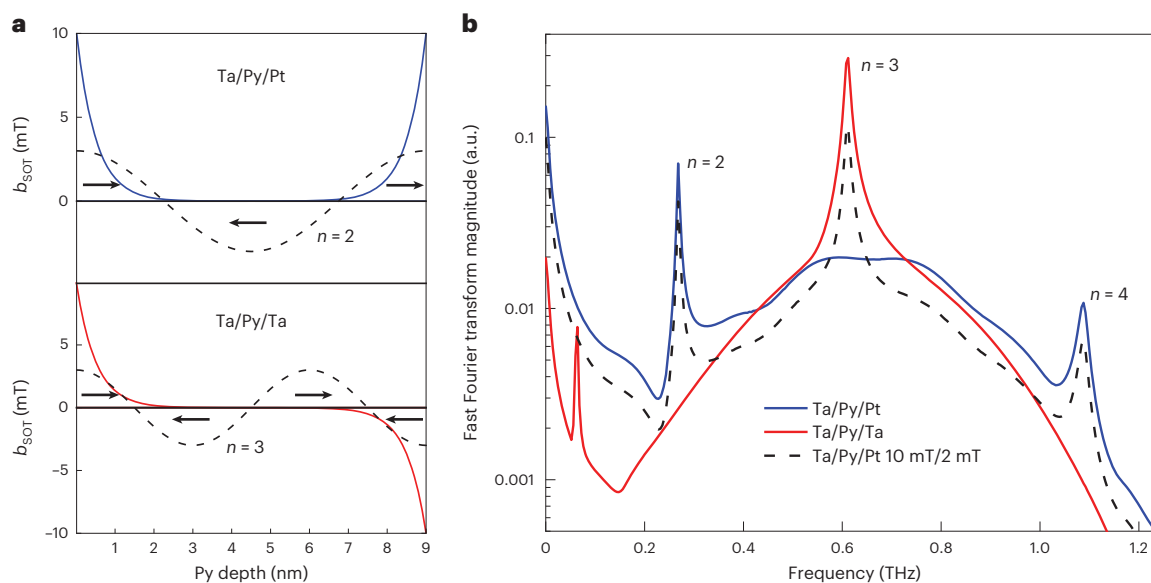


Fig. 4 | Micromagnetic modelling of the SWR excitations. **a**, Schematic illustration of a 10 mT b_{SOT} field that is localized at a depth of 2 nm at the two interfaces in the asymmetric Ta/Py/Pt (black line, top panel) and symmetric Ta/Py/Ta (red line, bottom panel) samples with 9 nm Py layer. For the asymmetric (symmetric) sample, the SOT fields localized at the two Py interfaces are parallel (antiparallel) with respect to each other. Black arrows illustrate the z-axis-projected magnetization dynamical components across the Py thickness. One can see that the in-phase precession of the magnetization at the two interfaces supports the even- n modes ($n = 2$, black dashed line in the top panel), while the

antiphase precession results in the odd- n modes ($n = 3$, black dashed line in the bottom panel). All modes are unpinned, as the interface anisotropy is not strong enough anymore to pin the exchange-dominated spin waves. **b**, Fast Fourier transform spectra for the magnetization dynamics in the asymmetric Ta/Py/Pt (blue line) and symmetric Ta/Py/Ta (red line) samples. The spectrum for the asymmetric interfaces with different SOT-field amplitudes (10 mT and 2 mT, black dashed line) at the two interfaces demonstrates $n = 2, 3$ and 4 modes. All three modes are detected in the 12-nm-thick sample, where the thickness of the metallic layer is comparable to the probe light penetration depth.

Having verified that the terahertz magnetic field does not contribute to the spin-wave excitation, we estimated the magnitude of \mathbf{H}_{FL} . To do so, we first considered the large refractive index of the metallic films, and calculated the absorbed terahertz power using the transfer matrix method^{41–43}. Next, we estimated the electric current density, which causes the terahertz power absorption (see Supplementary Note 4 and Supplementary Fig. 4 for details). The current density was calculated to be about $j = 10^{12} \text{ A m}^{-2}$. We assumed an SOT efficiency $\mu_0 H_{\text{FL}}/j = 10^{-14} \text{ T A}^{-1} \text{ m}^2$ (ref.²⁶) and, accordingly, arrived at $\mu_0 H_{\text{FL}} = 10 \text{ mT}$. We further localized the field $b_{\text{SOT}} = \mu_0 H_{\text{FL}} = 10 \text{ mT}$ at the two interfaces of the 9-nm-thick Py layer within a depth comparable to the spin coherence length, as schematically shown in Fig. 4a. The spin coherence length was assumed to be 2 nm, which is a reasonable value for 3d metals and for Py in particular^{39,44,45}. Furthermore, our simulations revealed that the chosen spin coherence length in the interval between 1 nm and 3 nm did not notably influence the SWR amplitudes in the 9 nm Py. Figure 4b plots the simulated spectra for the parallel (as shown in the top panel in Fig. 4a) and antiparallel (bottom panel in Fig. 4a) alignment of b_{SOT} at the two interfaces of the Py layer. The parallel alignment corresponds to the asymmetric Ta/Py/Pt sample, as the opposite sign of the spin Hall angle in Ta and Pt resulted in the same torque direction at both Py interfaces, as schematically shown in Fig. 2a. Accordingly, the opposite direction of the field-like torque in the Ta/Py/Ta sample corresponded to the antiparallel alignment of b_{SOT} . The $n = 2$ mode in the asymmetric sample is evident (blue line in Fig. 4b). Furthermore, as expected, the symmetric sample did not display even- n modes (red line in Fig. 4b), instead $n = 1$ and $n = 3$ modes have substantial amplitudes. These modes were not detected in our experiment as counter-propagating coherent spin waves (which are antiphase and have identical amplitudes) within the transient time of about 2 ps develop standing spin waves with a net-zero dynamical component projected along the z axis. This did not hold for the asymmetric Ta/Py/Pt sample, as the precession amplitudes at the Ta and Pt interfaces were different due to different

SOTs acting on the magnetization. This resulted in an in-depth asymmetrical profile of the dynamical components during the transient time, which was longer than the studied time-delay interval of 25 ps in Fig. 3a. The asymmetrical magnetization profile in turn allowed the detection of the magnetization dynamics in a Faraday geometry. Different magnetization excitation amplitudes at the two interfaces are also expected to result in the odd- n modes. This scenario was verified using micromagnetic modelling by adjusting b_{SOT} at the two interfaces to be 10 mT at the Pt side and 2 mT at the Ta side. The corresponding Fourier spectra are presented in Fig. 4b (dashed black line). Besides the even- n modes, we obtained the $n = 3$ mode with a substantial amplitude. This mode, however, was not detected in the Ta/Py/Pt with 9 nm Py, presumably due to the fact that at 0.6 THz the mode was strongly damped. Additionally, at 0.6 THz, the pump pulse amplitude in the experimental spectral density was about 30% of the peak amplitude at 0.3 THz (Extended Data Fig. 1). The signal from the $n = 3$ mode is therefore expected to be threefold smaller than the signal from the $n = 2$ mode. Furthermore, the asymmetry ratio in b_{SOT} (10 mT/2 mT) at the two interfaces could be smaller, resulting in a smaller amplitude of the $n = 3$ mode. Nevertheless, the higher-order modes ($n = 3$ and $n = 4$) were resolved when the thickness of the Py layer became comparable to the laser-probe light penetration depth in the 12 nm Py sample (Fig. 3).

Discussion

Using time-resolved magneto-optics, we unambiguously demonstrate the efficient excitation of nanometre-wavelength coherent spin waves, driven by terahertz radiation, in a ferromagnetic layer sandwiched by different heavy metals with spin Hall angles of opposite sign. Our experimental and theoretical studies of asymmetric Ta/Py/Pt versus symmetric Ta/Py/Ta systems rule out the possibility that the terahertz magnetic field alone is the source for the SWR, detected in the asymmetric sample. Exploiting the opposite sign of the spin Hall angle in Ta and Pt, and the antisymmetric nature of the field-like torque under

Article

<https://doi.org/10.1038/s41567-022-01908-1>

magnetization reversal and sample flipping, we demonstrate that the SOT induced by the terahertz field pulse in the heavy metal layer is the driving force for the terahertz magnons. The efficient excitation of the $n = 2$ mode in the asymmetric Ta/Py/Pt samples is explained by the fact that the magnetization at the two interfaces of the Py layer experiences a torque in the same direction (Fig. 2a). Such in-phase precession at the two interfaces meets the criteria for the observation of the $n = 2$ mode, as schematically shown in the top panel in Fig. 4a. The mode frequency increases quadratically with decreasing Py thickness, according to equation (1), and reaches a maximum of 0.6 THz in 6-nm-thick Py. The lifetime of the 0.6 THz mode is, however, two times shorter than the 0.29 THz mode in 9 nm Py. The decrease of the mode lifetime with frequency is presumably one of the main reasons why the higher harmonic signals (above 0.6 THz) are absent in our experiment. As soon as the laser-probe light penetration depth becomes comparable to the Py thickness in the 12 nm Py, we were able to resolve the $n = 3$ mode. This indicates that the SOT-induced magnetization dynamics amplitudes are different at the Ta and Pt interfaces. The asymmetric torques at two different interfaces are expected, as the SOT efficiency at the Ta interface is usually smaller than at the Pt one²⁶. In the case of symmetric interfaces (that is, in the Ta/Py/Ta sample), the SOT generates counter-propagating coherent magnon packets, which are in antiphase. Consequently, they cancel out each other in the Py layer, and standing spin-wave modes with an even number of n are not excited. The odd-number PSSW modes in the Ta/Py/Ta sample cannot be detected in our experimental geometry for the reasons discussed above. The assumed SOT efficiency $\mu_0 H_{\text{FL}}/j = 10^{-14} \text{ T A}^{-1} \text{ m}^2$ is equivalent to about a $\mu_0 H_{\text{FL}} = 10 \text{ mT}$ field and is assumed to be similar to that in magnetotransport measurements^{26,46} according to the theoretical predictions^{27,28}. We note, however, that the exact verification of the SOT efficiency at terahertz frequencies requires further studies with calibrated Faraday angles using high magnetic fields. These studies are of great interest, as they offer contactless and lithography-free characterization of SOT efficiency in complex heterostructures.

Our work demonstrates the coupling of terahertz light with magnon modes of corresponding energy. Unlike optically induced spin waves^{9–14}, this terahertz-frequency magnon excitation via SOT is linear with the amplitude of the terahertz field, which allows us to achieve coherent and efficient control over the excitation, which is of much fundamental and applied interest. Furthermore, the layered metallic stacks based on an encapsulated ferromagnetic thin film act as an intrinsic terahertz magnon source at zero magnetic field, and offer low-cost fabrication and easy integration into existing technologies^{47–49}, thus opening an attractive pathway towards low-power terahertz-frequency magnonics and spintronics at the nanoscale.

Online content

Any methods, additional references, Nature Portfolio reporting summaries, source data, extended data, supplementary information, acknowledgements, peer review information; details of author contributions and competing interests; and statements of data and code availability are available at <https://doi.org/10.1038/s41567-022-01908-1>.

References

- Kirilyuk, A., Kimel, A. V. & Rasing, T. Ultrafast optical manipulation of magnetic order. *Rev. Mod. Phys.* **82**, 2731–2784 (2010).
- Walowski, J. & Münzenberg, M. Perspective: ultrafast magnetism and THz spintronics. *J. Appl. Phys.* **120**, 140901 (2016).
- Barman, A. et al. The 2021 magnonic roadmap. *J. Phys. Condens. Matter* **33**, 423001 (2021).
- Jungwirth, T., Marti, X., Wadley, P. & Wunderlich, J. Antiferromagnetic spintronics. *Nat. Nanotechnol.* **11**, 231–241 (2016).
- Baltz, V. et al. Antiferromagnetic spintronics. *Rev. Mod. Phys.* **90**, 015005 (2018).
- Hortensius, J. R. et al. Coherent spin-wave transport in an antiferromagnet. *Nat. Phys.* **17**, 1001–1006 (2021).
- Li, J. et al. Spin current from sub-terahertz-generated antiferromagnetic magnons. *Nature* **578**, 70–74 (2020).
- Vaidya, P. et al. Subterahertz spin pumping from an insulating antiferromagnets. *Science* **368**, 160–165 (2020).
- Razdolski, I. et al. Nanoscale interface confinement of ultrafast spin transfer torque driving non-uniform spin dynamics. *Nat. Commun.* **8**, 15007 (2017).
- Lalieu, M. L. M., Helgers, P. L. J. & Koopmans, B. Absorption and generation of femtosecond laser-pulse excited spin currents in noncollinear magnetic bilayers. *Phys. Rev. B* **96**, 014417 (2017).
- Ulrichs, H. & Razdolski, I. Micromagnetic view on magnon generation by femtosecond spin current pulses. *Phys. Rev. B* **98**, 054429 (2018).
- Lalieu, M. L. M., Lavrijsen, R., Duine, R. A. & Koopmans, B. Investigating optically excited terahertz standing spin waves using noncollinear magnetic bilayers. *Phys. Rev. B* **99**, 084439 (2019).
- Choi, G.-M., Lee, D.-K., Lee, K.-J. & Lee, H.-W. Coherent spin waves driven by optical spin-orbit torque. *Phys. Rev. B* **102**, 014437 (2020).
- Brandt, L. et al. Effective exchange interaction for terahertz spin waves in iron layers. *Phys. Rev. B* **104**, 094415 (2021).
- Kampfrath, T. et al. Coherent terahertz control of antiferromagnetic spin waves. *Nat. Photon.* **5**, 31–34 (2011).
- Yamaguchi, K., Nakajima, M. & Suemoto, T. Coherent control of spin precession motion with impulsive magnetic fields of half-cycle terahertz radiation. *Phys. Rev. Lett.* **105**, 237201 (2010).
- Vicario, C. et al. Off-resonant magnetization dynamics phase-locked to an intense phase-stable terahertz transient. *Nat. Photon.* **7**, 720–723 (2013).
- Baierl, S. et al. Terahertz-driven nonlinear spin response of antiferromagnetic nickel oxide. *Phys. Rev. Lett.* **117**, 197201 (2016).
- Baierl, S. et al. Nonlinear spin control by terahertz-driven anisotropy fields. *Nat. Photon.* **10**, 715–718 (2016).
- Bonetti, S. et al. THz-driven ultrafast spin-lattice scattering in amorphous metallic ferromagnets. *Phys. Rev. Lett.* **117**, 087205 (2016).
- Bocklage, L. Model of THz magnetization dynamics. *Sci. Rep.* **6**, 22767 (2016).
- Shalaby, M. et al. Coherent and incoherent ultrafast magnetization dynamics in 3d ferromagnets driven by extreme terahertz fields. *Phys. Rev. B* **98**, 014405 (2018).
- Hudl, M. et al. Nonlinear magnetization dynamics driven by strong terahertz fields. *Phys. Rev. Lett.* **123**, 197204 (2019).
- Blank, T. G. H. et al. THz-scale field-induced spin dynamics in ferromagnetic iron garnets. *Phys. Rev. Lett.* **127**, 037203 (2021).
- Neeraj, K. et al. Inertial spin dynamics in ferromagnets. *Nat. Phys.* **17**, 245–250 (2021).
- Manchon, A. et al. Current-induced spin-orbit torques in ferromagnetic and antiferromagnetic systems. *Rev. Mod. Phys.* **91**, 035004 (2019).
- Guimarães, F. S. M., Bouaziz, J., Dias, M. S. & Lounis, S. Spin-orbit torques and their associated effective fields from gigahertz to terahertz. *Commun. Phys.* **3**, 19 (2020).
- Reiss, D. A., Kampfrath, T. & Brouwer, P. W. Theory of spin-Hall magnetoresistance in the ac terahertz regime. *Phys. Rev. B* **104**, 024415 (2021).
- Garello, K. et al. Symmetry and magnitude of spin-orbit torques in ferromagnetic heterostructures. *Nat. Nanotechnol.* **8**, 587–593 (2013).
- Montazeri, M. et al. Magneto-optical investigation of spin-orbit torques in metallic and insulating magnetic heterostructures. *Nat. Commun.* **6**, 8958 (2015).

31. Avci, C. O. et al. Fieldlike and antidamping spin-orbit torques in as-grown and annealed Ta/CoFeB/MgO layers. *Phys. Rev. B* **89**, 214419 (2014).
32. Salikhov, R. et al. Gilbert damping in NiFeGd compounds: ferromagnetic resonance versus time-resolved spectroscopy. *Phys. Rev. B* **99**, 104412 (2019).
33. Imamura, N. & Chikazumi, S. Determination of exchange stiffness constant using high speed switching of Fe-Ni magnetic thin films. *J. Phys. Soc. Jpn* **25**, 125–132 (1968).
34. Langer, M. et al. Parameter-free determination of the exchange constant in thin films using magnonic patterning. *Appl. Phys. Lett.* **108**, 102402 (2016).
35. van Kampen, M. et al. All-optical probe of coherent spin waves. *Phys. Rev. Lett.* **88**, 227201 (2002).
36. Givens, M. P. Optical properties of metals. *Solid State Phys.* **6**, 313–352 (1958).
37. Bäuerle, D. *Laser Processing and Chemistry* 3rd edn (Springer, 2000).
38. Tserkovnyak, Y., Hankiewicz, E. M. & Vignale, G. Transverse spin diffusion in ferromagnets. *Phys. Rev. B* **79**, 094415 (2009).
39. Li, Y. & Bailey, W. E. Wave-number-dependent Gilbert damping in metallic ferromagnets. *Phys. Rev. Lett.* **116**, 117602 (2016).
40. Vansteenkiste, A. et al. The design and verification of MuMax3. *AIP Adv.* **4**, 107133 (2014).
41. Born, M. & Wolf, E. *Principles of Optics* 6th edn (Cambridge Univ. Press, 1999).
42. Jackson, J. D. *Classical Electrodynamics* 3rd edn (Wiley, 1999).
43. Alber, L., Scalera, V., Unikandanunni, V., Schick, D. & Bonetti, S. NTMpy: an open source package for solving coupled parabolic differential equations in the framework of the three-temperature model. *Comp. Phys. Commun.* **265**, 107990 (2021).
44. Bass, J. & Pratt, W. P. Jr. Spin-diffusion lengths in metals and alloys, and spin-flipping at metal/metal interfaces: an experimentalist's critical review. *J. Phys. Condens. Matter* **19**, 183201 (2007).
45. Ghosh, A., Auffret, S., Ebels, U. & Bailey, W. E. Penetration depth of transverse spin current in ultrathin ferromagnets. *Phys. Rev. Lett.* **109**, 127202 (2012).
46. Nguyen, M.-H., Ralph, D. C. & Buhrman, R. A. Spin torque study of the spin Hall conductivity and spin diffusion length in platinum thin films with varying resistivity. *Phys. Rev. Lett.* **116**, 126601 (2016).
47. Torrejon, J. et al. Neuromorphic computing with nanoscale spintronic oscillators. *Nature* **547**, 428–431 (2017).
48. Seifert, T. et al. Efficient metallic spintronic emitters of ultrabroadband terahertz radiation. *Nat. Photon.* **10**, 483–488 (2016).
49. Makarov, A., Windbacher, T., Sverdlov, V. & Selberherr, S. CMOS-compatible spintronic devices: a review. *Semicond. Sci. Technol.* **31**, 113006 (2016).

Publisher's note Springer Nature remains neutral with regard to jurisdictional claims in published maps and institutional affiliations.

Open Access This article is licensed under a Creative Commons Attribution 4.0 International License, which permits use, sharing, adaptation, distribution and reproduction in any medium or format, as long as you give appropriate credit to the original author(s) and the source, provide a link to the Creative Commons license, and indicate if changes were made. The images or other third party material in this article are included in the article's Creative Commons license, unless indicated otherwise in a credit line to the material. If material is not included in the article's Creative Commons license and your intended use is not permitted by statutory regulation or exceeds the permitted use, you will need to obtain permission directly from the copyright holder. To view a copy of this license, visit <http://creativecommons.org/licenses/by/4.0/>.

© The Author(s) 2023

Article

<https://doi.org/10.1038/s41567-022-01908-1>**Methods****Sample fabrication**

Samples of Ta(3 nm)/Py(9 nm)/Ta(3 nm) and Ta(3 nm)/Py(d_{py})/Pt(2 nm) where $d_{\text{py}} = 6$ nm, 7 nm, 8.1 nm, 8.6 nm, 9 nm, 9.6 nm and 12 nm were fabricated at room temperature by d.c.-magnetron sputter deposition in a 0.4 Pa Ar atmosphere in an ultrahigh-vacuum BESTEC system. We used 3-mm-thick double-side polished quartz (SiO₂) and sapphire (Al₂O₃) substrates. The thicknesses of all layers were controlled via the deposition time. Before the sample fabrication, the sputter rate of each individual material was calibrated using X-ray reflectivity characterization of the corresponding film. For the magnetic characterization we used a 0.1–50 GHz vector network analyser ferromagnetic resonance set-up.

Pump-probe measurement

In the experiment a laser system with a 1 kHz repetition rate, 1.5 mJ pulse energy, 800 nm central wavelength and 100 fs pulse duration was used. The laser pulses were split into two branches: one for terahertz pulse generation and the other for magneto-optical probing. The first pulse, with a pulse energy of about 1.2 mJ, generated a single-cycle terahertz pulse via a tilted pulse front scheme in a lithium niobate (LiNbO₃) crystal. The terahertz pulse was then refocused onto the sample surface with full-width at half-maximum spot diameter of 0.8 mm and a pulse energy of 2 μJ . The probe pulse was transmitted through the sample and was spatially overlapped with the pump pulse. The temporal delay between the two pulses was controlled using a linear delay stage. The terahertz-induced rotation of the probe pulse polarization was measured with a balanced pair of photodiodes using a half-wave plate and Wollaston prism placed behind the sample.

The peak electric field of (50 ± 5 MV m⁻¹ of the linearly polarized terahertz pulse was measured using electro-optical sampling. The H-field amplitude was estimated to be 160 mT using $B = E/c$, where B is the terahertz induction and c is the velocity of light. All experiments were performed in a dry nitrogen gas atmosphere to suppress absorption of the terahertz radiation by water vapour in air.

Micromagnetic modelling

Micromagnetic simulations were performed using a custom version of the open-source GPU-accelerated micromagnetic solver MuMax3⁴⁰, which relies on the time integration of the Landau–Lifshitz–Gilbert equation of motion of the magnetization on a rectangular grid. The ferromagnetic layers of different thicknesses were modelled using a segment of 3×3 cells in the layer plane and 64 cells along the layer's thickness. The lateral edge length of the cells was set to 5 nm, whereas the cell size along the thickness direction varied between 78 and 203 pm, depending on the chosen layer thickness. To simulate an infinitely extended layer, we applied true periodic boundary conditions in the lateral directions. For the material parameters, we set a saturation magnetization of $\mu_0 M_s = 1$ T, an exchange stiffness constant of $A_{\text{ex}} = 8$ pJ m⁻¹, an out-of-plane anisotropy of $K_u = 25$ kJ m⁻³ and a Gilbert damping constant of $\alpha = 0.01$. Asymmetric surface anisotropy was implemented using additional out-of-plane anisotropies with constants $K_{u,i} = lK_{u,i}$ in only the surface cells of the layer, where l is the cell size along the thickness direction and the surface anisotropy constants $K_{s,1} = 0.1$ mJ m⁻² and $K_{s,2} = 0.2$ mJ m⁻². The in-plane-saturated equilibrium state was found by applying an external magnetic field of $B_{\text{DC}} = 50$ mT. Spin-wave dynamics were excited using a SOT field with a pulse profile:

$$b_{\text{SOT}}(z, t) = [b_p \exp(-\lambda_p z)] \sin(\omega_p t) \exp(-t^2/t_p^2),$$

where the pulse parameters $\omega_p = 4.4$ THz and $t_p^2 = 1.6$ ps² are empirical, fitting the terahertz pump pulse spectrum. The field

b_{SOT} ($b_p = 10$ mT with a skin depth $\lambda_p = 1$ –3 nm, according to the spin coherence length in Py) were applied in the film plane and perpendicular to the direction of magnetization (that is, perpendicular to B_{DC}). The magnetization dynamics was simulated for 250 ps and sampled every 100 fs. Subsequently, a fast Fourier transform of the time evolution of the magnetization was performed for each discretization cell to obtain the spectral response as a sum of all cell contributions.

Data availability

Source data are provided with this paper. All other data that support the finding of this work are available from the corresponding authors upon request.

Code availability

The mathematical code that supports the findings of the study is available via GitHub at <https://github.com/mumax3>. The MuMax3 scripts are provided in Supplementary Code 1.

Acknowledgements

We are grateful to T. Naumann and J. Heinze for experimental and technical support. Parts of this research were carried out at ELBE at the Helmholtz-Zentrum Dresden-Rossendorf e.V., a member of the Helmholtz Association. R.A.G. acknowledges support from Fondo Nacional de Desarrollo Científico y Tecnológico (FONDECYT) under grant agreement no. 1210607.

Author contributions

R.S., J.L. and S.K. conceived and designed the experiment. R.S. and O.H. designed and fabricated the samples. I.I., A.P., J.-C.D., T.V.A.G.d.O. and S.K. carried out the measurements. L.K., A.K. and R.A.G. performed theoretical calculations and micromagnetic simulations. S.B. performed the transfer matrix method calculations. R.S. and K.L. measured and analysed the ferromagnetic resonance. All authors contributed substantially to the discussion and data interpretation. R.S., S.B., O.H., J.L. and S.K. wrote the manuscript with important input from all authors.

Funding

Open access funding provided by Helmholtz-Zentrum Dresden - Rossendorf e. V..

Competing interests

The authors declare no competing interests.

Additional information

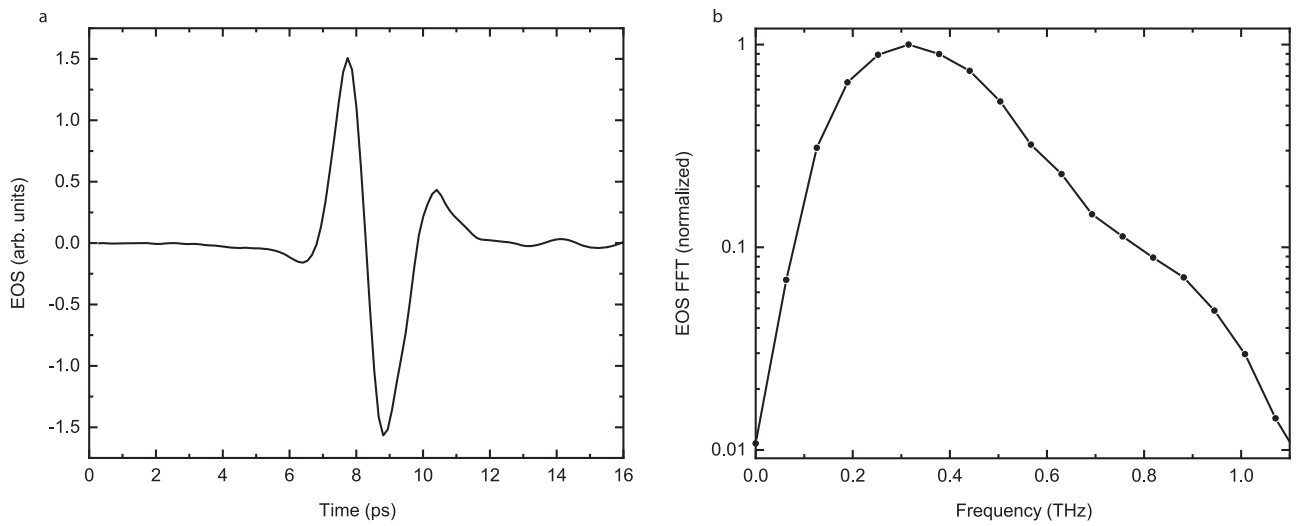
Extended data is available for this paper at <https://doi.org/10.1038/s41567-022-01908-1>.

Supplementary information The online version contains supplementary material available at <https://doi.org/10.1038/s41567-022-01908-1>.

Correspondence and requests for materials should be addressed to Ruslan Salikhov or Sergey Kovalev.

Peer review information *Nature Physics* thanks Akashdeep Kamra and Markus Münzenberg for their contribution to the peer review of this work.

Reprints and permissions information is available at www.nature.com/reprints.



Extended Data Fig. 1 | Temporal and spectral characteristics of THz-pump pulse. a, EOS signal from the broadband THz radiation, displaying the time profile of the single-cycle THz-pump pulse. **b,** Fourier spectrum of the THz pulse normalized to the peak amplitude.

Integration of Multifunctional Epitaxial (Magnetic) Shape Memory Films in Silicon Microtechnology

Lukas Fink, Satyakam Kar,* Klara Lünser, Kornelius Nielsch, Heiko Reith, and Sebastian Fähler

Magnetic shape memory alloys exhibit various multifunctional properties, which range from high stroke actuation and magnetocaloric refrigeration to thermomagnetic energy harvesting. Most of these applications benefit from miniaturization and a single crystalline state. Epitaxial film growth is so far only possible on some oxidic substrates, but they are expensive and incompatible with standard microsystem technologies. Here, epitaxial growth of Ni–Mn–based Heusler alloys with single crystal-like properties on silicon substrates is demonstrated by using a SrTiO₃ buffer. It is shown that this allows using standard microfabrication technologies to prepare partly freestanding patterns. This approach is versatile, as its applicability for the NiTi shape memory alloy is demonstrated and spintronic and thermoelectric Heusler alloys are discussed. This paves the way for integrating additional multifunctional effects into state-of-the-art microelectronic and micromechanical technology, which is based on silicon.

due to ferromagnetism, and twin boundaries due to ferroelasticity.^[3] Coupling of both ferroic properties enables various emerging applications. In particular, Ni–Mn–based Heusler alloys achieve actuation with a high stroke of up to 12%,^[4] enable efficient magnetocaloric refrigeration,^[5] and allow thermomagnetic harvesting of low-grade waste heat.^[6] Optimum performance is often obtained only in single crystals, for example, actuation by a magnetically induced reorientation is inhibited by large angle grain boundaries.^[7] The outstanding properties in bulk single crystals have motivated intense research on epitaxial films, which represent the thin film counterpart. Compared to bulk, films exhibit a much higher surface to volume ratio, which accelerates the heat exchange and accordingly

1. Introduction

Multiferroic materials combine more than one ferroic property such as ferromagnetism, ferroelectricity, and ferroelasticity.^[1] Two major research lines emerged from multiferroics. First, magnetoelectric materials, which exhibit coupling between ferromagnetism and ferroelectricity.^[2] Second, magnetic shape memory alloys, which exhibit both, domain walls


results in very high cycle frequencies and power densities for any caloric^[8] or thermomagnetic^[6] application. Furthermore, multifunctional Heusler alloys follow the concept “the material is the machine,”^[9] and thus are ideally suited for miniaturization since no additional parts like levers and valves are required, which would complicate microfabrication substantially. The required epitaxial growth has been achieved on various single crystal oxidic substrates like Al₂O₃,^[10,11] SrTiO₃,^[12] and MgO,^[13] as well as other materials like NaCl^[14] and GaAs.^[15] However, these substrates are both expensive and incompatible with standard silicon microtechnology, which hampered the application of multifunctional Heusler alloys within microsystems up to now.

Here, we demonstrate epitaxial growth of Ni–Mn–based Heusler alloys on Si substrates in (001)-orientation. We show that these magnetic shape memory films are compatible with standard microsystem technologies like photolithography, anisotropic etching, and silicon-on-insulator (SOI) substrates. This allows for an easy fabrication route for partly freestanding patterned structures, which we exemplify with some generic geometries. These structures are ferroelastic and ferromagnetic—the two ferroic properties enabling all multifunctionalities of these Heusler alloys. We further demonstrate a direct transfer of our approach to the NiTi system, the most applied shape memory alloy for actuator,^[16–18] elastocaloric,^[19] and biomedical applications.^[16,20–22] Many other functional materials would also benefit from such an integration and we discuss this for the rich class of Heusler alloys, which exhibit extraordinary spintronic^[23] and thermoelectric^[24] properties. Similar breakthroughs for system integration have been achieved recently for

L. Fink, S. Kar, K. Lünser, S. Fähler
Helmholtz-Zentrum Dresden-Rossendorf
Institute of Ion Beam Physics and Materials Research
Bautzner Landstraße 400, 01328 Dresden, Germany
E-mail: s.kar@ifw-dresden.de

L. Fink, S. Kar, K. Lünser, K. Nielsch, H. Reith
Leibniz IFW Dresden
Institute for Metallic Materials
Helmholtzstraße 20, 01069 Dresden, Germany

L. Fink, S. Kar, K. Lünser, K. Nielsch
TU Dresden
Institute of Materials Science
01062 Dresden, Germany

 The ORCID identification number(s) for the author(s) of this article can be found under <https://doi.org/10.1002/adfm.202305273>

© 2023 The Authors. Advanced Functional Materials published by Wiley-VCH GmbH. This is an open access article under the terms of the Creative Commons Attribution License, which permits use, distribution and reproduction in any medium, provided the original work is properly cited.

DOI: 10.1002/adfm.202305273

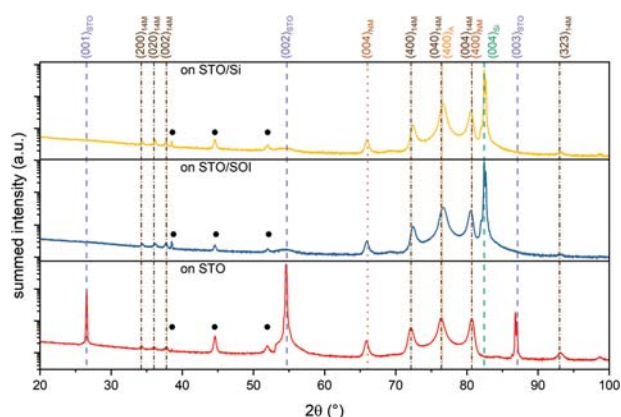


Figure 1. Diffractograms of $\text{Ni}_{54}\text{Mn}_{19}\text{Ga}_{27}$ films deposited at 400 °C on different substrates. Except for substrate reflections, only $\{00l\}$ reflections of the martensitic phases are visible, which reveal that the films grown on Si substrates are martensitic at room temperature and exhibit a pronounced texture. Black dots mark reflections originating from the substrate holder.

silicon photonics^[25] and ferroelectrics.^[26] Thus, our versatile approach is a decisive step for integrating a large variety of emerging functional properties in today's microelectronic and micro-machining technology, which is based on silicon.

2. Results and Discussion

Starting point for epitaxial growth are Si (001) substrates that are covered with a 4 nm thick epitaxial SrTiO_3 (in short STO) buffer layer. This buffer was developed for optoelectronic applications of barium titanate^[26] and 4" wafers are available commercially.^[27] Despite the large misfit of 5% between STO and Ni–Mn–based Heusler alloys, epitaxial growth is possible.^[12] This mismatch can be reduced by a Cr buffer, which also can be etched selectively.^[28] For the formation of L_{21} ordered Heusler alloy, substrates are heated to 400 °C during deposition. Focusing on the ternary Ni–Mn–Ga prototype system, we will show first, that we can grow epitaxial films on STO-buffered Si substrates, second, that these films show microstructural and magnetic properties typical for Ni–Mn–Ga single crystals, and third, that we can apply standard silicon technology to produce partially freestanding microsystems.

First indications of epitaxial growth on Si substrates come from θ – 2θ XRD measurements of 500 nm thick $\text{Ni}_{54}\text{Mn}_{19}\text{Ga}_{27}$ films grown with a 20 nm thick Cr buffer on STO/Si and STO/SOI, which are shown in **Figure 1** along with a film grown on a single crystalline STO substrate as a reference. Except for substrate reflections, we only observe a set of $\{00l\}$ reflections, which indicate a preferential alignment of the unit cells. All film reflections can be indexed by non-modulated (NM) and 14M modulated martensite—two martensite structures, which are closely related by adaptivity.^[29] The presence of martensitic phase at room temperature reveals that the martensitic (=ferroelastic) transition occurred at some higher temperature. In the following, we use the term martensitic instead of ferroelastic to increase the readability for the shape memory community. The martensitic transformation from the cubic austenite state results in a reduction of crystal symmetry, and accordingly, we

observe a set of reflections, which represents the different lattice parameters of this reduced symmetry (tetragonal $(00l)_{\text{NM}}$ and $(l00)_{\text{NM}}$, and orthorhombic $(l00)_{14\text{M}}$, $(0l0)_{14\text{M}}$, and $(00l)_{14\text{M}}$). In the cubic austenitic state, this peak splitting does not exist. We demonstrate this for a film with a different composition, which remains austenitic down to room temperature (Figure S1, Supporting Information). Lattice parameters change from $a_{\text{A}} = 0.578$ nm to $a_{14\text{M}} = 0.607$ nm, $b_{14\text{M}} = 0.578$ nm, $c_{14\text{M}} = 0.554$ nm, $c_{\text{NM}} = 0.658$ nm, and $a_{\text{NM}} = 0.554$ nm. All the austenitic and martensitic films exhibit very similar values on different substrates (The reported values are averages. Individual values are in Table S1, Supporting Information). The associated lattice distortion ($1 - c/a$) is often taken as the ferroelastic order parameter.

To accommodate the change in lattice parameters during a martensitic transformation, it is necessary to combine differently oriented variants of the martensite, which are connected to each other with twin boundaries. This transformation requires a slight tilt and rotation of the lattice by a few degrees, as described by the phenomenological theory of martensite,^[30] and observed for this particular system in TEM.^[31,32] In our measurements, we account for this by showing for each sample the sum of XRD measurements, where the substrate normal was tilted in steps of 1° between 0° and 10° away from Bragg–Brentano geometry.^[33] To sum up, these diffractograms originate from a single crystalline film grown within the high temperature austenite state, which transformed to the ferroelastic martensitic state at room temperature.

To probe epitaxial growth, pole figures are depicted in **Figure 2a–c** for the three different substrates. All $(020)_{14\text{M}}$ pole figures exhibit the four-fold symmetry induced by the cubic substrates in (001) orientation. High-intensity spots split up and cluster around a tilt angle (ψ) of 45°. As analyzed in detail before,^[13,33] this splitting originates from the reduction of crystal symmetry during the martensitic transition of a single crystalline film, grown epitaxially in cubic austenite state at high deposition temperatures. The pole figure of the film grown on STO/Si is rotated by 45° around the substrate normal with respect to the films grown on STO and STO/SOI. This originates from different substrate architectures, as sketched in Figure 2d–f. To minimize the misfit between the Heusler alloy and STO, both unit cells are rotated by 45° with respect to each other.^[12] The same rotation occurs when STO is grown on Si. To compensate for this, the top Si layer on SOI substrate was rotated by 45° during bonding step. The Cr buffer used for these experiments is optional, as films grown without this buffer reveal the same pole figure and microstructure (Figure S2, Supporting Information). To sum up, these measurements confirm that our approach allows growing Ni–Mn–Ga Heusler films epitaxially on Si substrates.

In the following, we will demonstrate that our films exhibit the typical microstructure and magnetic properties of single-crystalline Ni–Mn–Ga films. Twinning is the most obvious consequence of a martensitic transformation. During the transformation, a high number of transformation twins form; in Ni–Mn–Ga films, the transformation even results in several levels of twin boundaries nested into each other.^[31] The twin boundaries and their high mobility are essential for superelasticity, the shape memory effect, and magnetically induced reorientation observed in these alloys.^[3] In our films, twin boundaries

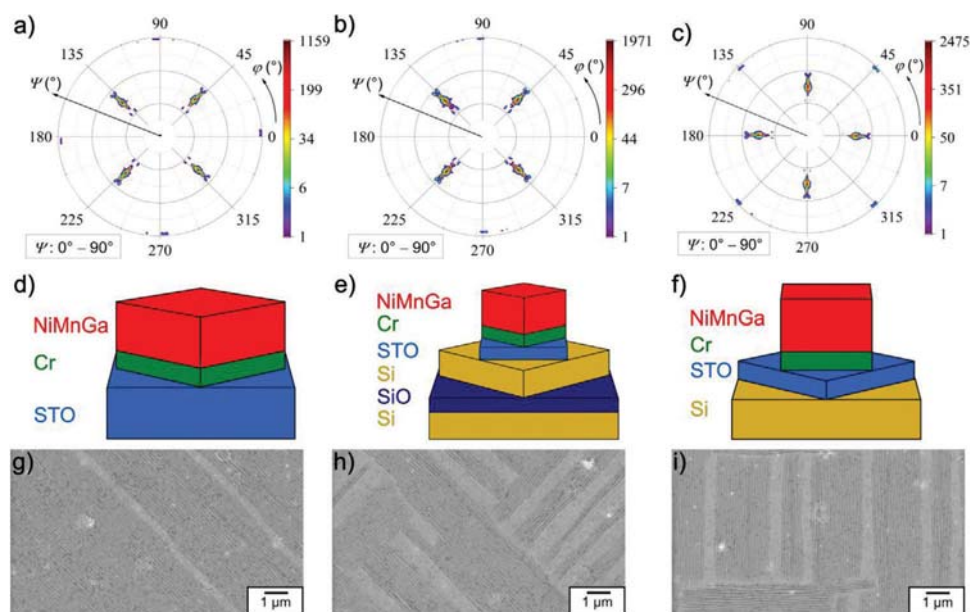


Figure 2. a–f) Epitaxial growth of Ni–Mn–Ga films is confirmed by the four-fold symmetry of $(202)_{14M}$ pole figure measurements (a–c) for the three different film architectures sketched in (d–f). The orientation of Ni–Mn–Ga unit cell of the film on STO/Si is rotated by 45° with respect to the films on STO and STO/SOI, as discussed within the text. SEM micrographs in (g–i) illustrate the twinned morphology of each film. Traces of the twin boundaries are aligned in parallel to $[100]_{\text{Ni-Mn-Ga}}$ and $[010]_{\text{Ni-Mn-Ga}}$ directions on the Ni–Mn–Ga surface. For these experiments, an optional Cr buffer was used. All figures are oriented parallel to the substrate edges.

can be seen as characteristic parallel lines in SEM images (Figure 2g–i). These twin boundaries are at the mesoscale level of hierarchical martensite microstructure and occur during the nucleation and growth stage of the martensite. The geometrical description of these stages in epitaxial Ni–Mn–Ga films can be found in our previous works.^[31,34] In Ni–Mn–Ga, twin boundaries are slightly tilted and rotated away from $\{110\}$ planes (as described before) and from the six possible orientations in bulk, in these films we only observe the so-called type X subsets, where the twin boundary is inclined by 45° to the substrate normal and traces follow either $[100]_{\text{Ni-Mn-Ga}}$ or $[010]_{\text{Ni-Mn-Ga}}$ directions on the film surface.^[31,35] Twin boundaries in (i) are rotated by 45° with respect to those visible in (g) and (h) due to the differences in the substrate architecture mentioned before (Figure 2d–f). Due to the four-fold symmetry of the cubic substrates, two equivalent orientations of the parallel lines on the film surface are possible, which are also clearly visible for both films grown on Si. For films grown on STO single crystals, the regions of parallel twin boundaries are much larger, and thus different orientations are not captured in the scanned region.

To probe single crystal-like behavior, we performed magnetization measurements in dependence of temperature, field, and direction (Figure 3). The properties of all three films agree within a few Kelvin; thus in the following text, we give average values (see Table S2, Supporting Information, for values of each film, and Figure S3, Supporting Information, for the measurements of the film grown on STO single crystal). A temperature sweep at a low magnetic field of 0.01 T applied in-plane reveals the following transitions during cooling: Below the Curie temperature of 328 K, magnetization increases steeply due to the magnetic transition from paramagnetic austenite to ferromagnetic

austenite. A Curie transition is of second order and therefore proceeds without hysteresis. At 301 K, the magnetization drops steeply, which is commonly attributed to the martensite start temperature M_S , where the low magnetic field does not allow aligning magnetization due to the high magnetocrystalline anisotropy of martensite. This

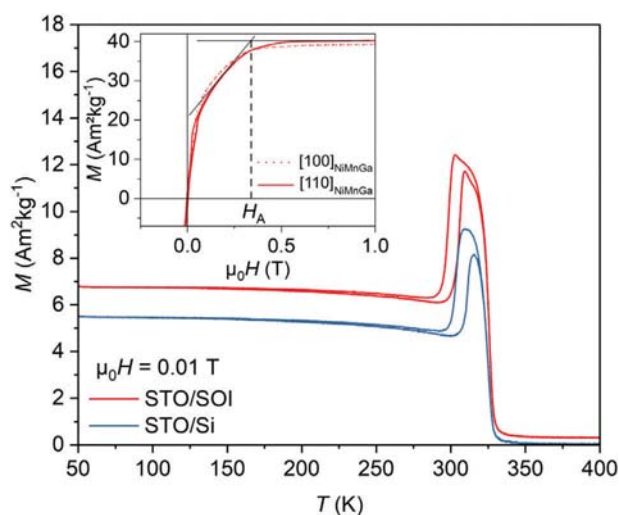


Figure 3. Single crystal-like magnetic properties of epitaxial Ni–Mn–Ga films grown on STO/Si (blue) and STO/SOI (red). Temperature dependent measurements reveal the transition temperatures, as described within the text. The inset shows field dependent measurements within the martensitic state at 300 K. Epitaxial growth allows to measure the difference between $[100]_{\text{Ni-Mn-Ga}}$ and $[110]_{\text{Ni-Mn-Ga}}$ directions and to derive the anisotropy field H_A , as described within the text.

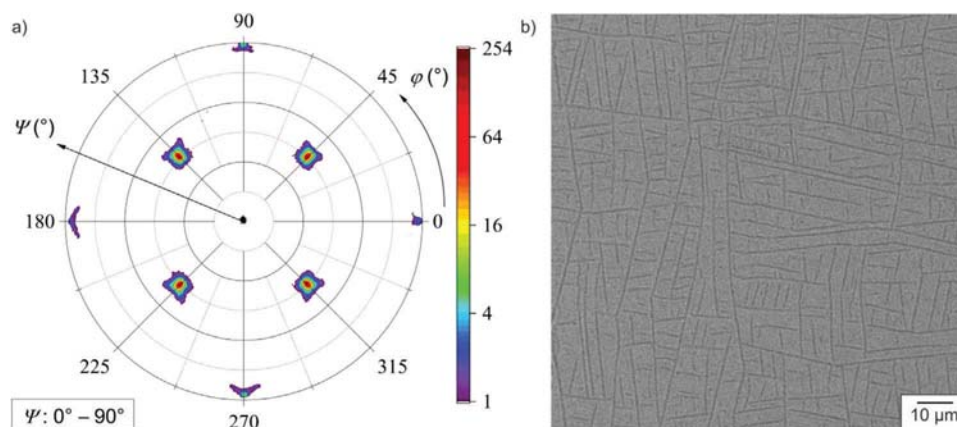


Figure 4. Epitaxially grown NiTi shape memory films on STO/SOI. a) The (110) pole figure shows that the film grows epitaxially on the silicon substrate. b) In an SEM micrograph, martensitic twins are visible as straight traces with distinct orientations to the substrate.

decrease of magnetization is finished at 295 K, which defines the martensite finish temperature M_F . During heating, the reverse transformation to austenite occurs and accordingly, $A_S = 303$ K and $A_F = 308$ K are obtained. As characteristic of a first-order martensitic transformation, the reverse transformation occurs at higher temperatures than the forward transformation. The measured hysteresis of 6 K is typical for epitaxial Ni–Mn–Ga films.^[12,13,33] As these measurements are performed in a field far below the anisotropy field, magnetization is not saturated and thus, slight differences in sample alignment result in differences in magnetization between the samples. To probe the field dependency, the inset in Figure 3 shows magnetization curves at 300 K within the martensitic state. Measurements along $[100]_{\text{Ni–Mn–Ga}}$ and $[110]_{\text{Ni–Mn–Ga}}$ differ due to the magnetocrystalline anisotropy of martensite, which can be probed due to the single crystalline growth of these films. Following the procedure described,^[13] we obtain from the anisotropy field H_A an anisotropy constant $k_1 = 1.1 \times 10^5 \text{ Jm}^{-3}$, which is close to the value $k_1 = 1.7 \times 10^5 \text{ Jm}^{-3}$ of a 14M single crystal.^[36] Also, the saturation magnetization of $M_{\text{sat}} = 34 \text{ Am}^2 \text{ kg}^{-1}$ is close to the bulk value of $35 \text{ Am}^2 \text{ kg}^{-1}$.^[37]

To illustrate the versatility of our approach, we used STO-buffered Si substrates also for the epitaxial growth of NiTi films. Up to now, either polycrystalline films^[16] or epitaxial films on oxidic substrates^[38,39] had been available for this system. For optimum properties, NiTi requires different deposition and heat treatment conditions compared to Ni–Mn–Ga, as described in the Experimental Section. However, we could directly use the growth parameters optimized for MgO substrates^[40] for the growth on STO/SOI, which illustrates that our approach requires a minimum adaption of existing processes. The 500 nm thick film, depicted in **Figure 4**, is a) epitaxial as evidenced by the (110) pole figure measurement, b) having a twinned martensitic microstructure. The epitaxial growth relation is $\text{Si}(001)[110] \parallel \text{STO}(001)[100] \parallel \text{Cr}(001)[110] \parallel \text{NiTi}(001)[110]$, similar to the architecture sketched in Figure 2e. Though polycrystalline NiTi films on Si are already used today,^[16] epitaxial growth of NiTi will have the same functional advantages of bulk single crystals: a higher pseudo-elastic and -plastic strain,^[41] and a higher elastocaloric effect.^[19]

To demonstrate the feasibility of integrating epitaxial Heusler films into silicon microtechnology, we fabricated two archetypical geometries for partly freestanding microsystems. Top-down microfabrication steps are sketched in **Figure 5** and are briefly described in the caption. As Si can be selectively etched, we omit the Cr buffer. Details are given in the Experimental Section. Criteria for method selection and optimization will be published elsewhere. **Figure 6** shows exemplarily two microsystem geometries. The top row shows several of these microsystems to illustrate reproducibility. The bottom row is a zoom-in of one microsystem, demonstrating the presence of twin boundaries and thus proving that these microsystems are in the martensitic state at room temperature. On the left side, a bending actuator is shown, which can utilize the shape memory effect.^[42] To allow bending, the cantilever must be freestanding. For Joule heating, an electric current can be passed through the double-beam cantilever. The current is provided through the contact pads, which must be connected to the substrate. This example illustrates the advantage of our approach, as it allows an easy combination of freestanding parts with parts attached to a silicon substrate. The right side image illustrates a geometry where a freestanding spring is connected with a mass—a geometry that can utilize the strong damping properties of shape memory alloys at the nanoscale.^[43]

Our approach can be directly adapted for other multifunctional microsystems. For example, a thermomagnetic micro-oscillator^[6] just requires replacing the spring with a straight cantilever. To utilize the magnetocaloric properties of these Heusler alloys, one can prepare partly freestanding films, which avoids the unfavorable large heat capacity of the thick substrate compared to the thin magnetocaloric film.^[44] For this application, larger freestanding areas are beneficial, which can be prepared by anisotropic etching of the silicon substrate (without SOI) from the backside. For caloric and thermomagnetic applications, the magnetic properties can be tuned by adding Cu to Ni–Mn–Ga.^[45] Accordingly, we used this quaternary alloy for our microsystems. The versatility to use different compositions is decisive for Ni–Mn–based Heusler alloys since each multifunctional property is optimal at a particular alloy system and composition.^[3] Last but not least, our approach is feasible for micromachining of self-folding origami, which utilizes NiTi as bending actuators and

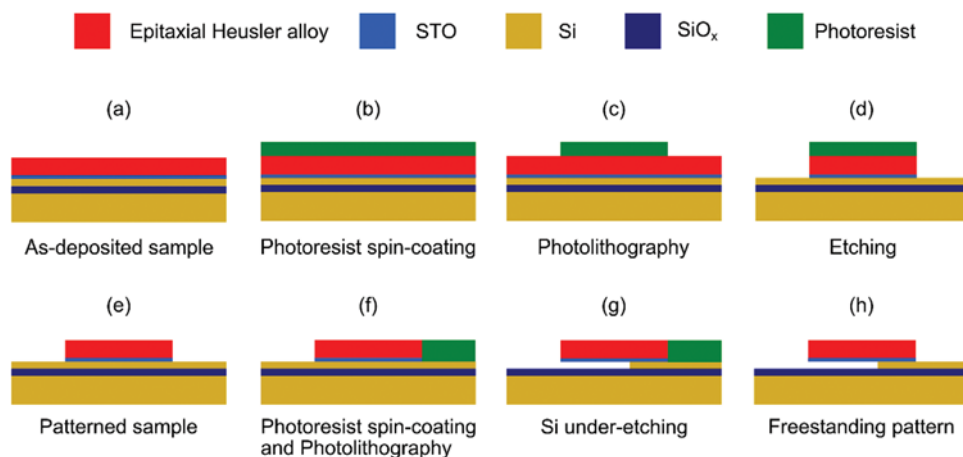


Figure 5. Process steps for fabricating partly freestanding patterned structures of epitaxial Heusler films in monolithic silicon microsystems. a) Starting with the epitaxial Heusler film grown on STO/SOI substrate, b) a photoresist is spin-coated, which is then c) exposed and developed by laser lithography to get the pattern design. d) The exposed regions of the film are etched by Ar ions to transfer the pattern design through the epitaxial film. e) The photoresist is then removed by acetone to obtain a patterned sample. f) The patterned sample is spin-coated again with a photoresist and undergoes laser lithography to reveal areas of the sample for under-etching the top Si layer of SOI substrate. g) The top Si layer is under-etched isotropically by XeF_2 gas. h) The photoresist is then removed by O_2 plasma to obtain partly freestanding structures.

switchable Heusler alloys as fixtures.^[46] These examples illustrate that monolithic micromachining of partly freestanding devices is possible, without the need of manually transferring epitaxial grown films and patterns to another substrate.^[6,42,47] Thus, our approach allows for batch fabrication, which is decisive for both, further miniaturization and future mass production.

3. Conclusion and Outlook

To conclude, a thin epitaxial SrTiO_3 (STO) buffer enables epitaxial growth of Ni–Mn–based Heusler alloys on silicon substrates. Our approach is compatible with silicon-on-insulator substrates and thus allows using standard techniques for the

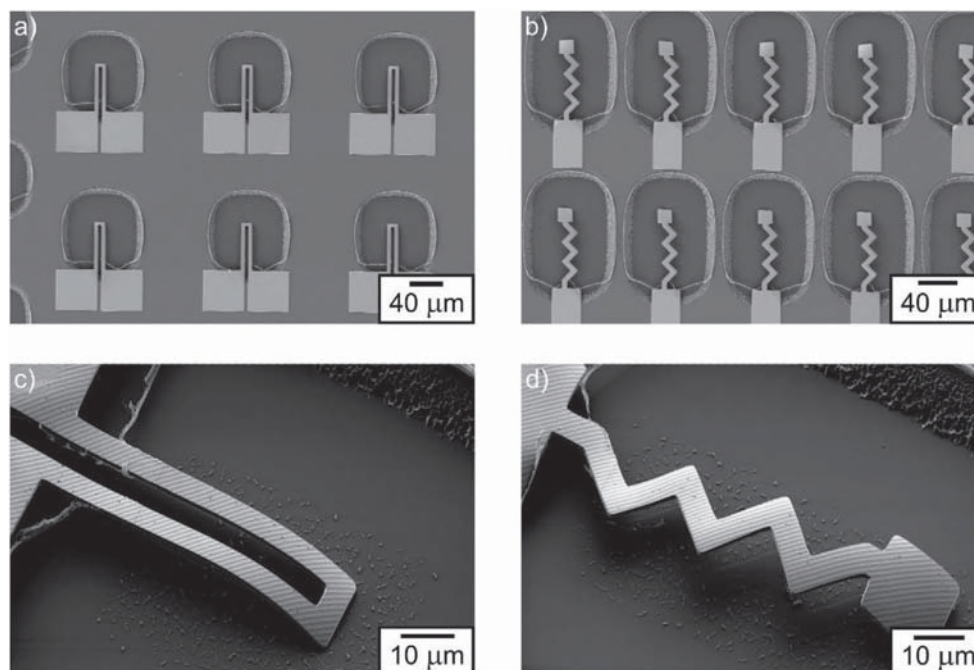


Figure 6. Monolithic microsystems utilizing partly freestanding $\text{Ni}_{52}\text{Mn}_{19}\text{Ga}_{26}\text{Cu}_3$ films epitaxially grown on STO/SOI. In the left column, we show shape memory bending microactuator with contact pads, in the right column we show micro-damper. Principle of operation for both microsystems is described within the text. The top row shows several of these microsystems, whereas in the bottom row, details of one system are depicted. At this magnification, the twinned martensitic microstructure becomes visible.

monolithic fabrication of partly freestanding patterns. This enables combining multifunctional elements of these Heusler alloys with today's microelectronic and micromechanical systems. Our approach is flexible, as it allows using different film compositions and architecture to obtain optimum multifunctional properties. Moreover, it also enables epitaxial growth of NiTi, which is the most used non-magnetic shape memory alloy today.

As an outlook, we note that Heusler alloys exhibit many more outstanding functional and fundamental properties, including spintronic,^[23] thermoelectric,^[24] topological insulator,^[48] and unconventional superconductivity properties.^[49] Spintronic applications, for example, benefit from the full spin polarization of half-metallic Heusler alloys. When grown epitaxially, for example, Co₂FeSi reaches polarized spin currents, which are one order of magnitude higher than polycrystalline films.^[50] However, on silicon, epitaxial growth is limited due to interdiffusion beyond a film deposition temperature of 60 °C, which by far is not sufficient to induce the required chemical order in Heusler alloys.^[51] A high effort is therefore put into the epitaxial growth on GaAs and Ge substrates.^[52] Our approach of using an epitaxial STO buffer promises to solve this issue and make many functional properties of Heusler alloys integrable into silicon technology.

4. Experimental Section

As described in detail before,^[12,13] for epitaxial growth of 500 nm thick Ni–Mn–Ga film, DC magnetron sputtering of a 4" Ni₄₈Mn₂₂Ga₃₀ alloy target was performed. For the 500 nm thick Ni–Mn–Ga–Cu film, a 2" Cu target was co-sputtered. 4 nm STO/Si (001) and STO/SOI (4 nm STO/7 μm Si/1 μm SiO₂/Si (001)) substrates were purchased from Lumiphase and single crystal SrTiO₃ (001) substrates from Crystec. Prior to film deposition, an additional 20 nm thick Cr buffer was deposited at 300 °C (Figures 1, 2, and 3) or no buffer was used (Figure 6 and Figure S2, Supporting Information). Film microstructure and composition were examined using a Zeiss SIGMA 300 SEM fitted with a Smart EDX detector. Structure was investigated by X-ray diffraction using θ – 2θ scans in a slightly tilted Bragg–Brentano geometry using Co-K α radiation in a Bruker D8 advance system. Temperature and field dependent magnetic properties were measured with a vibrating sample magnetometer attached to a Versalab-free system from Quantum Design.

The epitaxial NiTi film was grown by sputter deposition, as described in.^[40] A 50 nm thick Cr buffer layer was deposited on the STO/SOI substrate at a deposition temperature of 500 °C, followed by the 500 nm thick NiTi film deposited at 525 °C. The 4" NiTi target had a composition of Ni_{48.6}Ti_{51.4}. A Zeiss LEO Gemini SEM was used to characterize the film microstructure. XRD texture measurements of the prepared films were performed in a Panalytical X'Pert diffractometer using Cu-K α radiation.

Partly freestanding structures on the epitaxial Ni–Mn–Ga–Cu film were fabricated using photolithography and dry etching techniques. A 1.5 μm thick AZ 15nXT photoresist was used as mask during etching of film and a 1.5 μm thick AZ 5214E photoresist was used as mask during under-etching of the top Si layer of the SOI substrate. The photoresists were exposed using a laser-writer (MLA 100, wavelength of 365 nm) and developed in AZ 726 MIF solution. The Ni–Mn–Ga–Cu film was etched by Ar ion beam etching in a scia Mill 150 tool (etching parameters: Ar flow rate in ion source: 12 sccm, He substrate back-cooling flow rate: 5 sccm, beam voltage: 700 V, chiller temperature: 273 K). The under-etching of Si was performed in a Xactix e2 XeF₂ gas etching tool (pressure: 400 Pa, duration: 60 s).

Supporting Information

Supporting Information is available from the Wiley Online Library or from the author.

Acknowledgements

The authors thank Ruben Hühne and Artur Erbe for discussions. Part of this work was funded by the Deutsche Forschungsgemeinschaft (DFG) projects FA 453/13 and FA 453/14, and a BAM-IFW Tandem project.

Open access funding enabled and organized by Projekt DEAL.

Conflict of Interest

The authors declare no conflict of interest.

Data Availability Statement

The data that support the findings of this study are openly available in [RODARE] at [https://doi.org/10.14278/rodare.2293], reference number [2293].

Keywords

epitaxial film growth, magnetic shape memory alloys, Ni₂MnGa, NiTi, silicon microtechnology

Received: May 12, 2023

Revised: July 3, 2023

Published online: August 23, 2023

- [1] H. Schmid, *Ferroelectrics* **1994**, *162*, 317.
- [2] W. Eerenstein, N. D. Mathur, J. F. Scott, *Nature* **2006**, *442*, 759.
- [3] O. Heczko, H. Seiner, S. Fähler, *MRS Bull.* **2022**, *47*, 618.
- [4] A. Sozinov, N. Lanska, A. Soroka, W. Zou, *Appl. Phys. Lett.* **2013**, *102*, 021902.
- [5] J. Liu, T. Gottschall, K. P. Skokov, J. D. Moore, O. Gutfleisch, *Nat. Mater.* **2012**, *11*, 620.
- [6] M. Gueltig, F. Wendler, H. Ossmer, M. Ohtsuka, H. Miki, T. Takagi, M. Kohl, *Adv. Energy Mater.* **2017**, *7*, 1601879.
- [7] D. C. Dunand, P. Müllner, *Adv. Mater.* **2011**, *23*, 216.
- [8] S. Fähler, V. K. Pecharsky, *MRS Bull.* **2018**, *43*, 264.
- [9] K. Bhattacharya, R. D. James, *Science* **2005**, *307*, 53.
- [10] G. Jakob, H. J. Elmers, *J. Magn. Magn. Mater.* **2007**, *310*, 2779.
- [11] K. Lünser, A. Diestel, K. Nielsch, S. Fähler, *Materials* **2020**, *13*, 3674.
- [12] O. Heczko, M. Thomas, J. Buschbeck, L. Schultz, S. Fähler, *Appl. Phys. Lett.* **2008**, *92*, 072502.
- [13] M. Thomas, O. Heczko, J. Buschbeck, U. K. Rößler, J. McCord, N. Scheerbaum, L. Schultz, S. Fähler, *New J Phys* **2008**, *10*, 023040.
- [14] M. Thomas, O. Heczko, J. Buschbeck, Y. W. Lai, J. McCord, S. Kaufmann, L. Schultz, S. Fähler, *Adv. Mater.* **2009**, *21*, 3708.
- [15] J. W. Dong, L. C. Chen, C. J. Palmstrøm, R. D. James, S. McKernan, *Appl. Phys. Lett.* **1999**, *75*, 1443.
- [16] S. Miyazaki, Y. Q. Fu, W. M. Huang, *Thin Film Shape Memory Alloys: Fundamentals and Device Applications*, Cambridge University Press, Cambridge **2009**.
- [17] S. Seok, C. D. Onal, K.-J. Cho, R. J. Wood, D. Rus, S. Kim, *IEEE ASME Trans. Mechatron.* **2013**, *18*, 1485.
- [18] D. K. Patel, X. Huang, Y. Luo, M. Mungekar, M. K. Jawed, L. Yao, C. Majidi, *Adv. Mater. Technol.* **2023**, *8*, 2201259.
- [19] F. Xiao, X. Liang, H. Chen, Z. Li, Z. Li, X. Jin, T. Fukuda, *Scr. Mater.* **2019**, *168*, 86.
- [20] S. Tottori, L. Zhang, F. Qiu, K. K. Krawczyk, A. Franco-Obregón, B. J. Nelson, *Adv. Mater.* **2012**, *24*, 811.
- [21] R. Nauber, S. R. Goudou, M. Goeckenjan, M. Bornhäuser, C. Ribeiro, M. Medina-Sánchez, *Nat. Commun.* **2023**, *14*, 728.

- [22] H. Zhang, B. Xu, Y. Ouyang, Y. Wang, H. Zhu, G. Huang, J. Cui, Y. Mei, *Research* **2022**, 2022, 9842752.
- [23] R. A. de Groot, F. M. Mueller, P. G. van Engen, K. H. J. Buschow, *Phys. Rev. Lett.* **1983**, 50, 2024.
- [24] W. G. Zeier, J. Schmitt, G. Hautier, U. Aydemir, Z. M. Gibbs, C. Felser, G. J. Snyder, *Nat. Rev. Mater.* **2016**, 1, 16032.
- [25] V. R. Almeida, C. A. Barrios, R. R. Panepucci, M. Lipson, *Nature* **2004**, 431, 1081.
- [26] S. Abel, T. Stöferle, C. Marchiori, C. Rossel, M. D. Rossell, R. Erni, D. Caimi, M. Sousa, A. Chelnokov, B. J. Offrein, J. Fompeyrine, *Nat. Commun.* **2013**, 4, 1671.
- [27] Lumiphase Corporation – Efficient Photonic Engines, <https://www.lumiphase.com/> (accessed: May 2023).
- [28] A. Backen, S. R. Yeduru, M. Kohl, S. Baunack, A. Diestel, B. Holzapfel, L. Schultz, S. Fähler, *Acta Mater.* **2010**, 58, 3415.
- [29] S. Kaufmann, U. K. Rößler, O. Heczko, M. Wuttig, J. Buschbeck, L. Schultz, S. Fähler, *Phys. Rev. Lett.* **2010**, 104, 145702.
- [30] K. Bhattacharya, *Microstructure of Martensite: Why It Forms and How It Gives Rise To The Shape-Memory Effect*, Oxford University Press, Oxford **2003**.
- [31] S. Schwabe, R. Niemann, A. Backen, D. Wolf, C. Damm, T. Walter, H. Seiner, O. Heczko, K. Nielsch, S. Fähler, *Adv. Funct. Mater.* **2021**, 31, 2005715.
- [32] L. Zhou, M. M. Schneider, A. Giri, K. Cho, Y. Sohn, *Acta Mater.* **2017**, 134, 93.
- [33] J. Buschbeck, R. Niemann, O. Heczko, M. Thomas, L. Schultz, S. Fähler, *Acta Mater.* **2009**, 57, 2516.
- [34] R. Niemann, A. Backen, S. Kauffmann-Weiss, C. Behler, U. K. Rößler, H. Seiner, O. Heczko, K. Nielsch, L. Schultz, S. Fähler, *Acta Mater.* **2017**, 132, 327.
- [35] M. T. Ghahfarokhi, A. Chirkova, F. Maccari, F. Casoli, S. Ener, K. P. Skokov, R. Cabassi, O. Gutfleisch, F. Albertini, *Acta Mater.* **2021**, 221, 117356.
- [36] L. Straka, O. Heczko, K. Ullakko, *J. Magn. Magn. Mater.* **2004**, 272, 2049.
- [37] A. Tekgül, K. Şarlar, İ. Küçük, *J. Magn. Magn. Mater.* **2019**, 469, 183.
- [38] J. Buschbeck, J. K. Kawasaki, A. Kozhanov, R. D. James, C. J. Palmström, *Appl. Phys. Lett.* **2011**, 98, 191901.
- [39] S. Kauffmann-Weiss, S. Hahn, C. Weigelt, L. Schultz, M. F.-X. Wagner, S. Fähler, *Acta Mater.* **2017**, 132, 255.
- [40] K. Lünser, A. Undisz, K. Nielsch, S. Fähler, *JPhys Mater.* **2023**, 6, 035002.
- [41] Y. C. Shu, K. Bhattacharya, *Acta Mater.* **1998**, 46, 5457.
- [42] M. Kohl, M. Schmitt, A. Backen, L. Schultz, B. Krevet, S. Fähler, *Appl. Phys. Lett.* **2014**, 104, 043111.
- [43] J. S. Juan, M. L. Nó, C. A. Schuh, *Nat. Nanotechnol.* **2009**, 4, 415.
- [44] A. Diestel, R. Niemann, B. Schleicher, S. Schwabe, L. Schultz, S. Fähler, *J. Appl. Phys.* **2015**, 118, 023908.
- [45] L. Fink, K. Nielsch, S. Fähler, *J. Alloys Compd.* **2023**, 966, 171435.
- [46] L. Seigner, O. Bezsmertna, S. Fähler, G. K. Tshikwand, F. Wendler, M. Kohl, at The 1st Int. Electronic Conf. on Actuator Technology: Materials, Devices and Applications, Basel, Switzerland, November **2020**.
- [47] M. Kohl, M. Gueltig, V. Pinneker, R. Yin, F. Wendler, B. Krevet, *Micro-machines* **2014**, 5, 1135.
- [48] S. Chadov, X. Qi, J. Kübler, G. H. Fecher, C. Felser, S. C. Zhang, *Nat. Mater.* **2010**, 9, 541.
- [49] Y. Nakajima, R. Hu, K. Kirshenbaum, A. Hughes, P. Syers, X. Wang, K. Wang, R. Wang, S. R. Saha, D. Pratt, J. W. Lynn, J. Paglione, *Sci. Adv.* **2015**, 1, e1500242.
- [50] T. Kimura, N. Hashimoto, S. Yamada, M. Miyao, K. Hamaya, *NPG Asia Mater.* **2012**, 4, e9.
- [51] S. Yamada, K. Yamamoto, K. Ueda, Y. Ando, K. Hamaya, T. Sadoh, M. Miyao, *Thin Solid Films* **2010**, 518, S278.
- [52] K. Hamaya, M. Yamada, *MRS Bull.* **2022**, 47, 584.



Pattern recognition in reciprocal space with a magnon-scattering reservoir

Received: 7 November 2022

Accepted: 13 June 2023

Published online: 04 July 2023

Lukas Körber^{1,2,5}✉, Christopher Heins^{1,2,5}, Tobias Hula^{1,3}, Joo-Von Kim⁴,
Sonia Thlang⁴, Helmut Schultheiss^{1,2}, Jürgen Fassbender^{1,2} &
Katrin Schultheiss¹✉

Magnons are elementary excitations in magnetic materials and undergo non-linear multimode scattering processes at large input powers. In experiments and simulations, we show that the interaction between magnon modes of a confined magnetic vortex can be harnessed for pattern recognition. We study the magnetic response to signals comprising sine wave pulses with frequencies corresponding to radial mode excitations. Three-magnon scattering results in the excitation of different azimuthal modes, whose amplitudes depend strongly on the input sequences. We show that recognition rates as high as 99.4% can be attained for four-symbol sequences using the scattered modes, with strong performance maintained with the presence of amplitude noise in the inputs.

A key challenge in modern electronics is to develop low-power solutions for information processing tasks such as pattern recognition on noisy or incomplete data. One promising approach is physical reservoir computing, which exploits the nonlinearity and recurrence of dynamical systems (the reservoir) as a computational resource^{1–4}. Examples include a diverse range of materials such as water⁵, optoelectronic systems^{6–9}, silicon photonics¹⁰, microcavity lasers¹¹, organic electrochemical transistors¹², dynamic memristors¹³, nanowire networks¹⁴, and magnetic devices^{15–21}.

The physical reservoir embodies a recurrent neural network. A natural implementation comprises interconnected nonlinear elements in space (spatial multiplexing, Fig. 1a), where information is fed into the system via input nodes representing distinct spatial elements, and the dynamical state is read out through another set of output nodes^{5,12,14,22}. Another approach involves mapping the network onto a set of virtual nodes in time by using delayed-feedback dynamics on a single nonlinear node (temporal multiplexing, Fig. 1b)^{6–9,13,18}, which reduces the complexity in spatial connectivity at the expense of more intricate time-dependent signal processing.

Here, we study an alternative paradigm in which we exploit instead the dynamics in the *modal space* of a magnetic element. This

scheme relies on magnon interactions in magnetic materials whereby inputs and outputs correspond to particular eigenmodes of a micromagnetic state. Micrometer-sized magnetic structures can exhibit hundreds of modes in the GHz range²³. Processes such as three-magnon-scattering interconnect the modes with each other and, with that, provide the nonlinearity and recurrence required for computing. We refer to this approach as modal multiplexing with signals evolving in reciprocal space, in which the actual computation is performed. This is distinct from other wave-based schemes where information is processed with wave propagation and interference in real space^{11,16,19,24,25}, and differs from temporal multiplexing where virtual nodes are constructed with delayed feedback^{6–9,13,18}. The latter also includes reservoirs based on optical cavities where multimode dynamics (such as frequency combs) are exploited but the output spaces are still constructed by temporal multiplexing^{26–28}.

We illustrate the concept of modal multiplexing with a pattern recognition task using a magnon-scattering reservoir (MSR). The patterns comprise a sequence of symbols “A” and “B” represented by radiofrequency (rf) signals, which consist of sine wave pulses with two distinct frequencies, f_A and f_B , and amplitudes $b_{rf,A}$ and $b_{rf,B}$ as shown in Fig. 1d. An example of the power spectrum of the input sequence is

¹Institut für Ionenstrahlphysik und Materialforschung, Helmholtz-Zentrum Dresden - Rossendorf, Bautzner Landstr. 400, Dresden D-01328, Germany. ²Fakultät Physik, Technische Universität Dresden, Dresden D-01062, Germany. ³Institut für Physik, Technische Universität Chemnitz, Chemnitz D-09107, Germany.

⁴Centre de Nanosciences et de Nanotechnologies, CNRS, Université Paris-Saclay, 91120 Palaiseau, France. ⁵These authors contributed equally: Lukas Körber, Christopher Heins. ✉ e-mail: l.koerber@hzdr.de; k.schultheiss@hzdr.de

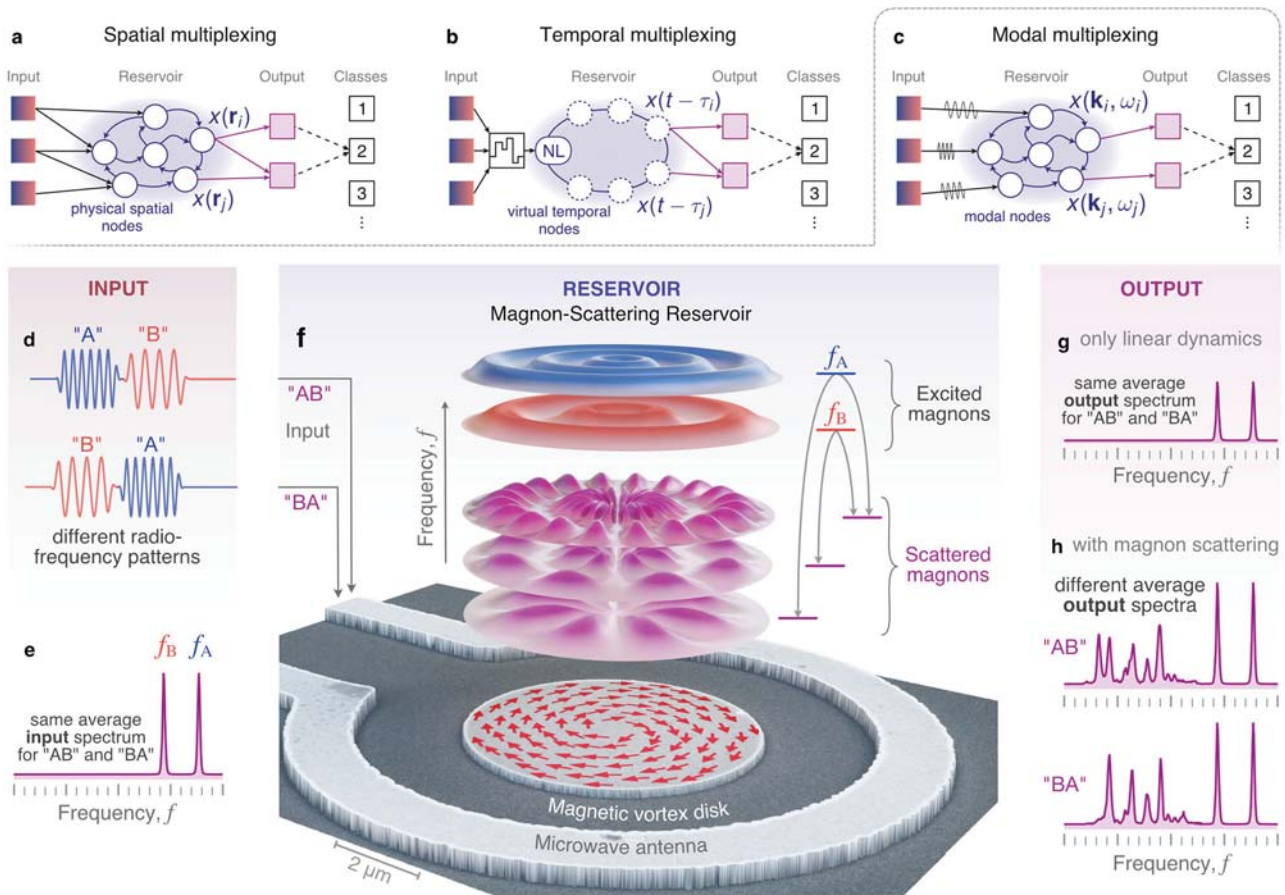


Fig. 1 | Working principle of a magnon-scattering reservoir (MSR). Sketches of different reservoirs based on **a** spatial, **b** temporal, and **c** modal multiplexing, the concept behind the MSR. **d** Radiofrequency pulses with different temporal order but **e** the same average frequency content are used to trigger **f** nonlinear scattering

between the magnon eigenmodes in a magnetic vortex disk. The dynamic response is experimentally detected using Brillouin-light-scattering microscopy (see Methods). In contrast to a linear system (**g**), the MSR produces different outputs depending on the temporal order of the input (**h**).

given in Fig. 1e. The rf pulses generate oscillating magnetic fields along the z direction through an Ω -shaped antenna, which surrounds a $5.1 \mu\text{m}$ wide, 50-nm thick $\text{Ni}_{81}\text{Fe}_{19}$ disk which hosts a magnetic vortex as a ground state (Fig. 1f). f_A and f_B are chosen to coincide with the frequencies of primary radial eigenmodes of the vortex, which, when excited above a given threshold, result in the excitation of secondary azimuthal eigenmodes through three-magnon-scattering processes²³. In our previous work²⁹, we have shown that individual three-magnon splitting channels, e.g. exciting only f_A , can be stimulated below their threshold power, and their temporal evolution is significantly modified by additionally exciting one of the secondary modes. In ref. 29, this stimulation was achieved by magnons propagating in a waveguide adjacent to the vortex disk. Here, as a logical extension, the role of the stimulating magnon is provided by the secondary modes of another (active) three-magnon channel f_B , a process that we refer to as cross-stimulated three-magnon splitting. The operation of our MSR strongly relies on the fact that the cross-stimulation between f_B and f_A is not reciprocal due to the involved nonlinear transients. In other words, the effect of channel f_A on the channel f_B via cross-stimulation differs from the feedback of f_B on f_A .

The power spectrum of excited magnons is obtained experimentally through micro-focused Brillouin light scattering spectroscopy (μBLS), where a portion of the disk is probed (see Methods and Supplementary Fig. 1a). It is important to note that in the linear response regime neither the input spectrum (Fig. 1e) nor the directly-excited magnon spectrum (Fig. 1g) gives any information about the actual sequence of “A” and “B” (e.g., “AB” and “BA” are equivalent). This

means that no linear classifier can be employed. However, when nonlinear processes are at play, magnon-scattering, and associated transient processes result in distinct spectral signatures that can be used to distinguish between different input sequences (Fig. 1h).

Results

Figure 2 illustrates the role of three-magnon splitting (3MS), the primary nonlinear process at play for the MSR, in which a strongly-excited primary magnon splits into two secondary magnons under the conservation of energy and momentum. In experiments, we choose 20-ns pulses of $f_A = 8.9 \text{ GHz}$ (20 dBm) and $f_B = 7.4 \text{ GHz}$ (24 dBm), which excite different radial modes of the vortex above their respective power threshold for 3MS, to represent the symbols “A” and “B”, respectively (Fig. 2a). The magnon intensity is probed as a function of frequency and time using time-resolved (TR) μBLS (see Methods) and is color-coded in Fig. 2b. We measure not only the directly excited primary magnons at f_A and f_B , but also magnons at frequencies around half the respective excitation frequencies which result from the nonlinearity of spontaneous 3MS (see Fig. 2c)^{23,29}. Here, only the scattering channel with the lowest power threshold is active while other allowed scattering channels remain silent (depicted by dotted lines in Fig. 2c).

Cross-stimulation occurs when signals “A” and “B” overlap in time, as shown in Fig. 2d. Two different primary magnons that share a common secondary mode, as is depicted in Fig. 2f, can result in two 3MS channels that mutually cross-stimulate each other, even below their intrinsic thresholds and along silent channels²⁹. Thus, within the overlap interval, the pumped secondary magnon of the first symbol

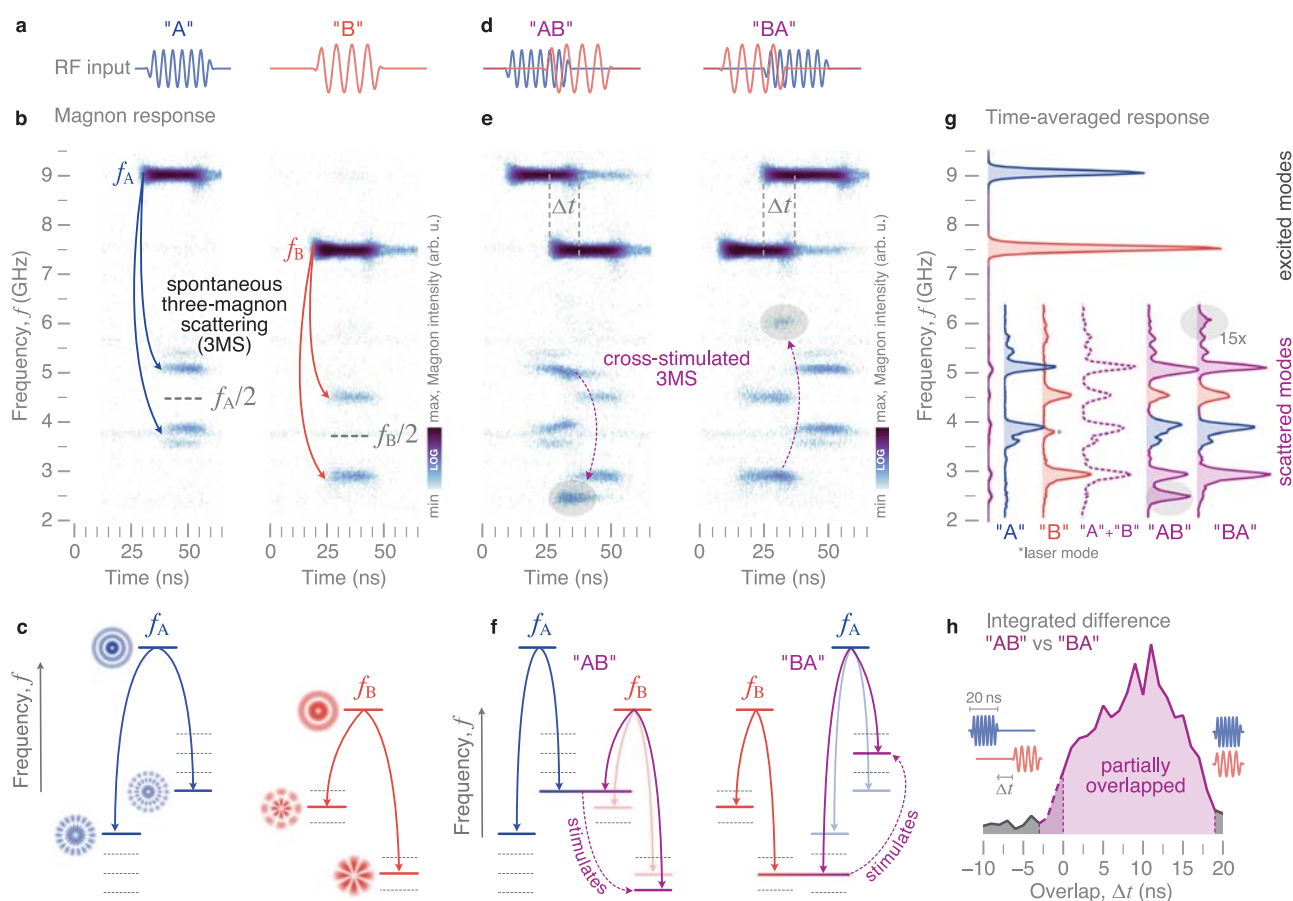


Fig. 2 | Physical background of the magnon-scattering reservoir (MSR). When pumped strongly by microwave fields (a), a directly-excited primary magnon splits into two secondary magnons (b) via spontaneous 3MS (c). **b** Time-resolved frequency response of the MSR to two different input frequencies experimentally measured with TR- μ BLS. **d** Driving the MSR with two different, temporally overlapping microwave pulses “A” and “B” leads to **e**, **f** cross-stimulated 3MS between the channels and to additional peaks in the measured frequency response.

g Experimentally measured output spectra integrated over time which is different depending on the temporal order of the pulses. Different colors denote different contributions from the two input signals. Blue peaks result from input “A” only, red peaks from “B”, and purple peaks from cross-stimulation. **h** The integrated difference between the spectra of “AB” and “BA” shows that the responses are different when the pulses overlap in time.

influences the primary mode scattering of the second symbol, and vice versa, leading to the primary mode scattering into multiple pairs of secondary modes (Fig. 2e).

Because cross-stimulation strongly depends on the temporal order of the primary excitation (Fig. 2f), it provides an important physical resource for processing the temporal sequence of our “AB” signals. This is shown by the experimental results plotted in Fig. 2g, where we compare the time-averaged power spectra for the “AB” and “BA” sequences. These spectra are computed by integrating the temporal data in Fig. 2e. When only signal “A” or only signal “B” is applied, we measure conventional spontaneous 3MS of the respective primary modes with the secondary modes already discussed above in context of Fig. 2b. Within the overlap interval, the mutual cross-stimulation leads to additional peaks in the scattered mode spectrum. As highlighted by shaded areas in Fig. 2e, g, the frequencies and amplitudes of these additional scattered modes strongly depend on the temporal order of the two input signals. Consequently, the average spectra of “AB” and “BA” are different from each other, and neither can be constructed from a simple superposition of the average spectra of “A” and “B” individually (Fig. 2g). This is the key principle that underpins how the MSR processes temporal signals.

To highlight the significance of the transient times, we vary the overlap Δt of the symbols “A” and “B” in experiments and determine the frequency-averaged difference between the time-averaged spectra of “AB” and “BA” (Fig. 2h). This difference is zero when the two input

pulses do not overlap since no cross-stimulation takes place. With increasing overlap, however, cross-stimulation between the two pulses becomes more significant and leads to a difference in the output of the reservoir. This difference vanishes again when the input pulses fully overlap and, thus, arrive at the same time.

In order to explore the capabilities of the presented MSR, the complexity of the input signals was further increased experimentally. Figure 3a shows the nonlinear response to the four-symbol pulse pattern “ABAB” measured by TR- μ BLS. In contrast to a reference spectrum composed by a simple linear superposition of two consecutive “AB” patterns, shown in Fig. 3b, the real spectrum of the four-symbol response contains additional features which are generated by cross-stimulated scattering when two pulses overlap. The differences are highlighted by the shaded areas in Fig. 3a and circled areas in Fig. 3b, respectively. This behavior illustrates that cross-stimulation can result in distinct features that allow distinguishing also longer patterns. This is further exemplified in Fig. 3c, which shows the time-averaged BLS spectra of the six four-symbol combinations comprising two “A” and two “B”. Like the data in Fig. 2, transient processes from cross-stimulation generate distinct power spectra for the six combinations, which would be indistinguishable in the linear response regime.

Since the experimental data discussed so far requires the integration of thousands of pulse cycles, we rely on micromagnetic simulations to quantify the capacity of the MSR for recognizing all

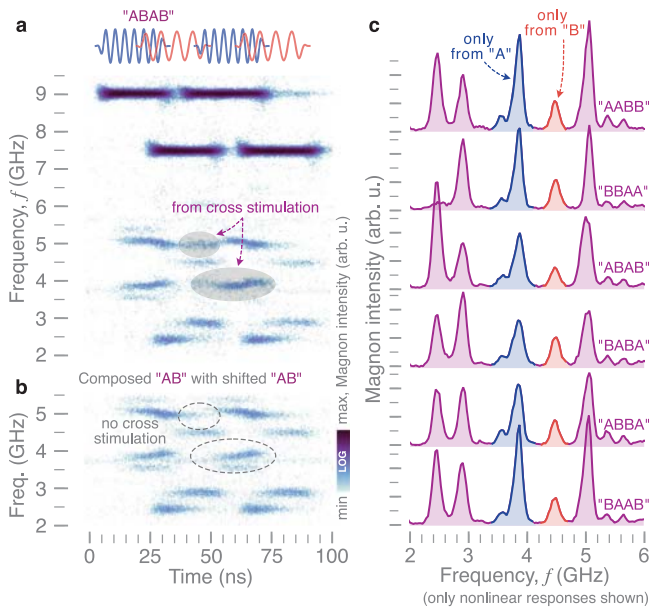


Fig. 3 | Performance of the MSR for longer temporal patterns characterized experimentally. **a** Time-resolved spectral response of the MSR to a four-symbol microwave pattern “ABAB”, detected experimentally with TR- μ BLS. **b** For reference, the spectrum of “AB” is overlaid with a shifted version of itself. Differences between composed and real spectrum (due to cross-stimulated magnon scattering) are highlighted by shaded and circled areas. **c** Average output spectra of the MSR for different four-symbol patterns with the same average input-frequency content but clearly different nonlinear responses.

possible combinations of four-symbol sequences composed from “A” and “B” (see Methods). Thereby, we are able to analyze individual pulse sequences and study the influence of thermal noise and amplitude fluctuations on the recognition rate of the MSR. Figure 4a shows a simulated power spectrum (at $T=300$ K) for the input pattern “ABAB” with $f_A = 8.9$ GHz ($b_{rf,A} = 3$ mT) and $f_B = 7.4$ GHz ($b_{rf,B} = 3.5$ mT), with the field strengths chosen to be above the respective power threshold for 3MS. The output spaces of the reservoir are defined by subdividing the time-averaged power spectrum into frequency bins of different widths. To emphasize the importance of the scattering (interconnection) between the different magnon modes, we study the performance of the MSR for two separate output spaces (Fig. 4a). One output space for the scattered modes is constructed over a 4-GHz window below f_A and f_B , where the different frequency bins result in an output vector with 16–80 components depending on the bin size (see Supplementary Note 1). For comparison, a two-dimensional output space corresponding to the directly-excited modes is constructed by averaging within bins centered around f_A and f_B . Note that, here, analyzing the directly-excited modes does not correspond to a linear classifier, as these modes themselves experience nonlinear feedback (amplitude losses, frequency shift, etc.) above their power threshold for 3MS.

For each four-symbol sequence, 200 micromagnetic simulations were executed with different realizations of the thermal field in order to generate distinct output states. Supervised learning using logistic regression was then performed on this data set to construct trained models of the output states based on either the directly-excited or scattered modes. The accuracy of these models for different combinations of input frequencies $f_A = 8.9$ GHz, $f_B = 7.2$ GHz, $f_C = 6.5$ GHz, $f_D = 10.7$ GHz (and corresponding input strengths $b_{rf,i}$) is shown in Fig. 4b as a function of bin size. We find that the MSR performs comparably well when choosing different input frequencies (different radial modes) to represent the input symbols. Hence, an

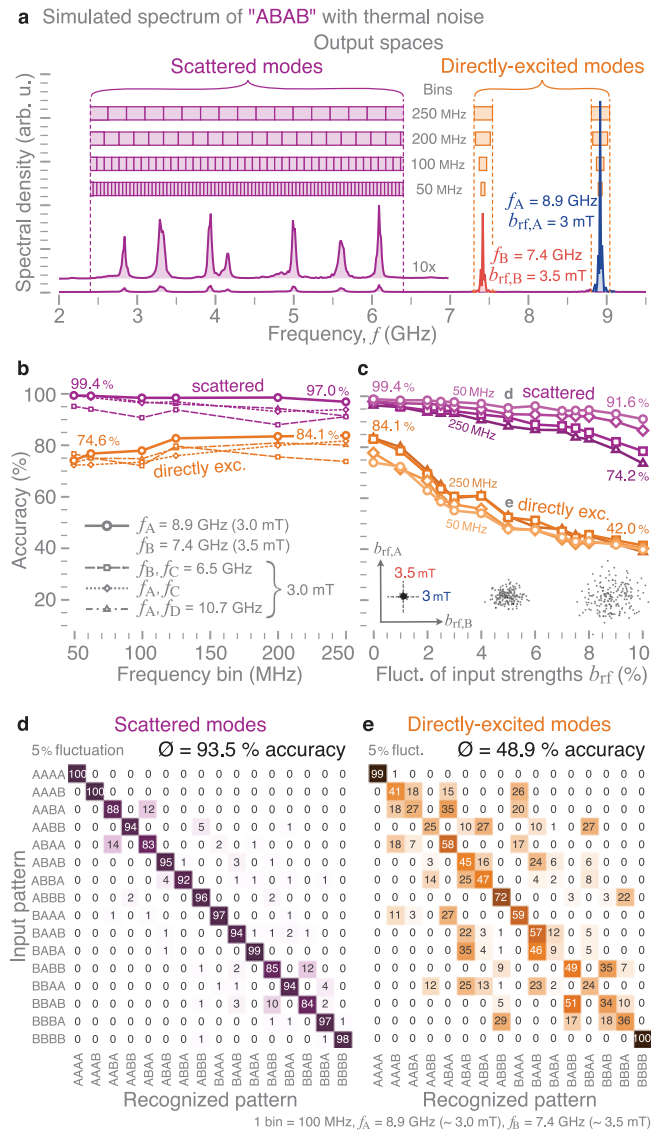


Fig. 4 | Micromagnetic modeling of pattern recognition capabilities. **a** Simulated spectrum of the pattern “ABAB” with the definition of different output spaces (scattered and directly excited modes) for the MSR. **b** Average detection accuracy of four-symbol patterns for different output spaces and excitation frequency and power combinations as a function of frequency bin sizes. **c** Accuracy for different output spaces and bin sizes as a function of power fluctuations in the input signals (depicted by the insets). **d, e** Corresponding confusion matrices for the two output spaces, respectively, both for the same frequency combination, bin size, and input power fluctuation.

extension of the input space to more than two frequencies/symbols (“ABC”, “BDC”, “ABCD”, etc.), or even to more broadband signals, is straightforward. To this end, Supplementary Note 2 contains the measured and simulated distinct nonlinear responses for different permutations of the three and four-frequency sequences “ABC” and “ABCD”.

Overall, the accuracy depends weakly on the bin size. The recognition rate slightly increases with increasing bin size for the directly-excited modes whereas it decreases marginally for the scattered modes. This can be understood from the fact that smaller bin sizes capture more features of the power spectrum of the scattered modes, while for the directly-excited modes, the larger bin sizes contain more information about potential nonlinear frequency shifts, which helps to separate the inputs. We observe that outputs based on the directly-excited modes can yield an accuracy of ~84%, while

scattered modes provide a notable improvement in performance, with an accuracy reaching 99.4% for the case considered in Fig. 4a.

In general, the scattered modes provide higher accuracy for pattern recognition compared with the directly-excited modes. The difference in accuracy becomes even more pronounced when amplitude fluctuations are present. Figure 4c illustrates how the accuracy evolves with the fluctuation strength, which represents the width of the normal distributions (in %), centered around the nominal values of $b_{rf,A}$ and $b_{rf,B}$, from which the field strengths are drawn, as shown in the inset for $b_{rf,A} = 3$ mT and $b_{rf,B} = 3.5$ mT. The performance of the MSR based on the directly-excited modes drops significantly with increasing fluctuation strength (42% accuracy at 10% fluctuation). However, recognition based on the scattered modes is much more resilient, with a decrease to only between -74% and -92% accuracy (depending on the bin size).

Figure 4d, e show confusion matrices for the scattered and directly-excited modes, respectively, both for the same set of parameters. They highlight the robustness of the MSR which is based on the scattered modes since it mainly fails to distinguish “AABA” from “ABAA” and “BBAB” from “BBAB” in -12% of the cases. The MSR based on the directly-excited modes, on the other hand, fails to recognize almost all of the patterns, except for the trivial cases of “AAAA” and “BBBB” for which there is practically no ambiguity in the inputs. These trends do not depend on the type of supervised learning used and highlight the important role of cross-stimulated 3MS in the MSR for the pattern recognition of noisy radiofrequency signals.

Discussion

Our findings demonstrate the possibility of performing reservoir computing in modal space utilizing the intrinsic nonlinear properties of a magnetic system, namely the scattering processes between magnons in a magnetic vortex disk. Temporal patterns encoded using two different input-frequency pulses can be distinguished with high accuracy. The results also indicate that input patterns can be extended to more broadband signals. We note that the technical design of the physical reservoir is extremely simple and requires very little pre-processing, while the complexity of the data handling arises mostly from the intrinsic nonlinear dynamics of the magnon system. Additionally, recent findings have shown that the magnon interactions in micrometer-sized disks can be modified significantly by small static magnetic fields³⁰, providing effective means to enhance the complexity of the magnon-scattering reservoir further. Although our current read-out scheme is based on optical methods, magnetoresistive sensors hold promising possibilities for an all-electric read-out.

Methods

Sample preparation and characterization

The magnetic disk housing the magnon-scattering reservoir for our experiments was manufactured in a two-step procedure: In a first step, using electron-beam evaporation and subsequent lift off, a magnetic disk with a diameter of 5.1 μm was patterned from a Ti(2)/Ni₈₁Fe₁₉(50)/Ti(5) film deposited on a SiO₂ substrate which had been capped with a 5-nm thick aluminum layer. All thicknesses are given in nanometers. In a second step, an Ω -shaped antenna used to excite magnon dynamics in the reservoir was patterned around the disk from a Ti(2)/Au(200), also using electron-beam evaporation and subsequent lift off. The inner and outer diameter of the antenna are 8.3 μm and 11.1 μm , respectively. An image of the sample, obtained with scanning electron microscopy, can be seen in Supplementary Fig. 1a.

Signal generation

The radiofrequency (rf) pulses were generated by two separate rf-sources set to a fixed frequency corresponding to pulse “A” and pulse “B”, respectively (see Supplementary Fig. 1b). In order to synchronize the two sources, a pattern generator (Pulstreamer by Swabian Instruments) was used to create a pattern of arbitrary shape gating the

rf-sources. The two generated microwave signals were combined and fed onto the Ω -shaped antenna using picoprobes.

Time-resolved Brillouin-light-scattering microscopy

All experimental measurements were carried out at room temperature. Magnon spectra were obtained by means of Brillouin-light-scattering microscopy as schematically shown in Supplementary Fig. 1b³¹. A monochromatic 532-nm laser (CW) was focused onto the sample surface using a 100x microscope lens with a numerical aperture of 0.7. The backscattered light was then directed into a Tandem Fabry-Pérot interferometer (TFPI) using a beam splitter (BS) in order to measure the frequency shift caused by inelastic scattering of photons and magnons. Control signals that encode the current state of the interferometer, signals of the photon counter inside the TFPI and a clock signal from the pattern generator were acquired continuously by a time-to-digital converter (Timetagger 20 by Swabian Instruments). From these data, the temporal evolution of the magnon spectra with respect to the stroboscopic rf excitation was reconstructed. During the experiments, the investigated structure was imaged using a red LED and a CCD camera (red beam path in Supplementary Fig. 1b). Displacements and drifts of the sample were tracked by an image recognition algorithm and compensated by the positioning system (XMS linear stages by Newport). The laser and imaging beam path were separated by the dichroic mirror as shown in Supplementary Fig. 1b. In order to ensure that all stationary magnon modes were measured, the signal was averaged over 10 positions across half the disk as seen in Supplementary Fig. 1a.

Micromagnetic simulations

Simulations of the vortex dynamics were performed using the open-source finite-difference micromagnetics code MuMax3³², which performs a time integration of the Landau-Lifshitz-Gilbert equation of motion of the magnetization $\mathbf{m}(\mathbf{r}, t)$,

$$\frac{\partial \mathbf{m}}{\partial t} = -\gamma \mathbf{m} \times (\mathbf{B}_{\text{eff}} + \mathbf{b}_{\text{th}}) + \alpha \mathbf{m} \times \frac{\partial \mathbf{m}}{\partial t}. \quad (1)$$

Here, $\mathbf{m}(\mathbf{r}, t) = \mathbf{M}(\mathbf{r}, t)/M_s$ is a unit vector representing the orientation of the magnetization field $\mathbf{M}(\mathbf{r}, t)$ with M_s being the saturation magnetization, $\gamma = g\mu_B/\hbar$ is the gyromagnetic constant, and α is the dimensionless Gilbert-damping constant. The effective field, $\mathbf{B}_{\text{eff}} = -\delta U/\delta \mathbf{m}$, represents a variational derivative of the total magnetic energy U with respect to the magnetization, where U contains contributions from the Zeeman, nearest-neighbor Heisenberg exchange, and dipole-dipole interactions. The term \mathbf{b}_{th} represents a stochastic field with zero mean, $\langle b_{\text{th}}^i(\mathbf{r}, t) \rangle = 0$ and spectral properties satisfying³³

$$\langle b_{\text{th}}^i(\mathbf{r}, t) b_{\text{th}}^j(\mathbf{r}', t') \rangle = \frac{2\alpha k_B T}{\gamma M_s V} \delta_{ij} \times \delta(\mathbf{r} - \mathbf{r}') \delta(t - t'), \quad (2)$$

with amplitudes drawn from a Gaussian distribution. Here, k_B is Boltzmann’s constant, T is the temperature, and V denotes the volume of the finite-difference cell. This stochastic term models the effect of thermal fluctuations acting on the magnetization dynamics. An adaptive time-step algorithm based on a sixth-order Runge-Kutta-Fehlberg method was used to perform the time integration³⁴.

We model our 50-nm thick, 5.1- μm diameter disk using $512 \times 512 \times 1$ finite-difference cells with $\gamma/2\pi = 29.6$ GHz/T, $M_s = 810$ kA/m, an exchange constant of $A_{\text{ex}} = 13$ pJ/m, and $\alpha = 0.008$. Previous work has shown that these simulation parameters provide excellent agreement with previous experimental results²³.

For the magnon dynamics shown in Fig. 4, we first obtain the magnetic ground state of the disk by initializing with a vortex state and subsequently relaxing the magnetization by minimizing the total magnetic energy in the absence of any static external applied fields.

Article

Magnons are then excited under a finite temperature of 300 K. First, we let the system evolve for 5 ns under the action of thermal fluctuations alone. A spatially uniform oscillating magnetic field $\mathbf{b}_{\text{rf}}(t) = b_{\text{rf}}(t)\mathbf{e}_z$ is then applied along the z direction, perpendicular to the film plane. Following the experimental work, the 4-symbol pulse patterns are encoded into $\mathbf{b}_{\text{rf}}(t)$ as a combination of two input-frequency signals,

$$b_{\text{rf}}(t) = W_A(t)b_{\text{rf},A} \sin(2\pi f_A t) + W_B(t)b_{\text{rf},B} \sin(2\pi f_B t). \quad (3)$$

$W_A(t)$ and $W_B(t)$ represent windowing functions where each “A” or “B” pattern lasts 20-ns with a 5-ns overlap between patterns. These windowing functions are illustrated in Supplementary Fig. 2 for the 16 4-symbol pulse patterns considered. The excitation field amplitude $b_{\text{rf},i}$ and frequency f_i for each pattern is given in the main text. After the end of the last pattern, the transient dynamics is computed for an additional 10 ns. The dynamics is simulated for a total duration of 80 ns for each 4-symbol pattern.

The power spectral density of the magnon excitations is computed by using a coarse-graining procedure (Supplementary Fig. 3).

The simulation geometry is further sub-divided using a triangle mesh (Supplementary Fig. 3a) in the film plane whereby we record the spatial average of the magnetization vector as a function of time, i.e., for a mesh element j ,

$$\mathbf{m}_j(t) = \frac{1}{V_j} \int_{V_j} d^3x \mathbf{m}(\mathbf{r}, t), \quad (4)$$

where V_j is the volume of the mesh element. With $V = \sum_j V_j$ representing the total volume, the total power spectral density $\mathcal{S}(\omega) = (1/V) \sum_j \mathcal{S}_j(\omega) V_j$ is then constructed from the discrete Fourier transform of the z component of the averaged magnetization for each element, $\mathcal{S}_j(\omega) = |\mathcal{M}_j(\omega)|^2$, where

$$\mathcal{M}_j(\omega) = \sum_{n=0}^{N-1} e^{-i\omega(n\Delta t)} m_{j,z}(n\Delta t), \quad (5)$$

$\Delta t = 20$ ps is the time-step, and $N = 8000$ is the total number of time steps. Supplementary Fig. 3a and b illustrate the power spectrum for individual regions, i.e., for Region 1 and Region 2 in Supplementary Fig. 3a, respectively. Even at the level of a single mesh region, we can clearly identify the directly excited modes at f_A and f_B , along with a number of scattered modes. Averaging over a quadrant of the disk gives the power spectrum in Supplementary Fig. 3d, where we can see a much-improved signal-to-noise ratio of the excited and scattered modes. Supplementary Fig. 3e shows the power spectrum averaged over all the mesh regions of the disk, which is qualitatively very similar to the quadrant-averaged result in Supplementary Fig. 3d. For this reason, we only used the quadrant-averaged spectra for the pattern recognition tasks in the interest of minimizing computation time without loss of generality. The construction of the output spaces from the obtained spectra is described in Supplementary Note 1.

Data availability

The numerical and experimental data used in this study are available in the RODARE database under <https://doi.org/10.14278/rodare.2344>.

Code availability

The software package used for micromagnetic simulations is found at <http://mumax.github.io/api.html>.

References

1. Jaeger, H. The “echo state” approach to analysing and training recurrent neural networks—with an erratum note. *Bonn, Germany: German National Research Center for Information Technology GMD Technical Report* **148**, 13 (2001).
2. Nakajima, K. Physical reservoir computing—an introductory perspective. *Jpn. J. Appl. Phys.* **59**, 060,501 (2020).
3. Tanaka, G. et al. Recent advances in physical reservoir computing: a review. *Neural Netw.* **115**, 100–123 (2019).
4. Maass, W., Natschläger, T. & Markram, H. Real-time computing without stable states: a new framework for neural computation based on perturbations. *Neural Comput.* **14**, 2531–2560 (2002).
5. Fernando, C., Sojakka, S. Pattern Recognition in a Bucket. pp. 588–597 https://doi.org/10.1007/978-3-540-39432-7_63 (2003).
6. Appeltant, L. et al. Information processing using a single dynamical node as complex system. *Nat. Commun.* **2**, 468 (2011).
7. Paquot, Y. et al. Optoelectronic reservoir computing. *Sci. Rep.* **2**, 287 (2012).
8. Ortín, S. et al. A unified framework for reservoir computing and extreme learning machines based on a single time-delayed neuron. *Sci. Rep.* **5**, 14,945 (2015).
9. Larger, L. et al. High-speed photonic reservoir computing using a time-delay-based architecture: million words per second classification. *Phys. Rev. X* **7**, 011,015 (2017).
10. Vandoorne, K. et al. Experimental demonstration of reservoir computing on a silicon photonics chip. *Nat. Commun.* **5**, 1–6 (2014).
11. Sunada, S. & Uchida, A. Photonic reservoir computing based on nonlinear wave dynamics at microscale. *Sci. Rep.* **9**, 19,078 (2019).
12. Cucchi, M. et al. Reservoir computing with biocompatible organic electrochemical networks for brain-inspired biosignal classification. *Sci. Adv.* **7**, eabh0693 (2021).
13. Zhong, Y. et al. Dynamic memristor-based reservoir computing for high-efficiency temporal signal processing. *Nat. Commun.* **12**, 408 (2021).
14. Milano, G. et al. In materia reservoir computing with a fully memristive architecture based on self-organizing nanowire networks. *Nat. Mater.* **21**, 195–202 (2022).
15. Torrejon, J. et al. Neuromorphic computing with nanoscale spintronic oscillators. *Nature* **547**, 428–431 (2017).
16. Nakane, R., Tanaka, G. & Hirose, A. Reservoir computing with spin waves excited in a garnet film. *IEEE Access* **6**, 4462–4469 (2018).
17. Kanao, T. et al. Reservoir computing on spin-torque oscillator array. *Phys. Rev. Appl.* **12**, 024,052 (2019).
18. Watt, S., Kostylev, M., Ustinov, A. B. & Kalinikos, B. A. Implementing a magnonic reservoir computer model based on time-delay multiplexing. *Phys. Rev. Appl.* **15**, 064,060 (2021).
19. Nakane, R., Hirose, A. & Tanaka, G. Spin waves propagating through a stripe magnetic domain structure and their applications to reservoir computing. *Phys. Rev. Res.* **3**, 033,243 (2021).
20. Gartside, J. C. et al. Reconfigurable training and reservoir computing in an artificial spin-vortex ice via spin-wave fingerprinting. *Nat. Nanotechnol.* **17**, 460–469 (2022).
21. Ababei, R. V. et al. Neuromorphic computation with a single magnetic domain wall. *Sci. Rep.* **11**, 1–13 (2021).
22. Kan, S. et al. Simple reservoir computing capitalizing on the non-linear response of materials: theory and physical implementations. *Phys. Rev. Appl.* **15**, 024,030 (2021).
23. Schultheiss, K. et al. Excitation of whispering gallery magnons in a magnetic vortex. *Phys. Rev. Lett.* **122**, 097,202 (2019).
24. Marcucci, G., Pierangeli, D. & Conti, C. Theory of neuromorphic computing by waves: machine learning by Rogue waves, dispersive shocks, and solitons. *Phys. Rev. Lett.* **125**, 093,901 (2020).
25. Papp, Á., Porod, W. & Csaba, G. Nanoscale neural network using non-linear spin-wave interference. *Nat. Commun.* **12**, 6422 (2021).
26. Butschek, L. et al. Photonic reservoir computer based on frequency multiplexing. *Opt. Lett.* **47**, 782–785 (2022).
27. Vatin, J., Rontani, D. & Sciamanna, M. Enhanced performance of a reservoir computer using polarization dynamics in vessels. *Opt. Lett.* **43**, 4497–4500 (2018).

28. Harkhoe, K. & Van der Sande, G. Delay-based reservoir computing using multimode semiconductor lasers: exploiting the rich carrier dynamics. *IEEE J. Sel. Top. Quant. Electron.* **25**, 1–9 (2019).
29. Körber, L. et al. Nonlocal stimulation of three-magnon splitting in a magnetic vortex. *Phys. Rev. Lett.* **125**, 207,203 (2020).
30. Körber, L. et al. Modification of three-magnon splitting in a flexed magnetic vortex. *Appl. Phys. Lett.* **122**, 092,401 (2023).
31. Sebastian, T., Schultheiss, K., Obry, B., Hillebrands, B., Schultheiss, H. Micro-focused Brillouin light scattering: imaging spin waves at the nanoscale. *Front. Phys.* **3**, <https://doi.org/10.3389/fphy.2015.00035> (2015).
32. Vansteenkiste, A. et al. The design and verification of MuMax3. *AIP Adv.* **4**, 107,133 (2014).
33. Brown, W. Thermal fluctuations of a single-domain particle. *Phys. Rev.* **130**, 1677–1686 (1963).
34. Leliaert, J. et al. Adaptively time stepping the stochastic Landau-Lifshitz-Gilbert equation at nonzero temperature: implementation and validation in MuMax³. *AIP Adv.* **7**, 125,010 (2017).

Acknowledgements

The authors are thankful to D. Rontani and K. Knobloch for providing feedback on the manuscript and fruitful discussions. This study was supported by the German Research Foundation (DFG) within programs SCHU 2922/1-1 (H.S., T.H., C.H.), KA 5069/1-1, and KA 5069/3-1 (L.K.), as well as by the French Research Agency (ANR) under contract No. ANR-20-CE24-0012 (MARIN) (S.T., J.V.K.). The project has received funding from the EU Research and Innovation Programme Horizon Europe under grant agreement no. 101070290 (NIMFEIA) (K.S.). Support by the Nanofabrication Facilities Rossendorf (NanoFaRo) at the IBC is gratefully acknowledged.

Author contributions

Conceptualization: H.S., J.V.K., K.S. Investigation: C.H. Simulation: J.V.K., S.T. Visualization: L.K., T.H., J.V.K., H.S. Funding acquisition: J.V.K., H.S., J.F. Project administration: H.S., K.S. Writing—original draft: L.K. Writing—review and editing: L.K., C.H., T.H., J.V.K., H.S., J.F., K.S.

Funding

Open Access funding enabled and organized by Projekt DEAL.

Competing interests

The authors declare no competing interests.

Additional information

Supplementary information The online version contains supplementary material available at <https://doi.org/10.1038/s41467-023-39452-y>.

Correspondence and requests for materials should be addressed to Lukas Körber or Katrin Schultheiss.

Peer review information *Nature Communications* thanks Gyorgy Csaba and the other, anonymous, reviewer(s) for their contribution to the peer review of this work. A peer review file is available.

Reprints and permissions information is available at <http://www.nature.com/reprints>

Publisher's note Springer Nature remains neutral with regard to jurisdictional claims in published maps and institutional affiliations.

Open Access This article is licensed under a Creative Commons Attribution 4.0 International License, which permits use, sharing, adaptation, distribution and reproduction in any medium or format, as long as you give appropriate credit to the original author(s) and the source, provide a link to the Creative Commons licence, and indicate if changes were made. The images or other third party material in this article are included in the article's Creative Commons licence, unless indicated otherwise in a credit line to the material. If material is not included in the article's Creative Commons licence and your intended use is not permitted by statutory regulation or exceeds the permitted use, you will need to obtain permission directly from the copyright holder. To view a copy of this licence, visit <http://creativecommons.org/licenses/by/4.0/>.

© The Author(s) 2023

Ferromagnetic Interlayer Coupling in CrSBr Crystals Irradiated by Ions

Fangchao Long, Mahdi Ghorbani-Asl, Kseniia Mosina, Yi Li, Kaiman Lin, Fabian Ganss, René Hübner, Zdenek Sofer, Florian Dirnberger,* Akashdeep Kamra, Arkady V. Krasheninnikov, Slawomir Prucnal, Manfred Helm, and Shengqiang Zhou*



Cite This: *Nano Lett.* 2023, 23, 8468–8473

ACCESS |

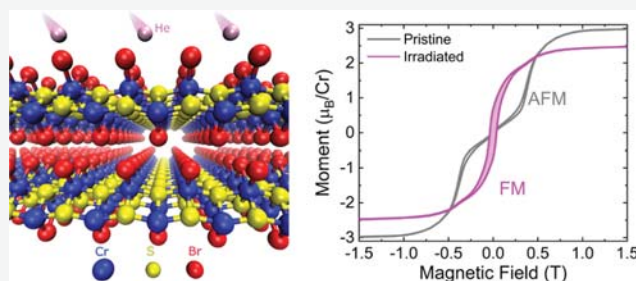
Metrics & More

Article Recommendations

Supporting Information

ABSTRACT: Layered magnetic materials are becoming a major platform for future spin-based applications. Particularly, the air-stable van der Waals compound CrSBr is attracting considerable interest due to its prominent magneto-transport and magneto-optical properties. In this work, we observe a transition from antiferromagnetic to ferromagnetic behavior in CrSBr crystals exposed to high-energy, non-magnetic ions. Already at moderate fluences, ion irradiation induces a remanent magnetization with hysteresis adapting to the easy-axis anisotropy of the pristine magnetic order up to a critical temperature of 110 K. Structure analysis of the irradiated crystals in conjunction with density functional theory calculations suggests that the displacement of constituent atoms due to collisions with ions and the formation of interstitials favors ferromagnetic order between the layers.

KEYWORDS: 2D magnets, 2D semiconductor, Defects, Ion irradiation, Induced ferromagnetism



Van der Waals (vdW) magnets are attracting considerable interest from the scientific community. The ability to isolate single layers that can be reassembled into complex heterostructures makes them particularly useful for spin-based technologies.¹ Two-dimensional (2D) ferromagnetism^{2,3} was first found in CrI₃ and Cr₂Ge₂Te₆, but these materials are not stable under ambient conditions.^{4,5} For instance, CrI₃, a prototypical vdW magnet, deteriorates within minutes in air, which strongly hampers the fabrication and investigation of devices made from this compound. Hence, considerable efforts devoted to the search for new vdW magnetic crystals brought forth a number of air-stable antiferromagnetic (AFM) compounds, such as those from the MPX₃ family (*M* = Mn, Fe, Ni; *X* = S, Se),⁶ and the layered magnetic semiconductor CrSBr.^{7,8} However, to exploit the full potential of vdW magnetic crystals for spin-based applications that require ferromagnetic (FM) coupling between magnetic moments, like magnetic memory devices, new experimental methods to control the magnetic coupling in vdW materials have to be developed.^{9,10}

Due to the pronounced correlations between magnons, photons, electrons, and phonons,^{7,11–14} CrSBr is emerging as one of the most promising materials for such applications. Up to the Néel temperature of $T_N = 132 \pm 1$ K, the FM spin order within each layer is compensated by an AFM arrangement of the vdW layers in the out-of-plane direction (*c*-axis),¹⁵ which is the reason for the vanishing net magnetization of pristine bulk

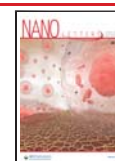
crystals. First-principles calculations of magnetic moments localized on the Cr ions predict a magnetic order up to 160 K in a single layer.^{7,16} Second harmonic generation¹⁷ and magneto-transport measurements^{7,18} determined the FM order of a single CrSBr layer to be around 150 K. Overall, bulk CrSBr is characterized by a relatively weak AFM coupling between the vdW layers, which is also apparent from the fact that a small field of 0.4 T applied along the easy-axis (*b*-axis) is sufficient to switch the magnetic order from AFM to FM.¹¹ The weak interaction between the layers makes CrSBr particularly susceptible to the modification of the magnetic order by external stimuli. Besides the recently demonstrated feasibility of strain and ligand substitution in altering the magnetic properties of CrSBr,^{19–22} ion irradiation may thus be a viable tool for modifying the magnetic structure with additional benefits, such as local patterning.

Here, we report a change of the magnetic interlayer coupling in bulk and few-layer CrSBr crystals irradiated with non-magnetic ions. In the absence of an applied field and below a

Received: May 23, 2023

Revised: August 31, 2023

Published: September 5, 2023



critical temperature of 110 K, the irradiated samples show sizable spontaneous magnetization which adapts to the easy-axis anisotropy of the pristine magnetic order and marks the transition of the magnetic ground state of irradiated CrSBr crystals from AFM to FM. Raman spectroscopy evidences the ion-fluence-dependent softening of the crystal lattice that is indicative of the formation of a large number of crystallographic defects. In conjunction with structure analysis, first-principles calculations suggest that the displacement of the atoms, particularly Cr, into interstitial positions between the vdW layers favors FM interlayer coupling. Our study highlights the potential of ion irradiation for nonchemical engineering of magnetism in vdW crystals.

Millimeter-sized bulk CrSBr crystals are synthesized using a chemical vapor transport method (see Supporting Information, Methods). Micro-Raman spectroscopy is performed using a linearly polarized, continuous-wave, 532 nm Nd:YAG laser for excitation, and magnetic properties are measured by a superconducting quantum interference device (Quantum Design, SQUID-VSM) magnetometer.

In our study, we subjected two types of CrSBr samples to He⁺ ion irradiation. The first type is a bulk crystal with a thickness of around 200 μm, the top surface of which is irradiated by 1.7-MeV He⁺ ions under different fluences. We start with an ion fluence of $4 \times 10^{14}/\text{cm}^2$ and monitor the ion-induced change in magnetic and structural properties using SQUID magnetometry and Raman spectroscopy. We then systematically repeat this experimental protocol, increasing the ion fluence at each step, until we reach a maximum fluence of $8 \times 10^{15}/\text{cm}^2$ (to indicate the fluence, the samples are named 4E14...8E15). To complement our investigation of this crystal, we study a second type of sample containing many small CrSBr flakes with a thickness of less than 1 μm that we obtain by exfoliation onto a silicon substrate. To achieve irradiation effects comparable to those in the large bulk crystal, we vary the energy of the He⁺ ions for the thin flake sample (see Supporting Information, Table S1).

As depicted in Figure 1a, each layer of CrSBr is composed of a buckled plane of CrS complexes surrounded by a sheet of Br atoms. Three characteristic modes, attributed to the A_g modes of the out-of-plane vibration, can be clearly identified in the Raman spectra (cf. Figure 1b,c,d).²³ The A_g¹ (113.8 cm⁻¹) and A_g³ (342.5 cm⁻¹) modes show maximum intensity when the laser polarization is parallel to the *b*-axis, while the A_g² (245.2 cm⁻¹) mode is most pronounced when the polarization is aligned with the *a*-axis, reflecting the strong structural anisotropy of the crystal structure. Even CrSBr crystals exposed to the largest ion fluences applied in our study maintain their atomic structure and this anisotropy. The gradual decrease in the peak intensity of the Raman signatures and the continuous shift toward smaller wavenumbers observed in Figure 1c,d (also see Figure S1) are generally attributed to a softening of the phonon modes resulting from defect-induced variations in the lattice spacing.²⁴ This observation is in line with a recent study of defects in mono- and few-layer CrSBr flakes irradiated by He ions, which also demonstrates the structural and electronic anisotropy.²⁵

From SRIM (Stopping and Range of Ions in Matter) simulations,²⁶ we calculate the average number of times an atom is displaced from its equilibrium lattice position during irradiation (displacement per atom, DPA), which allows us to estimate the depth profile of energy transferred from the energetic ions to the crystal matrix and thus the distribution of

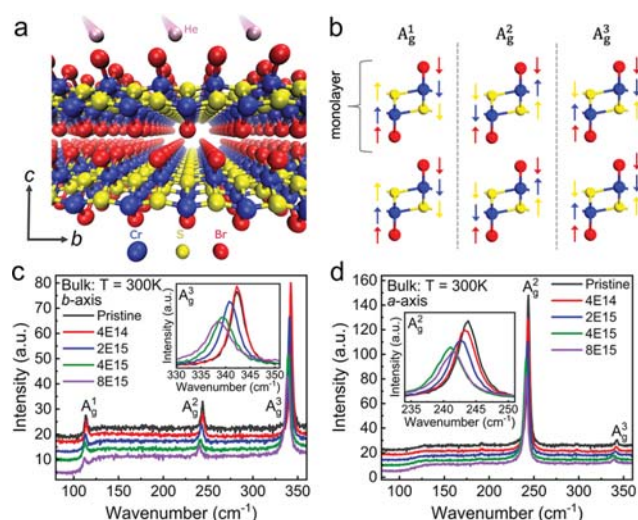


Figure 1. Schematic illustration of (a) He irradiation and (b) lattice vibration modes of CrSBr crystals. Color-coded arrows in (b) indicate the direction along which individual atoms move in the vibration. (c,d) Raman spectra from the 200-μm-thick bulk crystal measured after every ion irradiation step (the numbers correspond to ion fluences, e.g., 4E14 = $4 \times 10^{14}/\text{cm}^2$). The laser excitation was polarized along the *b*- and *a*-axis, respectively. The spectra are vertically offset for better visibility. The magnified views in the insets show a continuous reduction in wavenumber for the A_g³ and A_g² modes, indicating the gradual softening of the lattice with increasing ion fluence. The measurements were taken at ambient conditions.

defects created in the crystal. The DPA of the 200-μm-thick crystal shown in Figure 2a indicates that a low concentration of defects with relatively homogeneous distribution is created in the top 4 μm of the crystal and that a high concentration of defects is expected to occur 5 to 6 μm below the surface. In the

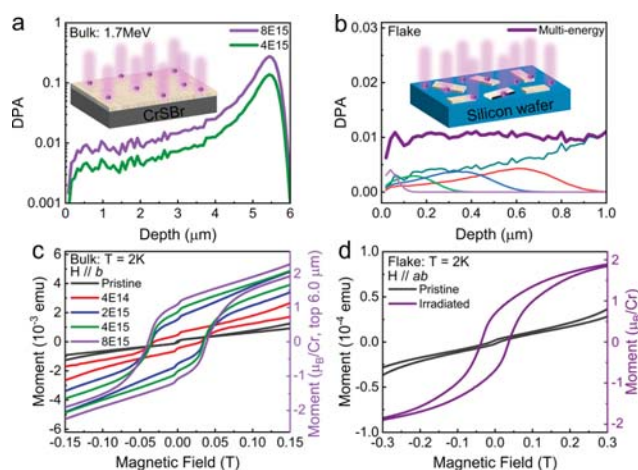


Figure 2. DPA for (a) the 200-μm-thick bulk sample with a fluence of $4 \times 10^{15}/\text{cm}^2$ (4E15) and $8 \times 10^{15}/\text{cm}^2$ (8E15); and (b) the flake sample (the thinner lines of different color represent the DPA induced by ions with different energy; see Table S1). The insets schematically show the sample geometry and effective thickness (the beige color). Magnetic hysteresis at 2 K for (c) the 200-μm-thick sample after irradiation at different fluences (the abrupt change near zero field is the antiferromagnetic signal from the unaffected bulk CrSBr) and (d) the flake sample after irradiation with a fluence equivalent to the maximum fluence used for the sample in (c). Measurements taken before irradiation shown for comparison are labeled pristine.

thin flake sample, on the other hand, defects are homogeneously distributed (Figure 2b). Overall, we expect a defect concentration comparable to that of the 200- μm -thick crystal created in the top 4 μm .

To investigate the influence of He^+ irradiation on the magnetic properties, we measure the field- and temperature-dependent magnetization in the 200- μm -thick bulk crystal and in the thin-flake sample using SQUID-magnetometry. Figure 2c and Figure S2 show the magnetization induced in the bulk crystal by a field applied along the b -axis. Before irradiation, the sample exhibits the typical AFM response expected for pristine CrSBr crystals.⁷ However, after we expose the crystal to ion irradiation, magnetic hysteresis centered at zero field is observed at fields up to 0.1 T. Upon increasing the irradiation fluence, this fingerprint of FM order becomes more and more prominent. At the same time, at fields around 0.5 T, we also observe a spin-flip transition that is characteristic of AFM-ordered CrSBr (see Figure S2). This observation is fully in line with the fact that only a fraction of the volume of the 200- μm -thick crystal is altered by ion irradiation. Hence, we observe a signal that has contributions from both the irradiated and pristine regions of the sample. For a fluence of $8 \times 10^{15}/\text{cm}^2$, we can estimate that the saturation magnetic moment in the irradiated volume amounts to $2 \mu_{\text{B}}/\text{Cr}$ by assuming an irradiation thickness of 6 μm according to Figure 2a. After 60 days storage at ambient conditions, we remeasured our sample and found no significant change in the magnetic response (see Figure S3).

The effect of ion irradiation on the magnetic properties is much more prominent in the second sample. For the thin flakes, we observe a full transition of the magnetic ground state from the AFM to FM after ion irradiation. As demonstrated by Figure 2d and the full-field measurements in Figure S2, magnetic hysteresis centered at zero field dominates the magnetic response after irradiation and the signatures of the AFM spin-flip transition are no longer observed. The saturation magnetization approaches $2 \mu_{\text{B}}/\text{Cr}$. Note that the saturation magnetization of Cr atoms in CrSBr is $3 \mu_{\text{B}}/\text{Cr}$.^{27,28} For the calculation, we assumed that the saturation magnetic moment is $3 \mu_{\text{B}}/\text{Cr}$ in the pristine sample, and there is no flake loss during sample handling. The in-plane magnetic anisotropy is not observed as a sharp spin-flip transition because individual flakes are randomly oriented on this sample.

In the next step, we investigate irradiation-induced changes of magnetic properties by temperature-dependent magnetization measurements conducted with an applied magnetic field of 0.1 T. Before irradiation, both samples show a peak of magnetization at a Néel temperature of around 131 K, reflecting the AFM ground state of pristine CrSBr crystals. After irradiation with He^+ ions, however, we observe a continuous increase of the magnetization of thin flakes as the temperature decreases (see Figure 3a), perfectly in line with our expectation of FM order in the irradiated samples. The critical temperature of the FM state is found to be 111 K. The magnetization of the 200- μm -thick bulk sample shows FM contributions as an increase in the absolute magnetization measured at low temperatures, since only a fraction of the volume is affected by ion irradiation. Nonetheless, the difference in the magnetic response after ion irradiation below 120 K is shown in Figure 3b.

To characterize the remanence of the irradiation-induced FM state, CrSBr samples are cooled from room temperature, while a field of 0.1 T is applied to saturate the FM

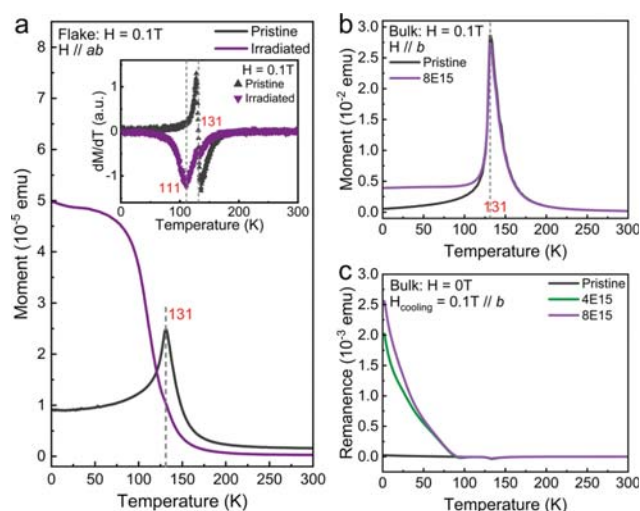


Figure 3. Temperature-dependent magnetization of the flake sample (a) and the bulk sample 8E15 along the b -axis (b) under an applied magnetic field of 0.1 T. In the inset to (a), the small kink in dM/dT at around 131 K is due to the antiferromagnetic signal of much thicker flakes, which are not fully irradiated through their thickness. Measurements on the pristine crystals are also shown for comparison. (c) Magnetic remanence of the 200- μm -thick bulk sample for two different fluences.

magnetization. When the temperature reaches 2 K, the magnetic field is set to zero. We then measure the remanence while increasing the temperature. The irradiated 200- μm -thick crystal exhibits sizable spontaneous magnetization below the critical temperature, as can be clearly seen in Figure 3c. We note that, while the magnetization of our bulk sample increases with irradiation fluence, the critical temperature always remains around 110 K for all fluences (see also Figure S4). Klein et al. suggested a potential defect-related phase after annealing with an onset arising also at around 110 K.²⁹

As outlined above, pristine CrSBr shows a magnetic easy axis along the crystallographic b -axis, while the a - and c -axis correspond to intermediate and hard magnetic axes. In another ion-irradiated bulk crystal sample, we measure the temperature-dependent remanence for fields applied along the a -, b -, and c -axis during cool-down. As Figure S5 shows, the amplitude of the remanence is largest when the field is applied along the b -axis. Ion irradiation has changed the magnetic ground state, but the magnetic easy axis is preserved. This result is in good agreement with the Raman measurements presented above, indicating that the crystalline anisotropy of CrSBr remains present even after irradiation, with the largest ion fluences used in our experiments.

The transfer of energy from high-energy ions to atoms in the crystal lattice leads to the formation of defects with very high concentrations. In our case here, the SRIM simulation results in a defect concentration of around 1% for the flake sample and the top 4 μm of the bulk sample (Figure 2a,b). The most common type of defects is assumed to be Frenkel pairs—a vacancy and an interstitial atom—which are created when an atom is displaced from its equilibrium position in the lattice into an interstitial position, leaving behind an empty lattice site. This kind of lattice disorder has been shown to modify conventional 3D magnetic materials.^{30,31}

We calculated the energetics of different types of vacancies and interstitials using 4×4 CrSBr bilayer supercells

corresponding to a defect concentration of $\sim 0.5\%$. The interstitial atoms were initially placed at different positions, and the most energetically favorable structure was identified. The formation energies for Cr, S, and Br vacancies and interstitials are summarized in Table 1. Assuming that

Table 1. Results of a Calculation of the Formation Energies of Different Vacancies (E_V), Interstitials (E_I), and Frenkel (E_F) Defects in the CrSBr Bilayer Structures

	E_V (eV)	E_I (eV)	E_F (eV)
S	5.89	-2.18	3.71
Cr	7.76	-2.81	4.95
Br	3.59	0.45	4.03

vacancies and interstitials are not interacting with each other, the Frenkel pair formation energy can be found by adding the formation energies of the isolated defects. Although the Frenkel pair formation energies are similar for three different elements, the lower values were found for S and Br, suggesting a higher concentration of these types of defects in the material. Br vacancies in CrSBr have been identified via scanning tunneling microscopy in a recent work,²⁹ which is consistent with our lowest vacancy formation energy found for Br (3.59 eV/atom). Table S2 lists the total magnetic moments for various vacancies and interstitials. While the net magnetic moment in pristine CrSBr is zero, our calculations show total magnetic moments of 2.0, 6.04, and 1.05 μ_B /supercell for S, Cr, and Br vacancies, respectively. In contrast, the S interstitial does not significantly change the magnetic moments of the pristine bilayer. The presence of magnetic character can be related to the shift between the spin-up- and spin-down-associated states in the electronic structure of the defective materials, as presented in Figures S6 and S7.

We further investigated the preferred magnetic ordering, including the energy difference between the lowest energy AFM and FM ordering (see Figure 4). For all types of interstitials, the moments of the interstitial atoms are aligned with the Cr atoms at the bottom and top, resulting in the energetically favorable FM order. Although the energy difference depends on the exchange parameter values, the

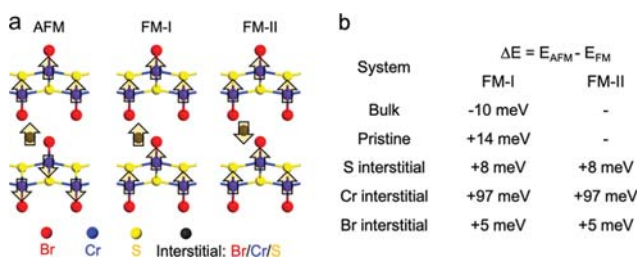


Figure 4. (a) Schematic representation of the magnetic configurations of interstitials in the CrSBr crystal. Regular Cr, S, and Br atoms are represented by smaller blue, yellow, and red circles, respectively. Orientations of the intralayer Cr spins are depicted by the arrows. Three spin configurations are considered for the bilayer CrSBr with interstitials. In the FM case, the magnetic moments of the interstitials can be aligned (FM-I) or antialigned (FM-II) with respect to those in the bottom and top layer. (b) The energy difference $\Delta E = E_{AFM} - E_{FM}$ between the AFM and FM configuration for the bulk system and bilayer with/without interstitials is given for the supercell. Interstitial density corresponds to $\sim 0.5\%$. A positive ΔE indicates that FM is favored over the AFM configuration.

FM preference was still found for various exchange values (Table S3). The effect is more pronounced in the CrSBr bilayer with Cr interstitials. The optimized structure of the CrSBr bilayer with Cr interstitial (Figure S8) indicates that the interstitial atom chooses a position in the void between the van der Waals gap atoms forming a covalent bond between the layers, which is consistent with the previous results.³² The first-nearest-neighbor exchange interactions between Cr–Br–Cr and Cr–S–Cr, as well as the second-nearest-neighbor exchange between Cr–S–Cr interactions, are the main causes of the ferromagnetism of the CrSBr monolayer.³³ The former exchange interaction is mediated by the orbital hybridization between Cr interstitials and inner Br atoms (Figure S9). As a result, the AFM coupling strength between the layers becomes weaker because of the appearance of defects.

We note that the change of the magnetic ground state observed after ion irradiation could in principle also be caused by lattice expansion, e.g., due to intercalation.⁹ However, X-ray diffraction and cross-sectional high-resolution scanning transmission electron microscopy measurements of our irradiated crystals (see Figures S10, S11) do not indicate any expansion of the lattice along the *c*-axis within the detection limit. Recent works have demonstrated the possibility of strain, hydrostatic pressure or structural phase transition in modifying the magnetic properties of CrSBr.^{19,22,32}

We observe a change of the magnetic ground state of the vdW magnet CrSBr after irradiation by non-magnetic ions. The fluence-dependent remanent magnetization of the irradiation-induced FM state exists up to a critical temperature of 110 K and adapts the magnetic easy axis anisotropy of the AFM order before irradiation. The saturation magnetic moment of FM magnetization is estimated to be close to the maximum magnetic moment of the constituent Cr atoms. First-principles calculations suggest that the displacement of atoms into interstitial positions by high-energy ions is responsible for the experimentally observed transition of the magnetic ground state as the interstitials facilitate ferromagnetic coupling between the layers (structural units) of CrSBr. We note that ion implantation is a mature technology for chip fabrication. Applying proper lithography, one can create artificial lateral structures. By tuning the energy of the ions and hence the penetration depth, it may further be possible, in a vdW heterostructure, to maximize the impact of ions for CrSBr but not the material on top. As a result, our approach may be applied to modify the magnetic properties of CrSBr even after fabrication of a vdW heterostructure.

■ ASSOCIATED CONTENT

Supporting Information

The Supporting Information is available free of charge at <https://pubs.acs.org/doi/10.1021/acs.nanolett.3c01920>.

Methods, He irradiation parameters for the flake sample, Calculated magnetic moments for various vacancies and interstitials, The energy difference between the AFM and FM configurations, Evolution of the Raman modes of A_g^1 and A_g^2 as a function of irradiation fluence, Magnetization curves at 2 K with a large field range, Magnetization curves at 2K for irradiated flake sample and after being exposed to the ambient condition for 60 days, Magnetic remanence of the bulk sample with different irradiation fluences, Magnetic remanence of the bulk sample 8E15 along different crystallographic

directions, Projected density of states (PDOS) of pristine and defective CrSBr monolayers with S, Cr, and Br vacancies, Projected density of states (PDOS) of pristine and defective CrSBr monolayers with S, Cr, and Br interstitials, Optimized structures of CrSBr bilayer with different interstitials, Projected density of states for CrSBr bilayer with Cr interstitial in FM and AFM ordering, X-ray diffraction of pristine CrSBr and sample 8E15, Cross-sectional high-resolution HAADF-STEM images and corresponding fast Fourier transforms (PDF)

■ AUTHOR INFORMATION

Corresponding Authors

Florian Dirnberger – *Institute of Applied Physics and Würzburg-Dresden Cluster of Excellence ct.qmat, Technische Universität Dresden, 01069 Dresden, Germany;*
Email: florian.dirnberger@tu-dresden.de

Shengqiang Zhou – *Helmholtz-Zentrum Dresden-Rossendorf, Institute of Ion Beam Physics and Materials Research, 01328 Dresden, Germany;* orcid.org/0000-0002-4885-799X;
Email: s.zhou@hzdr.de

Authors

Fangchao Long – *Helmholtz-Zentrum Dresden-Rossendorf, Institute of Ion Beam Physics and Materials Research, 01328 Dresden, Germany; TU Dresden, 01062 Dresden, Germany*

Mahdi Ghorbani-Asl – *Helmholtz-Zentrum Dresden-Rossendorf, Institute of Ion Beam Physics and Materials Research, 01328 Dresden, Germany;* orcid.org/0000-0003-3060-4369

Kseniia Mosina – *Department of Inorganic Chemistry, University of Chemistry and Technology Prague, 166 28 Prague 6, Czech Republic*

Yi Li – *Helmholtz-Zentrum Dresden-Rossendorf, Institute of Ion Beam Physics and Materials Research, 01328 Dresden, Germany; TU Dresden, 01062 Dresden, Germany;* orcid.org/0000-0001-9443-7817

Kaiman Lin – *Helmholtz-Zentrum Dresden-Rossendorf, Institute of Ion Beam Physics and Materials Research, 01328 Dresden, Germany; University of Michigan-Shanghai Jiao Tong University Joint Institute, Shanghai Jiao Tong University, Shanghai 200240, China*

Fabian Ganss – *Helmholtz-Zentrum Dresden-Rossendorf, Institute of Ion Beam Physics and Materials Research, 01328 Dresden, Germany*

René Hübner – *Helmholtz-Zentrum Dresden-Rossendorf, Institute of Ion Beam Physics and Materials Research, 01328 Dresden, Germany;* orcid.org/0000-0002-5200-6928

Zdenek Sofer – *Department of Inorganic Chemistry, University of Chemistry and Technology Prague, 166 28 Prague 6, Czech Republic;* orcid.org/0000-0002-1391-4448

Akashdeep Kamra – *Condensed Matter Physics Center (IFIMAC) and Departamento de Física Teórica de la Materia Condensada, Universidad Autónoma de Madrid, Ciudad Universitaria de Cantoblanco 28049 Madrid, Spain;* orcid.org/0000-0003-0743-1076

Arkady V. Krasheninnikov – *Helmholtz-Zentrum Dresden-Rossendorf, Institute of Ion Beam Physics and Materials Research, 01328 Dresden, Germany;* orcid.org/0000-0003-0074-7588

Slawomir Prucnal – *Helmholtz-Zentrum Dresden-Rossendorf, Institute of Ion Beam Physics and Materials Research, 01328 Dresden, Germany;* orcid.org/0000-0002-4088-6032

Manfred Helm – *Helmholtz-Zentrum Dresden-Rossendorf, Institute of Ion Beam Physics and Materials Research, 01328 Dresden, Germany; TU Dresden, 01062 Dresden, Germany*

Complete contact information is available at:
<https://pubs.acs.org/10.1021/acs.nanolett.3c01920>

Notes

The authors declare no competing financial interest.

■ ACKNOWLEDGMENTS

F.D. gratefully acknowledges financial support from Alexey Chernikov and the Würzburg-Dresden Cluster of Excellence on Complexity and Topology in Quantum Matter ct.qmat (EXC 2147, Project-ID 390858490). A.V.K. thanks the German Research Foundation (DFG) through projects KR 4866/9-1 and the collaborative research center “Chemistry of Synthetic 2D Materials” CRC-1415-417590517. Generous CPU time grants from the Technical University of Dresden computing cluster (TAURUS) and Gauss Centre for Supercomputing e.V. (www.gauss-centre.eu), Supercomputer HAWK at Höchstleistungsrechenzentrum Stuttgart (www.hlr.de), are greatly appreciated. A. K. acknowledges financial support from the Spanish Ministry for Science and Innovation – AEI Grant CEX2018-000805-M (through the “Maria de Maeztu” Programme for Units of Excellence in R&D) and grant RYC2021-031063-I funded by MCIN/AEI/10.13039/501100011033 and “European Union Next Generation EU/PRTR”. The authors thank Annette Kunz for TEM specimen preparation. Ion irradiation was performed at the Ion Beam Center (IBC) of HZDR. The use of the IBC TEM facilities and the funding of TEM Talos by the German Federal Ministry of Education and Research (BMBF), Grant No. 03SF0451, in the framework of HEMCP are acknowledged. F.L. thanks the financial support from China Scholarship Council (File No. 202108440218) for his stay in Germany. Z.S. was supported by ERC-CZ program (project LL2101) from Ministry of Education Youth and Sports (MEYS) and used large infrastructure from project reg. No. CZ.02.1.01/0.0/0.0/15_003/0000444 financed by the EFRR.

■ REFERENCES

- (1) Sierra, J. F.; Fabian, J.; Kawakami, R. K.; Roche, S.; Valenzuela, S. O. Van der Waals heterostructures for spintronics and optospintronics. *Nat. Nanotechnol.* **2021**, *16* (8), 856–868.
- (2) Huang, B.; Clark, G.; Navarro-Moratalla, E.; Klein, D. R.; Cheng, R.; Seyler, K. L.; Zhong, D.; Schmidgall, E.; McGuire, M. A.; Cobden, D. H.; Yao, W.; Xiao, D.; Jarillo-Herrero, P.; Xu, X. Layer-dependent ferromagnetism in a van der Waals crystal down to the monolayer limit. *Nature* **2017**, *546* (7657), 270–273.
- (3) Gong, C.; Li, L.; Li, Z.; Ji, H.; Stern, A.; Xia, Y.; Cao, T.; Bao, W.; Wang, C.; Wang, Y.; Qiu, Z. Q.; Cava, R. J.; Louie, S. G.; Xia, J.; Zhang, X. Discovery of intrinsic ferromagnetism in two-dimensional van der Waals crystals. *Nature* **2017**, *546* (7657), 265–269.
- (4) Rahman, S.; Liu, B.; Wang, B.; Tang, Y.; Lu, Y. Giant Photoluminescence Enhancement and Resonant Charge Transfer in Atomically Thin Two-Dimensional Cr₂Ge₂Te₆/WS₂ Heterostructures. *ACS Appl. Mater. Interfaces* **2021**, *13* (6), 7423–7433.
- (5) Shcherbakov, D.; Stepanov, P.; Weber, D.; Wang, Y.; Hu, J.; Zhu, Y.; Watanabe, K.; Taniguchi, T.; Mao, Z.; Windl, W.; Goldberger, J.; Bockrath, M.; Lau, C. N. Raman Spectroscopy,

- Photocatalytic Degradation, and Stabilization of Atomically Thin Chromium Tri-iodide. *Nano Lett.* **2018**, *18* (7), 4214–4219.
- (6) Long, G.; Henck, H.; Gibertini, M.; Dumcenco, D.; Wang, Z.; Taniguchi, T.; Watanabe, K.; Giannini, E.; Morpurgo, A. F. Persistence of Magnetism in Atomically Thin MnPS₃ Crystals. *Nano Lett.* **2020**, *20* (4), 2452–2459.
- (7) Telford, E. J.; Dismukes, A. H.; Dudley, R. L.; Wiscons, R. A.; Lee, K.; Chica, D. G.; Ziebel, M. E.; Han, M. G.; Yu, J.; Shabani, S.; Scheie, A.; Watanabe, K.; Taniguchi, T.; Xiao, D.; Zhu, Y.; Pasupathy, A. N.; Nuckolls, C.; Zhu, X.; Dean, C. R.; Roy, X. Coupling between magnetic order and charge transport in a two-dimensional magnetic semiconductor. *Nat. Mater.* **2022**, *21* (7), 754–760.
- (8) Göser, O.; Paul, W.; Kahle, H. G. Magnetic properties of CrSBr. *J. Magn. Magn. Mater.* **1990**, *92*, 129–136.
- (9) Pereira, J. M.; Tezze, D.; Ormazá, M.; Hueso, L. E.; Gobbi, M. Engineering Magnetism and Superconductivity in van der Waals Materials via Organic-Ion Intercalation. *Advanced Physics Research* **2023**, *2*, No. 2200084.
- (10) Wang, Q. H.; Bedoya-Pinto, A.; Blei, M.; Dismukes, A. H.; Hamo, A.; Jenkins, S.; Koperski, M.; Liu, Y.; Sun, Q. C.; Telford, E. J.; Kim, H. H.; Augustin, M.; Vool, U.; Yin, J. X.; Li, L. H.; Falin, A.; Dean, C. R.; Casanova, F.; Evans, R. F. L.; Chshiev, M.; Mishchenko, A.; Petrovic, C.; He, R.; Zhao, L.; Tsen, A. W.; Gerardot, B. D.; Brotons-Gisbert, M.; Guguchia, Z.; Roy, X.; Tongay, S.; Wang, Z.; Hasan, M. Z.; Wrachtrup, J.; Yacoby, A.; Fert, A.; Parkin, S.; Novoselov, K. S.; Dai, P.; Balicas, L.; Santos, E. J. G. The Magnetic Genome of Two-Dimensional van der Waals Materials. *ACS Nano* **2022**, *16* (5), 6960–7079.
- (11) Wilson, N. P.; Lee, K.; Cenker, J.; Xie, K.; Dismukes, A. H.; Telford, E. J.; Fonseca, J.; Sivakumar, S.; Dean, C.; Cao, T.; Roy, X.; Xu, X.; Zhu, X. Interlayer electronic coupling on demand in a 2D magnetic semiconductor. *Nat. Mater.* **2021**, *20* (12), 1657–1662.
- (12) Klein, J.; Pingault, B.; Florian, M.; Heissenbuttel, M. C.; Steinhoff, A.; Song, Z.; Torres, K.; Dirnberger, F.; Curtis, J. B.; Weile, M.; Penn, A.; Deilmann, T.; Dana, R.; Bushati, R.; Quan, J.; Luxa, J.; Sofer, Z.; Alu, A.; Menon, V. M.; Wurstbauer, U.; Rohlfing, M.; Narang, P.; Loncar, M.; Ross, F. M. The Bulk van der Waals Layered Magnet CrSBr is a Quasi-1D Material. *ACS Nano* **2023**, *17* (6), 5316–5328.
- (13) Ye, C.; Wang, C.; Wu, Q.; Liu, S.; Zhou, J.; Wang, G.; Soll, A.; Sofer, Z.; Yue, M.; Liu, X.; Tian, M.; Xiong, Q.; Ji, W.; Renshaw Wang, X. Layer-Dependent Interlayer Antiferromagnetic Spin Reorientation in Air-Stable Semiconductor CrSBr. *ACS Nano* **2022**, *16*, 11876–11883.
- (14) Dirnberger, F.; Quan, J.; Bushati, R.; Diederich, G. M.; Florian, M.; Klein, J.; Mosina, K.; Sofer, Z.; Xu, X.; Kamra, A.; García-Vidal, F. J.; Alù, A.; Menon, V. M. Magneto-optics in a van der Waals magnet tuned by self-hybridized polaritons. *Nature* **2023**, *620*, 533–537.
- (15) Telford, E. J.; Dismukes, A. H.; Lee, K.; Cheng, M.; Wieteska, A.; Bartholomew, A. K.; Chen, Y. S.; Xu, X.; Pasupathy, A. N.; Zhu, X.; Dean, C. R.; Roy, X. Layered Antiferromagnetism Induces Large Negative Magnetoresistance in the van der Waals Semiconductor CrSBr. *Adv. Mater.* **2020**, *32* (37), No. 2003240.
- (16) Guo, Y.; Zhang, Y.; Yuan, S.; Wang, B.; Wang, J. Chromium sulfide halide monolayers: intrinsic ferromagnetic semiconductors with large spin polarization and high carrier mobility. *Nanoscale* **2018**, *10* (37), 18036–18042.
- (17) Lee, K.; Dismukes, A. H.; Telford, E. J.; Wiscons, R. A.; Wang, J.; Xu, X.; Nuckolls, C.; Dean, C. R.; Roy, X.; Zhu, X. Magnetic Order and Symmetry in the 2D Semiconductor CrSBr. *Nano Lett.* **2021**, *21* (8), 3511–3517.
- (18) Boix-Constant, C.; Manas-Valero, S.; Ruiz, A. M.; Rybakov, A.; Konieczny, K. A.; Pillet, S.; Baldovi, J. J.; Coronado, E. Probing the Spin Dimensionality in Single-Layer CrSBr Van Der Waals Heterostructures by Magneto-Transport Measurements. *Adv. Mater.* **2022**, *34* (41), No. 2204940.
- (19) Cenker, J.; Sivakumar, S.; Xie, K.; Miller, A.; Thijssen, P.; Liu, Z.; Dismukes, A.; Fonseca, J.; Anderson, E.; Zhu, X.; Roy, X.; Xiao, D.; Chu, J. H.; Cao, T.; Xu, X. Reversible strain-induced magnetic phase transition in a van der Waals magnet. *Nat. Nanotechnol.* **2022**, *17* (3), 256–261.
- (20) Cenker, J.; Ovchinnikov, D.; Yang, H.; Chica, D. G.; Zhu, C.; Cai, J. Q.; Diederich, G.; Liu, Z. Y.; Zhu, X. Y.; Roy, X.; Cao, T.; Daniels, W. M.; Chu, J.-H.; Xiao, D.; Xu, X. D. Strain-programmable van der Waals magnetic tunnel junctions. *arXiv (Condensed Matter)* **2023**, *10*, 2301.03759.
- (21) Telford, E. J.; Chica, D. G.; Xie, K. C.; Manganaro, N. S.; Huang, C.-H.; Cox, J.; Dismukes, A. H.; Zhu, X. Y.; Walsh, J. P. S.; Cao, T.; Dean, C. R.; Roy, X.; Ziebel, M. E. Designing magnetic properties in CrSBr through hydrostatic pressure and ligand substitution. *arXiv (Condensed Matter)* **2022**, *5*, 2211.02788.
- (22) Pawbake, A.; Pelini, T.; Mohelsky, I.; Jana, D.; Breslavetz, I.; Cho, C.-W.; Orlita, M.; Potemski, M.; Measson, M.-A.; Wilson, N.; Mosina, K.; Soll, A.; Sofer, Z.; Piot, B. A.; Zhitomirsky, M. E.; Faugeras, C. Magneto-optical sensing of the pressure driven magnetic ground states in bulk CrSBr. *arXiv (Condensed Matter)* **2023**, *3*, 2303.01823.
- (23) Moro, F.; Ke, S.; del Águila, A. G.; Söll, A.; Sofer, Z.; Wu, Q.; Yue, M.; Li, L.; Liu, X.; Fanciulli, M. Revealing 2D Magnetism in a Bulk CrSBr Single Crystal by Electron Spin Resonance. *Adv. Funct. Mater.* **2022**, *32*, No. 2207044.
- (24) Parkin, W. M.; Balan, A.; Liang, L.; Das, P. M.; Lamparski, M.; Naylor, C. H.; Rodriguez-Manzo, J. A.; Johnson, A. T.; Meunier, V.; Drndic, M. Raman Shifts in Electron-Irradiated Monolayer MoS₂. *ACS Nano* **2016**, *10* (4), 4134–4142.
- (25) Torres, K.; Kuc, A.; Maschio, L.; Pham, T.; Reidy, K.; Dekanovsky, L.; Sofer, Z.; Ross, F. M.; Klein, J. Probing Defects and Spin-Phonon Coupling in CrSBr via Resonant Raman Scattering. *Adv. Funct. Mater.* **2023**, *33* (12), No. 2211366.
- (26) Ziegler, J. F.; Ziegler, M. D.; Biersack, J. P. SRIM – The stopping and range of ions in matter (2010). *Nucl. Instr. and Meth. B* **2010**, *268* (11–12), 1818–1823.
- (27) Jiang, Z.; Wang, P.; Xing, J.; Jiang, X.; Zhao, J. Screening and Design of Novel 2D Ferromagnetic Materials with High Curie Temperature above Room Temperature. *ACS Appl. Mater. Interfaces* **2018**, *10* (45), 39032–39039.
- (28) Lopez-Paz, S. A.; Guguchia, Z.; Pomjakushin, V. Y.; Witteveen, C.; Cervellino, A.; Luetkens, H.; Casati, N.; Morpurgo, A. F.; von Rohr, F. O. Dynamic magnetic crossover at the origin of the hidden-order in van der Waals antiferromagnet CrSBr. *Nat. Commun.* **2022**, *13* (1), 4745–4754.
- (29) Klein, J.; Song, Z.; Pingault, B.; Dirnberger, F.; Chi, H.; Curtis, J. B.; Dana, R.; Bushati, R.; Quan, J.; Dekanovsky, L.; Sofer, Z.; Alù, A.; Menon, V. M.; Moodera, J. S.; Loncar, M.; Narang, P.; Ross, F. M. Sensing the local magnetic environment through optically active defects in a layered magnetic semiconductor. *ACS Nano* **2023**, *17*, 288–299.
- (30) Fassbender, J. Nanopatterning: the chemical way to ion irradiation. *Nat. Nanotechnol.* **2012**, *7* (9), 554–555.
- (31) Nord, M.; Semisalova, A.; Kakay, A.; Hlawacek, G.; MacLaren, I.; Liersch, V.; Volkov, O. M.; Makarov, D.; Paterson, G. W.; Potzger, K.; Lindner, J.; Fassbender, J.; McGrouther, D.; Bali, R. Strain Anisotropy and Magnetic Domains in Embedded Nanomagnets. *Small* **2019**, *15* (52), No. 1904738.
- (32) Klein, J.; Pham, T.; Thomsen, J. D.; Curtis, J. B.; Denneulin, T.; Lorke, M.; Florian, M.; Steinhoff, A.; Wiscons, R. A.; Luxa, J.; Sofer, Z.; Jahnke, F.; Narang, P.; Ross, F. M. Control of structure and spin texture in the van der Waals layered magnet CrSBr. *Nat. Commun.* **2022**, *13* (1), 5420–5428.
- (33) Xu, X. M.; Wang, X. H.; Chang, P.; Chen, X. Y.; Guan, L. X.; Tao, J. G. Strong Spin-Phonon Coupling in Two-Dimensional Magnetic Semiconductor CrSBr. *J. Phys. Chem. C* **2022**, *126* (25), 10574–10583.

Novel Mixed-Dimensional hBN-Passivated Silicon Nanowire Reconfigurable Field Effect Transistors: Fabrication and Characterization

Sayantana Ghosh,* Muhammad Bilal Khan, Phanish Chava, Kenji Watanabe, Takashi Taniguchi, Slawomir Prucnal, René Hübner, Thomas Mikolajick, Artur Erbe, and Yordan M. Georgiev*



Cite This: *ACS Appl. Mater. Interfaces* 2023, 15, 40709–40718

ACCESS |

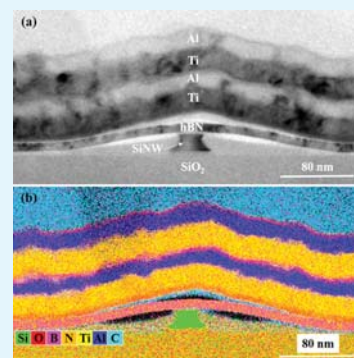
Metrics & More

Article Recommendations

Supporting Information

ABSTRACT: This work demonstrates the novel concept of a mixed-dimensional reconfigurable field effect transistor (RFET) by combining a one-dimensional (1D) channel material such as a silicon (Si) nanowire with a two-dimensional (2D) material as a gate dielectric. An RFET is an innovative device that can be dynamically programmed to perform as either an n- or p-FET by applying appropriate gate potentials. In this work, an insulating 2D material, hexagonal boron nitride (hBN), is introduced as a gate dielectric and encapsulation layer around the nanowire in place of a thermally grown or atomic-layer-deposited oxide. hBN flake was mechanically exfoliated and transferred onto a silicon nanowire-based RFET device using the dry viscoelastic stamping transfer technique. The thickness of the hBN flakes was investigated by atomic force microscopy and transmission electron microscopy. The ambipolar transfer characteristics of the Si-hBN RFETs with different gating architectures showed a significant improvement in the device's electrical parameters due to the encapsulation and passivation of the nanowire with the hBN flake. Both n- and p-type characteristics measured through the top gate exhibited a reduction of hysteresis by 10–20 V and an increase in the on–off ratio (I_{ON}/I_{OFF}) by 1 order of magnitude (up to 10^8) compared to the values measured for unpassivated nanowire. Specifically, the hBN encapsulation provided improved electrostatic top gate coupling, which is reflected in the enhanced subthreshold swing values of the devices. For a single nanowire, an improvement up to 0.97 and 0.5 V/dec in the n- and p-conduction, respectively, is observed. Due to their dynamic switching and polarity control, RFETs boast great potential in reducing the device count, lowering power consumption, and playing a crucial role in advanced electronic circuitry. The concept of mixed-dimensional RFET could further strengthen its functionality, opening up new pathways for future electronics.

KEYWORDS: mixed-dimensional reconfigurable FET, ambipolar, nickel silicide, flash lamp annealing, hBN encapsulation, subthreshold swing



INTRODUCTION

The physical downscaling of silicon-based MOSFET technology has reached its limitations. Subsequently, the quest for alternative technological solutions based on new materials and device concepts augments the downscaling of integrated circuits. One such state-of-the-art advancement that has been intensively researched in the past decade to improve the functionality of nanowire field effect transistors (FETs) is called reconfigurability.¹ Reconfigurability is based on electrostatic control of the transistor's polarity. Transistors that are built on this concept are called reconfigurable FETs (RFETs).² A nanowire RFET is a Schottky junction-based device that can be reversibly configured to n- or p-polarity by controlling the electrostatic potential applied at the polarity gates. Due to this property, the functional complexity of a system can be enhanced by these transistors without increasing the device count. In the most generic process, the device is based on an intrinsic Si nanowire with nickel (Ni) contact pads placed on

both ends. Subsequent annealing results in the formation of silicide regions in the nanowire. Consequently, silicide-Si-silicide Schottky junctions are formed. By control of the Schottky barrier at the two ends of the nanowire with the help of gate potentials, the type and flow of charge carriers within the channel can be dynamically modulated. For ambipolarity, an electrostatic potential on the back gate or a single top gate enables the n- or p-transport, depending on the polarity of the gate voltage.

An ambipolar RFET device can be switched to its ON state by the application of both positive and negative voltages. This

Received: April 4, 2023

Accepted: August 8, 2023

Published: August 22, 2023



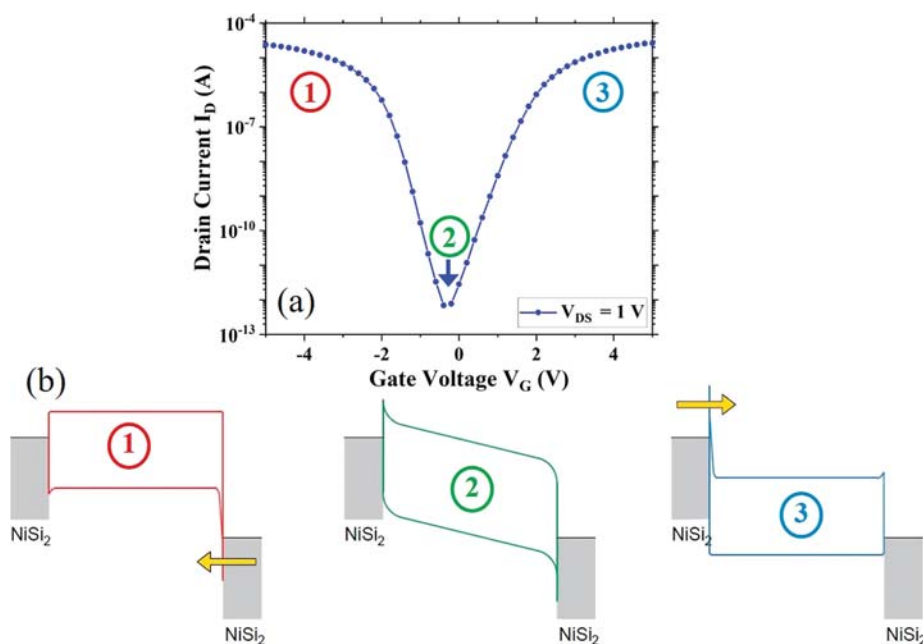


Figure 1. Ambipolar RFET characteristics (a) typical IV characteristics of a silicon nanowire RFET (b) energy band diagram of an ambipolar RFET under biased condition showing (1) hole conduction by tunneling with upward band bending, (2) off-state region dominated by high energy charge carrier conduction, and (3) electron conduction by tunneling with downward band bending.

nature of switching on the RFET device by sweeping the gate voltage from a high potential to a low potential is known as ambipolarity.³ In ambipolar devices, both types of charge carriers take part in the conduction in a single voltage sweep. The ambipolar RFET realized in this work is predominantly single-gated. This gate can be either a common back gate or a fabricated top gate. The gate electrode covers the Schottky junction region on either side of the nanowire channel. By applying a suitable voltage on the gate, the Schottky barrier is tuned accordingly to steer charge carriers into the channel for current conduction. In the OFF state of the device, the presence of both electron and hole barriers causes a limited off-current to flow, which is mainly due to high energy thermionic emission. When a positive bias voltage is applied to the gate structure, the energy of the bands is lowered, reducing the barrier height for the electrons. This leads to the injection of electrons into the channel by tunneling, contributing to an electron current or n-type conduction taking place. Simultaneously by sweeping the gate bias voltage to a low negative potential, the energy bands rise, reducing the barrier height for holes and promoting hole conduction. As the conduction band edge also rises at the same time, the electrons are blocked due to the high electron barrier height. Hence, the current is totally dominated by hole conduction only and is termed p-type conduction. The IV characteristics of an ambipolar RFET device and the band bending at different bias voltages are depicted in Figure 1.

As a single-gate architecture is used for ambipolar operation, the preferred gate structure is mostly the top gate. The top gate provides a better field effect capacitive coupling over the Schottky junctions and the nanowire channel than the back-gated architecture. This is due to the difference in thickness of the top gate dielectric and the buried oxide layer. The relation between the capacitance and the thickness of the dielectric is given by the following equation

$$C_{\text{ox}} = \frac{\epsilon_0 \kappa A}{t_{\text{ox}}} \quad (1)$$

where C_{ox} is the oxide capacitance which corresponds to capacitive coupling of the gate over the channel, ϵ_0 represents the relative permittivity of free space, κ is the dielectric constant, A is the area, and t_{ox} represents the thickness of the oxide or dielectric. Due to the lower thickness value of the top gate dielectric, a higher capacitive control of the channel is achieved, requiring a much smaller operational voltage for switching the device on. This also improves the subthreshold swing (SS) of the device.

Contrary to conventional transistors, charge carrier injection in the channel is selectively controlled at the Schottky junctions, thereby avoiding the need of having an inherently doped channel material. Tuning the Schottky barrier at both ends of the nanowire is one of the basic requirements for current transport in reconfigurable devices. This is achieved by electrostatic coupling and enhanced gate control over the channel material with a proper encapsulating and passivating dielectric material. Such transistors have been demonstrated using different channel materials such as carbon nanotubes,⁴ graphene,⁵ silicon (either as nanowires, utilizing FinFET or fully depleted silicon-on-insulator (FDSOI) transistors to achieve a high gate coupling),^{6–9} and 2D semiconductors.¹⁰ However, exploration of dielectric materials is relatively scarce.

The scientific exploration of 2D materials after the isolation of graphene in 2004¹¹ paved the way for a promising option in the field of nanoelectronics due to their stability at atomic thickness, high intrinsic mobility, optical transparency, and high strain limit compared to conventional semiconductors and insulators. One such material, which has excellent insulating properties with a large direct band gap of about 6 eV, is hexagonal boron nitride (hBN).^{12,13} 2D hBN has a structure analogous to graphene much like a honeycomb maze and is therefore known as “white graphene.” The hexagonal

sublattice of hBN consists of alternating boron and nitrogen atoms with the electron-deficient boron atoms laying directly above the electron-rich nitrogen atoms or vice versa in adjacent layers.¹⁴ The asymmetry in the sublattices causes polarized covalent bonds leading to the large band gap of hBN, making it act as an insulator. Interlayer van der Waals forces dictate the thickness of multilayer hBN, and the mechanically exfoliated monolayer is about 0.4 nm thick.¹⁴ Atomically thin hBN has flat interfaces due to the absence of surface dangling bonds and is, therefore, resistant to oxidation. It also acts as a good gate insulator with a dielectric constant ranging between 3 and 4 (similar or comparable to that of SiO₂)¹⁵ and can be even incorporated as an encapsulating layer for the active channel material of devices to prevent degradation of relatively unstable channel materials.¹⁶ hBN is chemically stable and can withstand 1000 °C at ambient conditions, 1400 °C in vacuum, and up to 2850 °C in an inert atmosphere.¹⁴ The thermal conductivity is about 484 W m⁻¹ K⁻¹ for 2D hBN with an elastic constant of 220–510 N m⁻¹ and a Young's modulus of about 1 TPa, thus making it an excellent material for flexible insulation.¹⁷

The top-down fabricated reconfigurable devices reported in this work are the first of their kind to incorporate silicon nanowires as the channel material along with 2D hBN as the gate dielectric and encapsulating layer. The focus of this work is on the development of the fabrication process, including structural studies of the device. Furthermore, the electrical transfer characteristics of such Si-hBN devices are measured based on different gating architectures to show a significant improvement in SS values, reduction of hysteresis, and increase in p and n on-currents due to the 2D encapsulation and passivation.

RESULTS AND DISCUSSION

The initial structural characterization of the mixed-dimensional RFET devices includes tapping-mode atomic force microscopy (AFM) analysis. Height profiles are extracted from multiple AFM scans to determine the thickness of the hBN flakes. Figure 2a shows an optical micrograph of two single nanowire-based devices.¹⁸ The first device is without an hBN dielectric layer, while the second device is capped with a thin hBN layer. AFM analysis is performed on these two devices, and the AFM topography is shown in Figure 2b. Three individual line profiles are drawn from the edges of the hBN flake to determine its thickness. The thickness of the hBN flake is approximately 10 nm, as can be seen from Figure 2c.

For further analysis of the hBN encapsulation of the nanowire, cross-sectional TEM analysis is performed. Figure 3 shows a representative bright-field TEM image. It is to be noted that the sectioning of the device is carried out across the single nanowire structure (i.e., perpendicular to the length of the nanowire). The cross-sectioning is performed to study and analyze the RFET device, especially the conformity of the hBN flake around the single nanowire. As seen from Figure 3a, the hierarchy of the RFET device starts with the buried SiO₂ layer at the bottom of the single nanowire channel. The nanowire channel has a trapezoidal shape with a height and a width of about 20 and 25 nm, respectively. The hBN thickness is confirmed to be approximately 10 nm and is shown to cover the nanowire channel from the top. On top of the dielectric layer, a stack of titanium (Ti) and aluminum (Al) acts as the gate electrode for the device.

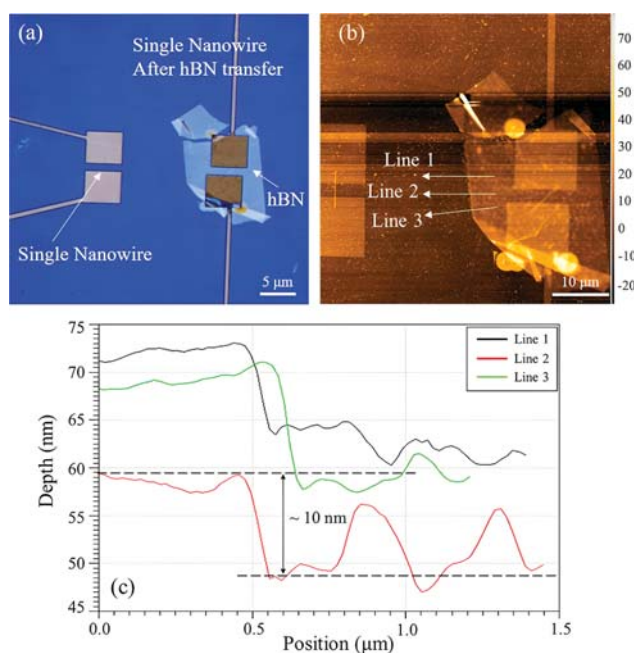


Figure 2. AFM characterization of the fabricated devices. (a) Visible light micrograph of two different single silicon nanowire devices with and without hBN dielectric layer. (b) AFM scan of the fabricated devices is shown in image (a). Lines 1, 2, and 3 are three different line profiles for determining the thickness of the hBN flake. (c) Thickness of hBN is based on the height profile lines 1, 2, and 3 in the image (b). Thickness of the hBN flake shown here is approximately 10 nm.

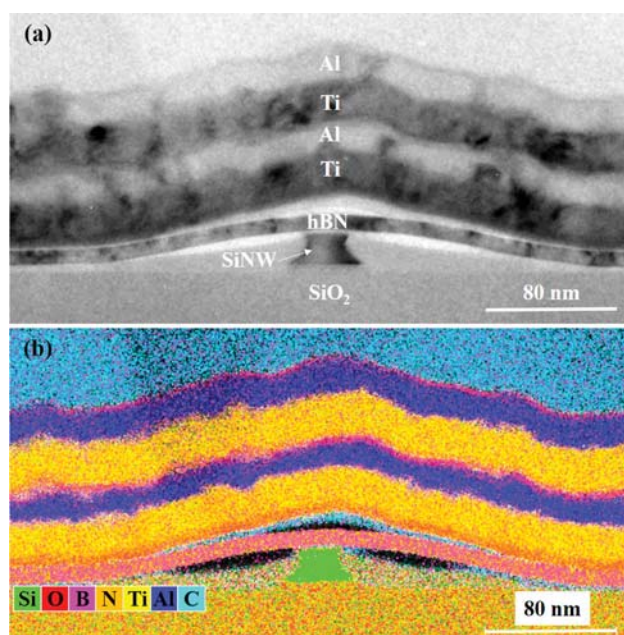


Figure 3. (a) Bright-field TEM micrograph of a sectioned nanowire device. The device structure consists of a buried SiO₂ layer underneath the silicon nanowire. On top of the nanowire channel is the hBN dielectric, which is shown to cover the nanowire. A stack of Ti and Al serves as the gate electrodes above the hBN. (b) Corresponding superimposed EDXS-based element distribution maps of the hBN-silicon-nanowire-based device.

The bright-field TEM image shows the stretch of the hBN flake and the position where it finally sits on the buried oxide

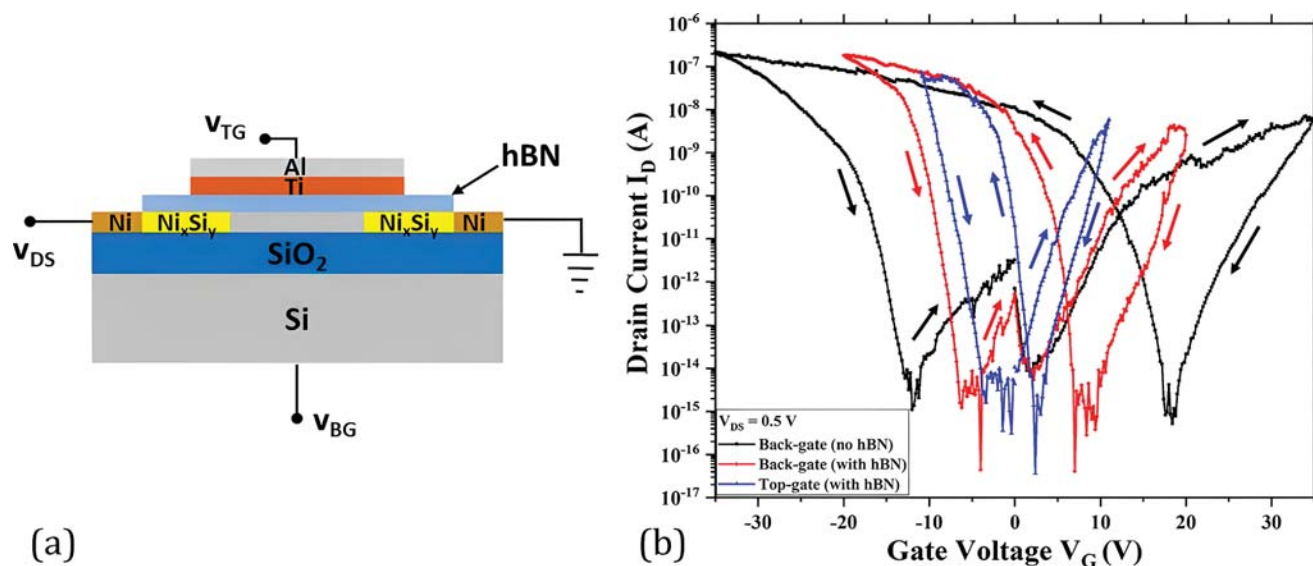


Figure 4. (a) Cross-sectional view of the device, including the voltage naming conventions used in this work. The device structure consists of a bottom Si layer on top of which is a 100 nm buried SiO₂ layer. The single nanowire is fabricated on top of the buried oxide layer. Ni contact pads are placed on both sides of the Si nanowire. Annealing creates Ni_xSi_y Schottky junctions in the nanowire. hBN is transferred on top of the device as the gate dielectric. A bilayer of Ti and Al serves as the top gate for the device. (b) Transfer characteristics of a single silicon nanowire-based device comprising an hBN flake as the dielectric layer. Different gating schemes are incorporated to deduce the IV characteristics. The length and width of the nanowire are 3 μm and 25 nm, respectively. The arrows in the transfer characteristics denote the direction of the curve based on the gate voltage sweep.

layer (away from the silicon nanowire channel). The structure of the top gate follows the curvature of the hBN flake. To study the element distribution in the sectioned device, a spectrum imaging analysis based on energy-dispersive X-ray spectroscopy (EDXS) is applied. The superposition of the corresponding element distribution maps of the device is shown in Figure 3b. The region enriched with boron (B) and nitrogen (N) confirms the presence of the hBN dielectric layer above the silicon nanowire channel. It is seen that the hBN flake sits on top of the silicon nanowire channel but does not conformally encapsulate its sidewalls. The EDXS-based analysis also confirms the presence of voids (denoted by the black areas in the element map). It is also to be noted that a dual layer of Ti and Al is evaporated on top of the hBN dielectric. The reason for using a dual-layer structure is that the first gate stack of Ti and Al was slightly misaligned with the silicon nanowire during the top gate fabrication. Hence, another broader layer of Ti and Al was precisely aligned and deposited above it for better capacitive coupling of the gate to the hBN stack. The growth of the oxide layer around the nanowire and in between the metal top gates (as seen in Figure 3b) is a likely phenomenon in ambient conditions. Such growth of oxide layers has also been outlined in previous studies regarding nanowire devices and silicidation.^{19,20} The presence of carbon (C) on top of the Ti and Al gate stack is due to the protective capping layer deposited during TEM specimen preparation. The formation of carbon with traces of silicon (Si) and oxygen (O) around the cross-section of the nanowire channel and above the hBN flake is mostly caused by the fabrication process of the device. Several scanning electron microscopy images were taken of the nanowire devices before and after hBN transfer in order to characterize the device. Thereby, organic substances on the surface of the sample were cracked and deposited as carbon layers.

Furthermore, the effect of hBN as a dielectric layer for silicon nanowire-based devices on their electrical properties is investigated. For this, the electrical measurements are carried out in an ambient atmosphere. The measurement schematic and transfer characteristics of a single nanowire-based device are presented in Figure 4. Three types of transfer characteristics are obtained by the following measurement schemes:

1. Back gating the device before hBN is transferred. The back gate voltage (V_{BG}) is swept between 35 and -35 V in a closed loop.
2. Back gating the device after the transfer of the hBN flake. V_{BG} is swept between 20 and -20 V in a closed loop.
3. Top gating the devices using hBN as the gate dielectric. The top gate voltage (V_{TG}) is swept between 10 and -10 V in a closed loop.

Lower gate voltages (V_G) are applied after hBN transfer to avoid the dielectric breakdown of the hBN. A drain to source voltage (V_{DS}) of 0.5 V is used to obtain the transfer characteristics. The device showed ambipolar behavior with improved electrostatic gate coupling after hBN transfer, which results in an enhanced SS value of the device (Table 1). The best values of SS are obtained by top gating the device. It is also evident from Figure 4b that the shift of the minima of the transfer curves is clearly reduced (toward the origin (0 V))

Table 1. SS Values of the hBN-Passivated Single Nanowire-Based Device Using Different Gating Schemes

carrier type	SS (V/dec)		
	back gate (without hBN)	back gate (with hBN)	top gate (with hBN)
n	1.82	1.68	0.97
p	1.07	0.78	0.50

after the transfer of the hBN flake. The characteristics also show an improvement in hysteresis after hBN transfer with the lowest hysteresis for the top-gated configuration. These are mainly due to the hBN passivation of the nanowire which reduces the interface charge states and charged hydroxyl sites.^{21,22} The hysteresis is calculated by taking the corresponding gate voltage value from the center of the subthreshold regime during successive forward and reverse voltage sweeps. This records the dynamics of charge trapping and detrapping in the nanowire channel and the interface. As seen from the graph in Figure 4b, the n- and p-conduction hysteresis reduces from 13 and 28 V, respectively, for back-gated unpassivated state to approximately 2.4 and 6.8 V for the hBN-encapsulated top-gated measurement. Simultaneously, the on-current (I_{ON}) and on–off ratio ($I_{\text{ON}}/I_{\text{OFF}}$) levels are enhanced after the passivation of the single nanowire by hBN and with the measurements recorded through the top gate. This is reflected by the modest increase in the n-type on–off ratio and 1 order of magnitude increase in the p-type ratio for the hBN-passivated top-gated measurements. The convention used for calculating I_{ON} and I_{OFF} is explained in detail in the Supporting Information (see Figure S1). The extracted electrical parameters of the hBN-passivated single nanowire-based device with different gating schemes are listed in Table 2.

Table 2. Extracted Parameters from the Transfer Characteristics of the hBN-Passivated Single Nanowire-Based Device at a V_{DS} of 0.5 V Using Different Gating Schemes

parameter	carrier type	back gate (without hBN)	back gate (with hBN)	top gate (with hBN)
I_{ON} (A)	n	5.8×10^{-9}	2.4×10^{-9}	5.7×10^{-9}
	p	8.4×10^{-9}	1.8×10^{-8}	2.6×10^{-8}
I_{OFF} (A)	n	7.8×10^{-16}	7.6×10^{-16}	8.4×10^{-16}
	p	8.2×10^{-16}	1.2×10^{-15}	8.4×10^{-16}
$I_{\text{ON}}/I_{\text{OFF}}$ ratio	n	$\sim 10^7$	$\sim 10^7$	$\sim 10^7$
	p	$\sim 10^7$	$\sim 10^7$	$\sim 10^8$
hysteresis (V)	n	13	6.2	2.4
	p	28	13.5	6.8

The output characteristics for the single nanowire-based device are shown in Figure S2. The corresponding off-state output characteristics are evaluated by a two-probe measurement for a V_{DS} sweep of 0 to 0.5 V keeping the V_{G} constant at 0 V (see Figure S2a). Three separate measurements are carried out at different times. The first measurement is before hBN is transferred on the nanowire, the second is after hBN is transferred, and the final measurement is after the top gate is fabricated. For the first two measurements (at such negligible V_{G}), a near linear regime is exhibited with a considerable increase in the drain current (I_{D}) after the passivation of the nanowire with hBN. For the final measurement after the top gate is fabricated, it is seen that the I_{D} has a significant increase in current with a characteristic showing Schottky type supra linear shape. Since the top gates help in better hBN encapsulation of the single nanowire, better dielectric passivation is expected. This might have led to superior charge carrier transport through the nanowire channel without the influence of the gate voltages. Simultaneously, the on-state output characteristics of the hBN ambipolar device are also

measured based on the top-gated transfer characteristics. For the n-type characteristics, V_{DS} is varied from 0.25 to 1 V while increasing the V_{TG} from 0 to 10 V in steps of 1 V (Figure S2b). For the p-type behavior, similar voltage steps are maintained but in a negative direction (see Figure S2c). A clear Schottky behavior is seen in both types of conduction for high values of V_{DS} , which provide a fair conclusion to the contact properties based on the ambipolar shape of the transfer characteristics. For the hole conduction, saturation is seen for low V_{TG} values. It is also to be noted that in both cases, I_{D} increases with an increase in V_{TG} . This implies that high V_{TG} enables more band bending at the Schottky junctions, leading to increased tunneling of carriers. This eventually leads to a higher current flow.

Additionally, to realize the role of the device performance based on the hBN thickness, two hBN-passivated single nanowire-based devices are compared. These two devices exhibit contrasting hBN thicknesses, with one measuring 10 nm and the other measuring 20 nm. The top-gated transfer characteristics of these two devices are obtained and are shown in the Supporting Information Figure S3. For both devices, the V_{TG} is swept in a butterfly loop while varying the V_{DS} from 0.25 to 1 V in steps of 0.25 V. It is clearly prominent from both the graphs that the devices exhibit ambipolar behavior with a distinctive rise in the I_{ON} levels for both the branches with the increase in V_{DS} . However, compared to the device with 20 nm hBN as a dielectric, the one with 10 nm shows higher on-currents, lower hysteresis, and better SS. The on–off ratio ($I_{\text{ON}}/I_{\text{OFF}}$) levels for the 10 nm hBN device are visible for more than one decade compared to the 20 nm hBN device. This is understandable since thinner hBN would provide better passivation and encapsulation to the single nanowire. This will, in turn, lead to the device exhibiting better electrical conduction due to reduced charge scattering. Furthermore, considering the measurements are conducted by top gating through the hBN dielectric, it is expected of the device with the thinner hBN to have a better capacitive coupling. This, in turn, improves the SS of the 10 nm hBN device compared to the 20 nm one. Finally, it is also observed that the hysteresis of the n- and p-branch is much lower for the thinner hBN device hinting at the absence of interface trap states and oxide charges due to the better passivation of the nanowire. In these scenarios, it is clearly understood that the tunability and reconfigurability of the devices are unaltered for either thickness of the hBN. However, the variability in thickness does play a vital role in enhancing the device's electrical performance. These results serve as a proof of concept that hBN can be employed as a gate dielectric for one-dimensional silicon nanowire-based devices, presented for the first time to the best of our knowledge. The electrostatic coupling can be further enhanced by improving the interface between hBN and the silicon nanowire. The quality, thickness, and uniformity of the hBN can also impact the device's performance. To achieve this, a well-controlled deposition of hBN using chemical vapor deposition (CVD) or epitaxy can be employed.²³ Furthermore, nanowires having smooth edges instead of sharp cuts can enable better contact between nanowire surfaces and hBN. Moreover, the properties of hBN can also be tuned, e.g., by doping or defect-induced variations.²⁴ This attribute can be exploited to flexibly fabricate devices to attain the desired performance.

To further understand the contact between the nanowires and hBN, the dielectric is also transferred on a nanowire array-based device. The array has 20 nanowires with a pitch of 200

nm. The transfer characteristics are listed in Figure 5. The three gating schemes are used similarly to the single nanowire-

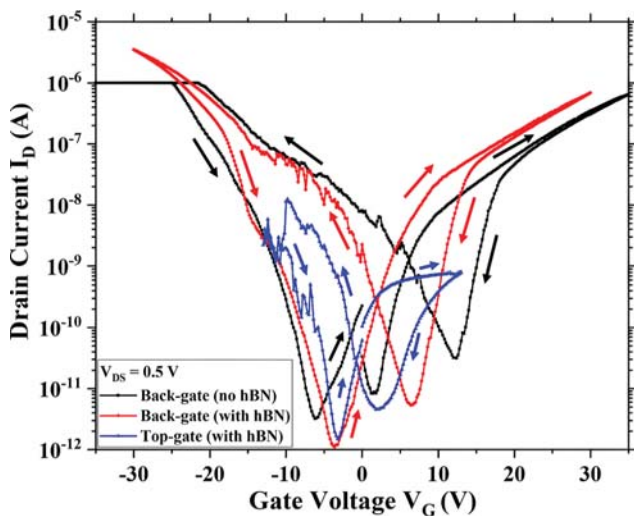


Figure 5. Transfer characteristics of a device consisting of a nanowire array. hBN is used as a dielectric layer. The lengths and widths of the nanowires are 3 μm and 25 nm, respectively. The pitch between the nanowires is 200 nm. The black curve shows a straight line below -20 V due to the compliance set in the measurement tool. For the rest of the transfer characteristics, the compliance was set at a higher drain current value. Similar to Figure 4b, the arrows in the transfer characteristics denote the direction of the curve based on the gate voltage sweep.

based device. With back gating, the device with the hBN flake showed an improvement in on- and off-currents and, hence, in the on-off ratio by nearly 2 orders of magnitude (Table 4).

Table 3. SS Values of hBN-Passivated Nanowire Array-Based Devices Using Different Gating Schemes

carrier type	SS (V/dec)		
	back-gate (without hBN)	back-gate (with hBN)	top-gate (with hBN)
n	2.56	1.76	3.05
p	5	3.06	1.5

Table 4. Extracted Parameters from the Transfer Characteristics of the hBN-Passivated Nanowire Array-Based Device at a V_{DS} of 0.5 V Using Different Gating Schemes

parameter	carrier type	back gate (without hBN)	back gate (with hBN)	top gate (with hBN)
I_{ON} (A)	n	6.4×10^{-7}	6.8×10^{-7}	8.0×10^{-10}
	p	7.3×10^{-8}	2.7×10^{-7}	8.2×10^{-9}
I_{OFF} (A)	n	3.2×10^{-11}	5.3×10^{-12}	4.5×10^{-12}
	p	3.2×10^{-11}	5.3×10^{-12}	4.5×10^{-12}
$I_{\text{ON}}/I_{\text{OFF}}$ ratio	n	$\sim 10^4$	$\sim 10^5$	$\sim 10^2$
	p	$\sim 10^3$	$\sim 10^5$	$\sim 10^3$
hysteresis (V)	n	8	7.6	6.9
	p	16	11	4.2

This means that passivation by hBN of the 20 nanowires helps to improve these parameters. Similarly from Figure 5, it is seen

that the shift of the transfer curve minima is largely reduced. Subsequently, the hysteresis of the device reduces from its unpassivated state to hBN-passivated top gate state (see Table 4) exactly analogous to how it was observed for the single nanowire-based device. However, it is also to be noted that compared to the single nanowire-based device, the nanowire array-based device has higher off-currents (almost 4 orders of magnitude). The reason for this can be that the minimum current I_{OFF} is dependent on the V_{DS} value, with V_{G} being negligible. Therefore at room temperature, with a considerable V_{DS} and negligible V_{G} , an adequate amount of thermally activated charge carriers can pass through the drain-source contacts. Nonetheless, for a single nanowire, this current value is low. However, it is understandable that the array-based device consists of 20 single nanowires in parallel. Each of these nanowires contributes charge carriers thermionically in the off-state, thus increasing the off-current. Furthermore, the device maintained the off-current when the transfer characteristics were obtained with top gating, but the on-current was reduced. This is attributed to the weak interface between nanowire arrays and hBN (Supporting Information Figure S4). Since nanowires have a pitch of 200 nm, hBN is seen to cover only the top part of the nanowires and not the sidewalls. With an increasing pitch of the nanowires, the hBN coverage of the nanowires can be expected to improve and vice versa. It is expected that for nanowire arrays with a larger distance between the nanowires, a thinner hBN would bend in the gap. This would provide passivation and encapsulation from all three sides of the nanowire. However, with a low pitch of 200 nm, the hBN only sits on the top of the nanowire and does not encapsulate it like in the case of the single nanowire-based device. Thus, although back-gated characteristics improved due to the added effect of the multiple nanowires, the top gate result degraded due to weak electrostatic coupling. This is reflected in the SS values of these measurements (Table 3). The SS values improved after hBN transfer with back gate measurements. Although both these measurements provide capacitive gate coupling through the same back gate, the measurement after hBN transfer has a better SS value due to the surface passivation of the nanowires by hBN. With hBN reducing the interface state density of the top surface of the nanowire, the SS value is strongly influenced.²⁵ However, the SS of the n-branch degraded with the top gate measurements compared to its back gate due to lower gate coupling through the hBN on the multiple nanowires.

Furthermore, a gate leakage current analysis is performed during each measurement step to prevent the flow of high current through the dielectric layer during continuous voltage scans. The repeated flow of high currents can eventually lead to dielectric breakdown and degradation of the hBN-passivated nanowire-based devices. The measured leakage current analysis for hBN-passivated single nanowire- and nanowire array-based devices with different gating schemes are shown in Supporting Information Figure S5. For both the single nanowire- and nanowire array-based devices, the leakage current is measured by sweeping the gate voltage from a low potential to a high potential. Repeated voltage scans that produce currents above 10 pA can be fatal for the dielectric and the device. Therefore, compliance of 10 pA was set in the measurement setup prior to the analysis. As seen from Figure S5, the gate leakage current I_{G} (denoted by the red curve) is always under the set limit of 10 pA and showed minimal leakage through the gate dielectric. In the scope of this work, a total of 18 nanowire devices are

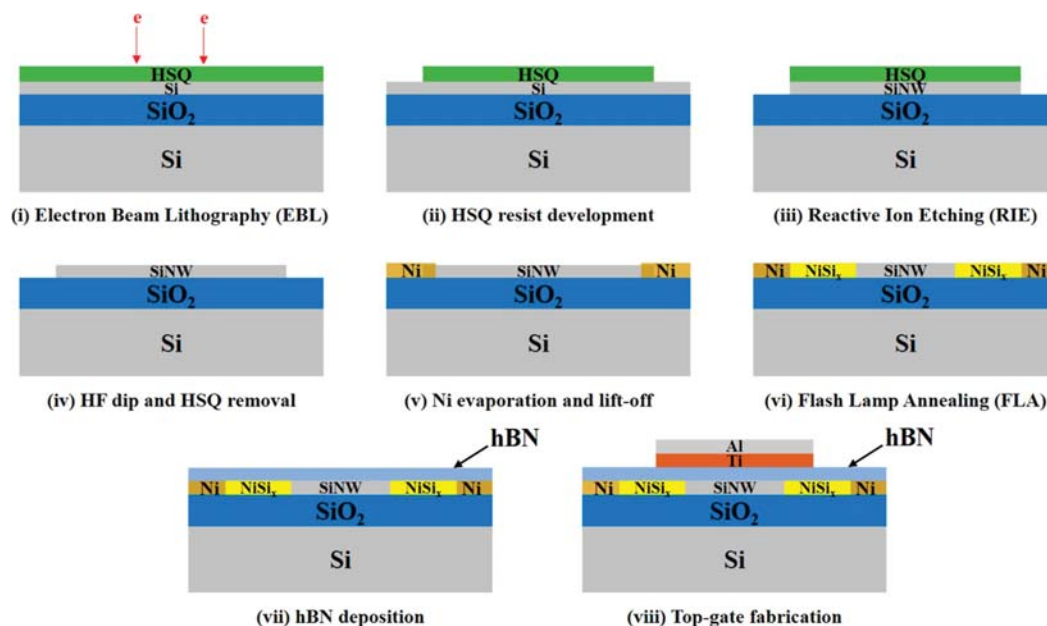


Figure 6. A schematic representation of the top-down fabrication process flow of the novel mixed-dimensional RFET device. (i) Starting with SOI substrate, a negative resist HSQ is spin-coated for patterning with EBL, (ii) development of HSQ resist creates the HSQ patterns in the shape of the nanowire, (iii) HSQ patterns are then transferred to the top 20 nm device layer using anisotropic reactive ion etching, (iv) HF dip is carried out to remove the top HSQ later, (v) source and drain Ni contact pads are fabricated by EBL, metal deposition, and lift-off technique, (vi) FLA creates the NiSi₂ Schottky junction inside the nanowire, (vii) exfoliated hBN is transferred onto the device by dry-stamping technique, and (viii) top gates are fabricated on top of the hBN layer by EBL, metal deposition, and lift-off.

fabricated. Out of 12 are single nanowires and 6 are nanowire array devices. Exfoliated hBN is successfully transferred to 12 of the devices, while the top gate is fabricated on 5 of them. Out of the five top-gated single nanowire-based devices, three are nominally identical with hBN thickness varying between 10 and 15 nm. The other two devices had significantly thicker hBN gate dielectric, which led to weaker gate coupling and considerably worse device characteristics (as explained in the earlier section). On the other hand, the three devices with thinner hBN consistently exhibited similar device performances. The electrical parameters of these nominally identical three devices are extracted to derive the statistical analysis including the mean values and standard deviations (SD). This is shown in Supporting Information Table S1. Figure S6 presents the extracted electrical parameters of the three devices along with their resulting mean and SD values. The SD values in Figure S6a–c are relatively higher than their mean values. This is because the currents extracted have deviations of a couple of orders of magnitude owing to the device-to-device variability. Since the nanowires are fabricated by a top-down approach, these devices are robust and stable. hBN also helps to protect the devices from the outside environment. Therefore, over an extended period of time, the devices maintained consistent functionality and performance. The fabrication of these 12 nanowire devices with hBN is also carried out over different time spans. Their similar device behavior implied the reproducibility of the devices and the reliability of the fabrication process that is employed.

EXPERIMENTAL SECTION

The substrate material used for the fabrication of a mixed-dimensional RFET is a $1 \times 1 \text{ cm}^2$ silicon-on-insulator (SOI) substrate. It consists of layers of silicon-insulator-silicon stacked on top of each other. The device or active top layer of the substrate consists of 20 nm intrinsic

silicon, followed by a 102 nm thick buried oxide (BO_x) layer and a 775 μm p-doped Si carrier wafer. In this work, the fabrication of nanowires is based on the top-down approach, which allows the large-scale integration of devices. The top-down approach involves the use of a substrate material, which is subjected to successive subtractive procedures to ultimately achieve a nanostructure. The detailed process of silicon nanowire fabrication is described in our previous work¹⁸ and schematically shown in Figure 6. At first, the SOI substrate is cleaned thoroughly in various chemicals, including Piranha solution, acetone, isopropanol (IPA), and deionized (DI) water. Then, a 2% hydrogen silsesquioxane (HSQ) (XR-1541 from DuPont) negative-tone resist is spin-coated on the substrate at 2000 rpm for 30 s, creating a 40 nm thick HSQ layer. The nanowires are exposed using a RAITH e-LINE PLUS electron beam lithography (EBL) system at an acceleration voltage of 10 kV, a base dose of 1000 $\mu\text{C cm}^{-2}$, an aperture with the size of 30 μm , and a beam area step size of 2 nm. The exposure parameters are optimized according to the nanowire dimensions and were used throughout this work for patterning the appropriate nanostructures. After the exposure, the substrate is subjected to a resist development, which removes the unexposed resist.²⁶ A SENTECH inductively coupled plasma reactive ion etching (ICP-RIE) Si 500 system is used to anisotropically transfer the HSQ pattern to the active device layer. The fabrication of source and drain Ni contacts at both ends of the nanowire includes a similar process of EBL patterning, metal deposition using a UHV e-beam evaporation system from BESTEC, and a lift-off process. Flash lamp annealing (FLA) is performed on the substrate after the Ni contact deposition to achieve diffusion of Ni into the nanowire to form the NiSi₂ phase.¹⁸ Ni silicidation in the nanowire creates a heterostructure of NiSi₂–Si–NiSi₂ forming two Schottky junctions on either side. A prior study was conducted to develop a Ni silicidation process of silicon nanowires by rapid thermal annealing (RTA).²⁷ This study was further continued to compare the results with FLA.¹⁸ The optimization of the FLA parameters with different energy densities, flash pulse durations, and various inert gas conditions was performed to achieve homogeneous Ni silicide formation in the nanowire. The optimum FLA treatment is obtained for the energy density of about 89 J cm^{-2} for 6 ms in continuous nitrogen flow.

The hBN flakes are prepared using the mechanical exfoliation technique²⁸ on a polydimethylsiloxane (PDMS) substrate (approximately $1 \times 1 \text{ cm}^2$) employing commercial scotch tape. Suitable hBN flakes are then identified with the help of an optical microscope based on their thickness, lateral dimensions, and uniformity. The hBN flakes are transferred onto the nanowire using the dry-stamping technique²⁹ by aligning the desired flake onto the nanowire with the help of a micromanipulator setup that is coupled to an optical microscope. The schematic of the hBN transfer process and optical micrographs of the mixed-dimensional RFET devices are shown in Figure 7. With

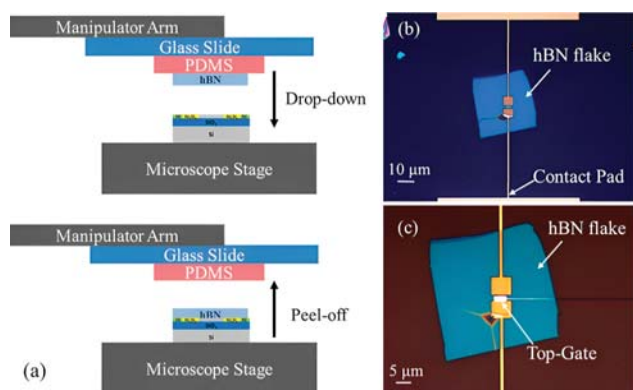


Figure 7. (a) Transfer of hBN flake indicating the steps of drop-down and peel-off process onto the silicon nanowire-based devices using the dry viscoelastic stamping transfer technique. (b) Visible-light micrograph image of a transferred hBN flake on a single silicon nanowire-based device showing the architecture of contact pads and connection lines. (c) Visible-light micrograph image of a mixed-dimensional RFET device with a top-gate present on the hBN layer.

favorable hBN flakes on the silicon nanowires, single top gates are placed based on EBL patterning, metal deposition, and lift-off processes. A stack of titanium (Ti) and aluminum (Al) is typically used as the top gate.

Bright-field transmission electron microscopy (TEM) images are recorded using an image-C_s-corrected TITAN 80-300 microscope (FEI) operated at an accelerating voltage of 300 kV. With a TALOS F200X microscope equipped with an X-FEG electron source and a Super-X EDX detector system (FEI), high-angle annular dark-field scanning TEM (HAADF-STEM) imaging and spectrum imaging analysis based on energy-dispersive X-ray spectroscopy (EDXS) are performed at 200 kV. Before (S)TEM analysis, the specimen mounted in a high-visibility low-background holder is placed for 8 s into a FISCHIONE 1020 plasma cleaner to eliminate any potential contamination. Cross-sectional TEM specimens of the mixed-dimensional RFET devices are prepared by in situ lift-out using a Helios 5 CX-focused ion beam (FIB) device (Thermo Fisher). To protect the sample surface, a carbon cap layer is deposited beginning with electron-beam-assisted and subsequently followed by Ga-FIB-assisted precursor decomposition. Afterward, the TEM lamella is prepared using a 30 keV Ga-FIB with adapted currents. Its transfer to a 3-post copper lift-out grid (Omniprobe) is done with an EasyLift EX nanomanipulator (Thermo Fisher). To minimize sidewall damage, Ga ions with only 5 keV energy are used for the final thinning of the TEM lamella to electron transparency. Tapping mode AFM analysis is carried out using a NANOFRAZOR SCHOLAR tool from HEIDELBERG INSTRUMENTS. For the electrical transfer characteristics measurements, a semiautomated SÜSS MICROTECH probe system PA200 connected with a 4200-SCS KEITHLEY INSTRUMENTS characterization system is used.

SUMMARY

A novel hybrid mixed-dimensional RFET concept is demonstrated by introducing 2D hBN in nanowire-based

electronics. The fabricated devices exhibit an improvement in SS values, a reduction in hysteresis, and an enhancement of the p and n on-currents. To conclude, hBN can be used as an effective dielectric and passivating layer for one-dimensional nanowire devices. Since the properties of the hBN can be tuned, versatile devices can be fabricated using this robust material. However, optimization of the device design and control over the hBN thickness is required for superior device performance. This first demonstration of hBN incorporation in nanowire-based devices potentially opens up a new paradigm in semiconductor electronics. Furthermore, system-level integration of these devices can be achieved using CVD or epitaxy-based deposition of hBN.

ASSOCIATED CONTENT

Supporting Information

The Supporting Information is available free of charge at <https://pubs.acs.org/doi/10.1021/acsami.3c04808>.

Information on the convention for calculation of on- and off-currents, on-state and off-state output characteristics, transfer characteristics based on different hBN thicknesses RFET devices, additional TEM and EDXS image of hBN-passivated silicon nanowire array-based device, and leakage current analysis (PDF)

AUTHOR INFORMATION

Corresponding Authors

Sayantana Ghosh – Institute of Ion Beam Physics and Materials Research, Helmholtz-Zentrum Dresden-Rossendorf (HZDR), Dresden 01328, Germany; Technische Universität Dresden, Dresden 01069, Germany; orcid.org/0000-0003-1347-1365; Email: s.ghosh@hzdr.de

Yordan M. Georgiev – Institute of Ion Beam Physics and Materials Research, Helmholtz-Zentrum Dresden-Rossendorf (HZDR), Dresden 01328, Germany; Institute of Electronics at the Bulgarian Academy of Sciences, Sofia 1784, Bulgaria; Email: y.georgiev@hzdr.de

Authors

Muhammad Bilal Khan – Institute of Ion Beam Physics and Materials Research, Helmholtz-Zentrum Dresden-Rossendorf (HZDR), Dresden 01328, Germany; orcid.org/0000-0003-4627-9433

Phanish Chava – Institute of Ion Beam Physics and Materials Research, Helmholtz-Zentrum Dresden-Rossendorf (HZDR), Dresden 01328, Germany; Technische Universität Dresden, Dresden 01069, Germany

Kenji Watanabe – National Institute for Materials Science, Tsukuba 305-0044, Japan; orcid.org/0000-0003-3701-8119

Takashi Taniguchi – National Institute for Materials Science, Tsukuba 305-0044, Japan; orcid.org/0000-0002-1467-3105

Slawomir Prucnal – Institute of Ion Beam Physics and Materials Research, Helmholtz-Zentrum Dresden-Rossendorf (HZDR), Dresden 01328, Germany; orcid.org/0000-0002-4088-6032

René Hübner – Institute of Ion Beam Physics and Materials Research, Helmholtz-Zentrum Dresden-Rossendorf (HZDR), Dresden 01328, Germany; orcid.org/0000-0002-5200-6928

Thomas Mikolajick – Namlab gGmbH, Dresden 01187, Germany; Technische Universität Dresden, Dresden 01069, Germany; Technische Universität Dresden, Center for Advancing Electronics Dresden (CfAED), Dresden 01069, Germany; orcid.org/0000-0003-3814-0378

Artur Erbe – Institute of Ion Beam Physics and Materials Research, Helmholtz-Zentrum Dresden-Rossendorf (HZDR), Dresden 01328, Germany; Technische Universität Dresden, Dresden 01069, Germany; Technische Universität Dresden, Center for Advancing Electronics Dresden (CfAED), Dresden 01069, Germany; orcid.org/0000-0001-6368-8728

Complete contact information is available at:
<https://pubs.acs.org/10.1021/acsami.3c04808>

Author Contributions

S.G., M.B.K., and P.C. contributed equally to this work. K.W. and T.T. provided the hBN crystals. S.P. and R.H. helped in FLA and structural characterization of the samples, respectively. T.M., A.E., and Y.M.G. supervised the work and reviewed the manuscript.

Notes

The authors declare no competing financial interest.

ACKNOWLEDGMENTS

We are thankful to T. Schönherr and C. Neisser for their help in the device fabrication and to A. Kunz for TEM specimen preparation. This work has received funding from the European Union's Horizon 2020 research and innovation programme under grant agreement no 899282 (RADICAL). We are also grateful to the HZDR Ion Beam Center TEM facilities and the funding of TEM Talos by the German Federal Ministry of Education and Research (BMBF; grant no. 03SF0451) in the framework of HEMCP.

REFERENCES

- (1) Simon, M.; Heinzig, A.; Trommer, J.; Baldauf, T.; Mikolajick, T.; Weber, W. M. Top-down Technology for Reconfigurable Nanowire FETs with Symmetric On-Currents. *IEEE Trans. Nanotechnol.* **2017**, *16*, 812–819.
- (2) Heinzig, A.; Slesazek, S.; Kreupl, F.; Mikolajick, T.; Weber, W. M. Reconfigurable Silicon Nanowire Transistors. *Nano Lett.* **2012**, *12*, 119–124.
- (3) Mikolajick, T.; Galderisi, G.; Rai, S.; Simon, M.; Böckle, R.; Sistani, M.; Cakirlar, C.; Bhattacharjee, N.; Mauersberger, T.; Heinzig, A.; et al. Reconfigurable Field Effect Transistors: A technology Enablers Perspective. *Solid-State Electron.* **2022**, *194*, 108381.
- (4) Lin, Y.-M.; Appenzeller, J.; Knoch, J.; Avouris, P. High-Performance Carbon Nanotube Field-Effect Transistor with Tunable Polarities. *IEEE Trans. Nanotechnol.* **2005**, *4*, 481–489.
- (5) Lin, Y.-M.; Chiu, H.-Y.; Jenkins, K. A.; Farmer, D. B.; Avouris, P.; Valdes-Garcia, A. Dual-Gate Graphene FETs with $f_{-}\{T\}$ of 50 GHz. *IEEE Electron Device Lett.* **2010**, *31*, 68–70.
- (6) Colli, A.; Tahraoui, A.; Fasoli, A.; Kivioja, J. M.; Milne, W. I.; Ferrari, A. C. Top-Gated Silicon Nanowire Transistors in a Single Fabrication Step. *ACS Nano* **2009**, *3*, 1587–1593.
- (7) Heinzig, A.; Mikolajick, T.; Trommer, J.; Grimm, D.; Weber, W. M. Dually Active Silicon Nanowire Transistors and Circuits with Equal Electron and Hole Transport. *Nano Lett.* **2013**, *13*, 4176–4181.
- (8) Khan, M.; Ghosh, S.; Prucnal, S.; Mauersberger, T.; Hübner, R.; Simon, M.; Mikolajick, T.; Erbe, A.; Georgiev, Y. Towards Scalable Reconfigurable Field Effect Transistor using Flash Lamp Annealing. *Device Research Conference (DRC)*, 2020; pp 1–2.
- (9) Sessi, V.; Simon, M.; Slesazek, S.; Drescher, M.; Mulaosmanovic, H.; Li, K.; Binder, R.; Waidmann, S.; Zeun, A.; Pawlik, A.-S.; et al. S2-2 Back-Bias Reconfigurable Field Effect

Transistor: A Flexible Add-On Functionality for 22 nm FDSOI. *2021 Silicon Nanoelectronics Workshop (SNW)*, 2021; pp 1–2.

- (10) Fei, W.; Trommer, J.; Lemme, M. C.; Mikolajick, T.; Heinzig, A. Emerging Reconfigurable Electronic Devices based on Two-dimensional Materials: A review. *InfoMat* **2022**, *4*, No. e12355.
- (11) Novoselov, K. S.; Geim, A. K.; Morozov, S. V.; Jiang, D.-e.; Zhang, Y.; Dubonos, S. V.; Grigorieva, I. V.; Firsov, A. A. Electric Field Effect in Atomically Thin Carbon Films. *science* **2004**, *306*, 666–669.
- (12) Watanabe, K.; Taniguchi, T.; Kanda, H. Direct-Bandgap Properties and Evidence for Ultraviolet Lasing of Hexagonal Boron Nitride Single Crystal. *Nat. Mater.* **2004**, *3*, 404–409.
- (13) Miró, P.; Audiffred, M.; Heine, T. An Atlas of Two-Dimensional Materials. *Chem. Soc. Rev.* **2014**, *43*, 6537–6554.
- (14) Bhimanapati, G.; Glavin, N.; Robinson, J. A. *Semiconductors and Semimetals*; Elsevier, 2016; Vol. 95, pp 101–147.
- (15) Lee, G.-H.; Cui, X.; Kim, Y. D.; Arefe, G.; Zhang, X.; Lee, C.-H.; Ye, F.; Watanabe, K.; Taniguchi, T.; Kim, P.; et al. Highly Stable, Dual-gated MoS₂ Transistors Encapsulated by Hexagonal Boron Nitride with Gate-controllable Contact, Resistance, and Threshold Voltage. *ACS Nano* **2015**, *9*, 7019–7026.
- (16) Arora, H.; Jung, Y.; Venanzi, T.; Watanabe, K.; Taniguchi, T.; Hübner, R.; Schneider, H.; Helm, M.; Hone, J. C.; Erbe, A. Effective Hexagonal Boron Nitride Passivation of Few-layered InSe and GaSe to Enhance their Electronic and Optical Properties. *ACS Appl. Mater. Interfaces* **2019**, *11*, 43480–43487.
- (17) Kumar, R.; Rajasekaran, G.; Parashar, A. Optimised Cut-off Function for Tersoff-like Potentials for a BN Nanosheet: a Molecular Dynamics Study. *Nanotechnology* **2016**, *27*, 085706.
- (18) Khan, M. B.; Prucnal, S.; Ghosh, S.; Deb, D.; Hübner, R.; Pohl, D.; Rebohle, L.; Mikolajick, T.; Erbe, A.; Georgiev, Y. M. Controlled Silicidation of Silicon Nanowires using Flash Lamp Annealing. *Langmuir* **2021**, *37*, 14284–14291.
- (19) Weber, W. M. Silicon to Nickel Silicide Longitudinal Nanowire Heterostructures: Synthesis, Electrical Characterization and Novel Devices. Ph.D. Thesis, Technische Universität München, 2008.
- (20) Bartur, M.; Nicolet, M.-A. Thermal Oxidation of Nickel Disilicide. *Appl. Phys. Lett.* **1982**, *40*, 175–177.
- (21) Paska, Y.; Haick, H. Interactive Effect of Hysteresis and Surface Chemistry on Gated Silicon Nanowire Gas Sensors. *ACS Appl. Mater. Interfaces* **2012**, *4*, 2604–2617.
- (22) Fahem, Z.; Csaba, G.; Erlen, C.; Lugli, P.; Weber, W.; Geelhaar, L.; Riechert, H. Analysis of the Hysteretic Behavior of Silicon Nanowire Transistors. *Phys. Status Solidi C* **2008**, *5*, 27–30.
- (23) Uchida, Y.; Kawahara, K.; Fukamachi, S.; Ago, H. Chemical Vapor Deposition Growth of Uniform Multilayer Hexagonal Boron Nitride driven by Structural Transformation of a Metal Thin Film. *ACS Appl. Electron. Mater.* **2020**, *2*, 3270–3278.
- (24) Zhang, K.; Feng, Y.; Wang, F.; Yang, Z.; Wang, J. Two Dimensional Hexagonal Boron Nitride (2D-hBN): Synthesis, Properties and Applications. *J. Mater. Chem. C* **2017**, *5*, 11992–12022.
- (25) Hamaide, G.; Allibert, F.; Hovel, H.; Cristoloveanu, S. Impact of Free-Surface Passivation on Silicon on Insulator Buried Interface Properties by Pseudotransistor Characterization. *J. Appl. Phys.* **2007**, *101*, 114513.
- (26) Henschel, W.; Georgiev, Y.; Kurz, H. Study of a High Contrast Process for Hydrogen Silsesquioxane as a Negative tone Electron Beam Resist. *J. Vac. Sci. Technol., B: Microelectron. Nanometer Struct.—Process., Meas., Phenom.* **2003**, *21*, 2018–2025.
- (27) Khan, M. B.; Deb, D.; Kerbusch, J.; Fuchs, F.; Löffler, M.; Banerjee, S.; Mühle, U.; Weber, W. M.; Gemming, S.; Schuster, J.; et al. Towards Reconfigurable Electronics: Silicidation of Top-Down Fabricated Silicon Nanowires. *Appl. Sci.* **2019**, *9*, 3462.
- (28) Gao, E.; Lin, S.-Z.; Qin, Z.; Buehler, M. J.; Feng, X.-Q.; Xu, Z. Mechanical exfoliation of Two-dimensional Materials. *J. Mech. Phys. Solids* **2018**, *115*, 248–262.
- (29) Castellanos-Gomez, A.; Buscema, M.; Molenaar, R.; Singh, V.; Janssen, L.; Van Der Zant, H. S.; Steele, G. A. Deterministic Transfer

of Two-dimensional Materials by All-Dry Viscoelastic Stamping. *2D Materials* **2014**, *1*, 011002.

Giant THz Nonlinearity in Topological and Trivial HgTe-Based Heterostructures

Tatiana A. Uaman Svetikova,* Thales V. A. G. de Oliveira, Alexej Pashkin, Alexey Ponomaryov, Christian Berger, Lena Fürst, Florian B. Bayer, Elena G. Novik, Hartmut Buhmann, Laurens W. Molenkamp, Manfred Helm, Tobias Kiessling, Stephan Winnerl, Sergey Kovalev,* and Georgy V. Astakhov*



Cite This: *ACS Photonics* 2023, 10, 3708–3714

ACCESS

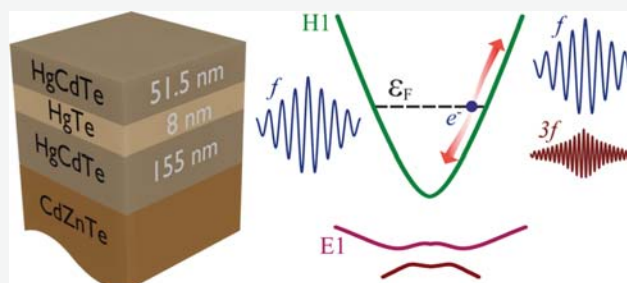
Metrics & More

Article Recommendations

Supporting Information

ABSTRACT: Nonlinear phenomena in the THz spectral domain are important for understanding the optoelectronic properties of quantum systems and provide a basis for modern information technologies. Here, we report a giant THz nonlinearity in high-mobility 2D topological insulators based on HgTe quantum wells, which manifests itself in a highly efficient third harmonic generation. We observe a third harmonic THz susceptibility several times higher than that in bare graphene and many orders of magnitude higher than that in trivial quantum well structures based on other materials. To explain the strong nonlinearity of HgTe-based heterostructures at the THz frequencies, we consider the acceleration of free carriers with a high mobility and variable dispersion. This acceleration model, for which the nonparabolicity of the band dispersion is key, in combination with independently measured scattering time and conductivity, is in good agreement with our experimental data in a wide temperature range for THz fields below the saturation. Our approach provides a route to material engineering for THz applications based on frequency conversion.

KEYWORDS: topological insulators, THz spectroscopy, high harmonic generation, 2D systems, HgTe



INTRODUCTION

Nonlinear effects have a variety of applications in different fields, including ultrashort pulse measurements, material characterization, and imaging spectroscopy. High harmonic generation, the multiplication of the photon energy, is a direct manifestation of the nonlinear interaction between light and matter. Quantum materials, such as graphene,^{1,2} superconductors,³ Dirac semimetals,^{4,5} and 3D topological insulators (TIs)^{6,7} possess extremely highly efficient third harmonic generation (THG) in the terahertz (THz) spectrum domain. Because of these appealing properties, these materials can meet the great demand for ultrafast signal processing and communication technologies. Indeed, recent experiments demonstrate the ability to electrically control the THz nonlinearity⁸ and enhance the THG efficiency by more than one order magnitude using metamaterials.^{7,9}

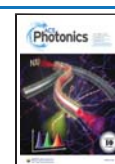
There are two theoretical approaches to explain the appearance of the THz third harmonic in Dirac materials. In both of them, the key ingredient is the linear energy-momentum dispersion of Dirac electrons as the THz nonlinearity vanishes for pure parabolic bands. In the acceleration model, THG arises from the nontrivial change of the electron velocity driven by the THz field.^{10–12} It

provides a good agreement for moderate THz intensity when the third harmonic amplitude is proportional to the cube of the incident THz field $E_{3\omega} \propto E_i^3$. For strong THz fields, the THG efficiency increases slower than E_i^3 and can even saturate at a certain level.⁷ This can be explained in the framework of a thermodynamic model, when the THz nonlinearity is caused by the absorption modulation due to the fast heating and cooling of Dirac Fermions.^{1,13}

Graphene possesses the strongest nonlinear third-order susceptibility $\chi^{(3)} \approx 10^{-9} \text{ m}^2 \text{ V}^{-2}$ among all solid-state systems, reported to date.¹ In strong THz fields, metamaterials based on the Bi_2Se_3 3D TI outperform graphene though the $\chi^{(3)}$ of the Dirac surface states is slightly lower. The reason for that is the absence of saturation of the THG efficiency for the achievable THz fields, which is the result of ultrafast dissipation of electronic heat via surface-bulk Coulomb interactions.⁷ In spite

Received: June 22, 2023

Published: September 21, 2023



of extremely strong THz nonlinearity, the THG efficiency is limited by the monolayer nature of graphene or the surface nature of Dirac carriers in 3D TIs.

THG has also been demonstrated in bulk silicon doped with boron, where it is caused by the band anharmonicity.¹⁴ The nonlinear susceptibility is relatively low, but normalized per charge carrier, it is comparable to that in the monolayer^{15,16} and bilayer graphene.¹⁷ An alternative approach is based on quantum well (QW) structures, where the electronic dispersion can deviate from the parabolic structure due to band mixing. Indeed, THG has been reported for AlInAs/GaInAs QW structures.¹⁸ However, $\chi^{(3)}$ in these structures is several orders of magnitude lower than that in graphene and TIs. We note that nonparabolicity is not the only mechanism, leading to THG in materials with trivial band structure. An alternative approach relies on quantized subbands in QWs. Earlier experiments have been performed at 30 THz with $\chi^{(3)} \approx 10^{-14} \text{ m}^2 \text{ V}^{-2}$.¹⁹ Though $\chi^{(3)}$ increases superlinearly with lowering frequency and the resonantly enhanced nonlinearity can be significantly stronger for frequencies around/below one THz, higher values have not been reported.

Here, we report extremely strong THz nonlinearity in 2D TIs based on single HgTe/CdTe QW.²⁰ Epitaxial HgTe layers have been investigated using linear cw and time-domain THz spectroscopy,^{21,22} including photogalvanic effect,²³ giant Faraday rotation,²⁴ and terahertz cyclotron emission,²⁵ but nonlinearity has not been reported so far. We find a nonlinear third-order susceptibility $\chi^{(3)} \approx 5 \times 10^{-9} \text{ m}^2 \text{ V}^{-2}$, i.e., a factor of 5 higher than that in graphene, representing the record value for bare materials without any field-enhancement structures. Such an exceptional performance is caused by two factors. First, though topological states are not required for THG, their presence guarantees a significant nonparabolicity of the dispersion.²⁶ Second, electrons in HgTe/CdTe QWs possess very high mobility²⁷ and, consequently, a long scattering time, comparable with the oscillation period of the THz field.

To understand the mechanism of highly efficient THG in 2D TIs at moderate THz fields, we consider coherent intraband acceleration of electrons with arbitrary dispersion, which is neither pure parabolic nor pure linear. We achieve a good qualitative agreement between the experimental data and acceleration model for a temperature range between 10 to 200 K with only one fitting parameter. Therefore, our experimental and theoretical approaches provide insight into the physical mechanisms leading to giant THz nonlinearity in high-mobility 2D topological insulators.

2D TOPOLOGICAL INSULATOR

The HgTe/(Cd_{0.68}Hg_{0.32}Te) QW is grown on an insulating (100)-oriented Cd_{0.96}Zn_{0.04}Te substrate by molecular beam epitaxy,²⁰ as schematically presented in Figure 1a. The QW thickness $d = 8 \text{ nm}$ is above the critical value $d_c = 6.3 \text{ nm}$, where the transition from trivial to topological QW occurs.²⁸ Using optical lithography, an 8-terminal Hall bar pattern with dimensions of $200 \times 1200 \mu\text{m}^2$ is structured into the layer stack with AuGe/Au as contact metals. We use it to measure the longitudinal and Hall resistances, as shown in Figure 1b for temperature $T = 10 \text{ K}$. These measurements yield the electron concentration $n_e = 2.8 \times 10^{11} \text{ cm}^{-2}$ and mobility $\mu = 207 \times 10^3 \text{ cm}^2 \text{ V}^{-1} \text{ s}^{-1}$. The corresponding sheet conductivity is $\sigma_0 = e\mu n_e = 9.2 \times 10^{-3} \Omega$.

The dispersion $\mathcal{E}(k)$ in the HgTe QW under study is presented in Figure 1c. It is calculated using an eight-band $\mathbf{k}\cdot\mathbf{p}$

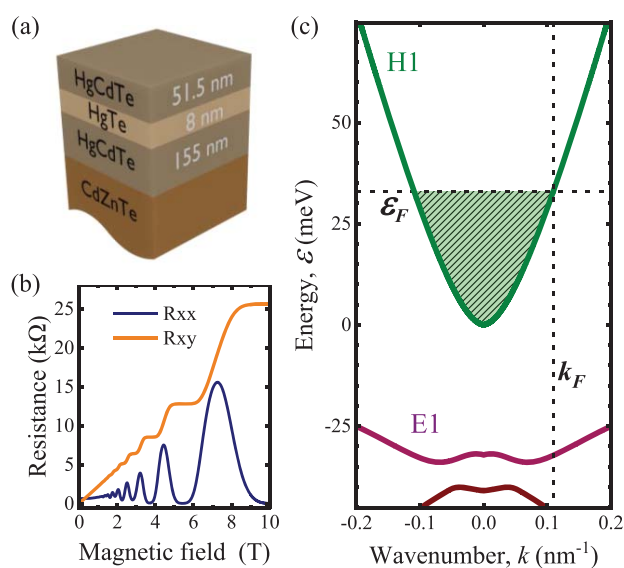


Figure 1. Band structure of 2D HgTe TI at $T = 10 \text{ K}$. (a) Schematic representation of an n -type HgTe/Cd_{0.68}Hg_{0.32}Te QW with a thickness $d = 8 \text{ nm}$. (b) Longitudinal resistance R_{xx} and Hall resistance R_{xy} are obtained from the Hall measurements. (c) Calculated dispersion using a $\mathbf{k}\cdot\mathbf{p}$ model as explained in the text. The valence band is shown in red, and the conduction band is shown in green. The Fermi level \mathcal{E}_F is obtained from the carrier concentration.

model in an envelope function approach.²⁶ This model takes into account the strong coupling between the lowest conduction $|\Gamma_6, \pm 1/2\rangle$ and the highest valence bands $|\Gamma_8, \pm 1/2\rangle$, $|\Gamma_8, \pm 3/2\rangle$, and $|\Gamma_7, \pm 1/2\rangle$ that causes mixing of the electronic states and induces nonparabolicity in the bands. An exact envelope-function approach of Burt²⁹ based on the correct operator ordering in the Hamiltonian is used to unambiguously determine the interface boundary conditions.

We perform calculations of the band dispersion for different temperatures considering the temperature-dependent band gap of the ternary material (Cd,Hg)Te³⁰ and the band structure parameters from the earlier theoretical work.²⁶ Our calculations point at the transition from topological to trivial QW at a temperature of about 110 K (Supporting Information), which is in agreement with our transport data discussed below. In the trivial state, the band structure is not inverted any more, and the lowest conduction and the highest valence band have E1 and H1 character, respectively. An example of the trivial band structure at room temperature is presented in the Supporting Information. We note that, at the transition point, the band structure has pure linear dispersion and mimics graphene.²⁸

The eigenvalue problem and Poisson equations for the 2D charge carriers in the QW are solved self-consistently to determine the Hartree potential and the charge distribution of the electrons in the QW. The latter is given by²⁶

$$\rho^e(z) = e \sum_i^{\text{CB}} \frac{1}{(2\pi)^2} \int \sum_{j=1}^8 |f_j^i(z)|^2 f_{\text{FD}}(\mathcal{E}_i - \mathcal{E}_F) d^2k \quad (1)$$

where e is the electron charge, the summation index i runs over all conduction band states, and index j runs over all components of the envelope functions $f_j(z)$ in the chosen eight-band basis, $f_{\text{FD}}(\mathcal{E} - \mathcal{E}_F)$ is the Fermi–Dirac function.

The strain effects due to the lattice mismatch between the QW and substrate are taken into account by applying the Bir–Pikus formalism.³¹ Taking the electron concentration $n_e = \int dz \rho^e(z)$ from the transport measurements, we solve eq 1 numerically and obtain the Fermi wavevector k_F and Fermi energy \mathcal{E}_F for all relevant temperatures. Particularly, we determine $k_F = 0.11 \text{ nm}^{-1}$ and $\mathcal{E}_F = 33 \text{ meV}$ for $T = 10 \text{ K}$, as shown by the dashed lines in Figure 1c. Correspondingly, the Fermi velocity is $v_F = 0.8 \times 10^6 \text{ m/s}$, which is comparable to that in graphene.

As far as the thickness is larger than the critical value of 6.3 nm at low temperature, the heavy hole-like subband H1 has higher energy than the electron-like subband E1, leading to topological states.²⁰ We note that even for trivial HgTe QWs with a thickness below the critical value or for higher temperatures, the nonparabolicity of the conduction band remains significant due to the interplay between the inverted band structure of HgTe and the size quantization.

ACCELERATION MODEL WITH ARBITRARY DISPERSION

Our model of nonlinear carrier dynamics in HgTe QWs is based on the acceleration theory, which was first developed for graphene.^{10,12} This theory involves solving the motion equation at a first-order term:

$$\frac{d\mathbf{k}(t)}{dt} = \frac{e}{\hbar} \mathbf{E}_t(t) - \frac{\mathbf{k}(t)}{\tau} \quad (2)$$

But unlike the previous approaches, we consider the carrier dispersion in a general form, where the energy in the conduction band \mathcal{E} should not necessarily be proportional to the wavevector \mathbf{k} (Supporting Information). We also neglect any angular dependence $\mathcal{E}(\mathbf{k}) = \mathcal{E}(k)$. The oscillating THz electric field with amplitude E_t inside the sample has the form $\mathbf{E}_t(t) = \hat{\mathbf{x}} E_t \cos(\omega t) = \hat{\mathbf{x}} 1/2 E_t e^{-i\omega t} + c.c.$, which is linearly polarized along $\hat{\mathbf{x}}$. Here, $f = \omega/2\pi$ is the THz frequency. Because in our experiments $f = 0.5 \text{ THz}$ and, consequently, $\mathcal{E}_F \gg \hbar\omega$, there are no interband transitions. By solving the equation of motion with energy-independent scattering time τ , we obtain the shift of the Fermi disk at time t as $\mathbf{k}_c(t) = k_{cx}(t)\hat{\mathbf{x}}$. In this case, the x component of the current density is given by the summation over all occupied states in the reciprocal space

$$J_x(t) = q \frac{e}{A} \sum_{\mathbf{k}, \text{occ}} v_x(\mathbf{k}) \quad (3)$$

where A is the sample area and the factor q accounts for the spin and valley degeneracy ($q = 4$ for graphene and $q = 2$ for HgTe QWs). The x component of the carrier velocity is $v_x(\mathbf{k}) = v(k) \cos(\theta)$, where θ is the angle between \mathbf{k} and $\hat{\mathbf{x}}$.

We convert the sum of eq 3 to an integral over θ and k :

$$J_x(t) = \frac{qe}{4\pi^2} \int_0^{2\pi} d\theta \cos(\theta) \int_0^\infty dk v(k) k \Theta(k_F - |k - k_c(t)|) \quad (4)$$

We then expand the integral in a Taylor series up to $O(k_{cx}^4)$ (Supporting Information). The coefficients with the terms k_{cx}^2 and k_{cx}^4 are proportional to even powers of $\cos(\theta)$. Therefore, after integration over θ from 0 to 2π , their contribution to $J_x(t)$ is zero. This is also valid for any system with the center of inversion. We then obtain the current density

$$J_x(t) = q \frac{e}{4\pi} v_F \left[k_F k_{cx}(t) - \frac{1}{8k_F} \eta k_{cx}^3(t) + O(k_{cx}^5) \right] \quad (5)$$

The parameter

$$\eta = 1 - \frac{v_F'}{v_F} k_F - \frac{v_F''}{v_F} k_F^2 \quad (6)$$

describes the nonlinearity (or nonparabolicity) of the dispersion. Here, v_F' and v_F'' are the first and second derivatives of the velocity defined as $v(k) = \frac{1}{\hbar} \frac{d\mathcal{E}(k)}{dk}$ with respect to k , respectively. It is straightforward to show that $\eta = 1$ and 0 for pure linear and pure parabolic dispersion, respectively. In the case of Figure 1c, we obtained $\eta = 0.73$.

The linear term in eq 5 gives the well-known Drude conductivity

$$\sigma^{(1)}(\omega) = \frac{\sigma_0}{1 - i\omega\tau}, \quad \text{where } \sigma_0 = \frac{qe^2 \mathcal{E}_{\text{eff}} \tau}{4\pi \hbar^2} \quad (7)$$

and $\mathcal{E}_{\text{eff}} = \hbar k_F v_F(k_F)$ is obtained at the Fermi energy. For the current density oscillating at the fundamental (ω) and third (3ω) harmonics, we obtain the nonlinear contributions to the THz conductivity due to the term $\propto k_{cx}^3(t)$ in eq 5 (Supporting Information). From that we determine the characteristic nonlinear field

$$E_{\text{nl}} = \frac{4\hbar k_F}{|e|} \sqrt{\frac{2(1 + \tau^2 \omega^2)}{3\eta\tau^2}} \quad (8)$$

when the third harmonic amplitude starts to deviate from the cubic dependence on the incident THz field. With $\eta = 1$, our results agree with the nonlinear THz conductivity derived for graphene.¹²

Using the Fresnel coefficients for the THz transmission and the approximation of a thin conducting film,³² we obtain the THG efficiency, i.e., the ratio of the third-harmonic ($E_{3\omega}$) and fundamental (E_ω) THz fields $\kappa = |E_{3\omega}/E_\omega|$ (Supporting Information). We consider the case of low conductivity, $|Z_0 \sigma_{\text{nl}}(\omega)| \ll 1 + n_s$. Here, $Z_0 = \sqrt{\mu_0/\epsilon_0} \approx 377 \Omega$ is the impedance of free space, $n_s = 3.42$ is the refractive index of the high-resistivity substrate, and $\sigma_{\text{nl}}(\omega) = \sigma^{(1)}(\omega) [1 - (E_t/E_{\text{nl}})^2]$ is the nonlinear conductivity, where E_t is the amplitude of the THz field inside the sample. In the case of moderate THz fields $E_t \ll E_{\text{nl}}$, the THG efficiency can be written in the form (Supporting Information)

$$\kappa = \frac{\eta}{16(1 + n_s)^2} \left(\frac{e\tau}{\hbar k_F} \right)^2 \frac{Z_0 \sigma_0}{(1 + \omega^2 \tau^2)^{3/2}} E_i^2 \quad (9)$$

Here, E_i is the amplitude of the incident THz field. According to the Tinkham equation, we can disregard etalon contributions by considering a phase factor arising from multiple reflections in a finite-thickness layer $E_\omega \propto E_i$.^{32,33} Therefore, the field conversion coefficient γd (d is the sample thickness) at the third harmonic, $E_{3\omega} = \gamma d E_i^3$, is proportional to κ and also depends on the THz conductivity $\sigma^{(1)}(\omega)$ at the fundamental harmonic ω and refractive index of substrate n_s .

In order to validate our theoretical approach, we first independently measure the scattering time τ in THz pump–probe experiments and DC conductivity σ_0 in transport experiments. We then use eq 7 to determine \mathcal{E}_{eff} . To obtain k_F and v_F separately, we calculate the dispersion $\mathcal{E}(k)$ and effective energy $\mathcal{E}_{\text{eff}}(k)$ using the $\mathbf{k}\cdot\mathbf{p}$ model, as shown in Figure 1. We then calculated the THG efficiency using eq 9 with the experimentally determined parameters. Finally, we perform a

direct comparison of the THz nonlinearity with our experimental data.

EXPERIMENTAL METHODS

Two-Color Pump–Probe Experiment. Our study employs a two-color pump–probe experiment with a mid-infrared (MIR) pump and a broadband terahertz (THz) probe. We excite electrons from the valence band into the conduction band inside the QW using pump pulses with $f = 28$ THz generated by the free-electron laser FELBE operating at a repetition rate of 13 MHz.³⁴ The relatively low pump photon energy of 115 meV ensures that the HgCdTe barriers (bandgap 0.5 eV) and CdZnTe substrate (bandgap 1.6 eV) are not excited. To probe the resulting response, we utilize broadband THz pulses from a photoconductive antenna excited by a Ti:sapphire amplifier system, which is synchronized with FELBE and has a repetition rate of 250 kHz. The probe THz spectrum spans from approximately 0.5 to 2 THz.

We probed the pump-induced change of the THz transmission for a fixed pump–probe delay. It is set to several ps after the maximum of the signal (Supporting Information) to ensure that the hot electrons have sufficient time to cool down via the energy transfer to the phonon bath. The experiments are conducted with a pump fluence of $0.026 \mu\text{J}/\text{cm}^2$, where signal saturation is negligible. We estimate the pump-induced changes in the carrier concentration to amount to $\Delta n_e = 3.5 \times 10^{10} \text{ cm}^{-2}$ (Supporting Information), which is by 1 order of magnitude lower than n_e . Therefore, the change in the Fermi level under the pump pulse can be neglected.

A fast Fourier transform (FFT) is applied to obtain reference (pump off) and signal (pump on) spectra, denoted as E_{off} and E_{on} , respectively. From the ratio $E_{\text{on}}/E_{\text{off}}$ we determine the pump-induced change in the complex conductivity $\Delta\sigma^{(1)}(\omega)$ using the standard thin-film approximation.³⁵ We fit the real part as $\text{Re}[\Delta\sigma^{(1)}(\omega)] \propto 1/(1 + \omega^2\tau^2)$ in accordance with eq 7. The experimental data points and fitting examples for $T = 10$ K are presented in Figure 2a. We omit the imaginary part of $\Delta\sigma^{(1)}(\omega)$, as it gives a much larger uncertainty in determining the scattering time. In the inset of Figure 2a, we plot $1/\text{Re}[\Delta\sigma]$ as a function of $f^2 = \omega^2/4\pi^2$. The intersection with the vertical axis gives the proportionality coefficient, and the slope allows us to obtain the scattering time, yielding $\tau = 1.5 \pm 0.3$ ps.

Using this procedure, we measure the scattering time in the temperature range of 10 to 150 K, as presented in Figure 2b. It slightly decreases with the temperature down to $\tau = 500 \pm 100$ fs at 150 K. Remarkably the scattering time in our HgTe 2D TI at given temperatures is significantly longer than that reported for graphene (47 fs),¹ Cd₃As₂ Dirac semimetal (145 or 10 fs)^{4,5} and Be₂Se₃ 3D TI (182 fs)⁶ with efficient THG. Such an unusually long scattering time might be related to the suppression of the electron backscattering in topological insulators.

Figure 2b presents the DC conductivity as a function of the temperature obtained from the aforementioned Hall measurements on the same sample. At low temperatures, $\sigma(0) = 9.2 \times 10^{-3} \Omega^{-1}$ and it drops down with rising temperature. In the temperature window from 100 to 160 K, no conductivities can be assigned. The temperature dependence of the band gap results in a gap closing in this region, and the transition from a topological to a trivial QW occurs (Supporting Information). For the large area sample used in this work, spatial

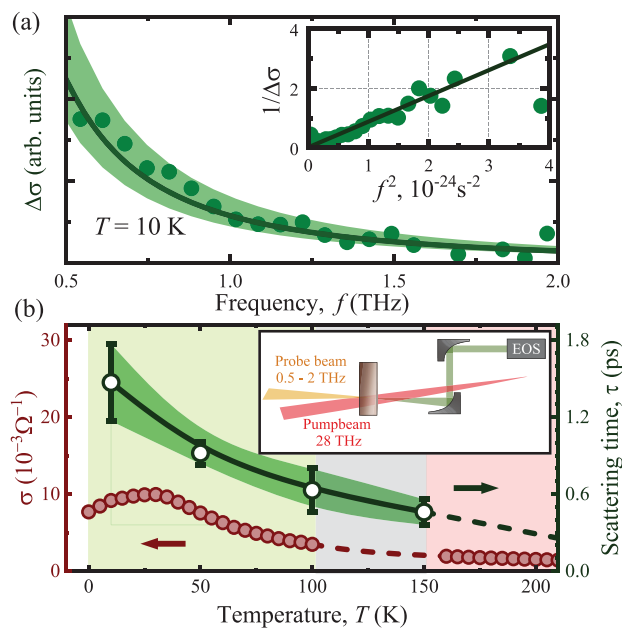


Figure 2. Linear response of an HgTe 2D TI. (a) The real part of the pump-induced change in the THz conductivity $\Delta\sigma(\omega = 2\pi f)$ is obtained from FFT of the time-domain signals. A Drude-type fit to eq 7 is shown by the solid line. The inset represents the same dependence in other coordinates $\frac{1}{\Delta\sigma}(f^2)$. (b) Temperature dependence of the scattering time τ obtained from the Drude fit (right axis) and the conductivity $\sigma(0)$ obtained from Hall measurements (left axis). The solid line is a polynomial interpolation of the experimental data for the scattering time. The dashed line is an extrapolation (interpolation) of the experimental data for the scattering time (conductivity). The inset shows a schematic representation of the pump–probe measurements. The distinct color zones in the figure represent different states of the HgTe quantum well (QW). The green zone corresponds to the topological state, the gray zone indicates an inhomogeneous transition region, and the red zone represents the trivial state.

inhomogeneities give rise to temperature-dependent percolation paths for the metallic regions upon band closing. In the transport measurements, this manifests as a strong coupling of the transverse and longitudinal conductance and the concept of sheet conductivity is not applicable to the sample as a whole. We, therefore, refrain from analyzing this temperature region.

We then estimate the scattering time from the conductivity and carrier concentration using eq 7 and calculate dispersion for the corresponding temperature. We obtain $\tau \approx 3.2$ and 0.5 ps at $T = 10$ and 200 K, respectively. At high temperatures, these values agree within error bars with the direct THz time-domain measurement of τ in Figure 2b, which is suggestive of the fact that the same microscopic mechanism applies. This is very likely scattering by phonons. The difference in τ at low temperatures stems from the fact that the THz-pump also results in a heating of the electron reservoir,^{36,37} which reduces the scattering time with respect to the cold electron bath in the transport measurement. For the evaluation of the THG, we therefore use the τ obtained by the pump–probe method for the remainder of this work.

Third Harmonic Generation. The experimental setup for the detection of THz nonlinearity is schematically presented in Figure 3a. We use intense pump pulses at $f = 0.5$ THz generated by tilted-wavefront optical rectification from a

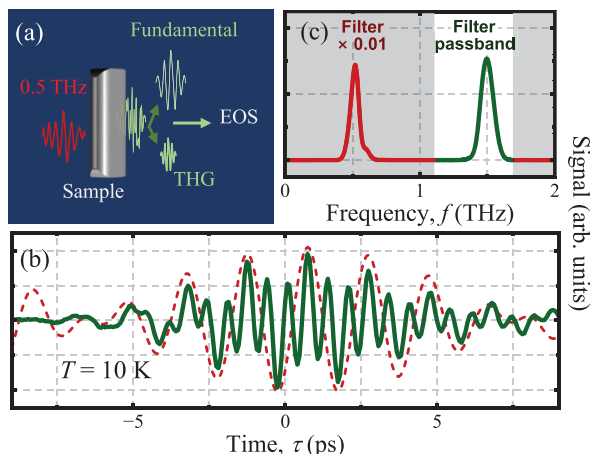


Figure 3. THG in a HgTe 2D TI. (a) Experimental scheme: the nonlinear interaction of a 10 ps long THz pulse at $f = 0.5$ THz with a 2D TI leads to THG. (b) The solid and dashed lines represent time-domain dynamics of the THz field transmitted through the sample with the HgTe QW and only the substrate, respectively. A bandpass filter at $3f \approx 1.5$ THz is used to suppress the fundamental harmonic amplitude by a factor of 100 for direct comparison with the third harmonic. (c) FFT of the time-domain THz signals shows the fundamental harmonic at 0.5 THz and the third harmonic at 1.5 THz. The green curve is located in the filter passband and the red curve is suppressed by ≈ 100 times.

LiNbO₃ crystal pumped with a femtosecond Ti:sapphire amplifier with a repetition rate of 1 kHz. A bandpass filter with a central frequency of 1.5 THz and 20% bandwidth suppresses the fundamental harmonic by a factor of 100, allowing selective detection of the third harmonic.

We use electro-optical sampling (EOS) to detect the time evolution of the THz field (Supporting Information). The time-domain signal after transmission through the sample at $T = 10$ K and a bandpass filter are shown in Figure 3b. It clearly contains the fundamental and third harmonics (solid line). For reference, we also measure transmission through the substrate without HgTe QW and observe only the fundamental harmonic (dashed line). An FFT spectrum of the transmitted signal is presented in Figure 3c. Indeed, it shows distinct peaks at 0.5 (fundamental) and 1.5 THz (THG). We then calculate the THG efficiency as the ratio of the areas under these peaks, taking into account the transmission spectrum of the bandpass filter. We obtain $\kappa = 0.7\%$ for Figure 3c.

DISCUSSION

To calculate the THG efficiency $\kappa = |E_{3\omega}|/|E_{\omega}|$ using eq 9, it is necessary to know all of the parameters involved. However, it should be noted that this calculation does not take into account the potential loss of power due to factors such as refraction in buffer layers. Thus, the effective field strength E_i used in the calculation may be smaller than the expected value of 60 kV/cm. To reconcile the theoretical prediction with experimental results regarding the fluence dependence of the THG efficiency at a temperature of 10 K, the incident THz field strength should be adjusted to a lower value of 42 kV/cm. This value is used for all other temperatures in our experiments.

We first analyze κ as a function of pulse energy $\xi_i \propto E_i^2$. The experimental data points are listed in Figure 4a. For the highest pulse energy, $\xi_i = 1.5 \mu\text{J}$, we estimate the maximum incident

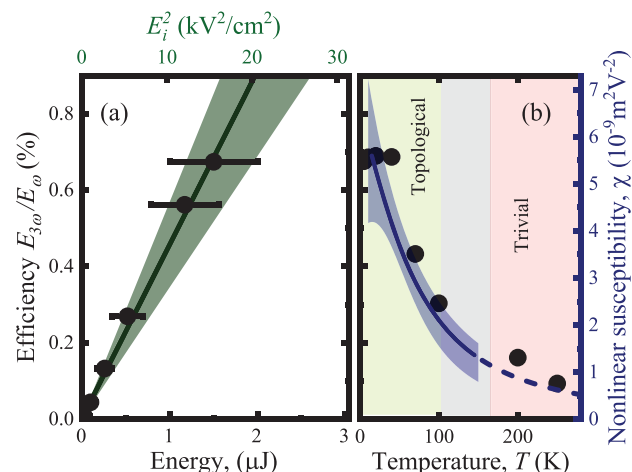


Figure 4. THG efficiency and nonlinear susceptibility. (a) Solid circles are the THG efficiency as a function of the THz pulse energy at $T = 10$ K (lower axis). The solid line is the calculation with eq 9 using relaxation time τ and conductivity σ_0 from independent measurements (upper axis). The shaded area represents the error due to the uncertainty of τ and σ_0 . (b) Temperature dependence of the nonlinear third-order susceptibility $\chi^{(3)}$. Solid circles represent the experimental points. The solid line is the calculation from the THG efficiency using eq 9, as explained in the text. The shaded area represents the error due to the uncertainty of τ and σ_0 . The dashed line is the calculation from the extrapolation of τ to higher temperatures.

THz field, $E_i^{(\text{max})} = 60$ kV/cm (Supporting Information). To compare our experimental data with the acceleration model of eqs 3–9, we calculate κ as shown by the solid line in Figure 4a. For this calculation, we take the scattering time τ and the conductivity σ_0 from Figure 2b. The Fermi wave vector k_F and the nonparabolicity parameter η are obtained from Figure 1c. To do this, we first use eq 7 to determine $\mathcal{E}_{\text{eff}} = \hbar k_F v_F$ from σ_0 and then separate k_F and v_F using Figure 1c. The best agreement with the experimental data is obtained if we assume $E_i^{(\text{max})} = 42$ kV/cm. Here, we use the advanced form of eq 9 as described in Supporting Information. Thus, the field values predicted by the theoretical model and those calculated from the THG experiments are nearly identical. The remaining differences can be attributed to unaccounted power losses and inaccuracies in the experimental setup.

To validate that our THG measurements are performed under conditions for which $E_{3\omega} \propto E_i^3$ or $\kappa \propto E_i^2 \propto \xi_i$, we calculate the characteristic nonlinear THz field E_{nl} using eq 8. We obtain $E_{\text{nl}} = 61$ kV/cm for $T = 10$ K and $E_{\text{nl}} = 70$ kV/cm for $T = 150$ K. Therefore, we have $E_i < E_{\text{nl}}$ and we can safely neglect contributions beyond the third order in the expansion of the equation (Supporting Information) to the third harmonic generation, which is in agreement with the experimental data of Figure 4a.

We obtain the field conversion coefficient at the third harmonic $\gamma d \approx 2.1 \times 10^{-15} \text{ m}^2/\text{V}^2$ assuming $E_i^{(\text{max})} = 42$ kV/cm using the experimental data of Figure 4a. To compare the giant THz nonlinearity in HgTe QWs with other materials, we convert this value to the nonlinear third-order susceptibility $\chi^{(3)}$ (Supporting Information), as shown in Figure 4b. It is $\chi^{(3)} \approx 5 \times 10^{-9} \text{ m}^2/\text{V}^2$ at $T = 10$ K, which is several times higher than the record value reported for graphene.¹ With increasing temperature, it drops to $\chi^{(3)} \approx 3 \times 10^{-10} \text{ m}^2/\text{V}^2$ at $T = 250$ K,

which is mostly caused by a decrease of the scattering time and conductivity with increasing temperature, according to Figure 2b. To ensure consistency, we conduct calculations utilizing the acceleration model. First, we calculate the THG efficiency using eq 9. The temperature dependence of the Fermi–Dirac distribution is considered in our approach when the position of the Fermi energy \mathcal{E}_F (or chemical potential) is determined from the electron concentration using eq 1, as presented in the Supporting Information. In combination with the calculated dispersion of the conduction band for each temperature, it allows the determination of k_F in eq 9. The temperature dependence of DC conductivity σ_0 and scattering time τ are measured separately and presented in Figure 2b. These values are then used in eq 9 to calculate the temperature dependence of the THG efficiency. Subsequently, we determined the nonlinear susceptibility. The results of these calculations are represented by the solid line in Figure 4b. The parameters for this model are obtained from independent measurements at each temperature, and we found very good agreement with the experiment.

CONCLUSION

We observe a giant THz nonlinearity of 2D TIs based on HgTe QWs. It is detected as an extremely efficient THG under the propagation of 0.5 THz pulses. The effective nonlinear third-order susceptibility at cryogenic temperature is several times higher than the record value for solid state, which was reported for graphene,¹ and several orders of magnitude stronger than in other QW structures.^{18,19} The carrier density in our HgTe QW $n_e = 2.8 \times 10^{11} \text{ cm}^{-2}$ is by 1 order of magnitude lower than in the reference graphene sample. Therefore, the nonlinear response $\chi^{(3)}$ per charge carrier is higher than in graphene¹ and silicon.¹⁴ As a consequence, we are able to observe THG even for incident fields $E_i < 10 \text{ kV/cm}$. Further improvement can be realized using multiple QWs, metamaterials^{7,9} and topological photonic structures.³⁸ Our findings can be applied for on-chip optoelectronics and communication.

ASSOCIATED CONTENT

Supporting Information

The Supporting Information is available free of charge at <https://pubs.acs.org/doi/10.1021/acsphotonics.3c00867>.

A theoretical model for THG; THG efficiency; Experimental methods; Calculation; Band structure (PDF)

AUTHOR INFORMATION

Corresponding Authors

Tatiana A. Uaman Svetikova – Helmholtz-Zentrum Dresden-Rossendorf, 01328 Dresden, Germany; Technische Universität Dresden, 01062 Dresden, Germany; Email: t.uaman-svetikova@hzdr.de

Sergey Kovalev – Helmholtz-Zentrum Dresden-Rossendorf, 01328 Dresden, Germany; orcid.org/0000-0002-2290-1016; Email: s.kovalev@hzdr.de

Georgiy V. Astakhov – Helmholtz-Zentrum Dresden-Rossendorf, 01328 Dresden, Germany; orcid.org/0000-0003-1807-3534; Email: g.astakhov@hzdr.de

Authors

Thales V. A. G. de Oliveira – Helmholtz-Zentrum Dresden-Rossendorf, 01328 Dresden, Germany; orcid.org/0000-0002-4886-0654

Alexej Pashkin – Helmholtz-Zentrum Dresden-Rossendorf, 01328 Dresden, Germany

Alexey Ponomaryov – Helmholtz-Zentrum Dresden-Rossendorf, 01328 Dresden, Germany

Christian Berger – Physikalisches Institut (EP3), Universität Würzburg, 97074 Würzburg, Germany

Lena Fürst – Physikalisches Institut (EP3), Universität Würzburg, 97074 Würzburg, Germany

Florian B. Bayer – Physikalisches Institut (EP3), Universität Würzburg, 97074 Würzburg, Germany

Elena G. Novik – Technische Universität Dresden, 01062 Dresden, Germany

Hartmut Buhmann – Physikalisches Institut (EP3), Universität Würzburg, 97074 Würzburg, Germany

Laurens W. Molenkamp – Physikalisches Institut (EP3), Universität Würzburg, 97074 Würzburg, Germany; orcid.org/0000-0003-4833-5179

Manfred Helm – Helmholtz-Zentrum Dresden-Rossendorf, 01328 Dresden, Germany; Technische Universität Dresden, 01062 Dresden, Germany

Tobias Kiessling – Physikalisches Institut, Universität Würzburg, 97074 Würzburg, Germany

Stephan Winnerl – Helmholtz-Zentrum Dresden-Rossendorf, 01328 Dresden, Germany

Complete contact information is available at:

<https://pubs.acs.org/doi/10.1021/acsphotonics.3c00867>

Funding

T.A.U.S., T.K., L.W.M., and G.V.A. acknowledge financial support from the Würzburg-Dresden Cluster of Excellence on Complexity and Topology in Quantum Matter (EXC 2147, DFG project ID 390858490). C.B., L.F., F.B.B., H.B., L.W.M., and T.K. acknowledge financial support by the SFB1170 (DFG project ID 258499086).

Notes

The authors declare no competing financial interest.

ACKNOWLEDGMENTS

The authors thank S. A. Tarasenko for stimulating discussions on the theoretical approach. We would like to thank P. Michel and the FELBE/TELBE teams for support. Parts of this research were carried out at ELBE at the Helmholtz-Zentrum Dresden - Rossendorf e. V., a member of the Helmholtz Association.

REFERENCES

- (1) Hafez, H. A.; Kovalev, S.; Deinert, J.-C.; Mics, Z.; Green, B.; Awari, N.; Chen, M.; Germanskiy, S.; Lehnert, U.; Teichert, J.; et al. Extremely efficient terahertz high-harmonic generation in graphene by hot Dirac fermions. *Nature* **2018**, *561*, 507–511.
- (2) Arshad, A.; Koyun, H. N.; Salikhov, R.; Gensch, M.; Ilyakov, I.; Ponomaryov, A.; Prajapati, G. L.; de Oliveira, T. V. A. G.; Mavridou, K.; Lindner, J.; Deinert, J.-C.; Unl u, C. G.; Kovalev, S. Terahertz Harmonic Generation from Graphite Pencil Drawings. *Advanced Photonics Research* **2023**, *4*, No. 2300088.
- (3) Chu, H.; et al. Fano interference between collective modes in cuprate high-Tc superconductors. *Nat. Commun.* **2023**, *14*, 1343.
- (4) Kovalev, S.; Dantas, R. M. A.; Germanskiy, S.; Deinert, J.-C.; Green, B.; Ilyakov, I.; Awari, N.; Chen, M.; Bawatna, M.; Ling, J.; Xiu,

- F.; van Loosdrecht, P. H. M.; Surówka, P.; Oka, T.; Wang, Z. Non-perturbative terahertz high-harmonic generation in the three-dimensional Dirac semimetal Cd_3As_2 . *Nat. Commun.* **2020**, *11*, 2451.
- (5) Cheng, B.; Kanda, N.; Ikeda, T. N.; Matsuda, T.; Xia, P.; Schumann, T.; Stemmer, S.; Itatani, J.; Armitage, N. P.; Matsunaga, R. Efficient Terahertz Harmonic Generation with Coherent Acceleration of Electrons in the Dirac Semimetal Cd_3As_2 . *Phys. Rev. Lett.* **2020**, *124*, No. 117402.
- (6) Giorgianni, F.; et al. Strong nonlinear terahertz response induced by Dirac surface states in Bi_2Se_3 topological insulator. *Nat. Commun.* **2016**, *7*, No. 11421.
- (7) Tielrooij, K.-J.; et al. Milliwatt terahertz harmonic generation from topological insulator metamaterials. *Light: Science & Applications* **2022**, *11*, 315.
- (8) Kovalev, S.; et al. Electrical tunability of terahertz nonlinearity in graphene. *Science Advances* **2021**, *7*, No. eabf9809.
- (9) Deinert, J.-C.; et al. Grating-Graphene Metamaterial as a Platform for Terahertz Nonlinear Photonics. *ACS Nano* **2021**, *15*, 1145–1154.
- (10) Mikhailov, S. A. Non-linear electromagnetic response of graphene. *Europhys. Lett.* **2007**, *79*, No. 27002.
- (11) Al-Naib, I.; Poschmann, M.; Dignam, M. M. Optimizing third-harmonic generation at terahertz frequencies in graphene. *Phys. Rev. B* **2015**, *91*, No. 205407.
- (12) Navaeipour, P.; Dignam, M. M. Effects of microscopic scattering on terahertz third harmonic generation in monolayer graphene. *Phys. Rev. B* **2022**, *105*, No. 11431.
- (13) Mics, Z.; Tielrooij, K.-J.; Parvez, K.; Jensen, S. A.; Ivanov, I.; Feng, X.; Müllen, K.; Bonn, M.; Turchinovich, D. Thermodynamic picture of ultrafast charge transport in graphene. *Nat. Commun.* **2015**, *6*, 7655.
- (14) Meng, F.; Thomson, M. D.; ul Islam, Q.; Klug, B.; Pashkin, A.; Schneider, H.; Roskos, H. G. Intracavity third-harmonic generation in Si:B pumped by intense terahertz pulses. *Phys. Rev. B* **2020**, *102*, No. 075205.
- (15) Meng, F.; Walla, F.; Kovalev, S.; Deinert, J.-C.; Ilyakov, I.; Chen, M.; Ponomaryov, A.; Pavlov, S. G.; Hubers, H.-W.; Abrosimov, N. V.; Jungemann, C.; Roskos, H. G.; Thomson, M. D. Higher-harmonic generation in boron-doped silicon from band carriers and bound-dopant photoionization. *arXiv.2303.01564* **2023**, na.
- (16) Dessmann, N.; Le, N. H.; Eless, V.; Chick, S.; Saeedi, K.; Perez-Delgado, A.; Pavlov, S. G.; van der Meer, A. F.; Litvinenko, K. L.; Galbraith, I.; et al. Highly efficient THz four-wave mixing in doped silicon. *Light: Sci. Appl.* **2021**, *10*, 71.
- (17) Seidl, A.; Anvari, R.; Dignam, M. M.; Richter, P.; Seyller, T.; Schneider, H.; Helm, M.; Winnerl, S. Pump-induced terahertz anisotropy in bilayer graphene. *Phys. Rev. B* **2022**, *105*, No. 085404.
- (18) Markelz, A. G.; Gwinn, E. G. Nonlinear response of quantum-confined electrons in nonparabolic subbands. *J. Appl. Phys.* **1996**, *80*, 2533–2535.
- (19) Sirtori, C.; Capasso, F.; Sivco, D. L.; Cho, A. Y. Giant, triply resonant, third-order nonlinear susceptibility $\chi^{(3)}$ in coupled quantum wells. *Phys. Rev. Lett.* **1992**, *68*, 1010–1013.
- (20) König, M.; Wiedmann, S.; Brüne, C.; Roth, A.; Buhmann, H.; Molenkamp, L. W.; Qi, X.-L.; Zhang, S.-C. Quantum Spin Hall Insulator State in HgTe Quantum Wells. *Science* **2007**, *318*, 766–770.
- (21) Shuvaev, A. M.; Astakhov, G. V.; Brüne, C.; Buhmann, H.; Molenkamp, L. W.; Pimenov, A. Terahertz magneto-optical spectroscopy in HgTe thin films. *Semicond. Sci. Technol.* **2012**, *27*, No. 124004.
- (22) Hancock, J. N.; van Mechelen, J. L. M.; Kuzmenko, A. B.; van der Marel, D.; Brüne, C.; Novik, E. G.; Astakhov, G. V.; Buhmann, H.; Molenkamp, L. W. Surface State Charge Dynamics of a High-Mobility Three-Dimensional Topological Insulator. *Phys. Rev. Lett.* **2011**, *107*, No. 136803.
- (23) Dantscher, K.; Kozlov, D. A.; Scherr, M. T.; Gebert, S.; Bärenfänger, J.; Durnev, M. V.; Tarasenko, S. A.; Bel'kov, V. V.; Mikhailov, N. N.; Dvoretzky, S. A.; Kvon, Z. D.; Ziegler, J.; Weiss, D.; Ganichev, S. D. Photogalvanic probing of helical edge channels in two-dimensional HgTe topological insulators. *Phys. Rev. B* **2017**, *95*, No. 201103.
- (24) Shuvaev, A. M.; Astakhov, G. V.; Pimenov, A.; Brüne, C.; Buhmann, H.; Molenkamp, L. W. Giant Magneto-Optical Faraday Effect in HgTe Thin Films in the Terahertz Spectral Range. *Phys. Rev. Lett.* **2011**, *106*, No. 107404.
- (25) Gebert, S.; et al. Terahertz cyclotron emission from two-dimensional Dirac fermions. *Nat. Photonics* **2023**, *17*, 244–249.
- (26) Novik, E. G.; Pfeuffer-Jeschke, A.; Jungwirth, T.; Latussek, V.; Becker, C. R.; Landwehr, G.; Buhmann, H.; Molenkamp, L. W. Band structure of semimagnetic $\text{Hg}_{1-x}\text{Mn}_x\text{Te}$ quantum wells. *Phys. Rev. B* **2005**, *72*, No. 035321.
- (27) Bendias, K.; Shamim, S.; Herrmann, O.; Budewitz, A.; Shekhar, P.; Leubner, P.; Kleinlein, J.; Bocquillon, E.; Buhmann, H.; Molenkamp, L. W. High Mobility HgTe Microstructures for Quantum Spin Hall Studies. *Nano Lett.* **2018**, *18*, 4831–4836.
- (28) Bernevig, B. A.; Hughes, T. L.; Zhang, S.-C. Quantum spin Hall effect and topological phase transition in HgTe quantum wells. *Science* **2006**, *314*, 1757–1761.
- (29) Burt, M. G. Fundamentals of envelope function theory for electronic states and photonic modes in nanostructures. *J. Phys.: Condens. Matter* **1999**, *11*, 53.
- (30) Laurenti, J. P.; Camassel, J.; Bouhemadou, A.; Toulouse, B.; Legros, R.; Lussion, A. Temperature dependence of the fundamental absorption edge of mercury cadmium telluride. *J. Appl. Phys.* **1990**, *67*, 6454–6460.
- (31) Bir, G. L.; Pikus, G. E. *Symmetry and Strain-Induced Effects in Semiconductors*; Wiley: New York, 1974.
- (32) Tomaino, J. L.; Jameson, A. D.; Kevek, J. W.; Paul, M. J.; van der Zande, A. M.; Barton, R. A.; McEuen, P. L.; Minot, E. D.; Lee, Y.-S. Terahertz imaging and spectroscopy of large-area single-layer graphene. *Opt. Express* **2011**, *19*, 141.
- (33) Tinkham, M. Energy gap interpretation of experiments on infrared transmission through superconducting films. *Phys. Rev.* **1956**, *104*, 845.
- (34) Helm, M.; Winnerl, S.; Pashkin, A.; Klopff, J.; Deinert, J.-C.; Kovalev, S.; Evtushenko, P.; Lehnert, U.; Xiang, R.; Arnold, A.; et al. The ELBE infrared and THz facility at Helmholtz-Zentrum Dresden-Rossendorf. *Eur. Phys. J. Plus* **2023**, *138*, 158.
- (35) Joyce, H. J.; Boland, J. L.; Davies, C. L.; Baig, S. A.; Johnston, M. B. A review of the electrical properties of semiconductor nanowires: insights gained from terahertz conductivity spectroscopy. *Semicond. Sci. Technol.* **2016**, *31*, No. 103003.
- (36) Ulbrich, R. Energy relaxation of photoexcited hot electrons in GaAs. *Phys. Rev. B* **1973**, *8*, 5719.
- (37) Kiessling, T.; Quast, J.-H.; Kreisel, A.; Henn, T.; Ossau, W.; Molenkamp, L. Spatially resolved photocarrier energy relaxation in low-doped bulk GaAs. *Phys. Rev. B* **2012**, *86*, No. 161201.
- (38) Yang, Y.; Yamagami, Y.; Yu, X.; Pitchappa, P.; Webber, J.; Zhang, B.; Fujita, M.; Nagatsuma, T.; Singh, R. Terahertz topological photonics for on-chip communication. *Nat. Photonics* **2020**, *14*, 446–451.

Atom counting with accelerator mass spectrometry

Walter Kutschera^{*}

*Faculty of Physics—Isotope Physics, University of Vienna,
Vienna Environmental Research Accelerator (VERA),
Waehringstrasse 17, A-1090 Vienna, Austria*

A. J. Timothy Jull

*Geosciences and Physics, University of Arizona, Tucson, Arizona 85721-0077, USA
and Isotope Climatology and Environmental Research Centre (ICER),
Institute for Nuclear Research, 4026 Debrecen, Hungary*

Michael Paul

Racah Institute of Physics, The Hebrew University of Jerusalem, Jerusalem 91904, Israel

Anton Wallner

*Accelerator Mass Spectrometry and Isotope Research,
Helmholtz-Zentrum Dresden-Rossendorf,
Institute of Ion Beam Physics and Materials Research,
Bautzner Landstrasse 400, D-01328 Dresden, Germany
and Institute of Nuclear and Particle Physics, Technische Universität Dresden,
D-01062 Dresden, Germany*

(published 28 September 2023)

Accelerator mass spectrometry (AMS) was born in the late 1970s, when it was realized at nuclear physics laboratories that the accelerator systems can be used as a sensitive mass spectrometer to measure ultralow traces of long-lived radioisotopes. It soon became possible to measure radioisotope-to-stable-isotope ratios in the range from 10^{-12} to 10^{-16} by counting the radioisotope ions “atom by atom” and comparing the count rate with ion currents of stable isotopes ($1.6 \mu\text{A} = 1 \times 10^{13}$ singly charged ions/s). It turned out that electrostatic tandem accelerators are best suited for this, and there are now worldwide about 160 AMS facilities based on this principle. This review presents the history, technological developments, and research areas of AMS through the 45 yr since its discovery. Many different fields are touched by AMS measurements, including archaeology, astrophysics, atmospheric science, biology, climatology, cosmic-ray physics, environmental physics, forensic science, glaciology, geophysics, hydrology, ice core research, meteoritics, nuclear physics, oceanography, and particle physics. Since it is virtually impossible to discuss all fields in detail in this review, only specific fields with recent advances are highlighted in detail. For the others, an effort is made to provide relevant references for in-depth studies of the respective fields.

DOI: [10.1103/RevModPhys.95.035006](https://doi.org/10.1103/RevModPhys.95.035006)

CONTENTS

I. Introduction	2	III. Wide-Ranging Research Areas of AMS	25
A. History	2	A. Archaeology	25
B. Long-lived radionuclides	4	B. Biological research	27
II. Technical Aspects of AMS	6	C. Atmospheric science	29
A. Isotopic ratios: General principle of AMS measurements	6	D. Oceanographic and hydrospheric research	31
B. The choice of accelerator	7	E. Cryospheric research	32
C. Negative-ion sources and sample preparation	8	F. Lithospheric research	33
D. Background suppression	9	G. Anthropogenic radionuclides	33
E. Radionuclide detection and background identification	14	IV. Nuclear Physics and Astrophysics	34
F. AMS with positive ions and a heavy-ion linear accelerator	15	A. Nuclear physics	34
G. ATTA: An alternative method of atom counting	17	B. Astrophysics	37
H. Worldwide AMS facilities	18	C. Extraterrestrial matter	44
		V. Concluding Remarks	45
		List of Symbols and Abbreviations	46
		Acknowledgments	48
		References	48

^{*}Corresponding author: walter.kutschera@univie.ac.at

Roadmap for focused ion beam technologies

Cite as: Appl. Phys. Rev. **10**, 041311 (2023); doi: [10.1063/5.0162597](https://doi.org/10.1063/5.0162597)

Submitted: 15 June 2023 · Accepted: 13 October 2023 ·

Published Online: 26 December 2023 · Corrected: 26 January 2024

Katja Höflich,^{1,a)}  Gerhard Hobler,^{2,a)}  Frances I. Allen,^{3,a)}  Tom Wirtz,^{4,a)}  Gemma Rius,^{5,a)} 
 Lisa McElwee-White,⁶  Arkady V. Krasheninnikov,⁷  Matthias Schmidt,⁸  Ivo Utke,⁹  Nico Klingner,⁷ 
 Markus Osenberg,¹⁰  Rosa Córdoba,¹¹  Flyura Djurabekova,¹²  Ingo Manke,¹⁰  Philip Moll,¹³ 
 Mariachiara Manoccio,¹⁴  José María De Teresa,¹⁵  Lothar Bischoff,⁷  Johann Michler,⁹  Olivier De Castro,⁴ 
 Anne Delobbe,¹⁶  Peter Dunne,¹⁷  Oleksandr V. Dobrovolskiy,¹⁸  Natalie Frese,¹⁹  Armin Götzhäuser,¹⁹ 
 Paul Mazarov,²⁰  Dieter Koelle,²¹  Wolfhard Möller,⁷  Francesc Pérez-Murano,⁵  Patrick Philipp,⁴ 
 Florian Vollnhals,²²  and Gregor Hlawacek^{7,a)} 

AFFILIATIONS

¹Ferdinand-Braun-Institut gGmbH, Leibniz-Institut für Höchstfrequenztechnik, 12489 Berlin, Germany

²Institute of Solid-State Electronics, TU Wien, 1040 Vienna, Austria

³Department of Materials Science and Engineering, University of California, Berkeley, California 94720, USA

⁴Advanced Instrumentation for Nano-Analytics (AINA), MRT Department, Luxembourg Institute of Science and Technology (LIST), 4422 Belvaux, Luxembourg

⁵Institute of Microelectronics of Barcelona, IMB-CNM-CSIC, 08193 Cerdanyola del Vallès, Spain

⁶Department of Chemistry, University of Florida, Gainesville, Florida 32611-7200, USA

⁷Institute of Ion Beam Physics and Materials Research, Helmholtz-Zentrum Dresden-Rossendorf, 01328 Dresden, Germany

⁸Department of Isotope Biogeochemistry, Helmholtz-Centre for Environmental Research GmbH—UFZ, 04318 Leipzig, Germany

⁹Laboratory for Mechanics of Materials and Nanostructures, EMPA Swiss Federal Laboratories for Material Science and Technology, CH 3602 Thun, Switzerland

¹⁰Institute of Applied Materials, Helmholtz-Zentrum Berlin für Materialien und Energie, 14109 Berlin, Germany

¹¹Institute of Molecular Science, University of Valencia, 46980 Paterna, Spain

¹²Department of Physics, Helsinki Institute of Physics, University of Helsinki, 00014 Helsinki, Finland

¹³Max Planck Institute for the Structure and Dynamics of Matter, 22607 Hamburg, Germany

¹⁴CNR-NANOTEC Institute of Nanotechnology, 73100 Lecce, Italy

¹⁵Instituto de Nanociencia y Materiales de Aragón (INMA), Universidad de Zaragoza-CSIC, 50009 Zaragoza, Spain

¹⁶Orsay Physics S. A., 13710 Fuveau, France

¹⁷Université de Strasbourg, CNRS, IPCMS UMR 7504, 67034 Strasbourg, France

¹⁸Faculty of Physics, University of Vienna, 1090 Vienna, Austria

¹⁹Faculty of Physics, Physics of Supramolecular Systems, University of Bielefeld, 33615 Bielefeld, Germany

²⁰Raith GmbH, 44263 Dortmund, Germany

²¹Physikalisches Institut, Center for Quantum Science (CQ) and LISA⁺, Universität Tübingen, 72076 Tübingen, Germany

²²Institute for Nanotechnology and Correlative Microscopy gGmbH, 91301 Forchheim, Germany

^{a)}Authors to whom correspondence should be addressed: katja.hoeflich@fbh-berlin.de; gerhard.hobler@tuwien.ac.at; francesal-len@berkeley.edu; tom.wirtz@list.lu; gemma.rius@csic.es; and g.hlawacek@hzdr.de

ABSTRACT

The focused ion beam (FIB) is a powerful tool for fabrication, modification, and characterization of materials down to the nanoscale. Starting with the gallium FIB, which was originally intended for photomask repair in the semiconductor industry, there are now many different types

of FIB that are commercially available. These instruments use a range of ion species and are applied broadly in materials science, physics, chemistry, biology, medicine, and even archaeology. The goal of this roadmap is to provide an overview of FIB instrumentation, theory, techniques, and applications. By viewing FIB developments through the lens of various research communities, we aim to identify future pathways for ion source and instrumentation development, as well as emerging applications and opportunities for improved understanding of the complex interplay of ion–solid interactions. We intend to provide a guide for all scientists in the field that identifies common research interest and will support future fruitful interactions connecting tool development, experiment, and theory. While a comprehensive overview of the field is sought, it is not possible to cover all research related to FIB technologies in detail. We give examples of specific projects within the broader context, referencing original works and previous review articles throughout.

© 2023 Author(s). All article content, except where otherwise noted, is licensed under a Creative Commons Attribution (CC BY) license (<http://creativecommons.org/licenses/by/4.0/>). <https://doi.org/10.1063/5.0162597>

TABLE OF CONTENTS




I. INTRODUCTION.....	4	6. Study of irradiation damage mechanisms.....	34
II. INSTRUMENTATION.....	4	7. Outlook.....	35
A. Ion sources.....	4	C. FIB-based imaging and tomography.....	35
B. Beam transport.....	6	1. A brief history of FIB-based imaging and analysis.....	35
C. Analytical tools and detectors.....	8	2. HIM—A tool for imaging of the tiniest living objects.....	37
D. Other FIB accessories.....	10	3. FIB tomography in the life sciences.....	38
E. FIB processing of radioactive samples.....	10	4. FIB tomography of energy materials.....	40
F. Software and correlative approaches.....	11	5. Data processing of FIB tomographies.....	40
III. SIMULATION APPROACHES FOR FIB PROCESSING.....	12	6. Outlook.....	41
A. Simulation techniques based on the binary collision approximation (BCA).....	13	D. Elemental analysis using FIB-SIMS.....	41
1. Principles and limitations.....	13	1. Overview.....	41
2. Specific BCA codes.....	14	2. FIB-SIMS in materials science.....	41
3. BCA-based simulations of FIB processing.....	14	3. FIB-SIMS in the life sciences.....	42
B. Molecular dynamics and molecular statics.....	15	4. Outlook.....	42
1. Principles and simulation codes.....	15	E. Applications of gas-assisted FIB processing.....	43
2. Models for the potential energy function.....	16	1. Basics of ion induced chemistry.....	43
3. Applications of molecular dynamics to FIB irradiation.....	18	2. FIBID nanostructures for electronics.....	45
4. Limitations and extensions.....	19	3. FIBID nanostructures for mechanics.....	46
C. Kinetic Monte Carlo (kMC).....	20	4. FIBID nanostructures for photonics and plasmonics.....	47
D. Continuum modeling.....	20	5. Outlook.....	47
1. Ion implantation and milling.....	20	F. Novel and unconventional approaches in FIB processing.....	48
2. Gas-assisted deposition and etching.....	21	1. Resist patterning by FIB.....	48
3. Applications to FIB processing.....	23	2. Cryo-FIBID.....	49
IV. APPLICATIONS OF FOCUSED ION BEAMS.....	24	3. FIB irradiation of metalorganic spin-coated layers.....	49
A. Applications of subtractive FIB processing.....	25	4. FIB induced mass transport.....	50
1. FIB for materials science.....	25	5. Hybrid fabrication and heterogeneous integration.....	50
2. FIB for mechanical testing.....	25	6. Outlook.....	51
3. FIB in the semiconductor industry.....	27	V. ROADMAP.....	51
4. FIB for quantum materials.....	28	A. Drivers for future applications.....	51
5. FIB for photonics and plasmonics.....	28	B. The generic needs of the community.....	53
6. FIB fabrication of custom probes.....	29	C. Important future developments.....	55
7. Outlook.....	30	1. Ion beam generation and transport.....	55
B. Engineering materials properties through defects.....	30	2. Accessories and complementary instrumentation.....	56
1. Basics of irradiation induced defect creation.....	30	3. Automation and data management.....	59
2. Engineering electronic properties.....	31	4. Process modeling.....	61
3. Engineering magnetic properties.....	31	VI. EXECUTIVE SUMMARY AND PERSPECTIVE.....	62
4. Engineering optical/quantum properties.....	31		
5. Engineering of low-dimensional materials.....	34		

Band-to-band tunneling switches based on two-dimensional van der Waals heterojunctions

Cite as: Appl. Phys. Rev. **10**, 011318 (2023); doi: [10.1063/5.0130930](https://doi.org/10.1063/5.0130930)

Submitted: 16 October 2022 · Accepted: 8 March 2023 ·

Published Online: 23 March 2023

Phanish Chava,^{1,2,a)}  Zahra Fekri,¹  Yagnika Vekariya,¹  Thomas Mikolajick,^{2,3}  and Artur Erbe^{1,2} 

AFFILIATIONS

¹Helmholtz Zentrum Dresden-Rossendorf, Bautzner Landstrasse 400, 01328 Dresden, Germany

²Faculty of Electrical and Computer Engineering, Technische Universität Dresden, 01062 Dresden, Germany

³NaMLab gGmbH, 01187 Dresden, Germany

^{a)}Author to whom correspondence should be addressed: p.chava@hzdr.de

ABSTRACT

Quantum mechanical band-to-band tunneling is a type of carrier injection mechanism that is responsible for the electronic transport in devices like tunnel field effect transistors (TFETs), which hold great promise in reducing the subthreshold swing below the Boltzmann limit. This allows scaling down the operating voltage and the off-state leakage current at the same time, and thus reducing the power consumption of metal oxide semiconductor transistors. Conventional group IV or compound semiconductor materials suffer from interface and bulk traps, which hinder the device performance because of the increased trap-induced parasitics. Alternatives like two-dimensional materials (2DMs) are beneficial for realizing such devices due to their ultra-thin body and atomically sharp interfaces with van der Waals interactions, which significantly reduce the trap density, compared to their bulk counterparts, and hold the promise to finally achieve the desired low-voltage operation. In this review, we summarize the recent progress on such devices, with a major focus on heterojunctions made of different 2DMs. We review different types of emerging device concepts, architectures, and the tunneling mechanisms involved by analytically studying various simulations and experimental devices. We present our detailed perspective on the current developments, major roadblocks, and key strategies for further improvements of the TFET technology based on 2D heterojunctions to match industry requirements. The main goal of this paper is to introduce the reader to the concept of tunneling especially in van der Waals devices and provide an overview of the recent progress and challenges in the field.

Published under an exclusive license by AIP Publishing. <https://doi.org/10.1063/5.0130930>

TABLE OF CONTENTS

I. INTRODUCTION	1	A. 2D materials and band alignments	9
II. BAND-TO-BAND TUNNELING	2	B. Modeling van der Waals TFETs	9
A. The tunnel diode	2	1. Bardeen's transfer Hamiltonian model	9
B. Parasitic transport mechanisms	3	2. Non-equilibrium Green's function formalism ..	10
1. Shockley-Reed-Hall generation/recombination	3	C. Device simulations	10
2. Trap-assisted tunneling (TAT)	3	D. Experimental devices	12
III. TUNNEL FIELD EFFECT TRANSISTOR	4	V. BENCHMARKING	17
A. Basic structure and operating principles	4	A. Performance targets	17
B. Homojunction vs heterojunction	5	B. Simulations vs experiments	18
C. Effect of dimensionality	6	VI. CHALLENGES FOR 2D-2D HETEROJUNCTION	
D. Figures of merit and parameter extraction	7	TFETs	19
1. Subthreshold swing	7	A. Contact resistance and Schottky barriers	19
2. Current-based metrics	8	B. Fabrication issues	20
IV. 2D-2D HETEROJUNCTION TFETs	8	C. Gate dielectric and passivation layers	20
		VII. CONCLUSION	21

Statistics

5 μm

Image: HZDR / V. Iurchuk

User facilities and services

Ion Beam Center (IBC)

The Ion Beam Center (IBC) at HZDR combines various machines (electrostatic accelerators, ion implanters, low-energy and focused ion beam systems) into a unique facility used for ion beam modification and ion beam analysis of materials. The available energy range spans from a few eV to 60 MeV with a respective interaction depth in solids between 0.1 nm to 10 μm . In addition to standard broad beams also focused (down to 1 nm) and highly-charged ion beams with charge states up to 45+ are available. In combination with an allocated ion beam experiment, users can also profit from structural analysis (electron microscopy and spectroscopy, X-ray scattering techniques) and sample or device processing under clean-room conditions. At the 6-MV tandem accelerator, the DREAMS (DREsden AMS = accelerator mass spectrometry) facility is used for the determination of long-lived radionuclides, like ^7Be , ^{10}Be , ^{26}Al , ^{36}Cl , ^{41}Ca , ^{55}Fe , ^{129}I , and others. A schematic overview of the IBC including the description of the main beam lines and experimental stations is given on page 67 of this Annual Report. In 2023, about 13,400 beam time hours were delivered for 166 proposals of 136 users from 16 countries worldwide, performing experiments at IBC or using the capabilities for ion beam services.



The IBC has provided ion beam technology as a user and competence center for ion beam applications for more than 30 years. With respect to user beam time hours, the IBC is internationally leading, and has been supported by numerous national and European grants, and by industry.

The research activities cover both ion beam modification and ion beam analysis (IBA), as well as rare isotope detection capabilities (accelerator mass spectrometry, AMS).

The operation of IBC is accompanied by a strong in-house research at the affiliated host “Institute of Ion Beam Physics and Materials Research”, both in experiment and theory. Furthermore, the IBC strongly supports the commercial exploitation of ion beam technologies of partners from industry, which is essential for materials science applications. For ion beam services, the HZDR Innovation GmbH (spin-off of the HZDR) – www.hzdr-innovation.de – provides a direct and fast access to the IBC facilities based on individual contracts.

Recently, a new experimental end station for RBS with highest solid angle has been commissioned at our 6-MV accelerator. The core of this setup consists of 76 Si detectors arranged in 5 concentric rings around the sample. All detectors within one ring have intrinsically the same backscattering angle and their spectra can thus (after proper calibration and binning) be added to one common sum

spectrum. Thus, in the end, the 76 detectors produce only 5 spectra with different scattering angles, with each single detector having a solid angle of 9 msr, yielding in a total solid angle of about 680 msr or 10.8 % of the entire half-sphere for backscattering. The setup enables acquisition of RBS spectra with highest sensitivity and channeling maps on an extraordinary short time scale. Furthermore, our Low-Energy Ion NanoEngineering Facility (LEINEF) has been opened for user access. The aim of this facility is to broaden and advance experiments with ions of low (10 eV) to medium (<500 keV) energy interacting with surfaces and thin layers and to enable new experiments with cluster and hyperthermal ion beams. By using highly charged and cluster ions, the total deposited energy into the solid is extended beyond 10 eV/atom in a depth of only a few nanometers close to the surface leading to material states far from equilibrium. Combined with in-situ preparation and characterization by chemical and structural analysis before, during, and after ion processing, the study of ion induced modifications of surfaces, 2D materials, e.g. graphene, transition metal dichalcogenides (TMDs), and thin films becomes possible without deterioration.

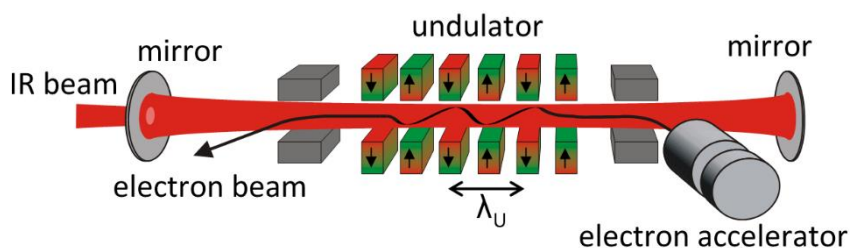
IBC activities are efficiently integrated into various Helmholtz programmes within the research field “Matter”. Since 2013, the IBC has been recognized as a large-scale facility within the “BMBF Verbundforschung” promoting long-term collaborations with universities. In addition, as of 2022 the IBC is coordinating the Horizon Europe project ReMade@ARI (REcyclable MAterials DEvelopment at Analytical Research Infrastructures), which offers comprehensive analytical services for research focusing on the development of new materials for the circular economy. (www.remade-project.eu) ReMade@ARI offers coordinated access to over 50 research infrastructures across Europe, including electron microscopy facilities, synchrotrons, free electron lasers, neutron sources, high magnetic field laboratories and ion or positron beam facilities.

Following the rules of a European and national user facility, access for scientific experiments to IBC is provided on the basis of a proposal procedure (www.hzdr.de/IBC) via the common HZDR user facility portal **HZDR-GATE** (gate.hzdr.de). Due to the availability of multiple machines and versatile instrumentation, IBC proposals can be submitted continuously. The scientific quality of the proposals is evaluated and ranked by an external international User Selection Panel. For successfully evaluated proposals, users get free access to IBC facilities for their experiments. The use of the IBC facilities includes the scientific and technical support during planning, execution, and evaluation of the experiments. For AMS samples preparation, two chemistry laboratories are available.

For more detailed information, please contact Dr. Stefan Facsko (s.facsko@hzdr.de), or Dr. René Heller (r.heller@hzdr.de), for AMS inquiries please refer to Prof. Anton Wallner (a.wallner@hzdr.de), and visit the IBC webpage: www.hzdr.de/IBC.

Free Electron Laser FELBE

FELBE is an acronym for the free-electron laser (FEL) at the Electron Linear accelerator with high Brilliance and low Emittance (ELBE) located at the Helmholtz-Zentrum Dresden-Rossendorf. The heart of ELBE is a superconducting linear accelerator operating in continuous-wave (cw) mode with a pulse repetition rate of 13 MHz. The electron beam (40 MeV, 1 mA max.) is guided to several laboratories where secondary beams (particle and electromagnetic) are generated. Two free-electron lasers (U37-FEL and U100-FEL) produce intense, coherent electromagnetic radiation in the mid and far infrared, which is tunable over a wide wavelength range (5–250 μm) by changing the electron energy or the undulator magnetic field. Main parameters of the infrared radiation produced by FELBE are as follows:



Wavelength λ	5 – 40 μm	FEL with undulator U37
	18 – 250 μm	FEL with undulator U100
Pulse energy	0.1 – 2 μJ	depends on wavelength
Pulse length	1 – 25 ps	depends on wavelength
Repetition rate	13 MHz	3 modes: <ul style="list-style-type: none"> • cw • macropulsed (> 100 μs, < 25 Hz) • single pulsed (Hz ... kHz)

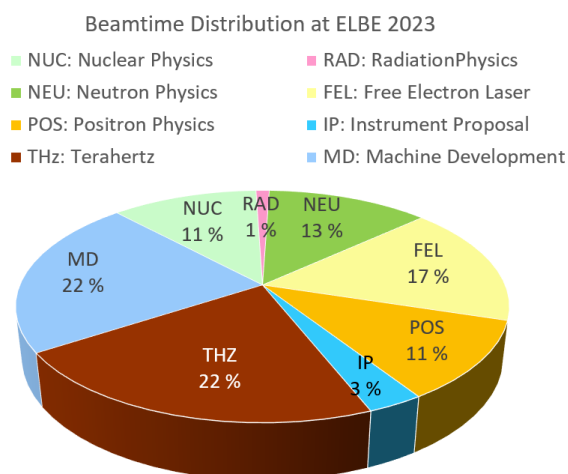
In addition, there is the THz beamline TELBE that is run by the Institute of Radiation Physics. TELBE delivers high-power pulses (up to 10 μJ) in the low THz range (0.1 to 2.5 THz) at a repetition rate of 100 kHz.

Typical applications are picosecond pump-probe spectroscopy (also in combination with several other femtosecond lasers, which are synchronized to the FEL), near-field microscopy, and nonlinear optics. The FELBE facility also serves as a far-infrared source for experiments at the Dresden High Magnetic Field Laboratory (HLD) involving pulsed magnetic fields up to 70 T.

The statistics show that the FEL used about 960 hours of beam time from the ELBE accelerator. This corresponds to 17 % of total beam time, which is again distributed among internal and external users.

For further information, please contact Prof. Manfred Helm (m.helm@hzdr.de) or visit the FELBE webpage www.hzdr.de/FELBE.

ELBE is a user facility and applications for beam time can be submitted twice a year, typically by April 15 and October 15.



Experimental equipment

Accelerators, ion implanters, and other ion processing tools

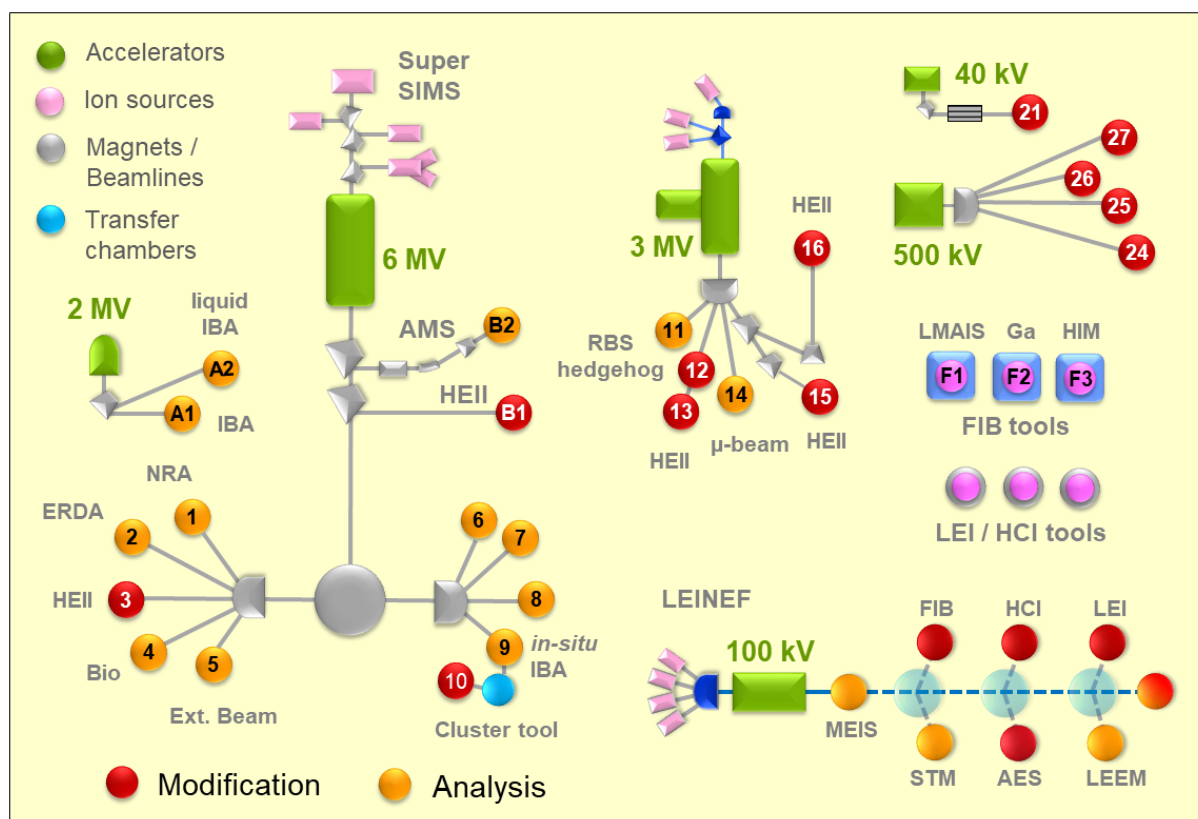
Van de Graaff Accelerator (VdG)	2 MV	TuR Dresden, DE
Tandetron Accelerator (T1)	3 MV	HVEE, NL
Tandetron Accelerator (T2)	6 MV	HVEE, NL
Low-Energy Ion Implanter	40 kV	Danfysik, DK
Low-Energy Ion Platform (LEINEF)	100 kV	HVEE, NL
High-Energy Ion Implanter	500 kV	HVEE, NL
Triple Focused Beam (TIBUSSII)	1 – 30 kV	Orsay Physics, FR
Mass-Separated Focused Ion Beam (FIB)	10 – 30 keV, >10 A/cm ²	Orsay Physics, FR
ORION NanoFab HIM (including GIS, Nanopatterning, TOF-SIMS, μ -manipulators and heater)	He, Ne ions, 5 – 35 keV, Resolution ~ 0.5/1.8 nm	Carl Zeiss Microscopy, DE
ORION PLUS HIM	He ions, 10 – 35 keV, Resolution 0.35 nm	Carl Zeiss Microscopy, DE
ORION PLUS HIM modified for STIM	He ions, 10 – 35 keV, Resolution 0.35 nm	Carl Zeiss Microscopy, DE
Highly-Charged Ion Facility	25 eV – 6 keV \times Q, Q = 1 ... 45 (Xe)	DREEBIT, DE; PREVAC, PL
Surface Modifications by Low-Energy Ion Irradiation	200 – 1200 eV	Home-built
UHV Ion Irradiation (Ar, He, etc.)	0.2 – 5 keV, Scan 10 \times 10 mm ²	Cremer, DE; VG, USA

Ion beam analysis (IBA)

A wide variety of advanced IBA techniques are available at the MV accelerators (see figure).

RBS	Rutherford-Backscattering Spectrometry	(A1), (A2), (5), (9), (11), (14)	VdG, T1, T2, HIM
RBS/C	RBS – Channeling	(A1)	VdG, T1
Liquid-RBS	Liquid Rutherford Backscattering Spectrometry	(A2)	VdG
MEIS	Medium Energy Ion Scattering	MEIS	LEINEF
BIO	(Living) Cell Irradiation	(4)	T2
ERDA	Elastic Recoil Detection Analysis	(2), (9)	T2
PIXE	Particle-Induced X-ray Emission	(A1), (A2), (5), (14)	VdG, T1, T2
PIGE	Particle-Induced gamma Emission	(5), (14)	T1, T2
NRA	Nuclear Reaction Analysis	(1), (14)	T1, T2
NMP	Nuclear Microprobe	(14)	T1

Some stations are equipped with additional process facilities enabling *in-situ* IBA investigations during ion irradiation, sputtering, deposition, annealing, investigations at solid-liquid interfaces, etc.



Schematic overview of the HZDR Ion Beam Center

Accelerator Mass Spectrometry (AMS)

AMS	Accelerator Mass Spectrometry	(B2)	T2
	(focused to long-lived radionuclides: ^7Be , ^{10}Be , ^{26}Al , ^{36}Cl , ^{41}Ca , ^{55}Fe , ^{129}I)		

Other particle-based analytical techniques

SEM	Scanning Electron Microscope (S4800 II)	1 – 30 keV + EDX	Hitachi, JP
TEM	Transmission Electron Microscope (Titan 80-300 with Image Corrector)	80 – 300 keV + EDX, EELS	FEI, NL
TEM	Transmission Electron Microscope (Talos F200X)	20 – 200 keV + SuperX EDX	FEI, NL
FIB/SEM	Focused Ion/Electron Cross Beam (NVision 40)	1 – 30 keV + EDX, EBSD	Carl Zeiss Microscopy, DE
FIB/SEM	Focused Ion/Electron Instrument (Helios 5 CX DualBeam)	0.5 – 30 keV	Thermo Fisher Sci. - FEI, US
AES	Auger Electron Spectroscopy	+ SAM, SEM, XPS, EDX, CL	Scienta Omicron, DE
LEEM	Low-Energy Electron Microscope (Spec-LEEM-III)	0 eV – 4.5 keV, Resolution < 6 nm + AES	Elmitec, DE
SIMS	Secondary Ion Mass Spectrometer (IMS7f-auto)	3 – 15 keV Cs and O beam	CAMECA, FR

Photon-based analytical techniques

XRD/XRR	X-Ray Diffractometers θ-θ Powder D8 Advance θ-θ 4-Circle Empyrean θ-θ 4-Circle SmartLab 3kW	Cu-Kα	<i>Bruker, DE</i> <i>PANalytical, NL</i> <i>Rigaku, JP</i>
SE	Angle-Dependent Spectroscopic Ellipsometry	250 – 1700 nm	<i>Woollam, US</i>
UV-Vis	Solid Spec 3700 DUV	190 – 3300 nm	<i>Shimadzu, JP</i>
FTIR	Fourier-Transform Infrared Spectrometer Ti:Sapphire Femtosecond Laser Femtosecond Optical Parametric Osci. Ti:Sapphire Femtosecond Amplifier Femtosecond Optical Parametric Amplifier	50 – 15000 cm ⁻¹ 78 MHz 1 kHz, 250 kHz	<i>Bruker, DE</i> <i>Spectra Physics, US</i> <i>APE, DE</i> <i>Coherent, US</i> <i>Light Conversion, LT</i>
THz-TDS	Terahertz Time-Domain Spectroscopy	0.1 – 4 THz	<i>Home-built</i>
Raman	Raman Spectroscopy In-situ Raman Spectroscopy	> 10 cm ⁻¹ > 100 cm ⁻¹	<i>Jobin-Yvon-Horiba, FR</i> <i>Jobin-Yvon-Horiba, FR</i>
PL	Photoluminescence (10 – 300 K) Micro-Photoluminescence	405 – 1550 nm < 0.5 μm	<i>Jobin-Yvon-Horiba, FR</i> <i>Jobin-Yvon-Horiba, FR</i>
TRPL	Time-Resolved Photoluminescence	τ = 3 ps – 2 ns τ > 5 ns	<i>Hamamatsu Phot., JP</i> <i>Stanford Res., US</i>
EL	Electroluminescence Optical Split-Coil Supercond. Magnet	300 – 1600 nm 7 T	<i>Jobin-Yvon-Horiba, FR</i> <i>Oxford Instr., UK</i>
PR	Photomodulated Reflectivity	300 – 1600 nm	<i>Jobin-Yvon-Horiba, FR</i>
PLE	Photoluminescence Excitation	300 – 1600 nm	<i>Jobin-Yvon-Horiba, FR</i>
OES	Optical Emission Spectroscopy	250 – 800 nm	<i>Jobin-Yvon-Horiba, FR</i>
Confocal	Confocal scanning photoluminescence microscope	~1 μm resol. 5 – 300 K	<i>Attocube, DE</i>
SSPD	Superconducting single photon detectors	800 – 1500 nm	<i>Single Quantum, NL</i>

Magnetic thin film analysis

MFM	Magnetic Force Microscope	~ 50 nm resol.	<i>VEECO; DI, US</i>
AFM/MFM	Magnetic Force Microscope	~ 50 nm resol.	<i>BRUKER ICON tool, US</i>
SQUID VSM	Vibrating Sample Magnetometer	± 7 T	<i>Quantum Design, US</i>
Vector- VSM	Vibrating Sample Magnetometer	± 2 T	<i>Microsense, US</i>
MOKE	Magneto-Optic Kerr Effect (in-plane)	± 0.35 T	<i>Home-built</i>
MOKE	Magneto-Optic Kerr Effect (perpend.)	± 2 T	<i>Home-built</i>
FR-MOKE	Frequency-Resolved Magneto-Optic KE	± 1.1 T	<i>Home-built</i>
SKM	Scanning Kerr Microscope		<i>Home-built</i>

	Kerr Microscope		<i>Evico Magnetics, DE</i>
VNA-FMR	Vector Network Analyzer Ferromagnetic Resonance	50 GHz	<i>Agilent, DE; Home-built</i>
Cryo-FMR	Variable-Temperature Ferromagnetic Resonance	3 – 300 K	<i>Attocube, DE; Home-built</i>
ME	Magnetoellipsometer		<i>LOT, DE; AMAC, US</i>
μBLS	Brillouin Light Scattering Microscope	± 0.8 T, 491 & 532 nm	<i>Home-built</i>
SKM	Scanning Kerr Microscope with RF Detection (Spectrum Analyzer)	± 0.5 T, 40 GHz	<i>Home-built</i>
MT-50G	High Frequency Magneto-Transport Setup	± 1.5 T, 50 GHz 250 ps	<i>Home-built</i>

Other analytical and measuring techniques

STM/AFM	UHV Scanning Probe Microscope (variable T)		<i>Omicron, DE</i>
AFM	Atomic Force Microscope (Contact, Tapping, Spreading)		<i>Bruker, US</i>
AFM	Atomic Force Microscope (with c-AFM, SCM-Module)		<i>Bruker, US</i>
Dektak	Dektak Surface Profilometer		<i>Bruker, US</i>
	Micro Indenter/Scratch Tester		<i>Shimatsu, JP</i>
MPMS	Mechanical Properties Measurement System – Stretcher		<i>Home-built</i>
	Wear Tester (pin-on disc)		<i>Home-built</i>
DSA	Drop Shape Analyzer DSA25 Standard	RT	<i>Krüss, DE</i>
MS	Mass Spectrometers (EQP-300, HPR-30)		<i>HIDEN, UK</i>
LP	Automated Langmuir Probe		<i>Impedans, IE</i>
HMS	Hall Measurement System	2 – 400 K, ≤ 9 T	<i>LakeShore, US</i>
PS-M	Cryogenic probe station CPX-VF	4.5 – 400 K, ≤ 2.5 T laser 473 / 785 nm	<i>LakeShore, US</i>
PS	Cryogenic probe station TTP-4A	4.5 – 400 K laser 473 / 785 nm	<i>LakeShore, US</i>
MCBJ	Mechanically controlled break junction setup	RT, liquid environm.	<i>Home-built</i>
vdP	Van-der-Pauw HMS Ecopia	LNT & 300 K, 0.5 T	<i>Bridge Technol., US</i>
MTD	Magneto-Transport Device	300 K, ≤ 3 T	<i>Home-built</i>
RS	Sheet-Rho-Scanner		<i>AIT, KR</i>
Redmag	Redmag Tensormeter System	280 – 350 K, 2.5 T	<i>Home-built</i>
Greymag	Greymag Tensormeter System	300 K, 0.7 T (360°)	<i>Home-built</i>
Greenmag	Tensormeter System (TMCS)	30 – 320 K, 1.3 T (360°)	<i>Tensor Instruments (HZDR Inno), DE</i>
SEM	Scanning Electron Microscope (Phenom XL)	5 – 15 keV + EDS	<i>Thermo Fisher Sci., US</i>
IV / CV	I-V and C-V Semi-Automatic Prober	-60 – 300 °C	<i>Süss, DE; Keithley, US</i>
IV / CV	I-V and C-V Analyzer		<i>Keithley, US</i>
BCS	Battery test system, 8 channels		<i>Bio-Logic Science, DE</i>
GC	Gas Chromatography (GC-2010)		<i>Shimadzu, JP</i>

ECW	Electrochemical workstation (CHI 760e)		<i>CH instruments, US</i>
FDA	Force displacement analysis machine		<i>Sauter, DE</i>
IV / VNA	I-V and VNA Prober for VHF, LCR and frequency analysis measurements	20 – 120 MHz	<i>Süss, DE; Cascade, US; Keysight, US</i>
OSCI	4-channel real time oscilloscope	1.5 GHz (BW), 5 GSa/s	<i>Keysight, US</i>
IR-Cam	TrueIR Thermal Imager	-20 – 350 °C	<i>Keysight, US</i>
CM	Confocal Microscope (Smartproof 5)	405 nm LED, z drive res. ~ 1 nm	<i>Carl Zeiss, DE</i>
FAS	Fluidic Analytic Setup – microscope, high speed camera, and fluidic pumps	2 GB 120 kfps, 5 modules	<i>Zeiss, DE; Photron, US; Cetoni, DE</i>

Deposition and processing techniques

Physical Deposition	2x DC / 2x RF Magnetron Sputter System, up to 4x 6" substrates	<i>Nordiko, UK</i>
	Thermal (2 sources) / Electron Beam (12 pockets) Evaporation System	<i>CREAVAC, DE</i>
	Thermal Evaporation	<i>Bal-Tec, LI</i>
	Thermal (1 source) / Electron Beam (7 pockets) Evaporation System	<i>BESTEC, DE</i>
	DC/RF Magnetron Sputter System, 4x 3" + 4x 2" magnetrons, substrate heating: RT – 950 °C, up to 4" wafers	<i>BESTEC, DE</i>
	DC/RF Magnetron Sputter System, 6x 2" confocal magnetrons, substrate heating: RT – 650 °C, up to 3" wafers	<i>AJA International, US</i>
	Dual Ion Beam Sputtering (IBAD), 6" targets, RT – 500 °C	<i>Home-built</i>
	High Power Impulse Magnetron Sputtering	<i>Melec, DE</i>
	Magnetron Sputter System (2 targets)	<i>Home-built</i>
	Thermal Evaporation System (Cr, Au)	<i>Leybold GmbH</i>
DC/RF Magnetron Sputter System (Au, up to 3" wafers)	<i>Denton Vacuum, LLC</i>	
PLD	Pulsed Laser Deposition	<i>SURFACE, DE</i>
Molecular Beam Epitaxy (MBE)	III-V Semiconductors	<i>Riber, FR</i>
	Metals	<i>CreaTec Fischer, DE</i>
Chemical Vapor Deposition (CVD)	Plasma Enhanced: a-Si, a-Ge, SiO ₂ , SiON, Si ₃ N ₄	<i>Oxford Instr., UK</i>
Atomic Layer Deposition (ALD)	Al ₂ O ₃ , HfO ₂ , ZnO	<i>Ultratech, US</i>
Dry Etching	ICP-RIE, Ø 6": CF ₄ , SF ₆ , C ₄ F ₈ with interferometric etch-stop monitor	<i>Sentech, DE</i>
	RIBE, Ø 6": Ar, CF ₄ with SIMS etch-stop monitor	<i>Roth & Rau, DE</i>
	Barrel reactor, Ø 4": O ₂ , Ar, N ₂	<i>Diener electronic, DE</i>
Etching/Cleaning	incl. Anisotropic Selective KOH Etching, Metal-Assisted Chemical Etching, Photoelectrochemical Etching	
Photolithography	Mask-Aligner MA6, Ø 6", < 2 µm accuracy; with two-side alignment	<i>Süss, DE</i>
	Direct Laser Writer DWL 66FS, Ø 8"x8", 2 µm accuracy	<i>Heidelberg Instr., DE</i>

	Laser Micro Writer ML, 10 µm accuracy	<i>Durham Magneto Optics, UK</i>
Electron Beam Lithography	Raith 150-TWO: Ø 6", 10 nm resolution e-Line Plus: Ø 4", 10 nm resolution	<i>Raith, DE</i> <i>Raith, DE</i>
Thermal Treatment	Room Temperature – 2000 °C	
	Oxidation and annealing furnace	<i>INNOTHERM, DE</i>
	Rapid Thermal Annealing JETFIRST 100	<i>JIPELEC, FR</i>
	Rapid Thermal Annealing AW 610	<i>Allwin21, USA</i>
	Flash-Lamp Units (0.5 – 20 ms)	<i>Home-built; FHR/DTF, DE</i>
	Combined Flash Lamp Sputter Tool (Magnetron sputtering plus flash lamp annealing 0.3 – 3 ms, up to 10 Hz)	<i>ROVAK GmbH, DE</i>
	RF Heating (Vacuum)	<i>JIPELEC, FR</i>
	Laser Annealing (CW, 808 nm, 450 W)	<i>LIMO, DE</i>
	Laser Annealing (30 ns pulse, 10 Hz, 308 nm, 500 mJ)	<i>COHERENT, USA</i>
	CVD Tube furnace (RT – 1200 °C, three channel gas)	<i>NBD, CN</i>
	Vacuum oven (RT – 250 °C, Vacuum < 133 Pa)	<i>LAB-KITS, CN</i>
	Vacuum oven (RT – 800 °C, Vacuum < 10 ⁻⁷ mbar)	<i>Xerion GmbH, DE</i>
Bonding Techniques	Ultrasonic Wire Bonding	<i>Kulicke & Soffa, US</i>
	Semi-automatic Wire-bonder:	<i>F & S Bondtec, AT</i>
	Gold-ball and wedge-wedge bonding	
	Ultrasonic generator: 60 kHz, 140 kHz	
	Wire deformation control software	
Cutting, Grinding, Polishing		<i>Bühler, DE</i>
Laser Cutter skylaser Mark20	110 x 110 cm ² , 20W@1064 nm	<i>Pfeifer Tech.&Inno., DE</i>
TEM Sample Preparation	Plan View and Cross Section incl. Ion Milling Equipment	<i>Gatan, US</i>
SEM / HIM Sample Preparation	Mechanical milling, sawing, grinding, polishing	<i>Leica, AUT</i>
	Argon cross-section milling, surface polishing	<i>Hitachi, JP</i>
Disperse and mixer	Mixer for pastes and emulsions	<i>IKA, DE</i>
Centrifuge	Max. 17850 rpm, -10 – 40 °C	<i>Thermo Scientific, US</i>
Climate chamber VC ³ 7018	-70 – 180 °C	<i>Vötsch, DE</i>
Microbiological safety work benches	SafeFAST Classic	<i>CARLO ERBA, DE</i>
Autoclave SHP Laboklav 25 MV		<i>SHP Steriltechnik AG, DE</i>
Glove box	Ar atmosphere	<i>SYLATECH, DE</i>

Doctoral training programme

Advanced Training Program

This programme for our doctoral researchers fosters not only professional qualification but also personal development by equipping young graduates with competencies for successful careers in a wide variety of positions in academia and industry.

The doctoral training programme aims at attracting and promoting excellence by educating promising doctoral researchers with backgrounds in physics, chemistry, materials science, and electrical engineering. During a period of three to four years, doctoral researchers benefit from well-structured, comprehensive training curricula and multiple mentorship, while performing cutting-edge research projects within one of the institute's departments.

A weekly PhD Seminar gives a training in presenting scientific results and the opportunity of exchange with junior, as well as senior colleagues from all departments. Every doctoral researcher is expected to present the progress of his/her project once a year.

The transferable skills courses offered in 2023 covered the topics "Scientific Presentation" introduced by Carsten Rohr from Munich and Katja Kaufmann from Dresden, and "Project management" presented by Matthias Zach from Göttingen and Anne-Christin Warskulat from Jena. All four courses were rated very well to excellent by the doctoral researchers.

Workshop NANONET+



The NANONET+ Workshop 2023 was conducted at the Youth Hostel Sayda in an informal, unhurried manner due to the weak data link from September 11th – 13th. The topic was "1D and 2D Materials and Devices for Electronic and Photonic Applications". The event was organized by the department "Nanoelectronics" of our institute in collaboration with the Chair for Integrated Photonic Devices at TU Dresden lead by Prof. Dr. Kambiz Jamshidi. The format of a "Hüttenseminar" was generously supported by the Heraeus Foundation Hanau. The workshop was attended by 32 participants of 13 nationalities. The name is derived from the International Helmholtz Research School for Nanoelectronic Networks (IHRS NANONET) which was supported by the Initiative and Networking Fund of the Helmholtz Association between 2012 and 2020, and was coordinated at our institute (www.hzdr.de/NanoNet).



Publications and patents

Books and chapters

1. Wallner, A.
Measurements of radioactive ^{60}Fe and ^{244}Pu deposits on Earth and Moon
in Isao Tanihata, Hiroshi Toki, Toshitaka Kajino: Handbook of Nuclear Physics, Singapore: Springer, 2023, 978-981-15-8818-1, pp. 1 – 47
2. Dobrovolskiy, O.V.; Pylypovskyi, O.; Skoric, L.; Fernandez-Pacheco, A.; van den Berg, A.; Ladak, S.; Huth, M.
Complex-shaped 3D nano-architectures for magnetism and superconductivity
in Denys Makarov and Denis Sheka: Curvilinear Micromagnetism: from fundamentals to applications, Cham, Switzerland: Springer, 2023, 978-3-031-09086-8, pp. 215 – 268
3. Makarov, D.; Pylypovskyi, O.
Magnetic nanostructures
in: Encyclopedia of Condensed Matter Physics, Vol. 2, Amsterdam, The Netherlands: Elsevier, 2023, pp. 112-131, DOI: 10.1016/B978-0-323-90800-9.00048-2

Publications in journals

1. Adelman, C.; Jenkins, A.; Pirro, P.; Schultheiß, K.; van Dijken, S.; Kruglyak, V.; Bortolotti, P.
Opportunities and challenges for spintronics
Europhysics News **544**, 28 (2023)
2. Arshad, A.; Koyun, H.N.; Salikhov, R.; Gensch, M.; Ilyakov, I.; Ponomaryov, O.; Prajapati, G.L.; Mavridou, K.; Lindner, J.; Deinert, J.-C.; Ünlü, C.; de Oliveira, T.; Kovalev, S.
Terahertz harmonic generation from graphite pencil drawings
Advanced Photonics Research **4**, 2300088 (2023)
3. Azarov, A.; Fernández, J.G.; Zhao, J.; Djurabekova, F.; He, H.; He, R.; Prytz, Ø.; Vines, L.; Bektas, U.; Chekhonin, P.; Klingner, N.; Hlawacek, G.; Kuznetsov, A.
Universal radiation tolerant semiconductor
Nature Communications **14**, 4855 (2023)
4. Barnowsky, T.; Krasheninnikov, A.; Friedrich, R.
A New Group of Two-Dimensional Non-van der Waals Materials with Ultra Low Exfoliation Energies
Advanced Electronic Materials **9**, 2201112 (2023)
5. Berkmann, F.; Steuer, O.; Ganss, F.; Prucnal, S.; Schwarz, D.; Fischer, I.A.; Schulze, J.
Sharp MIR plasmonic modes in gratings made of heavily doped pulsed laser-melted $\text{Ge}_{1-x}\text{Sn}_x$
Optical Materials Express **13**, 752 (2023)
6. Bora, A.; Lox, J.; Hübner, R.; Weiß, N.; Bahmani Jalali, H.; Di Stasio, F.; Steinbach, C.; Gaponik, N.; Lesnyak, V.
Composition-Dependent Optical Properties of Cu–Zn–In–Se Colloidal Nanocrystals Synthesized via Cation Exchange
Chemistry of Materials **35**, 4068 (2023)

7. Borany, J.; Engelmann, H.-J.; Heinig, K.-H.; Amat, E.; Hlawacek, G.; Klüpfel, F.; Hübner, R.; Möller, W.; Pourteau, M.-L.; Rademaker, G.; Rommel, M.; Baier, L.; Pichler, P.; Perez-Murano, F.; Tiron, R.
CMOS-compatible manufacturability of sub-15 nm Si/SiO₂/Si nanopillars containing single Si nanodots for single electron transistor applications
Semiconductor Science and Technology **38**, 055011 (2023)
8. Bran, C.; Fernandez Roldan, J.A.; Moreno, J.A.; Fraile Rodríguez, A.; Del Real, R.P.; Asenjo, A.; Saugar, E.; Marqués-Marchán, J.; Mohammed, H.; Foerster, M.; Aballe, L.; Kosel, J.; Vazquez, M.; Chubykalo-Fesenko, O.
Domain Wall Propagation and Pinning Induced by Current Pulses in Cylindrical Modulated Nanowires
Nanoscale **15**, 8387 (2023)
9. Buchner, M.; Lenz, K.; Ney, V.; Lindner, J.; Ney, A.
Spin pumping into a partially compensated antiferromagnetic/paramagnetic insulator
New Journal of Physics **25**, 073002 (2023)
10. Bui, M.N.; Rost, S.; Auge, M.; Zhou, L.; Friedrich, C.; Blügel, S.; Kretschmer, S.; Krasheninnikov, A.; Watanabe, K.; Taniguchi, T.; Hofsäss, H.C.; Grützmacher, D.; Kardynał, B.E.
Optical Properties of MoSe₂ Monolayer Implanted with Ultra-Low-Energy Cr Ions
ACS Applied Materials and Interfaces **15**, 35321 (2023)
11. Cai, X.; Chen, C.; Xie, L.; Wang, C.; Gui, Z.; Gao, Y.; Kentsch, U.; Zhou, G.; Gao, X.; Chen, Y.; Zhou, S.; Gao, W.; Liu, J.-M.; Zhu, Y.; Chen, D.
In-plane charged antiphase boundary and 180° domain wall in a ferroelectric film
Nature Communications **14**, 8174 (2023)
12. Cavaleiro, D.; Munnik, F.; Krause, M.; Carbo, E.; Ferreira, P.J.; Cavaleiro, A.; Fernandes, F.
The role of interfaces and morphology on silver diffusion in hard coatings
Surfaces and Interfaces **41**, 103182 (2023)
13. Chava, P.; Fekri, Z.; Vekariya, Y.N.; Mikolajick, T.; Erbe, A.
Band-to-band tunneling switches based on two-dimensional van der Waals heterojunctions
Applied Physics Reviews **10**, 011318 (2023)
14. Chen, K.; Luo, C.; Baudalet, F.; Maurya, A.; Thamizhavel, A.; Röblier, U.K.; Makarov, D.; Radu, F.
Evidence of the anomalous fluctuating magnetic state by pressure driven 4f valence change in EuNiGe₃
The Journal of Physical Chemistry Letters **14**, 1000 (2023)
15. Chepkasov, I.; Krasheninnikov, A.
Tetracene Crystals as Promising Anode Material for Alkali Metal Ion Batteries
Carbon **213**, 118190 (2023)
16. Choupanian, S.; Möller, W.; Seyring, M.; Pacholski, C.; Wendler, E.; Undisz, A.; Ronning, C.
Ion Irradiation-Induced Sinking of Ag Nanocubes into Substrates
Advanced Materials **11**, 2300570 (2023)
17. Choupanian, S.; Möller, W.; Seyring, M.; Ronning, C.
Low-energy ion channeling in nanocubes
Nano Research **16**, 1522 (2023)
18. Davies, F.; Mehlich, K.; Busse, C.; Krasheninnikov, A.
What governs the atomic structure of the interface between 2D transition metal dichalcogenides in lateral heterostructures?
2D Materials **11**, 015003 (2023)

19. Duan, J.; Liedke, M.O.; Dawidowski, W.; Li, R.; Butterling, M.; Hirschmann, E.; Wagner, A.; Wang, M.; Boyu Young, L.; Glen Lin, Y.-H.; Hong, M.; Helm, M.; Zhou, S.; Prucnal, S.
Fabrication and characterization of heavily doped n-type GaAs for mid-infrared plasmonics
Journal of Applied Physics **134**, 095102 (2023)
20. Düllmann, C.E.; Artes, E.; Dragoun, A.; Haas, R.; Jäger, E.; Kindler, B.; Lommel, B.; Mangold, K.M.; Meyer, C.C.; Mokry, C.; Munnik, F.; Rapps, M.; Renisch, D.; Runke, J.; Seibert, A.; Stöckl, M.; Thörle-Pospiech, P.; Trautmann, C.; Trautmann, N.; Yakushev, A.
Advancements in the fabrication and characterization of actinide targets for superheavy element production
Journal of Radioanalytical and Nuclear Chemistry **332**, 1505 (2023)
21. Esters, M.; Oses, C.; Divilov, S.; Eckert, H.; Friedrich, R.; Hicks, D.; Mehl, M.J.; Rose, F.; Smolyanyuk, A.; Calzolari, A.; Campilongo, X.; Toher, C.; Curtarolo, S.
aflow.org: a web ecosystem of databases, software and tools
Computational Materials Science **216**, 111808 (2023)
22. Fareed, A.; Rosalie, J.; Kumar, S.; Kar, S.; Hickel, T.; Fähler, S.; Maaß, R.
Incipient stress-induced phase transformation of a Ni-Mn-Ga Heusler alloy: A small-scale design challenge
Materials and Design **233**, 112259 (2023)
23. Fields, B.D.; Wallner, A.
Deep-Sea and Lunar Radioisotopes from Nearby Astrophysical Explosions
Annual Review of Nuclear and Particle Science **73**, 365 (2023)
24. Fink, L.; Kar, S.; Lünser, K.; Nielsch, K.; Reith, H.; Fähler, S.
Integration of Multifunctional Epitaxial (Magnetic) Shape Memory Films in Silicon Microtechnology
Advanced Functional Materials **33**, 2305273 (2023)
25. Fink, L.; Nielsch, K.; Fähler, S.
Tailoring of thermomagnetic properties in Ni-Mn-Ga films through Cu addition
Journal of Alloys and Compounds **966**, 171435 (2023)
26. Fogarassy, Z.; Kentsch, U.; Panjan, P.; Racz, A.S.
Experimental and theoretical study on the production of carbide-rich composite nano-coatings
Surfaces and Interfaces **38**, 102773 (2023)
27. Fotev, I.; Winnerl, S.; Aswartham, S.; Wurmehl, S.; Büchner, B.; Schneider, H.; Helm, M.; Pashkin, O.
Ultrafast Relaxation Dynamics of Spin-Density Wave Order in BaFe₂As₂ under High Pressures
Physical Review B **108**, 035101 (2023)

28. Fougères, C.; de Oliveira Santos, F.; José, J.; Michelagnoli, C.; Clément, E.; Kim, Y.H.; Lemasson, A.; Guimarães, V.; Barrientos, D.; Bemmerer, D.; Benzoni, G.; Boston, A.J.; Böttger, R.; Boulay, F.; Bracco, A.; Celikovic, I.; Cederwall, B.; Ciemala, M.; Delafosse, C.; Domingo-Pardo, C.; Dudouet, J.; Eberth, J.; Fülöp, Z.; González, V.; Gottardo, A.; Goupil, J.; Hess, H.; Jungclaus, A.; Kaskas, A.; Korichi, A.; Lenzi, S.M.; Leoni, S.; Li, H.; Ljungvall, J.; Lopez-Martens, A.; Menegazzo, R.; Mengoni, D.; Million, B.; Mrazek, J.; Napoli, D.R.; Navin, A.; Nyberg, J.; Podolyak, Z.; Pullia, A.; Quintana, B.; Ralet, D.; Redon, N.; Reiter, P.; Rezyunkina, K.; Saillant, F.; Salsac, M.D.; Sánchez-Benítez, A.M.; Sanchis, E.; Senyigit, M.; Siciliano, M.; Smirnova, N.A.; Sohler, D.; Stanoiu, M.; Theisen, C.; Valiente-Dobón, J.J.; Ujic, P.; Zielinska, M.
Search for ^{22}Na in novae supported by a novel method for measuring femtosecond nuclear lifetimes
Nature Communications **14**, 4536 (2023)
29. Gao, X.; Jiang, G.; Gao, C.; Prudnikau, A.; Hübner, R.; Zhan, J.; Zou, G.; Eychmüller, A.; Cai, B.
Interparticle Charge-Transport-Enhanced Electrochemiluminescence of Quantum-Dot Aerogels
Angewandte Chemie - International Edition **62**, e202214487 (2023)
30. Ge, Y.; Lünser, K.; Ganss, F.; Gaal, P.; Fink, L.; Fähler, S.
Growth and Martensitic Transformation of Ferromagnetic Co-Cr-Ga-Si Epitaxial Films
Science and Technology of Advanced Materials **24**, 2251368 (2023)
31. Ghosh, S.; Khan, M.B.; Chava, P.; Watanabe, K.; Taniguchi, T.; Prucnal, S.; Hübner, R.; Mikolajick, T.; Erbe, A.; Georgiev, Y.
Novel Mixed-Dimensional hBN-Passivated Silicon Nanowire Reconfigurable Field Effect Transistors: Fabrication and Characterization
ACS Applied Materials and Interfaces **15**, 40709 (2023)
32. Gladii, O.; Salikhov, R.; Hellwig, O.; Schultheiß, H.; Lindner, J.; Gallardo, R.
Spin wave non-reciprocity at the spin-flop transition region in synthetic antiferromagnets
Physical Review B **107**, 104419 (2023)
33. Grabec, T.; Soudná, Z.; Repčák, K.; Lünser, K.; Fähler, S.; Stoklasová, P.; Sedlák, P.; Seiner, H.
Guided acoustic waves in thin epitaxial films: experiment and inverse problem solution for NiTi
Ultrasonics **138**, 107211 (2023)
34. Gupta, P.; Jovic, V.; Hübner, R.; Anquillare, E.; Suschke, K.; Smith, K.E.; Markwitz, A.; Waterhouse, G.I.N.; Kennedy, J.
Influence of substrate composition on size and chemical state of ion beam synthesised Co nanoparticles – Towards fabrication of electrodes for energy devices
Materials Today Communications **34**, 105235 (2023)
35. Hache, T.; Körber, L.; Hula, T.; Lenz, K.; Kakay, A.; Hellwig, O.; Lindner, J.; Faßbender, J.; Schultheiß, H.
Control of Four-Magnon Scattering by Pure Spin Current in a Magnonic Waveguide
Physical Review Applied **20**, 014062 (2023)
36. Han, J.W.; Sai, P.; But, D.; Uykur, E.; Winnerl, S.; Kumar, G.; Chin, M.L.; Myers-Ward, R.L.; Dejarld, M.T.; Daniels, K.M.; Murphy, T.E.; Knap, W.; Mittendorff, M.
Strong transient magnetic fields induced by THz-driven plasmons in graphene disks
Nature Communications **14**, 7493 (2023)
37. Helm, M.; Winnerl, S.; Pashkin, O.; Klopff, J.M.; Deinert, J.-C.; Kovalev, S.; Evtushenko, P.; Lehnert, U.; Xiang, R.; Arnold, A.; Wagner, A.; Schmidt, S.M.; Schramm, U.; Cowan, T.; Michel, P.
The ELBE infrared and THz facility at Helmholtz-Zentrum Dresden - Rossendorf
European Physical Journal Plus **138**, 158 (2023)

38. Hilpmann, S.; Roßberg, A.; Steudtner, R.; Drobot, B.; Hübner, R.; Bok, F.; Prieur, D.; Bauters, S.; Kvashnina, K.; Stumpf, T.; Cherkouk, A.
Presence of uranium(V) during uranium(VI) reduction by *Desulfosporosinus hippei* DSM 8344T
Science of the Total Environment **875**, 162593 (2023)
39. Hoesch, M.; Fedchenko, O.; Wang, M.; Schlueter, C.; Potorochin, D.; Medjanik, K.; Babenkov, S.; Ciobanu, A.S.; Winkelmann, A.; Elmers, H.-J.; Zhou, S.; Helm, M.; Schönhense, G.
Active Sites of Te-hyperdoped Silicon by Hard X-ray Photoelectron Spectroscopy
Applied Physics Letters **122**, 252108 (2023)
40. Höflich, K.; Hobler, G.; Allen, F.I.; Wirtz, T.; Rius, G.; Krasheninnikov, A.; Schmidt, M.; Utke, I.; Klingner, N.; Osenberg, M.; McElwee-White, L.; Córdoba, R.; Djurabekova, F.; Manke, I.; Moll, P.; Manoccio, M.; de Teresa, J.M.; Bischoff, L.; Michler, J.; de Castro, O.; Delobbe, A.; Dunne, P.; Dobrovolskiy, O.V.; Freese, N.; Gölzhäuser, A.; Mazarov, P.; Koelle, D.; Möller, W.; Pérez-Murano, F.; Philipp, P.; Vollnhals, F.; Hlawacek, G.
Roadmap for focused ion beam technologies
Applied Physics Reviews **10**, 041311 (2023)
41. Huang, X.; Fu, S.; Lin, C.; Lu, Y.; Wang, M.; Zhang, P.; Huang, C.; Li, Z.; Liao, Z.; Zou, Y.; Li, J.; Zhou, S.; Helm, M.; Petkov, P.S.; Heine, T.; Bonn, M.; Wang, H.I.; Feng, X.; Dong, R.
Semiconducting Conjugated Coordination Polymer with High Charge Mobility Enabled by “4 + 2” Phenyl Ligands
Journal of the American Chemical Society **145**, 2430 (2023)
42. Ilyakov, I.; Brataas, A.; de Oliveira, T.; Ponomaryov, O.; Deinert, J.-C.; Hellwig, O.; Faßbender, J.; Lindner, J.; Salikhov, R.; Kovalev, S.
Efficient ultrafast field-driven spin current generation for spintronic terahertz frequency conversion
Nature Communications **14**, 7010 (2023)
43. Isele, M.; Hofmann, K.; Erbe, A.; Leiderer, P.; Nielaba, P.
Lane formation of colloidal particles driven in parallel by gravity
Physical Review E **108**, 034607 (2023)
44. Ishioka, K.; Pashkin, O.; Bernhard, C.; Petek, H.; Yao, X.; Demsar, J.
Selective coupling of coherent optical phonons in $\text{YBa}_2\text{Cu}_3\text{O}_7$ with electronic transitions
Physical Review B **107**, 184302 (2023)
45. Iurchuk, V.; Kozlov, O.; Sorokin, S.; Zhou, S.; Lindner, J.; Reshetniak, S.; Kravets, A.; Polishchuk, D.; Korenivski, V.
All-electrical operation of a Curie-switch at room temperature
Physical Review Applied **20**, 024009 (2023)
46. Iurchuk, V.; Pablo-Navarro, J.; Hula, T.; Narkovic, R.; Hlawacek, G.; Körber, L.; Kakay, A.; Schultheiß, H.; Faßbender, J.; Lenz, K.; Lindner, J.
Tailoring crosstalk between localized 1D spin-wave nanochannels using focused ion beams
Scientific Reports **13**, 764 (2023)
47. Iurchuk, V.; Sorokin, S.; Lindner, J.; Faßbender, J.; Kakay, A.
Piezostain as a Local Handle to Control Gyrotropic Dynamics of Magnetic Vortices
Physical Review Applied **20**, 024080 (2023)
48. Jain, M.; Kretschmer, S.; Höflich, K.; Lopes, J.M.J.; Krasheninnikov, A.
Atomistic Simulations of Defects Production under Ion Irradiation in Epitaxial Graphene on SiC
Physica Status Solidi (RRL) **17**, 2200292 (2023)

49. Jarc, G.; Mathengattil, S.Y.; Montanaro, A.; Giusti, F.; Rigoni, E.M.; Sergo, R.; Fassioli, F.; Winnerl, S.; Zilio, S.D.; Mihailovic, D.; Prelovšek, P.; Eckstein, M.; Fausti, D.
Cavity-mediated thermal control of metal-to-insulator transition in 1T-TaS₂
Nature **622**, 487 (2023)
50. Jessat, J.; John, W.; Moll, H.; Vogel, M.; Steudtner, R.; Drobot, B.; Hübner, R.; Stumpf, T.; Sachs, S.
Localization and chemical speciation of europium(III) in Brassica napus plants
Ecotoxicology and Environmental Safety **254**, 114741 (2023)
51. Józwiak, I.; Jagielski, J.; Ciepielewski, P.; Dumiszewska, E.; Piętak-Jurczak, K.; Kamiński, M.; Kentsch, U.
Depth-distribution of resistivity within ion-irradiated semiconductor layers revealed by low-kV scanning electron microscopy
Materials Science in Semiconductor Processing **165**, 107640 (2023)
52. Kameník, J.; Garba, R.; Stübner, K.; Lachner, J.; Rugel, G.; Veselovský, F.; Jansen, J.D.; Usik, V.; Kučera, J.
Processing of Korolevo samples aimed at AMS determination of in situ ¹⁰Be and ²⁶Al nuclides and their purity control using follow-up mass spectrometry scans
Journal of Radioanalytical and Nuclear Chemistry **332**, 1583 (2023)
53. Kar, S.; Ikeda, Y.; Lünser, K.; Woodcock, T.G.; Nielsch, K.; Reith, H.; Maaß, R.; Fähler, S.
Growth twins and premartensite microstructure in epitaxial Ni-Mn-Ga films
Acta Materialia **252**, 118902 (2023)
54. Kar, S.; Nielsch, K.; Fähler, S.; Reith, H.
Microfabrication Approaches on Magnetic Shape Memory Films
Advanced Engineering Materials **25**, 2301133 (2023)
55. Keil, T.; Hübner, R.; Worbs, A.
Die Morphologie der Schuppen der aus der Paläarktis bekannten Arten der Unterfamilie Procridinae Boisduval, 1828 (Lepidoptera, Zygaenidae) und deren Bedeutung für die Systematik und Phylogenie
Entomologische Nachrichten und Berichte **67**, 181 (2023)
56. Keller, T.F.; Shayduk, R.; Kim, C.; Mukharamova, N.; Dangwal Pandey, A.; Abuin, M.; Vonk, V.; Fernandez-Cuesta, I.; Barthelmess, M.; Frömter, R.; Zozulya, A.; Erbe, A.; Stierle, A.
Coherent x-ray diffraction of a semiregular Pt nanodot array
Physical Review B **108**, 134109 (2023)
57. Khavlyuk, P.; Mitrofanov, A.; Shamraienko, V.; Hübner, R.; Kresse, J.; Borchert, K.B.L.; Eychmüller, A.
Bimetallic Pt-Ni Two-Dimensional Interconnected Networks: Developing Self-Assembled Materials for Transparent Electronics
Chemistry of Materials **35**, 2864 (2023)
58. Kocjančič, B.; Avsec, K.; Šetina Batič, B.; Feizpour, D.; Godec, M.; Kralj-Iglič, V.; Podlipec, R.; Cör, A.; Debeljak, M.; Grant, J.T.; Jenko, M.; Dolinar, D.
The Impact of Al₂O₃ Particles from Grit-Blasted Ti₆Al₇Nb (Alloy) Implant Surfaces on Biocompatibility, Aseptic Loosening, and Infection
Materials **16**, 6867 (2023)
59. Komarov, F.F.; Vlasukova, L.A.; Milchanin, O.V.; Parkhomenko, I.N.; Berencen, Y.; Alzhanova, A.E.; Wang, T.; Zuk, J.
Optical properties of selenium-hyperdoped Si layers: Effects of laser and thermal treatment
Journal of Applied Spectroscopy **90**, 358 (2023)

60. Körber, L.; Heins, C.; Hula, T.; Kim, J.-V.; Thlang, S.; Schultheiß, H.; Faßbender, J.; Schultheiß, K.
Pattern recognition in reciprocal space with a magnon-scattering reservoir
Nature Communications **14**, 3954 (2023)
61. Körber, L.; Heins, C.; Soldatov, I.; Schäfer, R.; Kakay, A.; Schultheiß, H.; Schultheiß, K.
Modification of three-magnon splitting in a flexed magnetic vortex
Applied Physics Letters **122**, 092401 (2023)
62. Krause, M.; Hoppe, M.; Romero-Muñiz, C.; Mendez, A.; Munnik, F.; Garcia Valenzuela, A.; Schimpf, C.; Rafaja, D.; Escobar-Galindo, R.
Exceptionally high-temperature in-air stability of transparent conductive oxide tantalum-doped tin dioxide
Journal of Materials Chemistry A **11**, 17686 (2023)
63. Kresse, J.; Georgi, M.; Hübner, R.; Eychemüller, A.
Structural investigations of Au-Ni aerogels: morphology and element distribution
Nanoscale Advances **5**, 5487 (2023)
64. Kudriavtseva, A.; Codilean, A.T.; Sobel, E.R.; Landgraf, A.; Fülöp, R.-H.; Dzhumabaeva, A.; Abdrakhmatov, K.; Wilcken, K.M.; Schildgen, T.; Fink, D.; Fujioka, T.; Gong, L.; Rosenwinkel, S.; Merchel, S.; Rugel, G.
Impact of Quaternary Glaciations on Denudation Rates in North Pamir—Tian Shan Inferred From Cosmogenic ¹⁰Be and Low-Temperature Thermochronology
Journal of Geophysical Research - Earth Surface **128**, e2023JF007193 (2023)
65. Kuhrts, L.; Helmbrecht, L.; Noorduyn, W.L.; Pohl, D.; Sun, X.; Palatnik, A.; Wetzker, C.; Jantschke, A.; Schlierf, M.; Zlotnikov, I.
Recruiting Unicellular Algae for the Mass Production of Nanostructured Perovskites
Advanced Science **10**, 2300355 (2023)
66. Kurian, J.; Joseph, A.; Cherifi-Hertel, S.; Fowley, C.; Hlawacek, G.; Dunne, P.; Romeo, M.; Atcheson, G.; Coey, J.M.D.; Doudin, B.
Deterministic multi-level spin-orbit torque switching using focused He⁺ ion beam irradiation
Applied Physics Letters **122**, 032402 (2023)
67. Kutschera, W.; Jull, A.J.T.; Paul, M.; Wallner, A.
Atom Counting with Accelerator Mass Spectrometry
Reviews of Modern Physics **95**, 035006 (2023)
68. Lachner, J.; Rugel, G.; Vivo Vilches, C.; Koll, D.; Stübner, K.; Winkler, S.; Wallner, A.
Optimization of ¹⁰Be measurements at the 6 MV AMS facility DREAMS
Nuclear Instruments and Methods in Physics Research B **535**, 29 (2023)
69. Lai, L.; Chekhonin, P.; Akhmadaliev, S.; Brandenburg, J.-E.; Bergner, F.
Microstructural characterization of reactor pressure vessel steels
Metals **13**, 1339 (2023)
70. Lamb-Camarena, S.; Porrati, F.; Kuprava, A.; Wang, Q.; Urbánek, M.; Barth, S.; Makarov, D.; Huth, M.; Dobrovolskiy, O.V.
3D Magnonic Conduits by Direct Write Nanofabrication
Nanomaterials **13**, 1926 (2023)

71. Lewis, A.M.; Neudecker, D.; Carlson, A.D.; Smith, D.L.; Thompson, I.; Wallner, A.; Barry, D.P.; Bernstein, L.A.; Block, R.C.; Stephen Croft, Y.D.; Drosig, M.; Haight, R.C.; Herman, M.W.; Young Lee, H.; Otuka, N.; Sjöstrand, H.; Sobes, V.
Templates of expected measurement uncertainties for neutron-induced capture and charged-particle production cross section observables
EPJ Nuclear Sciences & Technologies **9**, 33 (2023)
72. Li, J.; Ghorbani Asl, M.; Lasek, K.; Pathirage, V.; Krasheninnikov, A.; Batzill, M.
A van der Waals Heterostructure with an Electronically Textured Moiré Pattern: PtSe₂/PtTe₂
ACS Nano **17**, 5913 (2023)
73. Li, J.; Hübner, R.; Deconinck, M.; Bora, A.; Göbel, M.; Schwarz, D.; Chen, G.; Wang, G.; Yang, S.A.; Vaynzof, Y.; Lesnyak, V.
Alloyed Re_xMo_{1-x}S₂ Nanoflakes with Enlarged Interlayer Distances for Hydrogen Evolution
ACS Applied Nano Materials **6**, 9475 (2023)
74. Li, S.; Wu, Y.; Asghar, W.; Li, F.; Zhang, Y.; He, Z.; Liu, J.; Wang, Y.; Liao, M.; Shang, J.; Ren, L.; Du, Y.; Makarov, D.; Liu, Y.; Li, R.-W.
Wearable Magnetic Field Sensor with Low Detection Limit and Wide Operation Range for Electronic Skin Applications
Advanced Science, 2304525 (2023)
75. Li, W.; Weng, B.; Sun, X.; Cai, B.; Hübner, R.; Luo, Y.; Du, R.
A Decade of Electrocatalysis with Metal Aerogels: A Perspective
Catalysts **13**, 167 (2023)
76. Li, Y.; Duan, J.; Berencen, Y.; Hübner, R.; Tsai, H.-S.; Kuo, C.-N.; Chin-Shan, L.; Helm, M.; Zhou, S.; Prucnal, S.
Formation of vertical SnSe/SnSe₂ p-n heterojunction by NH₃ plasma-induced phase transformation
Nanoscale Advances **5**, 443 (2023)
77. Li, Y.; Steuer, O.; Lin, K.; Samad, F.; Sokolova, D.; Erbe, A.; Helm, M.; Zhou, S.; Prucnal, S.
Influence of Dielectric Capping on the Optical Properties of Two-Dimensional Transition Metal Dichalcogenides: Implications for nano optoelectronics
ACS Applied Optical Materials **1**, 1733 (2023)
78. Li, Z.; Yuan, Y.; Hübner, R.; Rebohle, L.; Zhou, Y.; Helm, M.; Nielsch, K.; Prucnal, S.; Zhou, S.
B20 Weyl semimetal CoSi film fabricated by flash-lamp annealing
ACS Applied Materials and Interfaces **15**, 30517 (2023)
79. Liu, H.; Li, Y.; Yang, Q.; Zhou, S.; Jia, Y.
A tailored 100%-efficient 532/1064-nm demultiplexer in y-cut LiNbO₃ crystal
Optics Letters **48**, 787 (2023)
80. Liu, K.; Réhault, J.; Liang, B.; Hamsch, M.; Zhang, Y.; Seçkin, S.; Zhou, Y.; Shivhare, R.; Zhang, P.; Polozij, M.; König, T.A.F.; Qi, H.; Zhou, S.; Fery, A.; Mannsfeld, S.C.B.; Kaiser, U.; Heine, T.; Banerji, N.; Dong, R.; Feng, X.
A Quasi-2D Polypyrrole Film with Band-Like Transport Behavior and High Charge Carrier Mobility
Advanced Materials **35**, 2303288 (2023)

81. Liu, Q.; Lin, Y.-C.; Kretschmer, S.; Ghorbani Asl, M.; Solís-Fernández, P.; Siao, M.-D.; Chiu, P.-W.; Ago, H.; Krasheninnikov, A.; Suenaga, K.
Molybdenum Chloride Nanostructures with Giant Lattice Distortions Intercalated into Bilayer Graphene
ACS Nano **17**, 23659 (2023)
82. Liu, Y.; Lin, G.; Medina-Sánchez, M.; Guix, M.; Makarov, D.; Jin, D.
Responsive Magnetic Nanocomposites for Intelligent Shape-Morphing Microrobots
ACS Nano **17**, 8899 (2023)
83. Lokamani, M.; Kilibarda, F.; Günther, F.; Kelling, J.; Strobel, A.; Zahn, P.; Juckeland, G.; Gothelf, K.; Scheer, E.; Gemming, S.; Erbe, A.
Stretch Evolution of Electronic Coupling of the Thiophenyl Anchoring Group with Gold in Mechanically Controllable Break Junctions
The Journal of Physical Chemistry Letters **14**, 5709 (2023)
84. Long, F.; Ghorbani Asl, M.; Mosina, K.; Li, Y.; Lin, K.; Ganss, F.; Hübner, R.; Sofer, Z.; Dirnberger, F.; Kamra, A.; Krasheninnikov, A.; Prucnal, S.; Helm, M.; Zhou, S.
Ferromagnetic interlayer coupling in CrSBr crystals irradiated by ions
Nano Letters **23**, 8468 (2023)
85. Long, F.; Mosina, K.; Hübner, R.; Sofer, Z.; Klein, J.; Prucnal, S.; Helm, M.; Dirnberger, F.; Zhou, S.
Intrinsic magnetic properties of the layered antiferromagnet CrSBr
Applied Physics Letters **122**, 222401 (2023)
86. Lunardon, M.; Kosmala, T.; Ghorbani Asl, M.; Krasheninnikov, A.; Kolekar, S.; Durante, C.; Batzill, M.; Agnoli, S.; Granozzi, G.
Catalytic Activity of Defect-Engineered Transition Metal Dichalcogenides Mapped with Atomic Scale Precision by Electrochemical Scanning Tunneling Microscopy
ACS Energy Letters **8**, 972 (2023)
87. Lünser, K.; Undisz, A.; Nielsch, K.; Fähler, S.
How to grow single-crystalline and epitaxial NiTi films in (100)- and (111)-orientation
Journal of Physics: Materials **6**, 035002 (2023)
88. Lünser, K.; Undisz, A.; Wagner, M.F.-X.; Nielsch, K.; Fähler, S.
Solving the puzzle of hierarchical martensitic microstructures in NiTi by (111)-oriented epitaxial films
Materials Today Advances **20**, 100441 (2023)
89. Luo, Y.; Wang, C.; Chen, C.; Gao, Y.; Sun, F.; Li, C.; Yin, X.; Luo, C.; Kentsch, U.; Cai, X.; Bai, M.; Fan, Z.; Qin, M.; Zeng, M.; Dai, J.; Zhou, G.; Lu, X.; Lou, X.; Zhou, S.; Gao, X.; Chen, D.; Liu, J.-M.
Tripling energy storage density through order–disorder transition induced polar nanoregions in PbZrO₃ thin films by ion implantation
Applied Physics Reviews **10**, 011403 (2023)
90. Ma, L.; Li, S.; Wang, H.; Zhou, S.; Yang, T.
Ion irradiation of monolayer graphene-Nd:YAG hybrid waveguides: fabrication and laser
Optics Express **31**, 17769 (2023)
91. Macková, A.; Jagerová, A.; Lalik, O.; Mikšová, R.; Poustka, D.; Mistrík, J.; Holý, V.; Schutter, J.D.; Kentsch, U.; Marvan, P.; Azarov, A.; Galeckas, A.
Combined Au/Ag nanoparticle creation in ZnO nanopillars by ion implantation for optical response modulation and photocatalysis
Applied Surface Science **610**, 155556 (2023)

92. Magalhaes, S.; Salgado Cabaco, J.; Concepcion, O.; Buca, D.; Stachowicz, M.; Oliveira, F.; Cerqueira, M.F.; Lorenz, K.; Alves, E.
Combining x-ray real and reciprocal space mapping techniques to explore the epitaxial growth of semiconductors
Journal of Physics D: Applied Physics **56**, 245102 (2023)
93. Markó, D.; Cheenikundil, R.; Bauer, J.; Lenz, K.; Chuang, W.-C.; Lin, K.-W.; Wu, J.-C.; D'Aquino, M.; Hertel, R.; Schmool, D.S.
Interpretation of spin-wave modes in Co/Ag nanodot arrays probed by broadband ferromagnetic resonance
Physical Review Applied **20**, 024059 (2023)
94. Matthus, C.D.; Chava, P.; Watanabe, K.; Taniguchi, T.; Mikolajick, T.; Helm, M.; Erbe, A.
I-V-T Characteristics and Temperature Sensor Performance of a Fully-2D WSe₂/MoS₂ Heterojunction Diode at Cryogenic Temperatures
IEEE Journal of the Electron Devices Society **11**, 359 (2023)
95. Meng, F.; Walla, F.; Kovalev, S.; Deinert, J.-C.; Ilyakov, I.; Chen, M.; Ponomaryov, O.; Pavlov, S.G.; Hübers, H.-W.; Abrosimov, N.V.; Jungemann, C.; Roskos, H.G.; Thomson, M.D.
Higher-harmonic generation in boron-doped silicon from band carriers and bound-dopant photoionization
Physical Review Research **5**, 043141 (2023)
96. Metzkwow, N.; Klemmed, B.; Georgi, M.; Hübner, R.; Eychmüller, A.
Photoluminescence Properties of Lanthanide-Doped Alumina and YAG Aerogels
Journal of Physical Chemistry C **127**, 16995 (2023)
97. Mitrofanov, A.; Berencen, Y.; Sadrollahi, E.; Boldt, R.; Bodesheim, D.; Weiske, H.; Paulus, F.; Geck, J.; Cuniberti, G.; Kuc, A.; Voit, B.
Molecular engineering of naphthalene spacers in low-dimensional perovskites
Journal of Materials Chemistry C **11**, 5024 (2023)
98. Nadarajan, R.; Devaraj, M.; Satyanarayana, S.V.M.; Posselt, M.
Y doping of BaZrO₃ may lead to optimum conditions for proton conduction at operating temperature of solid oxide fuel cells: A first principles study
Materials Research Express **10**, 065504 (2023)
99. Neudecker, D.; Lewis, A.M.; Matthews, E.F.; Vanhoy, J.; Haight, R.C.; Smith, D.L.; Talou, P.; Croft, S.; Carlson, A.D.; Pierson, B.; Wallner, A.; Al-Adili, A.; Bernstein, L.; Capote, R.; Devlin, M.; Drogg, M.; Duke, D.L.; Finch, S.; Herman, M.W.; Kelly, K.J.; Koning, A.; Lovell, A.E.; Marini, P.; Montoya, K.; Nobre, G.P.A.; Paris, M.; Pritychenko, B.; Sjöstrand, H.; Snyder, L.; Sobes, V.; Solders, A.; Taieb, J.
Templates of expected measurement uncertainties
EPJ Nuclear Sciences & Technologies **9**, 35 (2023)
100. Ney, V.; Salikhov, R.; Lenz, K.; Hellwig, O.; Lindner, J.; Ney, A.
Influence of oxidic and metallic interfaces on the magnetic damping of Permalloy thin films
Physical Review Materials **7**, 124403 (2023)
101. Niggas, A.; Fischer, L.; Kretschmer, S.; Werl, M.; Biber, H.; Speckmann, C.; McEvoy, N.; Kotakoski, J.; Aumayr, F.; Krashenninikov, A.; Wilhelm, R.A.
Charge-exchange-dependent energy loss of H and He in freestanding monolayers of graphene and MoS₂
Physical Review A **108**, 062823 (2023)

102. Niranjan, K.; Krause, M.; Lungwitz, F.; Munnik, F.; Hübner, R.; Pemmasani, S.P.; Escobar Galindo, R.; Barshilia, H.C.
WAISiN-based solar selective coating stability-study under heating and cooling cycles in vacuum up to 800 °C using in situ Rutherford backscattering spectrometry and spectroscopic ellipsometry
Solar Energy Materials and Solar Cells **255**, 112305 (2023)
103. Obst, M.; Nörenberg, T.; Álvarez-Pérez, G.; de Oliveira, T.; Taboada-Gutiérrez, J.; Feres, F.H.; Kaps, F.G.; Hatem, O.; Luferau, A.; Nikitin, A.Y.; Klopff, J.M.; Alonso-González, P.; Kehr, S.C.; Eng, L.M.
Terahertz Twistoptics–Engineering Canalized Phonon Polaritons
ACS Nano **17**, 19313 (2023)
104. Oliveros Mata, E.S.; Xu, R.; Guo, L.; Makarov, D.
Magnetically aware actuating composites: Sensing features as inspiration for the next step in advanced magnetic soft robotics
Physical Review Applied **20**, 060501 (2023)
105. Opitz, L.; Hübner, R.; Shams Aldin Azzam, S.; Gilson, S.; Finkeldej, S.C.; Huittinen, N.M.
Investigations towards incorporation of Eu³⁺ and Cm³⁺ during ZrO₂ crystallization in aqueous solution
Scientific Reports **13**, 12276 (2023)
106. Oses, C.; Esters, M.; Hicks, D.; Divilov, S.; Eckert, H.; Friedrich, R.; Mehl, M.J.; Smolyanyuk, A.; Campilongo, X.; van de Walle, A.; Schroers, J.; Kusne, A.G.; Takeuchi, I.; Zurek, E.; Buongiorno Nardelli, M.; Fornari, M.; Lederer, Y.; Levy, O.; Toher, C.; Curtarolo, S.
aflow++: a C++ framework for autonomous materials design
Computational Materials Science **217**, 111889 (2023)
107. Pablo-Navarro, J.; Klingner, N.; Hlawacek, G.; Kakay, A.; Bischoff, L.; Narkovic, R.; Mazarov, P.; Hübner, R.; Meyer, F.; Pilz, W.; Lindner, J.; Lenz, K.
Direct magnetic manipulation of a permalloy nanostructure by a focused cobalt ion beam
Physical Review Applied **20**, 044068 (2023)
108. Patel, G.I.; Ganss, F.; Salikhov, R.; Stienen, S.; Fallarino, L.; Ehrler, R.; Gallardo, R.A.; Hellwig, O.; Lenz, K.; Lindner, J.
Structural and magnetic properties of thin cobalt films with mixed hcp and fcc phases
Physical Review B **108**, 184429 (2023)
109. Pathirage, V.; Lasek, K.; Krasheninnikov, A.; Komsa, H.P.; Batzill, M.
Mirror twin boundaries in WSe₂ induced by vanadium doping
Materials Today Nano **22**, 100314 (2023)
110. Patronis, N.; Mengoni, A.; Goula, S.; et al.
Status report of the n_TOF facility after the 2nd CERN long shutdown period
EPJ Techniques and Instrumentation **10**, 13 (2023)
111. Pile, S.; Ney, A.; Lenz, K.; Narkovic, R.; Lindner, J.; Wintz, S.; Förster, J.; Mayr, S.; Weigand, M.
Quantifying the spin-wave asymmetry in single and double rectangular Ni₈₀Fe₂₀ microstrips by TR-STXM, FMR and micromagnetic simulations
IEEE Transactions on Magnetics **59**, 1300905 (2023)
112. Polatkan, S.; Uykur, E.; Mohelsky, I.; Wyzula, J.; Orlita, M.; Shekhar, C.; Felser, C.; Dressel, M.; Pronin, A.V.
Exchange gap in GdPtBi probed by magneto-optics
Physical Review B **108**, L201201 (2023)

113. Polatkan, S.; Uykur, E.; Wyzula, J.; Orlita, M.; Shekhar, C.; Felser, C.; Dressel, M.; Pronin, A.V. **Magneto-optical response of the Weyl semimetal NbAs: Experimental results and hyperbolic-band computations**
Physical Review B **108**, L241201 (2023)
114. Pothineni, B.K.; Kollmann, S.; Li, X.; Grundmeier, G.; Erb, D.; Keller, A. **Adsorption of Ferritin at Nanofaceted Al₂O₃ Surfaces**
International Journal of Molecular Sciences **24**, 12808 (2023)
115. Prucnal, S.; Gago, R.; Gonzales Calatayud, D.; Rebohle, L.; Liedke, M.O.; Butterling, M.; Wagner, A.; Helm, M.; Zhou, S. **TiO₂ phase engineering by millisecond range annealing for highly efficient photocatalysis**
Journal of Physical Chemistry C **127**, 12686 (2023)
116. Pylypovskiy, O.; Hedrich, N.; Tomilo, A.; Kosub, T.; Wagner, K.; Hübner, R.; Shields, B.; Sheka, D.; Faßbender, J.; Maletinsky, P.; Makarov, D. **Interaction of domain walls with grain boundaries in uniaxial insulating antiferromagnets**
Physical Review Applied **20**, 014020 (2023)
117. Rachamin, R.; Di Falco, S.; Ferrari, A.; Giusti, V.; Müller, S.; Pronskikh, V. **Background Studies and Normalization of Signal Events in the Mu2e Experiment**
Journal of Instrumentation **18**, C11024 (2023)
118. Radic, D.; Peterlechner, M.; Posselt, M.; Bracht, H. **The Impact of Energy Filtering on Fluctuation Electron Microscopy**
Microscopy and Microanalysis **29**, 189 (2023)
119. Radić, D.; Peterlechner, M.; Posselt, M.; Bracht, H. **Fluctuation Electron Microscopy on Amorphous Silicon and Amorphous Germanium**
Microscopy and Microanalysis **29**, 477 (2023)
120. Radic, D.; Peterlechner, M.; Spangenberg, K.; Posselt, M.; Bracht, H. **Challenges of Electron Correlation Microscopy on Amorphous Silicon and Amorphous Germanium**
Microscopy and Microanalysis **29**, 1579 (2023)
121. Rajbhar, M.; Das, P.; Möller, W.; Chatterjee, S. **Core-Shell Nanostructures of Tungsten Oxide and Hydrogen Titanate for H₂ Gas Adsorption**
ACS Applied Nano Materials **6**, 212 (2023)
122. Ratajczak, R.; Guzewicz, E.; Prucnal, S.; Mieszczynski, C.; Jozwik, P.; Barlak, M.; Romaniuk, S.; Gieraltowska, S.; Wozniak, W.; Heller, R.; Kentsch, U.; Facsko, S. **Enhanced Luminescence of Yb³⁺ Ions Implanted to ZnO through the Selection of Optimal Implantation and Annealing Conditions**
Materials **16**, 1756 (2023)
123. Ratschinski, I.; Nagarajan, S.; Trommer, J.; Luferau, A.; Khan, M.B.; Erbe, A.; Georgiev, Y.; Mikolajick, T.; Smith, S.C.; König, D.; Hiller, D. **Significant Resistance Reduction in Modulation-Doped Silicon Nanowires via Aluminum-Induced Acceptor States in SiO₂**
Physica Status Solidi (A) **220**, 2300068 (2023)
124. Richter, M.; Sikorski, J.; Makushko, P.; Zabala, Y.; Venkiteswaran, V.K.; Makarov, D.; Misra, S. **Locally addressable energy efficient actuation of magnetic soft actuator array systems**
Advanced Science **10**, 2302077 (2023)

125. Rizzato, R.; Schalk, M.; Mohr, S.; Hermann, J.C.; Leibold, J.P.; Bruckmaier, F.; Salvitti, G.; Ji, P.; Astakhov, G.; Kentsch, U.; Helm, M.; Stier, A.V.; Finley, J.J.; Bucher, D.B.
Extending the coherence of spin defects in hBN enables advanced qubit control and quantum sensing
Nature Communications **14**, 5089 (2023)
126. Rubio-Giménez, V.; Arnauts, G.; Wang, M.; Oliveros Mata, E.S.; Huang, X.; Lan, T.; Tietze, M.L.; Kravchenko, D.E.; Smets, J.; Wauteraerts, N.; Khadiev, A.; Novikov, D.V.; Makarov, D.; Dong, R.; Ameloot, R.
Chemical Vapor Deposition and High-Resolution Patterning of a Highly Conductive Two-Dimensional Coordination Polymer Film
Journal of the American Chemical Society **145**, 152 (2023)
127. Ruiz Arce, D.D.; Jazavandi Ghamsari, S.; Erbe, A.; Samano, E.C.
Metallic Nanowires Self-Assembled in quasi-circular Nanomolds Templated by DNA Origami
International Journal of Molecular Sciences **24**, 13549 (2023)
128. Ruiz-Fresneda, M.A.; Schaefer, S.; Hübner, R.; Fahmy, K.; Merroun, M.L.
Exploring Antibacterial Activity and Bacterial-Mediated Allotropic Transition of Differentially Coated Selenium Nanoparticles
ACS Applied Materials and Interfaces **15**, 29958 (2023)
129. Salikhov, R.; Ilyakov, I.; Körber, L.; Kakay, A.; Gallardo, R.A.; Ponomaryov, O.; Deinert, J.-C.; de Oliveira, T.; Lenz, K.; Faßbender, J.; Bonetti, S.; Hellwig, O.; Lindner, J.; Kovalev, S.
Coupling of terahertz light with nanometre-wavelength magnon modes via spin-orbit torque
Nature Physics **13**, 529 (2023)
130. Samad, F.; Hellwig, O.
Determining the preferred directions of magnetisation in cubic crystals using symmetric polynomial inequalities
Emergent Scientist **7**, 1 (2023)
131. Sandoval Bojorquez, D.I.; Janićijević, Ž.; Palestina Romero, B.; Oliveros Mata, E.S.; Laube, M.; Feldmann, A.; Kegler, A.; Drewitz, L.; Fowley, C.; Pietzsch, J.; Faßbender, J.; Tonn, T.; Bachmann, M.; Baraban, L.
Impedimetric Nanobiosensor for the Detection of SARS-CoV-2 Antigens and Antibodies
ACS Sensors **8**, 576 (2023)
132. Scharf, S.; Notz, S.; Thomas, R.; Mehring, M.; Tegenkamp, C.; Formánek, P.; Hübner, R.; Lang, H.
Porous Magnesium Oxide by Twin Polymerization: From Hybrid Materials to Catalysis
European Journal of Inorganic Chemistry **26**, e202200663 (2023)
133. Scheffler, D.; Steuer, O.; Zhou, S.; Siegl, L.; Goennenwein, S.T.B.; Lammel, M.
Aluminium substituted yttrium iron garnet thin films with reduced Curie temperature
Physical Review Materials **7**, 094405 (2023)
134. Schütt, J.; Nhalil, H.; Faßbender, J.; Klein, L.; Grosz, A.; Makarov, D.
Modular droplet-based fluidics for large volume libraries of individual multiparametric codes in lab-on-chip systems
Advanced Sensor Research **2**, 2300101 (2023)

135. Shaikh, M.S.; Wen, S.; Catuneanu, M.-T.; Wang, M.; Erbe, A.; Prucnal, S.; Rebohle, L.; Zhou, S.; Jamshidi, K.; Helm, M.; Berencen, Y.
On-chip lateral Si:Te PIN photodiodes for room-temperature detection in the telecom optical wavelength bands
Optics Express **31**, 26451 (2023)
136. Sheina, V.; Lang, G.; Stolyarov, V.; Marchenkov, V.; Naumov, S.; Perevalova, A.; Girard, J.-C.; Rodary, G.; David, C.; Romuald Sop, L.; Pierucci, D.; Ouerghi, A.; Cantin, J.-L.; Leridon, B.; Ghorbani Asl, M.; Krasheninnikov, A.; Aubin, H.
Hydrogenic Spin-Valley States of the Bromine Donor in 2H-MoTe₂
Communications Physics **6**, 135 (2023)
137. Shi, H.; Yi, A.; Ding, J.; Liu, X.; Qin, Q.; Yi, J.; Hu, J.; Wang, M.; Cai, D.; Wang, J.; Xu, K.; Mu, F.; Suga, T.; Heller, R.; Wang, M.; Zhou, S.; Xu, W.; Huang, K.; You, T.; Ou, X.
Defect evolution in GaN thin film heterogeneously integrated with CMOS-compatible Si(100) substrate by ion-cutting technology
Science China - Information Sciences **66**, 219403 (2023)
138. Shi, X.; Ling, Y.; Li, Y.; Li, G.; Li, J.; Wang, L.; Min, F.; Hübner, R.; Yuan, S.; Zhan, J.; Cai, B.
Complete Glucose Electrooxidation Enabled by Coordinatively Unsaturated Copper Sites in Metal-Organic Frameworks
Angewandte Chemie - International Edition **62**, e202316257 (2023)
139. Singh, P.; Ghosh, S.; Jain, M.; Singh, A.; Singh, R.; Balal, M.; Roy Barman, S.; Kentsch, U.; Zhou, S.; Bhattacharya, S.; Srivastava, P.
Highly Enhanced Defects Driven Room Temperature Ferromagnetism in Mixed-phase MoS₂-MoO_x Films
Journal of Physical Chemistry C **127**, 16010 (2023)
140. Skopinski, L.; Kretschmer, S.; Ernst, P.; Herder, M.; Madauß, L.; Breuer, L.; Krasheninnikov, A.; Schleberger, M.
Velocity distributions of particles sputtered from supported two-dimensional MoS₂ during highly charged ion irradiation
Physical Review B **107**, 075418 (2023)
141. Sobolev, S.; Lanz, A.P.; Dong, T.; Pokharel, A.; Kabanov, V.; Xu, T.-Q.; Wang, Y.; Gan, Z.-Z.; Shi, L.-Y.; Wang, N.-L.; Pashkin, O.; Uykur, E.; Winnerl, S.; Helm, M.; Demsar, J.
Possible Eliashberg-Type Superconductivity Enhancement Effects in a Two-Band Superconductor MgB₂ Driven by Narrow-Band THz Pulses
Physical Review Letters **131**, 186903 (2023)
142. Sojková, M.; Piš, I.; Hrdá, J.; Vojteková, T.; Pribusová Slušná, L.; Vegso, K.; Siffalovic, P.; Nadazdy, P.; Dobročka, E.; Krbal, M.; Fons, P.J.; Munnik, F.; Magnano, E.; Hulman, M.; Bondino, F.
Lithium-induced reorientation of few-layer MoS₂ films
Chemistry of Materials **35**, 6246 (2023)
143. Sorokin, S.; Anwar, M.S.; Hlawacek, G.; Boucher, R.; Salgado Cabaco, J.; Potzger, K.; Lindner, J.; Faßbender, J.; Bali, R.
Transport properties of Fe₆₀Al₄₀ during the B2 to A2 structural phase transition
New Journal of Physics **25**, 093036 (2023)
144. Steinbach, D.; Neubert, R.; Gersdorf, S.; Schimpf, C.; Erb, D.; Rafaja, D.; Plamper, F.A.; Mertens, F.
Morphology and orientation change of layer-by-layer deposited one- and two-dimensional coordination polymer nanocrystals containing rhodium paddle-wheel units
CrystEngComm **25**, 4568 (2023)

145. Steuer, O.; Schwarz, D.; Oehme, M.; Schulze, J.; Maćzko, H.; Kudrawiec, R.; Fischer, I.A.; Heller, R.; Hübner, R.; Khan, M.M.; Georgiev, Y.; Zhou, S.; Helm, M.; Prucnal, S.
Band-gap and strain engineering in GeSn alloys using post-growth pulsed laser melting
Journal of Physics: Condensed Matter **35**, 055302 (2023)
146. Storm, A.; Köster, J.; Ghorbani Asl, M.; Kretschmer, S.; Gorelik, T.E.; Kinyanjui, M.K.; Krasheninnikov, A.; Kaiser, U.
Electron-Beam- and Thermal-Annealing-Induced Structural Transformations in Few-Layer MnPS₃
ACS Nano **17**, 4250 (2023)
147. Storm, A.; Köster, J.; Ghorbani Asl, M.; Kretschmer, S.; Gorelik, T.E.; Krasheninnikov, A.; Kaiser, U.
Structural transformations in few-layer MnPSe₃ stimulated by thermal annealing and electron irradiation
Journal of Physical Chemistry C **127**, 24713 (2023)
148. Stübner, K.; Balco, G.; Schmeißer, N.
RIVERSAND: A new tool for efficient computation of catchmentwide erosion rates
Radiocarbon (2023), DOI: 10.1017/RDC.2023.74
149. Subakti, S.; Daqiqshirazi, M.; Wolf, D.; Linck, M.; Kern, F.L.; Jain, M.; Kretschmer, S.; Krasheninnikov, A.; Brumme, T.; Lubk, A.
Electron holographic mapping of structural reconstruction at mono- and bilayer steps of h-BN
Physical Review Research **5**, 033137 (2023)
150. Titze, M.; Poplawsky, J.D.; Kretschmer, S.; Krasheninnikov, A.; Doyle, B.L.; Bielejec, E.S.; Hobler, G.; Belianinov, A.
Measurement and Simulation of Ultra-Low-Energy Ion–Solid Interaction Dynamics
Micromachines **14**, 1884 (2023)
151. Tsirlin, A.A.; Ortiz, B.R.; Dressel, M.; Wilson, S.D.; Winnerl, S.; Uykur, E.
Effect of nonhydrostatic pressure on the superconducting kagome metal CsV₃Sb₅
Physical Review B **107**, 174107 (2023)
152. Uaman Svetikova, T.A.; de Oliveira, T.; Pashkin, A.; Ponomaryov, O.; Berger, C.; Fuerst, L.; Bayer, F.; Novik, E.; Buhmann, H.; Molenkamp, L.; Helm, M.; Kiessling, T.; Winnerl, S.; Kovalev, S.; Astakhov, G.
Giant THz nonlinearity in topological and trivial HgTe-based heterostructures
ACS Photonics **10**, 3708 (2023)
153. Unutulmazsoy, Y.; Kalanov, D.; Oh, K.; Karimi Aghda, S.; Gerlach, J.W.; Braun, N.; Munnik, F.; Lotnyk, A.; Schneider, J.M.; Anders, A.
Towards decoupling the effects of kinetic and potential ion energies: Ion flux dependent structural properties of thin (V,Al)N films deposited by pulsed filtered cathodic arc
Journal of Vacuum Science & Technology A **41**, 063106 (2023)
154. Uzunova, V.; Körber, L.; Kavvadia, A.; Quasebarth, G.; Schultheiß, H.; Kakay, A.; Ivanov, B.
Nontrivial Aharonov-Bohm effect and alternating dispersion of magnons in cone-state ferromagnetic rings
Physical Review B **108**, 174445 (2023)
155. Vallinayagam, M.; Sudheer, A.E.; Aravindh, A.S.; Devaraj, M.; Nadarajan, R.; Katta, R.; Posselt, M.; Zschornak, M.
Novel Metalless Chalcogen-Based Janus Layers: A Density Functional Theory Study
Journal of Physical Chemistry C **127**, 17029 (2023)

156. Vasselon, T.; Hernandez-Minguez, A.; Hollenbach, M.; Astakhov, G.; Santos, P.V.
Acoustically induced spin resonances of silicon-vacancy centers in 4H-SiC
Physical Review Applied **20**, 034017 (2023)
157. Vivo Vilches, C.; Rugel, G.; Lachner, J.; Koll, D.; Stübner, K.; Fichter, S.; Winkler, S.; Wallner, A.
Pushing the limits of ^{41}Ca AMS with CaF_2 targets at DREAMS
Nuclear Instruments and Methods in Physics Research B **540**, 188 (2023)
158. Volkov, O.; Wolf, D.; Pylypovskyi, O.; Kakay, A.; Sheka, D.D.; Büchner, B.; Faßbender, J.; Lubk, A.; Makarov, D.
Chirality coupling in topological magnetic textures with multiple magnetochiral parameters
Nature Communications **14**, 1491 (2023)
159. Wang, C.; Herranz, J.; Hübner, R.; Schmidt, T.J.; Eychmüller, A.
Element Distributions in Bimetallic Aerogels
Accounts of Chemical Research **56**, 237 (2023)
160. Wang, M.; Shaikh, M.S.; Kentsch, U.; Heller, R.; Zhou, S.
Sub-band gap infrared absorption in Si implanted with Mg
Semiconductor Science and Technology **38**, 014001 (2023)
161. Wang, M.; Wang, G.; Naisa, C.; Fu, Y.; Manoj Gali, S.; Paasch, S.; Wang, M.; Wittkaemper, H.; Papp, C.; Brunner, E.; Zhou, S.; Beljonne, D.; Steinrück, H.-P.; Dong, R.; Feng, X.
Poly(benzimidazobenzophenanthroline)-Ladder-Type Two-Dimensional Conjugated Covalent Organic Framework for Fast Proton Storage
Angewandte Chemie - International Edition **62**, e202310937 (2023)
162. Wang, S.; Scandurra, L.; Hübner, R.; Gro Nielsen, U.; Wu, C.
Tailored Particle Catalysts for Multistep One-pot Chemoenzymatic Cascade in Pickering Emulsions
ChemCatChem **15**, e202201229 (2023)
163. Weinert, T.; Erb, D.; Hübner, R.; Facsko, S.
Bottom-up Fabrication of FeSb_2 Nanowires on Crystalline GaAs Substrates with Ion-induced Pre-patterning
Frontiers in Physics **11**, 1149608 (2023)
164. Wen, S.; Shaikh, M.S.; Steuer, O.; Prucnal, S.; Grenzer, J.; Hübner, R.; Turek, M.; Pyszniak, K.; Reiter, S.; Fischer, I.A.; Georgiev, Y.; Helm, M.; Wu, S.; Luo, J.-W.; Zhou, S.; Berencen, Y.
Room-temperature extended short-wave infrared GeSn photodetectors realized by ion beam techniques
Applied Physics Letters **123**, 081109 (2023)
165. Wenzel, M.; Tsirlin, A.A.; Capitani, F.; Chan, Y.T.; Ortiz, B.R.; Wilson, S.D.; Dressel, M.; Uykur, E.
Pressure evolution of electron dynamics in the superconducting kagome metal CsV_3Sb_5
npj Quantum Materials **8**, 45 (2023)
166. Wieser, A.; Lachner, J.; Martschini, M.; Zok, D.; Priller, A.; Steier, P.; Golser, R.
Detection of ^{135}Cs & ^{137}Cs in environmental samples by AMS
Nuclear Instruments and Methods in Physics Research B **538**, 36 (2023)
167. Wilhelm, R.A.; Deuzeman, M.J.; Rai, S.; Husinsky, W.; Szabo, P.S.; Biber, H.; Stadlmayr, R.; Cupak, C.; Hundsbichler, J.; Lemell, C.; Möller, W.; Mutzke, A.; Hobler, G.; Versolato, O.O.; Aumayr, F.; Hoekstra, R.
On the missing single collision peak in low energy heavy ion scattering
Nuclear Instruments and Methods in Physics Research B **544**, 165123 (2023)

168. Winkler, S.; Mbele, V.; Khosa, R.; Corbett, L.; Bierman, P.; Hidy, A.; Brown, T.; Makhubela, T.; Kramers, J.; Tooth, S.
¹⁰Be at iThemba LABS using a silicon nitride membrane stack as absorber for isobar suppression
Nuclear Instruments and Methods in Physics Research B **540**, 102 (2023)
169. Woodborne, S.; Miller, D.; Evans, M.; Winkler, S.
Radiocarbon-dated evidence for Late Pleistocene and Holocene coastal change at Yzerfontein, Western Cape, South Africa
South African Journal of Science **119**, 15505 (2023)
170. Xiao, H.; Li, S.; He, Z.; Wu, Y.; Gao, Z.; Hu, C.; Hu, S.; Wang, S.; Liu, C.; Shang, J.; Liao, M.; Makarov, D.; Liu, Y.; Li, R.-W.
Dual Mode Strain–Temperature Sensor with High Stimuli Discriminability and Resolution for Smart Wearables
Advanced Functional Materials **18**, 2214907 (2023)
171. Xue, G.; Li, Y.; Du, R.; Wang, J.; Hübner, R.; Gao, M.; Hu, Y.
Leveraging Ligand and Composition Effects: Morphology-Tailorable Pt–Bi Bimetallic Aerogels for Enhanced (Photo-)Electrocatalysis
Small **19**, 2301288 (2023)
172. Yong, L.; Pang, C.; Amekura, H.; Schumann, T.; Peng, L.; Zhixian, W.; Haocheng, L.; Li, R.
Fine-tuning of plasmonics by Au@AuY/Au core-shell nanoparticle monolayer for enhancement of third-order nonlinearity
Applied Surface Science **631**, 157582 (2023)
173. Yu, C.-C.; Ormeci, A.; Veremchuk, I.; Feng, X.-J.; Prots, Y.; Krnel, M.; Koželj, P.; Schmidt, M.; Burkhardt, U.; Böhme, B.; Akselrud, L.; Baitinger, M.; Grin, Y.
Na₂Ga₇: A Zintl–Wade Phase Related to “α-Tetragonal Boron”
Inorganic Chemistry **62**, 9054 (2023)
174. Zhang, J.; Reif, J.; Strobel, C.; Chava, P.; Erbe, A.; Voigt, A.; Mikolajick, T.; Kirchner, R.
Dry release of MEMS origami using thin Al₂O₃ films for facet-based device integration
Micro and Nano Engineering **19**, 100179 (2023)
175. Zhang, X.; Ghorbani Asl, M.; Zhang, Y.; Krasheninnikov, A.
Quasi-2D fcc lithium crystals inside defective bi-layer graphene: insights from first-principles calculations
Materials Today Energy **34**, 101293 (2023)
176. Zhang, X.; Wang, C.; Chen, K.; Clark, A.H.; Hübner, R.; Zhan, J.; Zhang, L.; Eychmüller, A.; Cai, B.
Optimizing the Pd Sites in Pure Metallic Aerogels for Efficient Electrocatalytic H₂O₂ Production
Advanced Materials **35**, 2211512 (2023)
177. Zhang, X.; Wang, T.; Wang, C.; Hübner, R.; Eychmüller, A.; Zhan, J.; Cai, B.
Bimetallic Pt-Hg Aerogels for Electrocatalytic Upgrading of Ethanol to Acetate
Small **19**, 2207557 (2023)
178. Zheng, Y.; Petersen, A.S.; Wan, H.; Hübner, R.; Zhang, J.; Wang, J.; Qi, H.; Ye, Y.; Liang, C.; Yang, J.; Cui, Z.; Meng, Y.; Zheng, Z.; Rossmeisl, J.; Liu, W.
Scalable and Controllable Synthesis of Pt-Ni Bunched-Nanocages Aerogels as Efficient Electrocatalysts for Oxygen Reduction Reaction
Advanced Energy Materials **13**, 2204257 (2023)

Active Patents and Patent Applications

1. **Flüssigmetall-Ionenquelle zur Erzeugung von Lithium-Ionenstrahlen**
P0709 102007027097.8 DE
2. **Strahlungsdetektor, Verwendung eines Strahlungsdetektors und Verfahren zur Herstellung eines Strahlungsdetektors**
P0907 102009017505.9 DE
3. **Integrated non-volatile memory elements, design and use**
P1108 102011051767.7 DE, US
4. **Magnetisierbare Einzel- und Mehrschichtstrukturen, deren Herstellung und Verwendung**
P1109 102011052217.4 DE
5. **Carrier material for electrically polarizable biomaterials, polyelectrolyte materials, atoms, ions and molecules; its manufacture and use**
P1112 12772707.1 AT, CH, DE, US
6. **Integrierter nichtflüchtiger Analogspeicher**
P1204 102012102326.3 DE
7. **Integrierte Elektrode mit nichtflüchtig positionierbarer, statisch geladener Grenzschicht, Aufbau und Verwendung**
P1205 102012104425.2 DE
8. **Magnetooptik mit optischen Polarisationsgittern aus strukturierten unmagnetischen Metallen**
P1309 112014001145.2 DE
9. **Magnetisierbare Halbleiter und Oxide mit permanenter Magnetisierung, deren Herstellung und Verwendung**
P1313 102013209278.4 DE
10. **Variable capacitance diode, method for producing a variable capacitance diode, and storage device and detector comprising such a variable capacitance diode**
P1403 102014105639.6 CN, DE, US
11. **Strukturierungsverfahren**
P1404 102014107458.0 CN, DE
12. **Complementary resistance switch**
P1505 15166520.5 BE, DE, FR, GB
13. **Complementary resistance switch, contact-connected polycrystalline piezo- or ferroelectric thin-film layer, method for encrypting a bit sequence**
P1506 14/761,319 US
14. **Method and circuit arrangement for encrypting and decrypting a bit sequence**
P1507 14703281.7 DE, FR, GB
15. **Complementary resistance switch, contact-connected polycrystalline piezo- or ferroelectric thin-film layer, method for encrypting a bit sequence**
P1508 14/800,785 US
16. **Self-cleaning high temperature resistant solar selective coating**
P1510 P201431972 ES
17. **Method for producing silicon-based anodes for secondary batteries**
P1603 201780011186.2 AT, CH, CN, DE, ES, FR, GB, IT, PL, US

18. **Method and means for operating a complementary analogue reconfigurable memristive resistive switch and use thereof as an artificial synapse**
P1604 *102016205860.6* *CN, DE, US*
19. **Ionenmikroskopievorrichtung**
P1608 *102016112328.5* *DE*
20. **THz-Antenne und Vorrichtung zum Senden und/oder Empfangen von THz-Strahlung**
P1609 *102016116900.5* *DE*
21. **Vorrichtung und Verfahren zur Umwandlung thermischer Energie in elektrische Energie**
P1614 *102017126803.0* *DE*
22. **Apparatus for characterizing the electrical resistance of a measurement object**
P1702 *102017105317.4* *CN, DE, EP, US*
23. **Schichtanordnung, elektronisches Bauteil mit einer Schichtanordnung und Verwendung einer Schichtanordnung**
P1703 *102017109082.7* *DE*
24. **Vorrichtung und Verfahren zum Erzeugen von Ionenpulsen**
P1709 *102017218456.6* *DE*
25. **Teilchenspektrometer und Teilchenspektrometrieverfahren**
P1803 *102018106412.8* *DE*
26. **Method for continuously determining all of the components of the resistance tensor of thin films**
P1804 *102018106466.7* *CN, DE, EP, US*
27. **Transparent specimen slide**
P1805 *102018107810.2* *DE, US*
28. **Method for the reconfiguration of a vortex density in a rare earth manganate, a non-volatile impedance switch and use thereof**
P1809 *102018112605.0* *CN, DE, EP, US*
29. **Schichtabfolge zur Erzeugung von Elektrolumineszenz und deren Verwendung**
P1813 *102018117210.9* *DE*
30. **Verfahren zur Herstellung eines keramischen Materials mit lokal einstellbarem Permeabilitätsgradienten, dessen Anwendung in einem Beschichtungsverfahren sowie dessen Verwendung**
P1819 *102018125270.6* *DE*
31. **Verfahren zum Herstellen eines gedruckten magnetischen Funktionselements und gedrucktes magnetisches Funktionselement**
P1908 *102019211970.0* *DE, EP*
32. **Vorrichtung zur gezielten Anordnung von in einem Analyten gelösten, elektrisch polarisierbaren Materialien, Verfahren zur Bestimmung eines isoelektrischen Punktes eines elektrisch isolierenden Materials, Verfahren zum gezielten Anordnen eines in einem Analyten gelösten elektrisch polarisierbaren Materials**
P2001 *102020200470.6* *DE, EP*
33. **Einrichtung zur Nutzung von thermischer Energie mit einem Formgedächtnismaterial**
P2015 *102020118363.1* *DE*

Concluded scientific degrees

PhD theses

1. Echresh, Ahmad
Highly-doped germanium nanowires: fabrication, characterization, and application
TU Dresden, 30.06.2023
2. Hula, Tobias
Experimental characterization of four-magnon scattering processes in ferromagnetic conduits
TU Chemnitz, 23.08.2023
3. Koll, Dominik
A 10-million year time profile of interstellar influx to Earth mapped through supernova ^{60}Fe and r-process ^{244}Pu
TU Dresden, 08.11.2023
4. Körber, Lukas
Spin waves in curved magnetic shells
TU Dresden, 28.06.2023
5. Lungwitz, Frank
Development of tantalum-doped tin oxide as new solar selective material for solar thermal power plants
TU Chemnitz, 28.07.2023

Bachelor/Master/Diploma theses

1. Bhattacharya, Debadreeto
Fabrication and characterisation of junctionless nanowire transistors (JNTs) for gas-phase sensing
TU Dresden (M.Sc.), 27.10.2023
2. Chennur, Madhuri
Electrical contacting of nanostructures assembled by DNA origami techniques
TU Dresden (M.Sc.), 07.07.2023
3. Vahle, Josua Simon
Bestimmung der kosmogenen Radionuklide ^{10}Be und ^{26}Al in ausgewählten Mondproben mittels Beschleuniger-Massenspektrometrie
TU Dresden (B.Sc.), 27.11.2023
4. Vieler, Leonie
Defektcharakterisierung von Gateoxiden für die Anwendung von Spin-Halbleiter-Qubits
TU Dresden (M.Sc.), 25.07.2023

Awards and honors

1. **Akhmadaliev, Shavkat; von Borany, Johannes; Görlich, Manuel; Hilliges, Heike; Lang, Kai; Mester, René; Reichel, André; Tarnow, Thomas; Vollmer, Andreas; Weise, Axel; Winkelmann, Jürgen; Eisenwinder, Stefan; Jarschel, Kay; Kentsch, Ulrich; Ludewig, Frank; Nierobisch, Franziska; Putzke, Tobias, and Facsko, Stefan**

The IBC Implanter Team, part of the department “Ion Beam Center”, has been presented with the **HZDR Transfer Award 2023** in recognition of ‘their outstanding commitment to providing beam time for the semiconductor industry’.

2. **Fekri, Zahra**

Doctoral researcher in the department “NanoElectronics” received a **Travel Grant** to the **Graphene 2023 Conference**.

3. **Friedrich, Rico**

PostDocs in the group “Atomistic simulations of irradiation-induced phenomena” was appointed as an **TU Dresden Young Investigator** upon the establishment of the **DRESDEN concept Research Group** ‘Autonomous Materials Thermodynamics (AutoMaT)’.

4. **Ghosh, Sayantan**

Doctoral researcher in the department “Nanoelectronics” received the **Student Award** of the **NanoNet+ Workshop 1D and 2D Materials and Devices for Electronic and Photonic Applications**, Görlitz, Germany, September 11 –13, 2023 for his oral contribution ‘Junctionless Nanowire Transistors: From Devices to Sensing Applications’.

5. **Helm, Manfred**

Head of the institute was appointed as an **APS Fellow** and an **APS Outstanding Referee** by the American Physical Society (APS).

6. **Körber, Lukas**

Doctoral researcher in the department “Magnetism” successfully defended his doctoral thesis entitled *Spin waves in curved magnetic shells* with the highest honors, ‘**Summa Cum Laude**’, at the Faculty of Physics of TU Dresden on June 28th, 2023.

In recognition of this achievement, he was awarded the **Helmholtz Doctoral Award 2023** (Research Area MATTER, Track A), and the **HZDR Doctoral Award 2023**.

7. **Koll, Dominik**

Doctoral researcher in the department “Accelerator Mass Spectrometry and Isotope Research” received the **Best Presentation Award** at the **HZDR Doctoral Seminar 2023**.

8. **Krasheninnikov, Arkady**

Head of the group “Atomistic Simulations of Irradiation-induced Phenomena” was once again announced as **Highly Cited Researcher 2023** by Clarivate Analytics (Web of Science), Jersey, UK.

9. **Makarov, Denys**

Head of the department “Intelligent Materials and Systems” was appointed as **Administrative Committee Member** of the **IEEE Magnetism Society**.

10. **Neumann, Bruno**

Doctoral researcher in the department “Magnetism” obtained the Best **Poster Award** at the **Dresden Days on Magnetocalorics (DDMC 2023)** for his contribution *Heroic harvesting of waste heat with a thermoelastic generator*.

11. **Sequeira, Miguel**

PostDocs in the group “Ion Beam Analysis” obtained a **2022 Outstanding Reviewer Award** by **IOP Publishing**.

12. **Roldan, Fernandez**

PostDoc in the department “Intelligent Materials and Systems” obtained a scholarship of the Alexander von Humboldt Foundation.

13. **Uykur, Ece**

PostDoc in the department “Spectroscopy” obtained the **Habilitation in Physics** of the **University Stuttgart** with a thesis on *Unconventional carriers in Kagome metals*.

14. **Volkov, Oleksii and Pylypovskyi, Oleksandr**

PostDocs in the department “Intelligent Materials and Systems” won the **HZDR Research Award 2023** for their *theoretical and experimental investigations to understand chiral symmetry breaking in magnetic 3D-textures*.

15. **Wolf, Janis**

Doctoral researcher in the department “Accelerator Mass Spectrometry and Isotope Research” obtained the **Women in Nuclear (WiN) Germany Award 2023** for her Master’s thesis “Study of Actinide Signatures as Potential Markers for the Anthropocene”.

Invited conference contributions

1. Astakhov, G.
Application of focused ion beams for quantum and information technologies
Sino-German Symposium Defect Engineering in SiC and Other Wide Bandgap Semiconductor, 23.-24.10.2023, Conference Center, SUSTech, Shenzhen, Guangdong, China
2. Astakhov, G.
Hybrid quantum technologies with spin qubits in SiC
Seminar at the Institute of Applied Quantum Technologies, 09.02.2023, Erlangen, Germany
3. Astakhov, G.; Hollenbach, M.; Klingner, N.; Jagtap, N.; Bischoff, L.; Fowley, C.; Kentsch, U.; Hlawacek, G.; Erbe, A.; Abrosimov, N.V.; Berencen, Y.; Helm, M.
Ion-induced telecom single-photon emitters in silicon
4th Science Workshop of the Program MML, 27.-29.09.2023, Jena, Germany
4. Astakhov, G.; Hollenbach, M.; Klingner, N.; Jagtap, N.; Bischoff, L.; Fowley, C.; Kentsch, U.; Hlawacek, G.; Erbe, A.; Abrosimov, N.V.; Helm, M.; Berencen, Y.
Ion-induced telecom single-photon emitters in silicon
25th International Conference on the Electronic Properties of Two-Dimensional Systems (EP2DS-25) and 21st International Conference on Modulated Semiconductor Structures (MSS-21), 10.-14.07.2023, Grenoble, France
5. Astakhov, G.; Hollenbach, M.; Klingner, N.; Jagtap, N.; Bischoff, L.; Fowley, C.; Kentsch, U.; Hlawacek, G.; Erbe, A.; Abrosimov, N.V.; Helm, M.; Berencen, Y.
Ion-induced telecom single photon emitters in silicon
Workshop on Spin-Photon Interfaces for Quantum Communication, 01.09.2023, Vienna, Austria
6. Bali, R.; Potzger, K.; Lindner, J.; Faßbender, J.
Magneto-structural phase transitions for direct magnetic patterning
7th International Conference on Nanostructuring by Ion Beams (ICNIB 2023), 02.-04.11.2023, Dehradun, Indien
7. Berencen, Y.
Strategic wafer-scale creation of telecom single-photon emitters in silicon for large-scale quantum photonic integrated circuits
2023 RAISIN – Roadmap for Applications of Implanted Single Impurities Network, 06.-08.09.2023, University of Surrey, Guildford, United Kingdom
8. Fichter, S.; Wallner, A.
Accelerator Mass Spectrometry of Actinides – Radiochemical Separations and Capabilities
SANDA Workshop, 06.12.2023, Geel, Belgien
9. Fink, L.; Kar, S.; Lünser, K.; Nielsch, K.; Reith, H.; Fähler, S.
Integration of Multifunctional Epitaxial (Magnetic) Shape Memory Films in Silicon Microtechnology
Bokomat, 28.-29.09.2023, Bochum, Deutschland
10. Friedrich, R.
Data-Driven Research for the Discovery of Novel Two-Dimensional and Ionic Materials
Invited talk at BTU Cottbus-Senftenberg, 20.01.2023, Cottbus, Deutschland
11. Friedrich, R.
Data-Driven Materials Science
HZDR Data Management Day, 21.11.2023, Dresden, Deutschland
12. Friedrich, R.
Data-driven Design of Novel Materials and Interfaces Enabling Future Technologies
DRESDEN-concept lunch retreat, 21.09.2023, Dresden, Deutschland
13. Friedrich, R.
The Multi-Dimensional Problem of Discovering Novel (Two-Dimensional) Materials
AFLOW seminar, 09.11.2023, online

14. Friedrich, R.
Geometry Optimization in 2D Materials
DFG SPP 2244 Summer School 2023, 29.08.2023, Dresden, Deutschland
15. Friedrich, R.
Data-Driven Research for the Discovery of Novel Two-Dimensional and Ionic Material
Retreat of the Felser Department of the Max Planck Institute for the Chemical Physics of Solids, 11.-13.01.2023, Bad Schandau, Deutschland
16. Friedrich, R.
Discovering Two-Dimensional Non-van der Waals Materials by Data-driven Research
2nd China-Germany bilateral meeting on topological devices, 2D materials and the future of spintronics, 03.-04.08.2023, Mainz, Deutschland
17. Friedrich, R.; Eckert, H.; Divilov, S.; Curtarolo, S.
AFLOW: Integrated infrastructure for computational materials discovery
International Summer School Materials 4.0, 23.08.2023, Dresden, Deutschland
18. Hilliard, D.; Balaghi, L.; Tauchnitz, T.; Hübner, R.; Fotev, I.; Rana, R.; Pashkin, O.; Vasileiadis, I.; Chatzopoulou, P.; Florini, N.; Dimitrakopoulos, G.P.; Komninou, P.; Winnerl, S.; Schneider, H.; Helm, M.; Dimakis, E.
III-V semiconductor nanowires with unique heterostructure possibilities
XXXVII Panhellenic Conference on Solid State Physics and Materials Science, 17.09.2023, Thessaloniki, Greece
19. Hlawacek, G.
Materials Science with FIBs across Applications and Fluencies at the HZDR Ion Beam Center.
CINT User meeting, 19.-20.09.2023, Santa Fe, USA
20. Honda, M.; Martschini, M.; Lachner, J.; Wieser, A.; Marchhart, O.; Steier, P.; Golser, R.; Sakaguchi, A.
Frontiers of challenging studies utilizing accelerator mass spectrometry in geoscience
71st Annual Conference on Mass Spectrometry, Japan, 15.-17.05.2023, Osaka, Japan
21. Klingner, N.; Hlawacek, G.; Facsko, S.; Wedel, G.; Grunze, S.; Kirschke, T.; Lange, B.; Findeisen, S.; Silvent, J.; Delobbe, A.
TIBUSSII - the first triple beam single ion implantation setup for quantum applications
AVS 69, 09.11.2023, Portland, USA
22. Krause, M.; Niranjana, K.; Barshilia, H.; Escobar-Galindo, R.
Solar thermal energy applications - state of the art and current challenges
V2023 - International conference and Exhibition, 18.-21.09.2023, Dresden, Deutschland
23. Luferau, A.; Dimakis, E.; Pashkin, O.; Winnerl, S.; Helm, M.
Time-resolved THz spectroscopy of single nanowires
10th International Symposium on Terahertz-Related Devices and Technologies (TeraTech 2023), 04.-08.09.2023, Aizu-Wakamatsu, Japan
24. Makarov, D.
Curvilinear magnetism: fundamentals and applications
IEEE Advances in Magnetism conference (AIM2023), 15.-18.01.2023, Moena, Italy
25. Makarov, D.
Curvilinear and 3D micromagnetism: geometrically curved ferro- and antiferromagnets
68th Annual Conference on Magnetism and Magnetic Materials, 30.10.-03.11.2023, Dallas, USA
26. Makarov, D.
Geometrically curved, skin-conformal and self-healable magnetoelectronics
8th International Conference on Superconductivity and Magnetism (ICSM2023), 04.-11.05.2023, Fethiye-Oludeniz, Turkey
27. Makarov, D.
Effects of geometry and topology in curvilinear ferro- and antiferromagnets
7th international conference "Nanomagnetism and spintronics" (Sol-SkyMag 2023), 19.-23.06.2023, San Sebastian, Spain

28. Makarov, D.
Flexible, printable and eco-sustainable magnetoelectronics
The 34th GCCCD Annual Conference "Chemistry and Chemical Engineering, Sensing the World", 02.-03.12.2023, Dresden, Germany
29. Makarov, D.
From curvilinear magnetism to shapeable magnetoelectronics
NATO advanced research workshop "Functional Spintronic Nanomaterials for Radiation Detection and Energy Harvesting", 25.-27.09.2023, Kyiv, Ukraine
30. Makarov, D.
Multifunctional nanostructures
2023 European School on Magnetism, 04.-15.09.2023, Madrid, Spain
31. Makarov, D.
Advanced fabrication
2023 European School on Magnetism, 04.-15.09.2023, Madrid, Spain
32. Makarov, D.
Magnetic composites: from printed, self-healable and eco-sustainable magnetoelectronics to smart magnetic soft robots
PETASPIN 2023 School on "Spintronics: fundamentals and applications" – II edition, 12.-15.12.2023, Messina, Italy
33. Makarov, D.
Curvilinear micromagnetism: from fundamentals to applications
8th Quantum Oxide Research Online Meeting (QUOROM-8), 16.02.2023, London, UK
34. Makarov, D.
Curvilinear magnetism: from fundamentals to applications
Zakopane School of Physics Breaking Frontiers: Submicron Structures in Physics and Biology, 23.-27.05.2023, Zakopane, Poland
35. Makarov, D.
Designing chiral magnetic responses by tailoring geometry of thin films: curvilinear ferro- and antiferromagnets
4th Solid-State Science & Research meeting (SCIRES), 28.-30.06.2023, Zagreb, Croatia
36. Makarov, D.
Tunable room-temperature non-linear Hall effect from the surfaces of elementary bismuth thin films
Annual meeting of the Lu Jiaxi international team, 25.-26.11.2023, Ningbo, China
37. Makarov, D.
Curvilinear and 3D low-dimensional magnetic architectures in research and technology
XII-Latin American Workshop on Magnetism, Magnetic Materials & their Applications, 16.-20.10.2023, Puerto Varas, Chile
38. Makarov, D.
Effects of geometry and topology in curvilinear ferro- and antiferromagnets
Seminar at the QuSpin Center for Quantum Spintronics, 20.-23.09.2023, Trondheim, Norway
39. Makarov, D.
Magnetoelectronics and Magnetic composites
Summer school of the RTG 2767 "Supracolloidal structures", 26.-28.06.2023, Chemnitz, Germany
40. Makarov, D.
Magnetic textures: from fundamentals to applications
IEEE Magnetics Society Summer School 2023, 11.-16.06.2023, Bari, Italy
41. Makarov, D.
Flexible, printable and self-healable magnetic field sensors for soft robotics and human-machine interfaces
LokoAssist Symposium, 20.-21.04.2023, Darmstadt, Germany

42. Neumann, B.; Fähler, S.
Efficiency-Optimized Setup for Low Grade Waste Heat Harvesting with Shape Memory Alloys
Bochumer Kolloquium für Martensitische Transformationen, 28.-29.09.2023, Bochum, Deutschland
43. Pashkin, O.
Nonlinear response of semiconductor under intense THz excitation
Joint ELI Workshop on Advanced Technologies, 04.-06.12.2023, Szeged, Hungary
44. Podlipec, R.; Štrancar, J.; Barlič, A.; Dolinar, D.; Jenko, M.
New high-resolution microscopy approaches for understanding biocompatibility of hip implants
5th International Symposium on Biomaterials (5ISB), 13.10.2023, Portorož, Slovenia
45. Pylypovskyi, O.
Magnetic soft robots from macro- to nanoscale
Bio Meets Magnetism, 10.02.2023, Dresden, Germany
46. Pylypovskyi, O.
Magnetic domains and flexomagnetism in Cr₂O₃
Intermag, 15.-19.05.2023, Sendai, Japan
47. Pylypovskyi, O.
Local and Nonlocal Effects of Geometry in Curvilinear Magnetic Nanoarchitectures
International Conference on Superconductivity and Magnetism - ICSM2023, 04.-11.05.2023, ölüdeniz-Fethiye, Turkey
48. Pylypovskyi, O.
Nanomagnetism and strain effects in magnetoelectric antiferromagnet Cr₂O₃
IEEE NAP 2023, 10.-15.09.2023, Bratislava, Slovakia
49. Pylypovskyi, O.
Strain-gradient-driven and magnetoelectric operation with order parameters in Cr₂O₃
META 2023, 18.-21.07.2023, Paris, France
50. Pylypovskyi, O.; Borysenko, Y.; Tomilo, A.; Sheka, D.; Makarov, D.
Chiral and anisotropic responses in curved antiferromagnetic spin chains
CMD30 FisMat 2023, 04.-08.09.2023, Milan, Italy
51. Schuba, S.; Zhao, X.; Illing, R.; Schütt, J.; Faßbender, J.; Baraban, L.; Makarov, D.
Antibacterial effect of nanoparticles
BioNanoSens Summer School, 05.-07.06.2023, HZDR, Germany
52. Schultheiß, K.
Pattern recognition with magnons
Advances in Magnetism 2023, 15.-18.01.2023, Moena, Italy
53. Schultheiß, K.
Pattern recognition with magnons
Joint European Magnetic Symposia (JEMS), 27.08.-01.09.2023, Madrid, Spanien
54. Schultheiß, K.
Pattern recognition with magnons
UK Institute of Physics Current Research in Magnetism (CRIM) Meeting, 21.09.2023, London, United Kingdom
55. Schultheiß, K.
Pattern recognition with magnons
IEEE Intermag 2023, 15.-19.03.2023, Sendai, Japan
56. Schultheiß, K.
Pattern recognition with magnons
Trends in MAGnetism 2023, 04.-08.09.2023, Rom, Italien

-
57. Uykur, E.
Optical studies of magnetic kagome metals: Effect of magnetism, localized carriers and phonons
Low-Energy Electrodynamics in Solids 2023, 25.-30.06.2023, Sankt Pölten, Austria
58. Volkov, O.
Magneto-chiral effects in geometrically curved magnetic architectures
NATO Advanced Research Workshop 2023, 25.-28.09.2023, Kyiv, Ukraine
59. Volkov, O.
Local and non-local effects in curvilinear micromagnetism
"Nanomaterials: Applications & Properties" (IEEE NAP) 2023, 11.-15.09.2023, Bratislava, Slovakia
60. Volkov, O.
Local and non-local chirality breaking effects in curvilinear nanoarchitectures
The Joint European Magnetic Symposia (JEMS) 2023, 28.08.-01.09.2023, Madrid, Spain
61. Winnerl, S.
Auger scattering in Landau-quantized graphene and $\text{Hg}_{0.83}\text{Cd}_{0.17}\text{Te}$
24th Conference on Applied Electromagnetics and Communication (ICECOM 2023), 27.-29.09.2023, Dubrovnik, Kroatien
62. Winnerl, S.; Seidl, A.; But, D.; Orlita, M.; Helm, M.
Low energy carrier dynamics in Landau quantized graphene and HgCdTe - Perspectives for optical gain?
22nd International Conference on Electron Dynamics in Semiconductors, Optoelectronics and Nanostructures (EDISON 22), 14.-18.08.2023, Münster, Deutschland
63. Zhou, S.
Defect engineering for oxide thin films by ion irradiation
E-MRS 2023 Fall Meeting, 18.-21.09.2023, Warsaw, Poland

Conferences, workshops, colloquia and seminars

Organization of conferences and workshops

1. Pylypovskyi, O., Wittmann, A.
776. WE-Heraeus-Seminar: Re-thinking Spintronics: From unconventional materials to novel technologies
04. - 06.01.2023, Bad Honnef, Germany
2. Makarov, D., Varvaro, G.
Technical session "Magnetism in geometrically curved and mechanically flexible surfaces", Advances in Magnetism 2023 (AiM2023)
15. - 18.01.2023, Moena, Italy
3. Krasheninnikov, A., Michely, T., Schleberger, M., Facsko, S.
750. WE-Heraeus-Seminar: Defects in Two-dimensional Materials
08. - 12.05.2023, Bad Honnef, Germany
4. Sun, N. X., Yamaguchi, M., Lee, D. W., Yabukami, S., Pylypovskyi, O., Makarov, D
International Symposium on Integrated Magnetism (iSIM2023)
14. - 15.05.2023, Sendai, Japan
5. Makarov, D.
Summer School „Smart Devices and Their Applications"
05. - 07.07.2023, HZDR, Dresden, Germany
6. Winnerl, S.
FWIH Retreat „Spectroscopy meets transport on the nanoscale"
06. - 07.07.2023, Neukirch/Lausitz, Germany
7. Makarov, D., Ortix, C., Varvaro, G., Sheka, D.D.
Minicolloquium "Curvilinear condensed matter", Joint Conference of the Italian and European Community of Condensed Matter Physics (CMD30 FisMat 2023)
04. - 08.09.2023, HZDR, Milan, Italy
8. Erbe, A.; Jamshidi, K.; Zahn, P.
Heraeus-Hütten-Seminar: 1D and 2D Materials and Devices for Electronic and Photonic Applications (NANONET+ Annual Workshop 2023)
11. - 13.09.2023, Sayda, Germany
9. Zhou, S., Pastor, D., Napolitani, E., Chang, G.-E.
E-MRS Fall Meeting 2023 - Symposium G: Ultra-doped semiconductors by non-equilibrium processing for electronic, photonic and spintronic applications
18. - 21.09.2023, Warsaw, Poland
10. Fähler, S., Gottschall, T.
Dresden Days on Magnetocalorics (DDMC 2023)
13. - 14.11.2023, HZDR, Dresden, Germany

Colloquia

1. Golberg, D.
Queensland University of Technology, Australia, and National Institute for Materials Science, Japan
Analysis of 1D and 2D nanomaterial properties and functions using in situ and operando transmission electron microscopy
12.06.2023
2. Krstic, V.
Friedrich-Alexander-Universität Erlangen-Nürnberg, Germany
Helical nanostructures: PT violation & (quantum) cooperative dichroism signatures
02.02.2023

3. Liu, J. P.
University of Texas at Arlington, USA
Magnetic hardening in low-dimensional ferromagnets
20.09.2023
4. Stobbe, S
Technical University of Denmark, Lyngby, Denmark
Dielectric photonic nanocavities with atomic-scale confinement
21.11.2023
5. Vázquez, M.
Instituto de Ciencia de Materiales de Madrid, Spain
Cylindrical micro- and nanowires: From curvature effects on magnetization to sensing applications
07.06.2023
6. Zhao, Q
Forschungszentrum Jülich, Germany
Toward energy efficiency electronics with nanowire transistors
23.06.2023

Seminars

1. Abert, C.
University of Vienna, Austria
Micromagnetic simulation of composite materials and efficient strategies for the solution of inverse magnetostatic problems
06.07.2023
2. Althammer, M.
Technische Universität München, Germany
Polycrystalline metallic thin films coupled to superconducting microwave resonators and bulk acoustic resonator
30.11.2023
3. Bhattacharyya, J.
Indian Institute of Technology Madras, India
Optical spectroscopy of organic semiconductors
02.06.2023
4. Bürkle, M.
Hochschule Karlsruhe
Activities at the mechatronic department of the faculty Mechanical Engineering and Mechatronics
04.07.2023
5. Busse, C.
Universität Siegen, Germany
Epitaxial 2D materials beyond graphene
23.02.2023
6. Escobar-Galindo, R.
Universidad Sevilla, Spain
Surface engineering solutions for additive manufactured materials
27.07.2023
7. Feige, J.
Technische Universität Berlin, Germany
Cosmic signatures in time-resolved records from the Atacama Desert, Chile
26.06.2023
8. Fenclová, K.
Czech Technical University Prague; Czech Republic
Fluoride target material for ^{26}Al measurements by Ion-Laser-InterAction Mass Spectrometry
14.06.2023

9. Gärtner, A.
Senckenberg Museum Dresden, Germany
Ferromanganese crusts and nodules – from supernovae detectors to climate archives
22.02.2023
10. Gomonay, H.
Johannes Gutenberg University of Mainz, Germany
Generation of THz coherent magnons in NiO via ultrafast magneto-elastic effects
22.03.2023
11. Götzhäuser, A.
Universität Bielefeld, Germany
Atomic aspects of crystal growth
27.02.2023
12. Ju, L.
Massachusetts Institute of Technology, USA
Electron Correlation and Coupling with Phonon in the Rhombohedral Stacked Graphene
30.01.2023
13. Karki, A.
Holst Center, The Netherlands
Scalable Large Area All-Printed Sensor Arrays
20.03.2023
14. Khosa, R.
iThemba Labs and University of Cape Town, South Africa
The Vaal, Orange and Olifants: Quantifying the rates of evolution of the Southern African landscape, one river at a time
02.11.2023
15. Kolesnik-Gray, M.
Friedrich-Alexander-Universität Erlangen-Nürnberg, Germany
Thickness-dependent transport properties of black phosphorus multilayers
02.02.2023
16. Komsa, H.-P.
University of Oulu, Finland
Engineering point and extended defects in 2D transition metal dichalcogenides
25.07.2023
17. Kou, L.
Queensland University of Technology, Australia
Ferroelectric and topological catalysis: Novel chemical reactions driven by physics
30.11.2023
18. Liu, X.
Aalto University, Finland
On the way to capturing full light spectrum
15.06.2023
19. Liu, Y.
Center for Quantum Devices, Niels Bohr Institute, University of Copenhagen, Denmark
Ferromagnetic hybrid nanowires for zero-field topological superconductivity
03.07.2023
20. Lofffield, J.
Alfred-Wegener-Institut, Bremerhaven, Germany
 ^{10}Be as synchronization tool in marine sediments
27.10.2023
21. Margeat, O.
Aix-Marseille Université, France
Solution-processed nanocrystals-based thin films for functional surfaces
27.06.2023
22. Mühl, T.
Leibniz-Institut für Festkörper- und Werkstoffforschung Dresden, Germany
Nanowire-based sensors for magnetic microscopy and nano-magnetometry
05.06.2023

23. Nembach, H.
National Institute of Standards and Technology, Boulder, Colorado, USA
Symmetric and anti-symmetric exchange in magnetic multilayers
22.08.2023
24. Park, D.
Technical University of Denmark, Lyngby, Denmark
Emergent piezoelectric and pyroelectric effects in forbidden centrosymmetric oxides
05.12.2023
25. Pflug, T.
Hochschule Mittweida, Germany
Laser-induced lattice reordering characterized by pump-probe reflectometry
13.11.2023
26. Piechotta, M.
Technische Universität Dresden, Germany
Investigation of neutron-induced γ -rays from Ge-nuclides in the region of interest of GERDA/LEGEND
17.05.2023
27. Reimers, S.
Johannes Gutenberg University Mainz, Germany
Equilibrium domain structure antiferromagnetic CuMnAs and Mn₂Au thin film devices
17.07.2023
28. Ritterbusch, F.
University of Science and Technology of China, Hefei, China
Dating of groundwater, ocean water and glacier ice with noble gas radioisotopes
06.07.2023
29. Rybakov, F.
Uppsala University, Sweden
Chirality of magnetic textures and antichiral ferromagnetism
24.04.2023
30. Thalakulam, M.
IISER Thiruvananthapuram, India
Macroscopic manifestation of backaction due to quantum tunnelling of electrons
21.12.2023
31. Thirunavukkuarasu, K.
Florida A&M University, Tallahassee, Florida, USA
Probing spin-phonon coupling in magnetic materials using magneto-Raman spectroscopy
23.06.2023
32. Tiwari, M.
University College London, UK
Nanoengineering interfaces for energy and healthcare
06.03.2023
33. von Hauff, E.
Fraunhofer FEP Dresden, Germany
Material science and interfacial analytics for energy and sensing applications
08.03.2023
34. Wojewoda, O.
Brno University of Technology, Czech Republic
Observing high-k magnons with Mie-resonance-enhanced Brillouin light scattering
12.01.2023
35. Yamaguchi, M.
New Industry Creation Hatchery Center, Tohoku University, Japan
Integrated magnetic noise suppressors to improve telecommunication receiver sensitivity against unwanted radio waves
08.09.2023

Exchange of researchers

Guests at our institute

1. Arias, Rodrigo
Universidad de Chile, Santiago, Chile, 08.01.-21.01.2023
2. Bao, Xilai
Ningbo Institute of Materials Technology and Engineering, Ningbo, China, 05.09.-20.12.2023
3. Bhattacharyya, Jayeeta
Indian Institute of Technology Madras, Chennai, India, 17.05.-15.06.2023
4. Brevis Garrido, Felipe Eduardo
Universidad Técnica Federico Santa María, Valparaíso, Chile, 19.09.2023-31.01.2024
5. Dutta, Rwik
Indian Institute of Science, Education and Research, Bhopal, India, 09.05.-21.07.2023
6. Gallardo, Rodolfo
Universidad Técnica Federico Santa María, Valparaíso, Chile, 13.01.-25.01.2023
7. Gill, Matthew
Memorial University of Newfoundland, St. John's, Canada, 02.05.-31.07.2023
8. Gurusekaran, Arvind
Free University of Bolzano, Italy, 01.04.-29.06.2023
9. Jiang, Yi
University of Cambridge, United Kingdom, 13.07.-30.09.2023
10. Kou, Liangzhi
Queensland University of Technology, Brisbane, Australia, 24.11.-24.12.2023
11. Lee, Ju-Won
Chung-Ang University, Republic of Korea, 01.04.-30.09.2023
12. Li, Ruijia
King's College, Cambridge, United Kingdom, 17.07.-01.09.2023
13. Li, Shengbin
Ningbo Institute of Materials Technology and Engineering, Ningbo, China, 01.07.-20.09.2023
14. Negrete Varela, Claudia Patricia
Universidad Católica del Norte, Antofagasta, Chile, 07.08.2023-28.05.2024
15. Palacios, Gabriel
University of La Verne, USA, 19.06.-23.08.2023
16. Ruiz Arce, David Daniel
Universidad Nacional Autónoma de México, Ensenada, México, 19.01.-16.04.2023
17. Thai Nguyen Vy, Susan
Trinity College Dublin, Ireland, 04.09.-03.11.2023
18. Ünlü, Cumhuri Gökhan
Pamukkale University, Denizli, Turkey, 16.05.2022-31.07.2023
19. Yaseen, Shafayet
The Hong Kong Polytechnic University, 01.08.-30.09.2023

Projects

The projects are listed by funding institution and project starting date. In addition, the institute has several bilateral service collaborations with industrial partners and research institutions. These activities are not included in the following overview.

European Projects

1	07/2018 – 04/2024	Swiss National Science Foundation (SNSF)	SNSF
	SINCHRON – ³²SI a New CHRONometer for nuclear dating		
	<i>Prof. A. Wallner</i>	<i>Phone: 0351 260 3274</i>	<i>a.wallner@hzdr.de</i>
2	01/2019 – 06/2023	European Union	EU
	RADIATE – Research and development with ion beams - Advancing technology in Europe		
	<i>Prof. J. Faßbender</i>	<i>Phone: 0351 260 3096</i>	<i>j.fassbender@hzdr.de</i>
3	10/2020 – 04/2024	European Union	EU
	BIONANOSENS – Deeping collaboration on novel biomolecular electronics based on “smart” nanomaterials		
	<i>Dr. D. Makarov</i>	<i>Phone: 0351 260 3273</i>	<i>d.makarov@hzdr.de</i>
4	11/2020 – 10/2024	European Cooperation in Science and Technology	COST
	FIT4NANO – Focused ion technology for nanomaterials		
	<i>Dr. G. Hlawacek</i>	<i>Phone: 0351 260 3409</i>	<i>g.hlawacek@hzdr.de</i>
5	11/2020 – 01/2025	European Union	EU
	RADICAL – Fundamental breakthrough in detection of atmospheric free radicals		
	<i>Dr. Y. Georgiev</i>	<i>Phone: 0351 260 2321</i>	<i>y.georgiev@hzdr.de</i>
6	05/2021 – 04/2025	European Union	EU
	ChETEC-INFRA – Chemical elements as tracers of the evolution of the cosmos - infrastructures for nuclear astrophysics		
	<i>Prof. A. Wallner</i>	<i>Phone: 0351 260 3274</i>	<i>a.wallner@hzdr.de</i>
7	01/2022 – 12/2024	Research Foundation – Flanders	FWO
	Vortex-driven particle separations in microflows		
	<i>Dr. D. Makarov</i>	<i>Phone: 0351 260 3273</i>	<i>d.makarov@hzdr.de</i>
8	10/2022 – 09/2025	European Union	EU
	MetroPOEM – Metrology for the harmonisation of measurements of environmental pollutants in Europe		
	<i>Dr. S. Winkler</i>	<i>Phone: 0351 260 3802</i>	<i>stephan.winkler@hzdr.de</i>
9	10/2022 – 09/2026	European Union	EU
	NIMFEIA – Nonlinear magnons for reservoir computing in reciprocal space		
	<i>Dr. K. Schultheiß</i>	<i>Phone: 0351 260 2919</i>	<i>k.schultheiss@hzdr.de</i>
10	10/2022 – 09/2026	European Union	EU
	REGO – Cognitive robotic tools for human-centered small-scale multi-robot operations		
	<i>Dr. D. Makarov</i>	<i>Phone: 0351 260 3273</i>	<i>d.makarov@hzdr.de</i>
11	09/2022 – 08/2026	European Union	EU
	ReMade@ARI – Recyclable materials development at analytical research infrastructures		
	<i>Dr. S. Facsko</i>	<i>Phone: 0351 260 2987</i>	<i>s.facsko@hzdr.de</i>
12	01/2023 – 04/2025	European Union	EU
	FLAME – Millisecond flash lamp treatment to improve the performance and reduce cost of SRF acceleration systems		
	<i>Dr. S. Prucnal</i>	<i>Phone: 0351 260 2065</i>	<i>s.prucnal@hzdr.de</i>
13	10/2023 – 09/2025	European Union	EU
	FlexiMMG – Flexible Sensors for portable Magnetomyography: Envisaging innovation and Unveiling opportunities		
	<i>Dr. D. Makarov</i>	<i>Phone: 0351 260 3273</i>	<i>d.makarov@hzdr.de</i>

Helmholtz Association Projects

- | | | | |
|---|-------------------|--|-----|
| 1 | 01/2019 – 12/2023 | Helmholtz-Gemeinschaft | HGF |
| | | CROSSING – Crossing borders and scales - an interdisciplinary approach | |
| | | <i>Dr. J. v. Borany Phone: 0351 260 3378 j.v.borany@hzdr.de</i> | |
| 2 | 12/2019 – 11/2024 | Helmholtz-Gemeinschaft | HGF |
| | | Helmholtz Innovation Lab – FlexiSens | |
| | | <i>Dr. D. Makarov Phone: 0351 260 3273 d.makarov@hzdr.de</i> | |
| 3 | 02/2020 – 01/2025 | Helmholtz-Gemeinschaft | HGF |
| | | Helmholtz Innovation Lab – UltraTherm | |
| | | <i>Dr. L. Rebohle Phone: 0351 260 3368 l.rebohle@hzdr.de</i> | |
| 4 | 02/2022 – 03/2024 | Helmholtz-Gemeinschaft | HGF |
| | | Helmholtz Enterprise – AppIFab – Memristor applications, artificial intelligence and fabrication | |
| | | <i>S. Krüger Phone: 0351 260 2180 s.krueger@hzdr.de</i> | |
| 5 | 04/2023 – 03/2025 | Helmholtz-Gemeinschaft | HGF |
| | | Helmholtz Validation - GasSens – Validation of new gas sensor concept based on 2D material black phosphorus | |
| | | <i>Prof. A. Erbe Phone: 0351 260 2366 a.erbe@hzdr.de</i> | |

German Science Foundation Projects

- | | | | |
|---|-------------------|---|-----|
| 1 | 10/2019 – 03/2023 | Deutsche Forschungsgemeinschaft | DFG |
| | | 3D transport of spin waves in curved nano-membranes | |
| | | <i>Dr. A. Kakay Phone: 0351 260 2689 a.kakay@hzdr.de</i> | |
| 2 | 11/2019 – 04/2023 | Deutsche Forschungsgemeinschaft | DFG |
| | | Functionalization of ultrathin MoS₂ by defect engineering | |
| | | <i>Dr. A. Krasheninnikov Phone: 0351 260 3148 a.krasheninnikov@hzdr.de</i> | |
| 3 | 02/2020 – 05/2023 | Deutsche Forschungsgemeinschaft | DFG |
| | | TRIGUS - Friction-induced interface and structure-changing processes in dry lubrication systems under defined atmospheres | |
| | | <i>Dr. M. Krause Phone: 0351 260 3578 matthias.krause@hzdr.de</i> | |
| 4 | 04/2020 – 08/2024 | Deutsche Forschungsgemeinschaft | DFG |
| | | CurvMag – Non-local chiral interactions in corrugated magnetic nanoshells | |
| | | <i>Dr. D. Makarov Phone: 0351 260 3273 d.makarov@hzdr.de</i> | |
| 5 | 07/2020 – 06/2024 | Deutsche Forschungsgemeinschaft | DFG |
| | | SFB 1415 – Chemistry of synthetic two-dimensional materials | |
| | | <i>Dr. A. Krasheninnikov Phone: 0351 260 3148 a.krasheninnikov@hzdr.de</i> | |
| 6 | 08/2020 – 01/2025 | Deutsche Forschungsgemeinschaft | DFG |
| | | AMSIGE – Topological order and its correlation to self-atom transport in amorphous materials: silicon and germanium as model systems | |
| | | <i>Dr. M. Posselt Phone: 0351 260 3279 m.posselt@hzdr.de</i> | |
| 7 | 09/2020 – 08/2023 | Deutsche Forschungsgemeinschaft | DFG |
| | | 3Dmag – Krümmungsinduzierte Effekte in magnetischen Nanostrukturen | |
| | | <i>Dr. D. Makarov Phone: 0351 260 3273 d.makarov@hzdr.de</i> | |
| 8 | 11/2020 – 10/2024 | Deutsche Forschungsgemeinschaft | DFG |
| | | miracuSi – Room-temperature broadband MIR photodetector based on Si:Te for wafer-scale integration | |
| | | <i>Dr. S. Zhou Phone: 0351 260 2484 s.zhou@hzdr.de</i> | |
| 9 | 12/2020 – 10/2024 | Deutsche Forschungsgemeinschaft | DFG |
| | | MUMAGI II – Microscopic understanding of disorder induced ferromagnetism in B2-alloy thin films II | |
| | | <i>Dr. R. Bali Phone: 0351 260 2919 r.bali@hzdr.de</i> | |

- | | | | |
|----|------------------------------|---|---------------------------------|
| 10 | 01/2021 – 03/2024 | Deutsche Forschungsgemeinschaft | DFG |
| | | eSensus – Compliant and breathable magnetoelectronics: towards electronic proprioception | |
| | <i>Dr. D. Makarov</i> | <i>Phone: 0351 260 3273</i> | <i>d.makarov@hzdr.de</i> |
| 11 | 04/2021 – 04/2025 | Deutsche Forschungsgemeinschaft | DFG |
| | | Hybrid nanomechanical systems including atom-scale defects based on silicon carbide | |
| | <i>Prof. A. Erbe</i> | <i>Phone: 0351 260 2366</i> | <i>a.erbe@hzdr.de</i> |
| 12 | 06/2021 – 04/2025 | Deutsche Forschungsgemeinschaft | DFG |
| | | Hybrid nanomechanical systems including atom-scale defects based on silicon carbide | |
| | <i>Dr. G. Astakhov</i> | <i>Phone: 0351 260 3894</i> | <i>g.astakhov@hzdr.de</i> |
| 13 | 06/2021 – 11/2024 | Deutsche Forschungsgemeinschaft | DFG |
| | | TRANSMAX – Transport and magnetic properties of disordered Cr₂AlC MAX phases | |
| | <i>Dr. R. Bali</i> | <i>Phone: 0351 260 2919</i> | <i>r.bali@hzdr.de</i> |
| 14 | 08/2021 – 07/2024 | Deutsche Forschungsgemeinschaft | DFG |
| | | TOPCURVE – Curvature-induced effects in magnetic nanostructures | |
| | <i>Dr. A. Kakay</i> | <i>Phone: +49 351 260 2689</i> | <i>a.kakay@hzdr.de</i> |
| 15 | 10/2021 – 10/2023 | Deutsche Forschungsgemeinschaft | DFG |
| | | Coupling effects in re-programmable micro-matter | |
| | <i>Dr. S. Fähler</i> | <i>Phone: 0351 260 2775</i> | <i>s.faeher@hzdr.de</i> |
| 16 | 01/2022 – 12/2024 | Deutsche Forschungsgemeinschaft | DFG |
| | | Search for magnetochiral responses in curvilinear geometries | |
| | <i>Dr. O. Volkov</i> | <i>Phone: 0351 260 2186</i> | <i>o.volkov@hzdr.de</i> |
| 17 | 01/2022 – 12/2024 | Deutsche Forschungsgemeinschaft | DFG |
| | | Spin-momentum relaxation dynamics of Dirac fermions in HgTe-based topological insulators | |
| | <i>Dr. G. Astakhov</i> | <i>Phone: 0351 260 3894</i> | <i>g.astakhov@hzdr.de</i> |
| 18 | 01/2022 – 06/2023 | Deutsche Forschungsgemeinschaft | DFG |
| | | Martensitic phase transformations and twinning in epitaxially grown nickel titanium films | |
| | <i>Dr. S. Fähler</i> | <i>Phone: 0351 260 2775</i> | <i>s.faeher@hzdr.de</i> |
| 19 | 02/2022 – 01/2025 | Deutsche Forschungsgemeinschaft | DFG |
| | | NaMeCat – Design of nanostructured noble-metal chalcogenide electrocatalysts for hydrogen evolution reaction | |
| | <i>Dr. A. Krasheninnikov</i> | <i>Phone: 0351 260 3148</i> | <i>a.krasheninnikov@hzdr.de</i> |
| 20 | 02/2022 – 02/2025 | Deutsche Forschungsgemeinschaft | DFG |
| | | Spin wave quantisation and non-linear scattering in non-reciprocal materials | |
| | <i>Dr. H. Schultheiß</i> | <i>Phone: 0351 260 3243</i> | <i>h.schultheiss@hzdr.de</i> |
| 21 | 03/2022 – 09/2025 | Deutsche Forschungsgemeinschaft | DFG |
| | | Interplay between frustrated, correlated and topological quantum electronic states in magnetic Kagome metals | |
| | <i>Dr. E. Uykur</i> | <i>Phone: 0351 260 2494</i> | <i>e.uykur@hzdr.de</i> |
| 22 | 04/2022 – 03/2025 | Deutsche Forschungsgemeinschaft | DFG |
| | | Influences and resistance development of microorganisms on low concentrations of nanomaterials in geometrically defined environments | |
| | <i>Dr. D. Makarov</i> | <i>Phone: 0351 260 3273</i> | <i>d.makarov@hzdr.de</i> |
| 23 | 04/2022 – 03/2025 | Deutsche Forschungsgemeinschaft | DFG |
| | | DNAorigel – A DNA origami-brick system for the fabrication of nanoelectronic elements | |
| | <i>Prof. A. Erbe</i> | <i>Phone: 0351 260 2366</i> | <i>a.erbe@hzdr.de</i> |
| 24 | 04/2022 – 09/2026 | Deutsche Forschungsgemeinschaft | DFG |
| | | Graduiertenkolleg 2767 – Supracolloidal structures: From materials to optical and electronic devices | |
| | <i>Prof. A. Erbe</i> | <i>Phone: 0351 260 2366</i> | <i>a.erbe@hzdr.de</i> |

- | | | | |
|----|-------------------|---|-----|
| 25 | 07/2022 – 06/2024 | Deutsche Forschungsgemeinschaft | DFG |
| | | Strain-tunable magnetic vortex oscillators | |
| | | <i>Dr. V. Iurchuk</i> <i>Phone: 0351 260 2049</i> <i>v.iurchuk@hzdr.de</i> | |
| 26 | 08/2022 – 07/2025 | Deutsche Forschungsgemeinschaft | DFG |
| | | Organic chromophores on ferromagnets illuminated: photochemical and magnetic study | |
| | | <i>Dr. A. Lindner</i> <i>Phone: 0351 260 2435</i> <i>a.lindner@hzdr.de</i> | |
| 27 | 08/2022 – 06/2023 | Deutsche Forschungsgemeinschaft | DFG |
| | | Thermal micro energy harvesting by thermomagnetic film actuation | |
| | | <i>Dr. S. Fähler</i> <i>Phone: 0351 260 2775</i> <i>s.faeher@hzdr.de</i> | |
| 28 | 11/2022 – 10/2024 | Deutsche Forschungsgemeinschaft | DFG |
| | | Effects of atomic defects at lateral and vertical metal-semiconductor interfaces on the properties of two-dimensional transition-metal dichalcogenide heterostructures | |
| | | <i>Dr. A. Krasheninnikov</i> <i>Phone: 0351 260 3148</i> <i>a.krasheninnikov@hzdr.de</i> | |
| 29 | 12/2022 – 11/2025 | Deutsche Forschungsgemeinschaft | DFG |
| | | New avenues to nanofabrication: assembly of vertical heterostructures from nanopatterned two-dimensional materials | |
| | | <i>Dr. A. Krasheninnikov</i> <i>Phone: 0351 260 3148</i> <i>a.krasheninnikov@hzdr.de</i> | |
| 30 | 12/2023 – 11/2026 | Deutsche Forschungsgemeinschaft | DFG |
| | | DeiMoS – The role of defects in 2D materials: From nano-scale structure to macroscopic properties | |
| | | <i>Prof. A. Erbe</i> <i>Phone: 0351 260 2366</i> <i>a.erbe@hzdr.de</i> | |

Federally and Saxony State Funded Projects

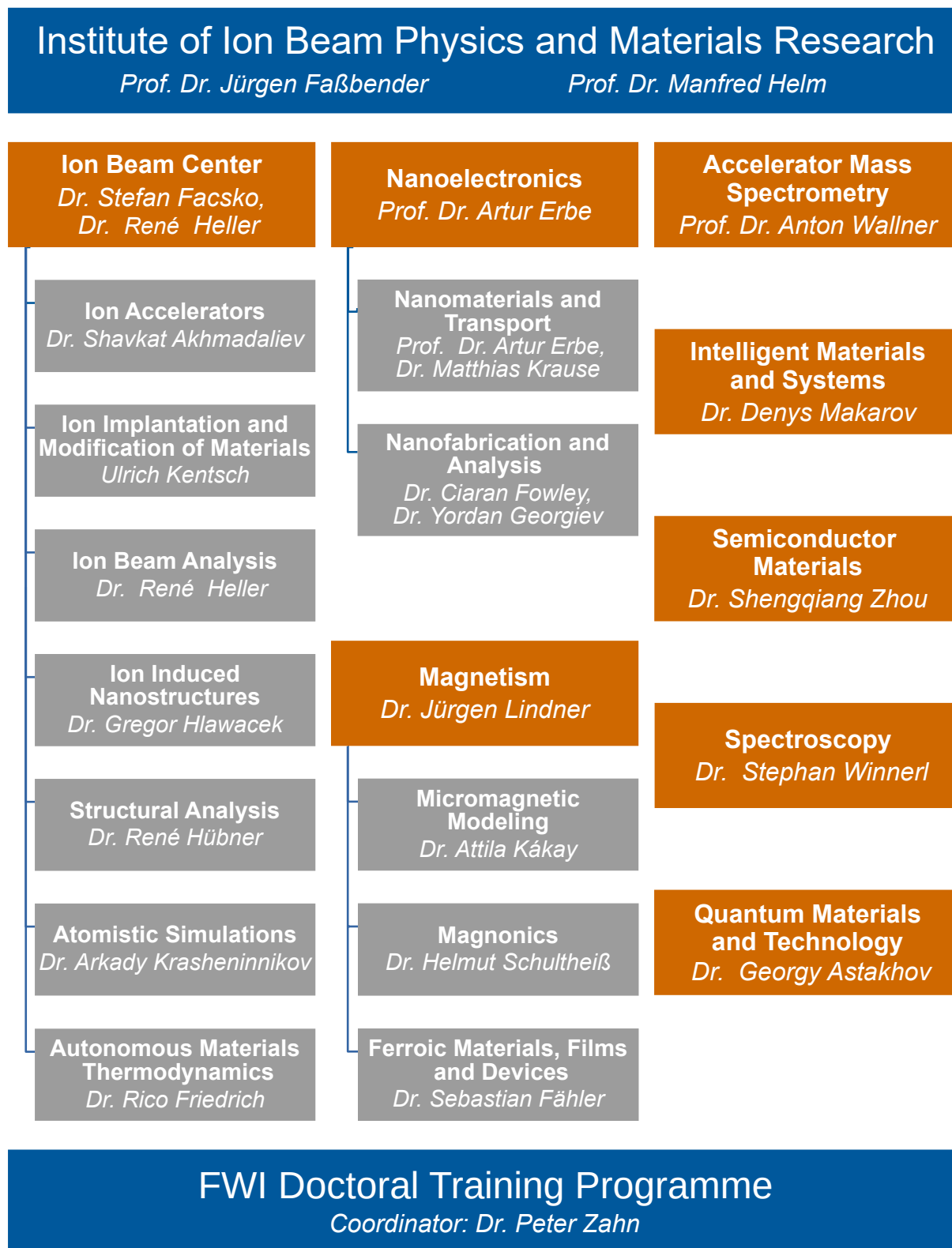
- | | | | |
|---|-------------------|--|------|
| 1 | 10/2019 – 03/2024 | Bundesministerium für Bildung und Forschung | BMBF |
| | | SiGeSn – Group IV-heterostructures for most advanced nanoelectronics devices | |
| | | <i>Dr. Y. Georgiev</i> <i>Phone: 0351 260 2321</i> <i>y.georgiev@hzdr.de</i>
<i>Dr. S. Prucnal</i> <i>Phone: 0351 260 2065</i> <i>s.prucnal@hzdr.de</i> | |
| 2 | 10/2019 – 03/2024 | Bundesministerium für Bildung und Forschung | BMBF |
| | | SPES3 – Black phosphorus in sensitive, selective, and stable sensors | |
| | | <i>Prof. A. Erbe</i> <i>Phone: 0351 260 2366</i> <i>a.erbe@hzdr.de</i> | |
| 3 | 10/2020 – 03/2024 | Bundesministerium für Wirtschaft und Klimaschutz | BMWK |
| | | RoSiLiB – Nanoporous Si anodes of lithium ion batteries by microdroplet quenching | |
| | | <i>Dr. K.-H. Heinig</i> <i>Phone: 0351 260 3288</i> <i>k.h.heinig@hzdr.de</i> | |
| 4 | 12/2020 – 01/2023 | Sächsische Aufbaubank | SAB |
| | | NanoNeuroNet – Nanostructures for neural networks | |
| | | <i>Prof. A. Erbe</i> <i>Phone: 0351 260 2366</i> <i>a.erbe@hzdr.de</i> | |
| 5 | 04/2021 – 03/2024 | Bundesministerium für Bildung und Forschung | BMBF |
| | | MAG4INK – Design and manufacture of printed magnetic field sensors for flexible electronics | |
| | | <i>Dr. D. Makarov</i> <i>Phone: 0351 260 3273</i> <i>d.makarov@hzdr.de</i> | |
| 6 | 07/2021 – 06/2025 | LeibnizX | LX |
| | | ENGRAVE – Defect-engineering in graphene via focused ion beam for tailored van der Waals epitaxy of h-BN | |
| | | <i>Dr. A. Krasheninnikov</i> <i>Phone: 0351 260 3148</i> <i>a.krasheninnikov@hzdr.de</i> | |
| 7 | 05/2022 – 04/2025 | Sächsische Aufbaubank | SAB |
| | | GoFIB – Gallium oxide fabrication with ion beams | |
| | | <i>Dr. G. Hlawacek</i> <i>Phone: 0351 260 3409</i> <i>g.hlawacek@hzdr.de</i> | |
| 8 | 07/2023 – 06/2026 | Sächsische Aufbaubank | SAB |
| | | OptiBeam – Future Mobility - Optical Characterization of Ion Beams | |
| | | <i>Dr. R. Heller</i> <i>Phone: 0351 260 3617</i> <i>r.heller@hzdr.de</i> | |
| 9 | 07/2023 – 06/2026 | Bundesministerium für Bildung und Forschung | BMBF |
| | | FKLIB – Si-wafer integrated solid state lithium ion battery: Coordination, conception, anode fabrication | |
| | | <i>Dr. C. Cherkouk</i> <i>Phone: 0351 260 2749</i> <i>cherkouk@hzdr.de</i> | |

- | | | | |
|----|-------------------|--|------|
| 10 | 09/2023 – 08/2025 | Bundesministerium für Wirtschaft und Klimaschutz | BMWK |
| | | MultiSens – Passive wireless read-out sensors based on additively manufactured multi-material resonant circuits | |
| | | <i>Dr. D. Makarov Phone: 0351 260 3273</i> | |
| | | <i>d.makarov@hzdr.de</i> | |
| 11 | 03/2023 – 05/2023 | Sächs. Staatsministerium f. Wissenschaft, Kultur & Tourismus | SMWK |
| | | Seed grant: PreProposal M.ERA-NET Call 2023 | |
| | | <i>Dr. S. Prucnal Phone: 0351 260 2065</i> | |
| | | <i>s.prucnal@hzdr.de</i> | |
| 12 | 04/2023 – 12/2023 | Sächs. Staatsministerium f. Wissenschaft, Kultur & Tourismus | SMWK |
| | | ScanQ – Scanning quantum magnetometer | |
| | | <i>Dr. G. Astakhov Phone: 0351 260 3894</i> | |
| | | <i>g.astakhov@hzdr.de</i> | |

Personnel Exchange Projects and Society Chairs

- | | | | |
|---|-------------------|--|------|
| 1 | 05/2017 – 12/2025 | Institute of Electrical and Electronics Engineers | IEEE |
| | | IEEE Magnetics Society – German chapter chair | |
| | | <i>Prof. J. Faßbender Phone: 0351 260 3096</i> | |
| | | <i>j.fassbender@hzdr.de</i> | |
| 2 | 03/2021 – 12/2024 | Sino-German-Center | SGC |
| | | Magnetosensitive e-skins for magnetic perception ability of human and soft robots | |
| | | <i>Dr. D. Makarov Phone: 0351 260 3273</i> | |
| | | <i>d.makarov@hzdr.de</i> | |
| 3 | 04/2021 – 03/2023 | Alexander-von-Humboldt-Stiftung | AvH |
| | | Alexander von Humboldt fellowship Dr. Li | |
| | | <i>Prof. M. Helm Phone: 0351 260 2260</i> | |
| | | <i>m.helm@hzdr.de</i> | |
| 4 | 04/2022 – 03/2024 | Alexander-von-Humboldt-Stiftung | AvH |
| | | Alexander von Humboldt fellowship Dr. Roldan | |
| | | <i>Dr. D. Makarov Phone: 0351 260 3273</i> | |
| | | <i>d.makarov@hzdr.de</i> | |
| 5 | 11/2023 – 12/2023 | Alexander-von-Humboldt-Stiftung | AvH |
| | | Alexander von Humboldt fellowship Prof. Kou | |
| | | <i>Dr. A. Krasheninnikov Phone: 0351 260 3148</i> | |
| | | <i>a.krasheninnikov@hzdr.de</i> | |

Organization chart



List of personnel 2023

DIRECTORS		OFFICE	
Prof. Dr. J. Faßbender		S. Gebel	
Prof. Dr. M. Helm		S. Kirch	
SCIENTIFIC STAFF			
Permanent staff		Non-permanent	
Dr. C. Akhmadaliev	Dr. G. Rugel	Dr. A. Anisimov (P)	Dr. D. Koll
Dr. G. Astakhov	Dr. H. Schultheiß	Dr. G. Balasubramanian (P)	Dr. L. Körber (P)
Dr. R. Bali	Prof. Dr. A. Wallner	Dr. Y. Berencén	Dr. S. Kretschmer (P)
Dr. E. Dimakis	Dr. S. Winnerl	Dr. L. Bischoff	Dr. N. Lambeva
Dr. D. Erb	Dr. P. Zahn	Dr. C. Cherkouk (P)	Dr. R. Li (P)
Prof. Dr. A. Erbe	Dr. S. Zhou	Dr. P. Das (P)	Dr. A. Lindner
Dr. S. Facsko		Dr. F. Davies (P)	Dr. S. Lohmann (P)
Dr. S. Fähler		Dr. A. Echresh	Dr. K. Lünser (P)
Dr. C. Fowley		Dr. H.-J. Engelmann (P)	Prof. Dr. W. Möller (P)
Dr. Y. Georgiev		Dr. J.A. Fernandez-Roldan (P)	Dr. I. Mönch (P)
Dr. M. Ghorbani-Asl		Dr. S. Fichter	Dr. R. Podlipec (P)
Dr. R. Heller		Dr. C. Folgner (P)	Dr. M. Posselt (P)
Dr. G. Hlawacek		Dr. R. Friedrich	Dr. O. Pylypovskiy
Dr. R. Hübner		Dr. F. Ganss	Dr. R. Rachamin
Dr. A. Kákay		Dr. A. Garcia Valenzuela (P)	Dr. R. Salikhov (P)
Dr. N. Klingner		Dr. O. Gladii (P)	Dr. K. Schultheiß
Dr. A. Krasheninnikov		Dr. K.-H. Heinig (P)	Dr. M. Sequeira (P)
Dr. M. Krause		Prof. Dr. O. Hellwig	Dr. K. Stübner
Dr. J. Lachner		Dr. M. Hollenbach	Dr. X. Sun
Dr. K. Lenz		Dr. V. Iurchuk (P)	Dr. E. Uykur
Dr. J. Lindner		Dr. M.B. Khan (P)	Dr. I. Veremchuk
Dr. D. Makarov		Dr. C. Kielar (P)	Dr. C. Vivo Vilches (P)
Dr. F. Munnik			Dr. O. Volkov
Dr. A. Pashkin			Dr. S. Winkler
Dr. K. Potzger			Dr. R. Xu (P)
Dr. S. Prucnal			Dr. Y. Zabala (P)
Dr. L. Rebohle			

TECHNICAL STAFF**Permanent staff**

Rb. Aniol
Rm. Aniol
M. Baum
C. Bischoff
T. Döring
S. Eisenwinder
M. Görlich
H. Gude
J. Heinze
A. Henschke
H. Hilliges
Dr. R. Illing
K. Jarschel
U. Kentsch
S. Klare
R. Krause

A. Kunz
K. Lang
H. Lange
U. Lucchesi
F. Ludewig
R. Mester
Dr. R. Narkovic
T. Naumann
C. Neisser
F. Nierobisch
T. Putzke
A. Reichel
B. Scheumann
G. Schnabel
A. Schneider
A. Scholz

T. Schönherr
C. Schubert
T. Schumann
A. Worbs
M. Steinert
T. Tarnow
Dr. T. Voitsekhivska
J. Wagner
A. Weise
A. Weißig
J. Winkelmann
R. Ziegenrücken
L. Zimmermann
J. Zscharschuch

Non-permanent staff

A. Berens (P)
S. Krüger (P)
R. Lehmann (P)
L. Scharf (P)
O. Standke
A. Vollmer
P. Weinreich
S. Worm

(P) Projects

DOCTORAL RESEARCHERS

V. Begeza	C. Heins	K. Mavridou	Y. Sun
M. Bejarano	D. Hilliard	B. Neumann	T. Svetikova Uaman
U. Bektas	N. Jagtap	A. Nihei	X. Wang
O. Bezsmertna	M. Jain	G. Patel	T. Weinert
J. Cabaco Salgado	M.M. Khan	B. Rodriguez Barea	P. Wen
M. Chennur	H. Koyun	F. Samad	S. Wen
M. Goncalves Faria	Yi Li	P. Santra	A. Wieser
Z. Fekri	K. Lin	S. Schuba	J. Wolf
Y. Ge	F. Long	M.S. Shaikh	N. Yuan
S. Ghosh	A. Luferau	A. Shaji Nair	G. Zhang
G. Gray San Martin	P. Makushko	S. Shakeel	A. Zid
P. Heinig	E.S. Oliveros Mata	O. Steuer	S. Zwickel

STUDENTS (diploma / MSc / BSc)

R. Abdelnaby	D. Bhattacharya	A. Rolofs	J.S. Vahle
Abdelfattah	J. Hussain	G. Schmidt	M. Wein
I. Babalola	A. Pandey	B. Siddaveerana	

Wissenschaftlich-Technische Berichte

HZDR-129 | 2024 | ISSN 2191-8708



Institute of Ion Beam Physics and Materials Research
Bautzner Landstrasse 400
01328 Dresden/Germany
Phone +49 351 260-2345
Fax +49 351 260-3285
<https://www.hzdr.de>

Member of the Helmholtz Association